

Topographically Induced Internal Waves and
Enhanced Vertical Mixing in an Estuary

Darrell Richard Mark Sturley


A thesis submitted in partial fulfilment of the
requirements of the Council for National Academic Awards
for the Degree of Doctor of Philosophy.

Sponsoring Establishment:
Polytechnic South West
Department of Marine Science & Technology.

Collaborating Establishment:
Institute of Oceanographic Sciences
Deacon Laboratory.

September 1990

POLYTECHNIC SOUTH WEST LIBRARY SERVICES	
Item No.	9000 34608-9
Class No.	T 551.4609 STU
Cont. No.	X70 2349886

90 0034608 9	TELEPEN
	

REFERENCE ONLY

Abstract

Topographically Induced Internal Waves and Enhanced Vertical Mixing in an Estuary

by

Darrell Richard Mark Sturley

Stratified tidal flow over topographic features has often been thought to give rise to enhanced vertical mixing in estuaries. So far no estimates have been made of the transfer of energy from the barotropic tide to internal waves, and subsequently to increased potential energy of the water column.

Observations have been made over a topographic depression at Cargreen in the Tamar Estuary. This work shows clearly the formation and evolution mechanisms for internal waves on the thermocline, on a neap and a spring tide. On a neap tide an internal wave formed as a nonlinear response to the tidal flow. It subsequently dissipated its energy to mixing through turbulence due to enhanced shear across the thermocline. On the spring tide the internal wave broke *in situ* in the form of a hydraulic jump. Estimates of the energy transfers are in excellent agreement with studies on the continental shelf edge, and in laboratory experiments of wave breaking, and are the first of their kind for estuaries.

A nonlinear, hydrostatic, two-layer numerical model of the flow has been applied to the Cargreen topography, for the neap and spring tide observations. The model predicts the maximum wave heights and energies well, but fails to reproduce the more subtle details of the thermocline response.

Other observations of the flow at Cargreen are put into a conceptual framework based on an internal Froude number, F_i , and it is indicated that $F_i = 2$ to 3 is appropriate for internal wave/hydraulic jump transitions at Cargreen.

Copyright

The copyright of this thesis rests with the author, and no quotation or information may be derived from it, for presentation or publication, without the author's prior written consent.

Declaration

No part of this thesis has been submitted for any award or degree at any other institute. Whilst registered for the degree of Doctor of Philosophy, the author has not been registered for another award of the Council for National Academic Awards or of any other academic institution.

Acknowledgements

I would like to take this opportunity to thank all the unseen helpers who have made this thesis possible, and show them my gratitude.

Supervision

Keith Dyer, David Huntley and Ken George provided excellent supervision and guidance.

Collaboration

Adrian New of IOSDL has been not only a valuable and creative fourth supervisor, but also a supportive and generous friend.

Spar Construction

Alan Hall of IOSDL provided many handy hints and cautionary words in the design phase. Rob Bonner of IOSDL was skilled and crafty in potting the thermistors. Ron Hill, Rod Jones and Barry Davis relieved me of much of the strain of rivetting, cutting, wiring and soldering. Thanks also to Frank Burrell and Trevor Parrott.

Boatwork

Trevor Parrott and Rod Jones were the ideal skippers on our many trips up the Tamar. Sheelagh Matear was the perfect first mate. Other crew members were Clive Sawyer, Andy Prideaux, Mike Bygrave, Tim Moffat, David Huntley, Rob Nicholls, Saad Alani, Jerry McCabe, Keith Dyer, Andy Rees, Bob Hopgood, Steve Foale, and Andrew Turner.

Computing

Geoff Bouch, and the staff of User Support Service at PSW Computing Centre, turned a blind eye to my many abuses of the mainframe. They were more than generous with resources.

Maps, Charts, Photographs and Diagrams

John Wiffill and Heather Kitts showed incredible artistry in making some of my figures. Sheelagh Matear took some great action shots for my first paper.

Finance

Devon County Council and Plymouth Polytechnic, now called Polytechnic South West, generously funded me through their Research Assistantship scheme, and asked for very little teaching in return.

Contents

1	Introduction	1
1.1	Motivation for this research	1
1.2	Outline of thesis structure	3
1.3	The wider project	3
2	A literature review	5
2.1	The continental shelf edge	5
2.2	Shelf topography	8
2.3	Fjords	8
2.4	Estuaries	9
2.5	Models	11
2.6	Estuarine circulation and mixing	12
3	The Cargreen site and survey methods	16
3.1	The Cargreen site	16
3.2	Survey methods	21
3.2.1	T-S Bridge	25
3.2.2	Current Meter	25
3.2.3	Echosounder	26
3.3	Estuarine Thermistor Spar	26
3.4	Survey dates	27
4	Observations of an internal wave during a neap tide	31
4.1	The Maxworthy (1979) model	32
4.2	Ancillary data	35
4.3	Echosounding data	44
4.4	Spar data	46
4.5	Quantitative comparison of data sets	48
4.5.1	Maximum thermocline displacement	49
4.5.2	Position of wave trough	51
4.5.3	Wavelength	53
4.5.4	Thermocline spreading and vertical extent	54
4.5.5	Potential energy excess	55
4.5.6	Wave energy	59
4.6	Conclusion	61
5	Observations of an internal wave during a spring tide	83

5.1	Ancillary data	84
5.2	Echosounding data	91
5.3	Spar data	93
5.4	Quantitative comparison of data sets	94
5.4.1	Froude number analysis	94
5.4.2	Internal wave height	96
5.4.3	Internal wave energy	96
6	Other observations at Cargreen	112
6.1	16 November 1987	112
6.2	30 November 1987	115
6.3	19 April 1989	119
6.4	Froude number analysis	122
7	A model of oscillatory flow in an idealised estuary	125
7.1	Physics of the model and the governing equations	126
7.2	Numerical scheme and radiation conditions	129
7.3	Stability criteria	131
7.4	Model configuration for the Tamar Estuary	132
7.4.1	The choice of other variables	135
7.5	Transients in the model	136
7.6	Model results for the standard configuration and an examination of intratidal behaviour	137
7.7	A non-dimensional analysis and an examination of general behaviour	146
7.7.1	Model results for $\frac{h_1}{H} = 0.4$, in the F', S plane	149
7.7.2	Model results for $\frac{h_1}{H} = 0.2$ in the F', S plane	153
7.8	Energy in the model	155
8	Modelling observed phenomena	156
8.1	Modelling the neap tide observations	157
8.1.1	Model configuration	157
8.1.2	General description	158
8.1.3	Direct comparison with observations	160
8.1.4	Results and comparison	163
8.1.5	Summary	176
8.2	Modelling the spring tide observations	177
8.2.1	Model configuration	177
8.2.2	General description	178
8.2.3	Results and comparison	180
8.2.4	Summary	184
8.3	Conclusions	185
8.3.1	Neap tide	185
8.3.2	Spring tide	185
8.3.3	Strengths and Deficiencies	185
9	Discussion	189

9.1	Observations	189
9.1.1	Neap tide study	189
9.1.2	Spring tide study	191
9.1.3	Summary and future directions	192
9.2	Modelling	195
9.2.1	Neap tide study	195
9.2.2	Spring tide study	196
9.2.3	Summary and future directions	196
9.3	Implications for estuarine circulation	197
9.3.1	Comparison with externally generated mixing	198
9.3.2	The final word	199
	References	201
	Appendix I	A1

List of Figures

3.1	The position of the Tamar Estuary in relation to the South West of Britain.	17
3.2	The position of the Cargreen site in relation to the Tamar Estuary.	18
3.3	The bathymetry at Cargreen which forms the depression in the estuary bed.	19
3.4	A schematic diagram of the bathymetry at Cargreen, showing the relative positions of the buoys and landmarks used to "fix" the position of <i>RV Catfish</i> in the longitudinal transects. . . .	24
3.5	River flow data for the Tamar (Gunnislake) from September to November, 1989 (Courtesy of the National Rivers Authority, South West Region).	28
4.1	The stages which form the conceptual model of lee wave formation	34
4.2	The vertical profiles of salinity at "45" on 6 November 1989. . .	36
4.3	The vertical profiles of temperature at "45" on 6 November 1989.	37
4.4	The vertical profiles of longitudinal velocity at "45" on 6 November 1989.	38
4.5	The vertical profiles of transverse velocity at "45" on 6 November 1989.	39
4.6	The magnitude of the depth averaged velocity at "45" on 6 November 1989.	40
4.7	The vertical profiles of longitudinal Richardson number at "45" on 6 November 1989.	41
4.8	Transect 5 at 12:45 on 6 November 1989.	65
4.9	Transect 6 at 13:00 on 6 November 1989.	66
4.10	Transect 7 at 13:15 on 6 November 1989.	67
4.11	Transect 8 at 13:30 on 6 November 1989.	68
4.12	Transect 9 at 14:15 on 6 November 1989.	69
4.13	Transect 10 at 14:30 on 6 November 1989.	70
4.14	Transect 11 at 14:45 on 6 November 1989.	71
4.15	Transect 12 at 15:15 on 6 November 1989.	72
4.16	Transect 13 at 15:30 on 6 November 1989.	73
4.17	Transect 14 at 15:45 on 6 November 1989.	74
4.18	Transect 15 at 16:00 on 6 November 1989.	75

4.19	Transect 16 at 16:15 on 6 November 1989.	76
4.20	Transect 17 at 16:25 on 6 November 1989.	77
4.21	Transect 18 at 16:45 on 6 November 1989.	78
4.22	The size of the observed maximum thermocline displacement.	79
4.23	The observed position of the wave trough.	80
4.24	The density profiles at positions "VA" and "RH".	81
4.25	The observed total wave energy.	82
5.1	The vertical profiles of salinity at "45" on 15 November 1989.	85
5.2	The vertical profiles of temperature at "45" on 15 November 1989.	86
5.3	The vertical profiles of longitudinal velocity at "45" on 15 November 1989.	87
5.4	The vertical profiles of transverse velocity at "45" on 15 November 1989.	88
5.5	The magnitude of the depth averaged velocity at "45" on 15 November 1989.	89
5.6	The wave height and magnitude of the depth averaged velocity at "45", on 15 November 1989	97
5.7	Transect 1 at 10:00 on 15 November 1989.	100
5.8	Transect 2 at 10:20 on 15 November 1989.	101
5.9	Transect 3 at 10:40 on 15 November 1989.	102
5.10	Transect 4 at 11:00 on 15 November 1989.	103
5.11	Transect 5 at 11:40 on 15 November 1989.	104
5.12	Transect 6 at 11:50 on 15 November 1989.	105
5.13	Transect 7 at 12:00 on 15 November 1989.	106
5.14	Transect 8 at 12:10 on 15 November 1989.	107
5.15	Transect 9 at 12:20 on 15 November 1989.	108
5.16	Transect 10 at 12:35 on 15 November 1989.	109
5.17	Transect 11 at 12:45 on 15 November 1989.	110
5.18	Transect 12 at 13:00 on 15 November 1989.	111
6.1	Longitudinal transects made at 2 hours (top) and 3 hours (bottom) after high water on 16 November 1987, at Cargreen.	114
6.2	Longitudinal transects made at 2 hours (top) and 2.5 hours (bottom) after high water, at Cargreen, on 30 November 1987.	117
6.3	Longitudinal transect made at 3.5 hours after high water on 30 November 1987, at Cargreen.	118
6.4	Acoustic backscatter measured at Cargreen on 19 April 1989.	120
7.1	The model geometry.	127
7.2	The bathymetry at Cargreen.	133
7.3	A model analogue of the Cargreen depression.	134
7.4	Model output for the standard configuration. HW+0 to HW+3.31.	139
7.5	Model output for the standard configuration. HW+3.51 to HW+4.34.	140

7.6	Model output for the standard configuration. HW+4.55 to HW+5.37.	141
7.7	Model output for the standard configuration. HW+5.58 to HW+6.2.	142
7.8	Non-dimensionalised wave height plotted against time.	143
7.9	Non-dimensionalised wavelength plotted against time.	145
7.10	Wave energy in the standard configuration plotted against time.	147
7.11	Normalised maximum wave heights plotted in the F', S plane for $h1/H=0.4$	151
7.12	Normalised maximum wave heights plotted in the F', S plane for $h1/H=0.2$	154
8.1	The magnitude of the depth averaged velocity, from "45" on 6 November 1989, with the sinusoidal approximation used in the model.	159
8.2	Schematic of transect 7 at 13:15 on 6 November 1989.	162
8.3	Schematic of transect 12 at 15:15 on 6 November 1989.	164
8.4	Schematic of transect 18 at 16:45 on 6 November 1989.	165
8.5	Observed maximum thermocline displacement and interfacial displacement from the model, in the sine forcing mode, for 6 November 1989.	166
8.6	Observed maximum thermocline displacement and interfacial displacement from the model, in the real forcing mode, for 6 November 1989.	167
8.7	Observed wave energy on 6 November 1989, together with the predictions from the model in the sine forcing mode.	170
8.8	Observed wave energy on 6 November 1989, together with the predictions from the model in the real forcing mode.	171
8.9	Observed wave trough position, on 6 November 1989, together with the results predicted by the model in the sine forcing mode.	173
8.10	Observed wave trough position, on 6 November 1989, together with the results predicted by the model in the real forcing mode.	174
8.11	The magnitude of the depth averaged velocity, from "45" on 15 November 1989, and the sinusoidal approximation used in the model.	179
8.12	Observed maximum thermocline displacement on 15 November 1989, together with the predictions from the model in the sine forcing mode.	181
8.13	Observed maximum thermocline displacement on 15 November 1989, together with the predictions from the model in the real forcing mode.	182

List of Tables

2.1	Internal wave energy dissipation rates.	6
2.2	Estimates of the efficiency of conversion of internal wave energy to increased potential energy in the water column. . . .	14
3.1	Tidal information relevant to Cargreen (George, 1979) & in parentheses Devonport (Admiralty Tide Tables, 1990).	20
3.2	The distances between the landmarks and buoys used for position fixing.	23
3.3	The performance characteristics of the Estuarine Thermistor Spar.	27
3.4	A summary of the surveys conducted at Cargreen.	29
3.5	A summary of the surveys performed at Beggar's Island in the mouth of the River Lynher.	30
4.1	Predicted times of tides for Cargreen (and Devonport) on 6 November 1989 (Admiralty Tide Tables, 1989).	35
4.2	The potential energy excess and mass excess at "45", "VA" and "RH" at 14:45 and 16:45.	57
5.1	Predicted times of tides for Cargreen (and Devonport) on 15 November 1989 (Admiralty Tide Tables, 1989).	84
5.2	The surface to bottom water density difference in kilograms per cubic metre.	90
5.3	The internal Froude number evolution over the bed depression at Cargreen, on 15 November 1989.	95
6.1	Values of the internal Froude number for the five conditions described in the text.	122

Chapter 1

Introduction

1.1 Motivation for this research

As more extensive exploitation is made of the marine environment, the need to understand the factors governing the driving processes necessarily becomes greater. Estuaries play an important role in that they interface rivers and oceans, and are host to a whole range of human activities (e.g. recreation, fishing, dredging, shipping, industry, and waste disposal). Consequently human influence on estuaries may have implications for the water quality and biological health of the whole marine system.

An understanding of estuarine circulation, mixing and flushing are essential if we are to exploit, manage and monitor the aquatic environment without degrading it. Mixing in estuaries is only partially understood, and mostly in terms of its grossly averaged behaviour. The role of transitional phenomena in stratified estuaries is one of the many important yet unexamined and unquantified processes in oceanography today. Studies from other

parts of the marine environment (e.g. fjords and the continental shelf edge), have indicated that stratified tidal flow over topography may provide an important intermittent contribution to the vertical turbulent salt flux. The work presented in this thesis is an attempt to understand and quantify the role of some these transitional phenomena in a partially stratified estuary.

Transitional phenomena seem to pervade all stratified fluids and study of them in estuaries may shed light on their behaviour in less accessible fluids. As Imberger (1987) succinctly points out

... even at the single-process level, much remains to be learned about the generation, maintenance and collapse of turbulent motions in a stratified shear flow. Estimation of the total or net mixing processes, seems to have received essentially no attention even though it is the norm in nature ... a careful experiment in a well-defined coastal environment may be scientifically much more rewarding than the open ocean experiments generally urged upon us by the funding agencies.

The Tamar is a unique and interesting example of a partially stratified estuary. Its size, stratification, tidal range, topography and location make it ideal for this kind of study. Preliminary studies by New & Dyer (1987b) indicated that the bed depression at Cargreen was a site for the generation of internal waves and mixing. For a first study this is an ideal and convenient site. It is hoped that others will be examined, and that some of the results obtained can be generalised to other topographic features.

The approach that was adopted for this research, was to consider the energetics of the mixing arising from internal wave activity. Estimates of the energy transfer, and the rate of the transfer, from larger scale motions

to smaller scales, is the most useful and rewarding information to be gained from this study.

It is hoped that an increased understanding, leading from this work, will help oceanographers to parameterise small-scale processes in models of estuary and ocean circulation.

1.2 Outline of thesis structure

This introduction and the literature review are intended to inform the reader why this work is important and what other workers have found. Chapter 3, on survey methods, describes where, how, when and under what conditions the observations were made. Chapters 4,5 and 6 describe the hydrodynamic behaviour possible at Cargreen - at neap and spring tides, and under a variety of other conditions. Chapters 7 and 8 describe the model, and are split into theory and application of the model to the observations. The discussion draws together the observations, modelling, theory and the published literature, to show that internal waves and mixing are more important in estuaries than we have so far assumed, and may be large intermittent contributors to the vertical turbulent salt flux.

1.3 The wider project

The observations presented in Chapters 4 and 5 are comprised mostly of echograms and thermal maps. The thermal maps are extremely rich in detail, and a thorough discussion of these will be left to future papers.

These maps were only possible because of the development of the Estuarine Thermistor Spar. It was realised early in the research project that, for accurate estimates of potential energy to be made, the detailed information required on vertical density distribution in the Tamar, could not be acquired by existing instrumentation. (A similar instrument to the Spar was built by IOS Deacon Laboratory, but was lost in the north east Atlantic in a storm in 1987/1988). The period from March 1988 to April 1989 was spent by the author developing and testing the Spar. The Spar construction accounts for a large fraction of the total time and effort spent towards achieving the results presented here. The Spar detail is described in Sturley & Dyer (1990) (Appendix I).

Chapter 2

A literature review

This chapter consists of a brief review of relevant literature on internal tides and waves, and subsequent mixing, produced by stratified tidal flow over topography. The following sections, describing internal wave observations, are ordered according to the scale of motion being considered. The continental shelf edge and shelf topography sections describe much larger scale motions than normally found in estuaries. These are included because the fluid dynamics are essentially the same. A final section is included which briefly discusses estuarine circulation and mixing, and describes a potential role for internal waves. The author would like to recommend the timely review by Huthnance (1989). It is an excellent introduction to this subject.

2.1 The continental shelf edge

In recent years considerable attention has been paid to the formation of internal tides and internal waves near the continental shelf edge. Their po-

Table 2.1: Internal wave energy dissipation rates.

Source	Rate of dissipation
Osborn & Burch (1980)	$\sim 3 \times 10^{-2} W m^{-2}$
Huthnance (1981)	$\sim 10^{-2} W m^{-2}$
Sandstrom & Elliott (1984)	$\sim 5 \times 10^{-2} W m^{-2}$
Holloway (1987)	$\sim 3 \times 10^{-2} W m^{-2}$
Sherwin (1988)	$10^{-3} W m^{-2}$
Sandstrom et al. (1989)	$8 \times 10^{-2} W m^{-2}$

tential for locally enhancing currents and bottom stirring, moving sediment, carrying nutrients, heat and energy, and causing vigorous vertical mixing, sometimes hundreds of kilometres from their source, have all attracted interest.

The energy transferred to internal waves from the barotropic tide, and the energy transferred from internal waves to increased potential energy of the water column, through mixing, are most relevant to this thesis. Baines (1982) has estimated a loss to internal tides of $1.45 \times 10^{10} W$ for the principal semidiurnal constituent M_2 , less than 1% of the total (i.e. global) M_2 tidal dissipation, $\sim 2 \times 10^{12} W$ (Lambeck, 1988). Locally the percentage transfer may be an order of magnitude higher. Fu & Holt (1984) estimated that the loss of tidal energy to internal tides was less than 10% of the dissipation in the Gulf of California.

The total dissipation and subsequent mixing induced by internal tides may be relatively small, but its distribution can be highly localised (in time and space), and may in some cases compare with, or exceed, bottom dissipation by strong tidal currents (Huthnance, 1981; Sherwin, 1988).

Table 2.1 shows a selection of estimates of the rate of energy dissipation of internal tides and waves. These dissipation rates may be highly localised in time (e.g. Osborn & Burch, 1980: dissipation takes place over 10 minutes in a half-tidal cycle), or in space (e.g. Sandstrom & Elliott, 1984: dissipation takes place over a distance of 10km). Holligan et al. (1985) and Thorpe (1987b) provide evidence that dissipation and mixing may take place remote from the generation site. Even though internal tide formation and dissipation may only occupy a small portion of the tidal cycle the intermittent contribution to local mixing is large.

Local vertical mixing near the shelf edge due to internal waves, although poorly quantified, has been shown to be important in supplying nutrients into the euphotic zone, thus increasing productivity (e.g. Pingree et al., 1982). New (1988) has applied an internal tide generation model to the Celtic Sea shelf edge, and shown specific areas where the Richardson number falls below its critical value, for spring tides and summer stratification. One conclusion is that there is scope for mixing in the thermocline through instabilities and overturning. Maze (1987) also noted the possibility of a neap-spring modulation in the mixing. Holloway (1988) established a climatology in stratification and internal tide activity on the Australian N. W. shelf edge. For a fuller description of internal tide and wave activity, and associated mixing, the reader is again referred to Huthnance (1989).

2.2 Shelf topography

Perhaps the most studied topographic feature on the shelf is Stellwagen Bank in Massachusetts Bay (e.g. observations: Halpern, 1971a, 1971b; Haury et al., 1979, 1983; Chereskin, 1983; and theory: Lee & Beardsley, 1974; Maxworthy, 1979; Hibiya, 1986, 1988). The internal waves produced by stratified tidal flow over this feature have shown potential for enhancing primary productivity.

Flow in straits has also received attention (e.g. Ziegenbein, 1969; Garrett, 1976). Hotchkiss & Wunsch (1982) examined the behaviour of the internal tide in Hudson Canyon, and found that internal wave energy appeared to mostly dissipate near the head of the canyon during landward propagation.

There are very few quantitative results, in evidence in the literature, on energy dissipation rates and transfer of energy to mixing, for internal tides produced on the shelf.

2.3 Fjords

The literature contains many accounts of internal waves and hydraulic jumps caused by tidal flow over sills in the mouths of fjords (e.g. Stigebrandt, 1976; Blackford, 1978; Farmer & Smith, 1980; Farmer, 1983; Farmer & Freeland, 1983; Blackford, 1984; Stacey, 1984, 1985; Farmer & Denton, 1985).

Freeland & Farmer (1980), Stacey (1984) and Stigebrandt & Aure (1989) have observed, in different fjords, that a substantial, and seasonally variable,

proportion of the barotropic tidal energy is withdrawn by the internal tide. E.g. Stigebrandt & Aure estimate that 60% to 85% of the barotropic tidal energy is accounted for by the internal tide in some fjords.

Stacey (1985) suggests that the tidally forced nonlinear sill processes, (hydraulic jumps etc.) that occur in Knight Inlet, are usually energetically of less importance than the internal tide.

Data from a large number of fjords on the Norwegian west coast is presented by Stigebrandt & Aure (1989). They separate their fjords into two categories: (i) those with internal tides predominantly generated at the mouths, and (ii) those with tidal jets at the mouths. They found that in the internal tide fjords, the efficiency of conversion of the barotropic tidal energy flux to vertical mixing in the water column, was about 5.6%. In fjords dominated by jets at the mouth the same efficiency is less than 1%. These estimates confirm the importance of internal wave induced mixing in fjord circulation.

2.4 Estuaries

Intense mixing events, which have been believed to be caused by phenomena such as hydraulic jumps and internal waves, have been reported by e.g. Gardner & Smith (1978), Partch & Smith (1978), Partch (1981), and New et al., 1986, 1987. Direct observations of the interaction of stratified tidal flows with topography in estuaries, have been rare (e.g. Gardner, 1984; Dyer & New, 1986; New & Dyer, 1987b; Pietrzak, 1990).

Gardner & Smith (1978) and Partch & Smith (1978) have shown that intense mixing events in the Duwamish Estuary, believed to be triggered by internal hydraulic jumps, have resulted in an erosion of the bottom homogeneous layer, a thickening of the pycnocline and an injection of turbulent fluid into the upper mixed layer. Partch & Smith (1978) postulated that the internal hydraulic jump was caused by the breaking of an internal wave, (produced by flow over topography), unable to travel upstream against the maximum ebb stream. They conclude that intense mixing by this mechanism is highly time dependent, and occurs at times when the flow approaches critical conditions. Large mixing events resulted in patches of mixed water over 4km long. The intense mixing periods described occupied 20% of the time in the tidal cycle, but accounted for 50% of the vertical turbulent salt flux. Thus Gardner & Smith (1978) and Partch & Smith (1978) highlighted a potentially important intermittent mixing mechanism in the Duwamish, but they did not attempt to relate potential energy gained through mixing to internal wave energy, or barotropic tidal energy.

Dyer & New (1986) show echograms of internal wave formation over topography in the Tees Estuary and the Test Estuary. In the Test, internal waves formed over a sharp step, much like the shelf edge. Observations made on a spring tide show that a wave grew in the increasing ebb stream, but eventually broke in the form of an overturning rotor. Observations made on a neap tide show that a wave formed in a similar manner, but progressed upstream in the slackening flow, evolved into solitary waves and eventually broke, away from the generation site. These authors provide no quantitative

analysis at all.

2.5 Models

Many laboratory models of stratified tidal flow over obstacles have been developed, notably those of Lee & Beardsley (1974), Maxworthy (1979), and Lansing & Maxworthy (1984). The results of these are summarised in Chapter 4, and provide a conceptual model.

There are also many analytical and numerical models of the generation of internal tides and waves over topography. The different approaches have been described by Huthnance (1989) as: (i) vertical structure models, (ii) 2 and 3-layered nonlinear models, (iii) calculations of the characteristics of the hyperbolic equation and (iv) full numerical models of realistic topography and stratification.

The layered models probably provide the most suitable analogue to the stratified estuarine environment (e.g. Lee & Su, 1977; Pingree et al., 1983; Wilmott & Edwards, 1987; Maze, 1987). These models predict on-shelf and off-shelf propagating internal tides and current surges, which are in good agreement with observations at the Celtic Sea shelf edge and in Knight Inlet.

Pingree et al. (1983) and Wilmott & Edwards (1987) models are based on the nonlinear long wave equations. These contain no dispersion and the nonlinear effects are balanced by diffusive attenuation. Thus in their model results, effects such as wave breaking, soliton fission and dispersion are not

observed. The idealised on-shelf response, of the modelled thermocline, is a bore-like propagation. This type of model has so far only been applied to the shelf edge and a large inlet. The applicability of this kind of model to the estuarine environment has not yet been tested.

2.6 Estuarine circulation and mixing

Overall mixing and dispersion in estuaries has been discussed extensively (e.g. Dyer, 1973; McDowell & O'Connor, 1977; Fischer et al., 1979; Nihoul, 1978; van de Kreeke, 1986; Wolfe, 1986; Nihoul & Jamart, 1987). In the past this discussion has been in terms of averaged quantities. The many observations in estuaries have reflected this expedient approach, but a growing awareness of its limitations has led to the need to re-examine circulation, as a collection of many temporally and spatially varying processes.

Estuaries ... are dominated by their boundary conditions which are highly and erratically variable in space and time. Yet much of the theory and description of estuarine systems has been given in terms of gross space and time averages. Although such theories have provided a useful basis for academic and practical work, their inadequacies are now apparent, especially when we wish to relate the dynamics of physical, chemical and biological processes (NERC, 1983).

The mechanisms which produce the vertical turbulent salt flux are perhaps the most important processes in an estuary, and often the least understood. The degree to which an estuary is vertically stratified, and the temporal and spatial variations in this stratification, determine in turn the distribution of biological and chemical species. The flushing characteristics

of an estuary are a product of individual mixing events, and yet are still evaluated on the basis of averaged quantities.

Although circulation and mixing in an estuary can be mostly understood, and quantified to first order, by averaged properties, the second order effects are poorly understood and often neglected. In the case of intense mixing periods, these "second order effects" can become temporarily of first order importance, for part or the whole of an estuary.

Specific mechanisms which trigger turbulence and vertical mixing can be categorised as either internal or external (Abraham, 1980). Externally generated mixing results from large shears, primarily arising from the interaction of tidal velocities with estuary bedforms. Internally generated mixing is a product of shear created by motions within the water column. Of most interest is mixing within and across density (salt) gradients. The mechanisms which generate a vertical transport of salt through turbulent fluxes are well defined, but often poorly quantified.

Intermittent, but large, contributors to the vertical salt flux have been especially hard to quantify. In well mixed estuaries bottom generated shear predominates. In highly stratified estuaries turbulence is primarily generated at the density interface(s). In partially stratified estuaries external and internal generation of turbulence, and mixing, may be equally important. The Tamar Estuary, for example, is nominally of the partially mixed type, but undergoes large changes in stratification in the upper and middle reaches, which are modulated by runoff and the spring-neap cycle (authors observations). This behaviour is not unique to the Tamar (e.g. Haas, 1977;

Table 2.2: Estimates of the efficiency of conversion of internal wave energy to increased potential energy in the water column.

$\frac{\Delta PE}{\Delta KE}$	Source
0.25	Koop(1976) $R_i = 0.043$
0.01	Koop(1976) $R_i = 0.2$
0.212 to 0.265	Thorpe(1973)
0.25	Thompson(1980) $R_i = 0.25$
0.26 ± 0.06	McEwan(1983a, 1983b)

Griffin & Leblond, 1990). Thus, during the neap-spring cycle, and seasonally, the relative contributions from internal and external mixing might vary considerably for this type of estuary.

The presence of internal waves may locally enhance shear in stratified estuaries, leading to the possibility of increased turbulent diffusion, or local overturning. Internal wave breaking also provides a potential source of energy for localised mixing. There have been many studies on the importance of internal wave breaking, and internal wave enhanced shear, in the ocean and in laboratory experiments (e.g. Thorpe, 1975; Osborn, 1980; Thompson, 1980; McEwan, 1983a, 1983b; Thorpe, 1987a). From such studies estimates have been made of the efficiency of conversion of internal wave energy to increased potential energy, $\frac{\Delta PE}{\Delta KE}$, in stratified fluids, through turbulent mixing caused by wave breaking or dissipation. Table 2.2 summarises some of these results. One of the conclusions from these studies is that $\frac{\Delta PE}{\Delta KE}$ is highly sensitive to the Richardson number, R_i ,

$$R_i = -\frac{g \delta \rho}{\rho \delta z} \left(\frac{\delta u}{\delta z} \right)^{-2} \quad (2.1)$$

and is largely dependent on the specific breaking or dissipation mechanism, but a value of $\frac{\Delta PE}{\Delta KE}$ in the range 0.1 to 0.25 has often been adopted for practical purposes. Estimates of $\frac{\Delta PE}{\Delta KE}$ from the environment are required to validate and improve these estimates. Because of the large energy densities associated with internal waves, even a value of $\frac{\Delta PE}{\Delta KE} = 0.1$ suggests that wave breaking and dissipation might be an important source of potential energy.

The extent to which internal waves, produced by stratified tidal flow over topography, will be important to any individual estuary will depend in turn on the degree of stratification, the tidal range and the bed topography itself, (e.g. the Tamar is a partially stratified macro-tidal estuary, with many pits and ridges in its bed, suitable for the formation of internal lee waves). For overall estuarine circulation, the contributions to the vertical turbulent salt flux from individual wave events, generated by topographic features, have to be quantified and superimposed, to get a clear idea of the overall importance of this phenomenon. This remains one of the unsolved problems in oceanography.

Chapter 3

The Cargreen site and survey methods

3.1 The Cargreen site

The Tamar Estuary is nominally a partially mixed estuary whose physical behaviour is relatively well understood (e.g. Uncles et al, 1985; George, 1975; George, 1979). Figures 3.1, 3.2 and 3.3 show the geographical position of the Tamar and the position of Cargreen in relation to the whole estuary including bathymetry. Cargreen is situated some 20km down estuary from the tidal limit at Weir Head and approximately 10km from the mouth where the Hamoaze meets Plymouth Sound. The depression in the estuary bed at Cargreen is situated on a constriction of the river by land that juts out from the Cornish side. The main channel at Cargreen is fairly straight for at least one kilometre both landward and seaward. At 1.5km seaward from

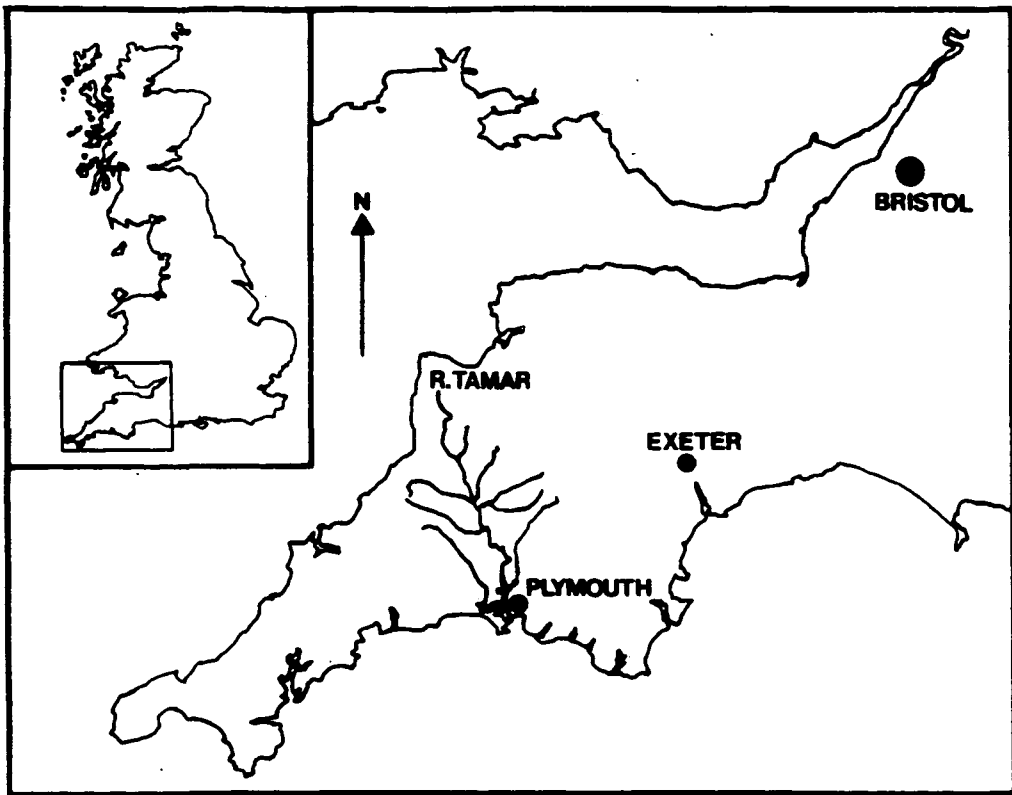


Figure 3.1: The position of the Tamar Estuary in relation to the South West of Britain. The Tamar forms a natural boundary between Devon and Cornwall.

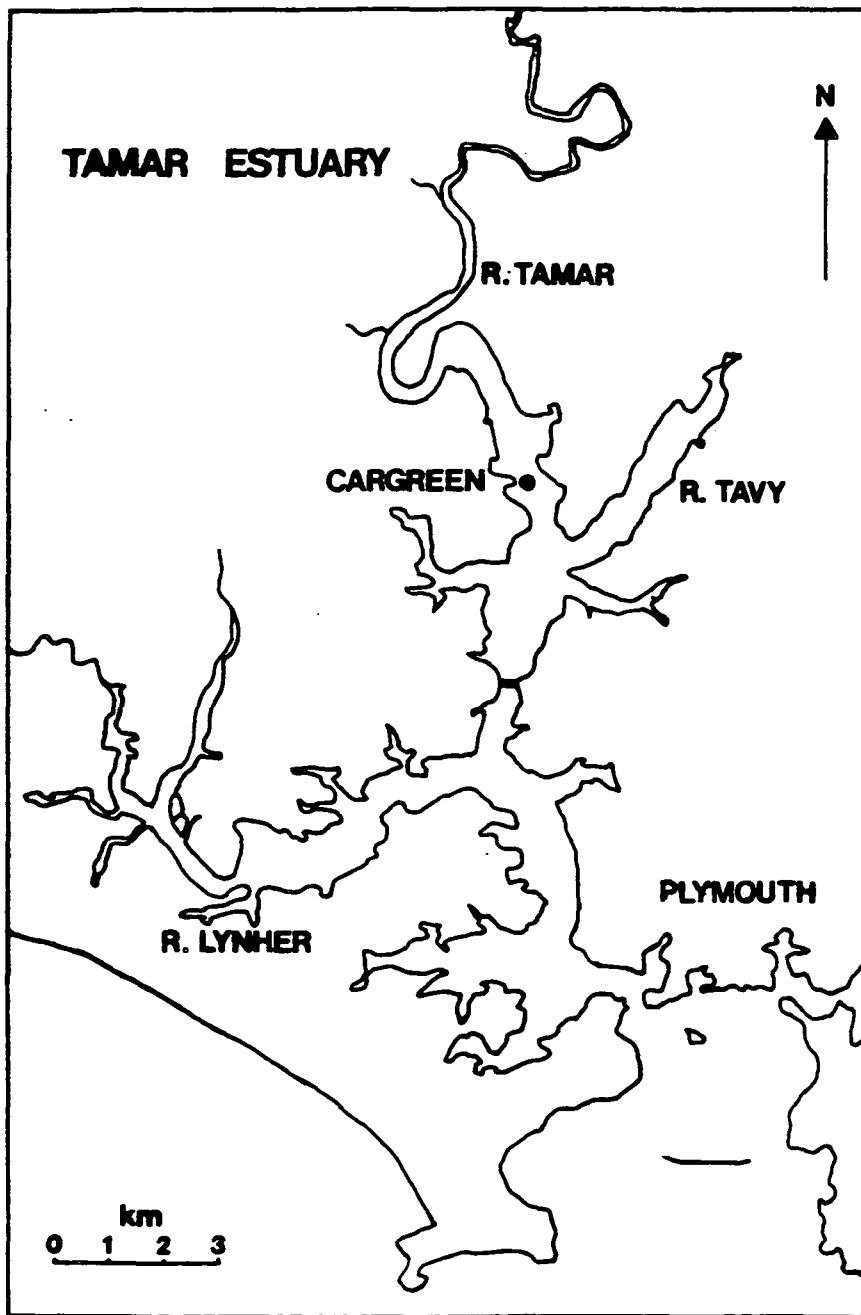


Figure 3.2: The position of the Cargreen site in relation to the Tamar Estuary.

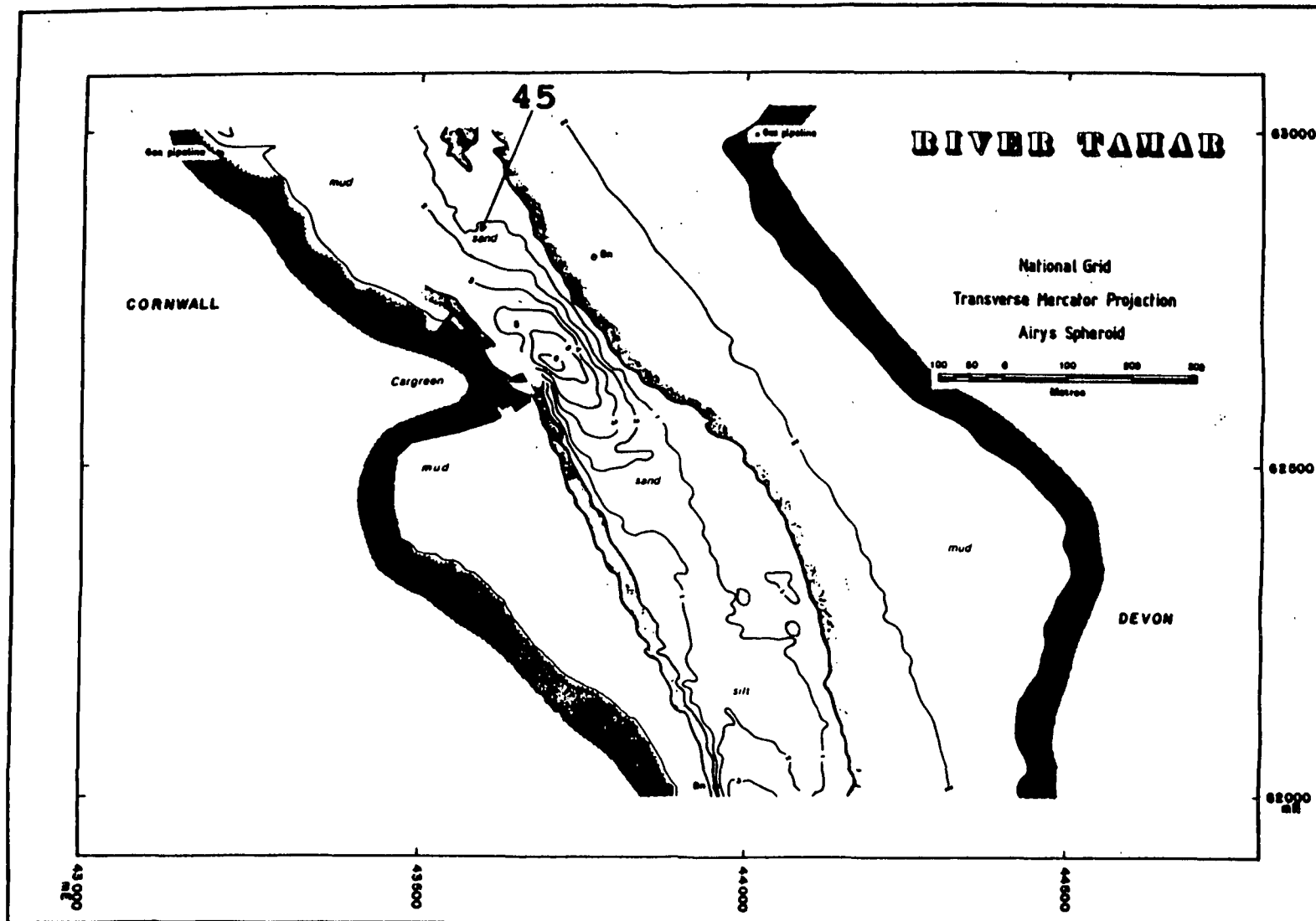


Figure 3.3: The bathymetry at Cargreen which forms the depression in the estuary bed. The position marked "45" indicates where the Eulerian measurements were taken.

Table 3.1: Tidal information relevant to Cargreen (George, 1979) & in parentheses Devonport (Admiralty Tide Tables, 1990).

Tide	Tide height (Chart Datum)	Depth of water over depression	Depth of water outside of depression
MHWS	5.6 <i>m</i> (5.5 <i>m</i>)	11.6 <i>m</i>	6.6 <i>m</i>
MHWN	4.5 <i>m</i> (4.4 <i>m</i>)	10.5 <i>m</i>	5.5 <i>m</i>
MLWN	2.2 <i>m</i> (2.2 <i>m</i>)	8.2 <i>m</i>	3.2 <i>m</i>
MLWS	0.7 <i>m</i> (0.8 <i>m</i>)	6.7 <i>m</i>	1.7 <i>m</i>
Mean Spring range		4.9 <i>m</i> (4.7 <i>m</i>)	
Mean Neap range		2.3 <i>m</i> (2.2 <i>m</i>)	

Cargreen the Tamar is joined by the Tavy and 3*km* landward the Tamar bends in a 180° incised meander at Hole's Hole. The bathymetry of the depression at Cargreen consists of ragged ellipses, which describe a long deep groove in the main estuary channel. On either side of the main channel are tidal mud flats. The centre of the depression is 6*m* deep, referred to Chart Datum (approximately the level of Lowest Astronomical Tide), while the bed landward and seaward of the depression is consistently flat at around 1*m* below C.D.

The tidal information for Cargreen is presented in table 3.1 (George, 1979). The data for Devonport is displayed in parentheses (Admiralty Tide Tables, 1990). Devonport is 10*km* seaward of Cargreen.

The tidal stream, in this region of the estuary, can reach over 1*ms*⁻¹ on spring tides in the top few metres of the water column (the author's observations). Together these factors make for very interesting hydrodynamics but very difficult boatwork.

Although the Tamar Estuary is nominally partially mixed its density

profile at Cargreen may range from well mixed to highly stratified. This is determined by the Tamar's highly variable fresh water input, tidal phase, wind strength, and hydrodynamics.

3.2 Survey methods

Early attempts to measure internal wave activity at Cargreen centred around making combinations of Eulerian and kinematic observations on a falling tide, mostly at neaps. It was early established that flood streams and spring tides were often too vigorous for the reliable formation of internal waves, and tended to give rise to either hydraulic jump conditions, or a well mixed stratification upstream of the depression, which precluded the possibility of topographically induced waves and mixing.

The Eulerian observations consisted of making vertical temperature and salinity profiles with a T-S bridge and tidal stream measurements with a current meter, on the upstream slope of the depression. These measurements represent the upstream, or approach, conditions for internal wave formation, and were obtained from a small launch moored at Cargreen Yacht Club buoy "45" (see figure 3.3). Measurements were taken at about 20 minute intervals at 0.5m or 1m vertical spacing.

The first kinematic observations consisted of making axial transects of the estuary in another launch using a 200kHz echosounder. The resulting echograms identified mid-water backscatter events and provided a virtual "snapshot" of the water column at short intervals. These sets of obser-

vations, however fascinating in their detail, were too incomplete to make energy or mixing estimates. One problem was that the backscatter events on the echograms may have been due to a variety of causes, not just the presence of a density gradient. The Eulerian measurements tended to support the hypothesis that the dark return lines on the echograms were the pycnocline (present as both a halocline and a thermocline), but there were ambiguities. Also the relatively long separation between Eulerian measurements meant that short lived mixing patches may have escaped detection. The current meter and the T-S bridge are instruments which can measure only with some subjectivity. The instruments have to be balanced by hand and eye in a variable field which may fluctuate wildly in time and space.

The Estuarine Thermistor Spar was developed to remove these problems. This instrument is capable of making temperature measurements at 25cm vertical separation, at 10Hz, in the top 4m of the water column, with a resolution of 0.005°C. Together with echosounding this allows one to examine the surface waters in fine detail. The final survey method comprised a combination of Eulerian observations from "45" and kinematic observations using the echosounder and Spar. The launch *RV Catfish* of the Institute of Marine Studies at Polytechnic South West was used to deploy these last two instruments.

Axial transects of the estuary were made in *RV Catfish* along a trot of buoys used for yacht moorings. The transects were at most 1km in length and the position of *RV Catfish* at various points was "fixed" using the yacht buoys and landmarks. The time of fix was also noted. A shore based survey

Table 3.2: The distances between the landmarks and buoys used for position fixing.

Portion of Transect	Distance in metres
BLQ - LQ	134 <i>m</i>
LQ - BR	87 <i>m</i>
BR - GP	46 <i>m</i>
GP - 45	59 <i>m</i>
45 - VI	78 <i>m</i>
VI - SW	27 <i>m</i>
SW - WP	70 <i>m</i>
WP - CH	59 <i>m</i>
CH - VA	144 <i>m</i>

was conducted after the field work to calculate the distances between the buoys and landmarks. This was performed using a theodolite and electronic distance measuring (infra red) equipment, locating the positions to within $\pm 3m$. Table 3.2 shows the distances between the fixes.

Figure 3.4 shows the bathymetry at Cargreen schematically. The positions of some of the fixes are indicated.

The axial surveys were limited in extent spatially by water depth being less than the Spar length (4*m*). When necessary the Spar was raised from the water to deploy only 2*m* or 3*m* of its length. This meant that the water over the depression was never examined right down to the bed. The thermocline, when present, sometimes went below the bottom sensor of the Spar and was lost from the data.

The surveys all started at slack water, or soon after, and continued until the following slack water, and for an hour or two longer when possible. The

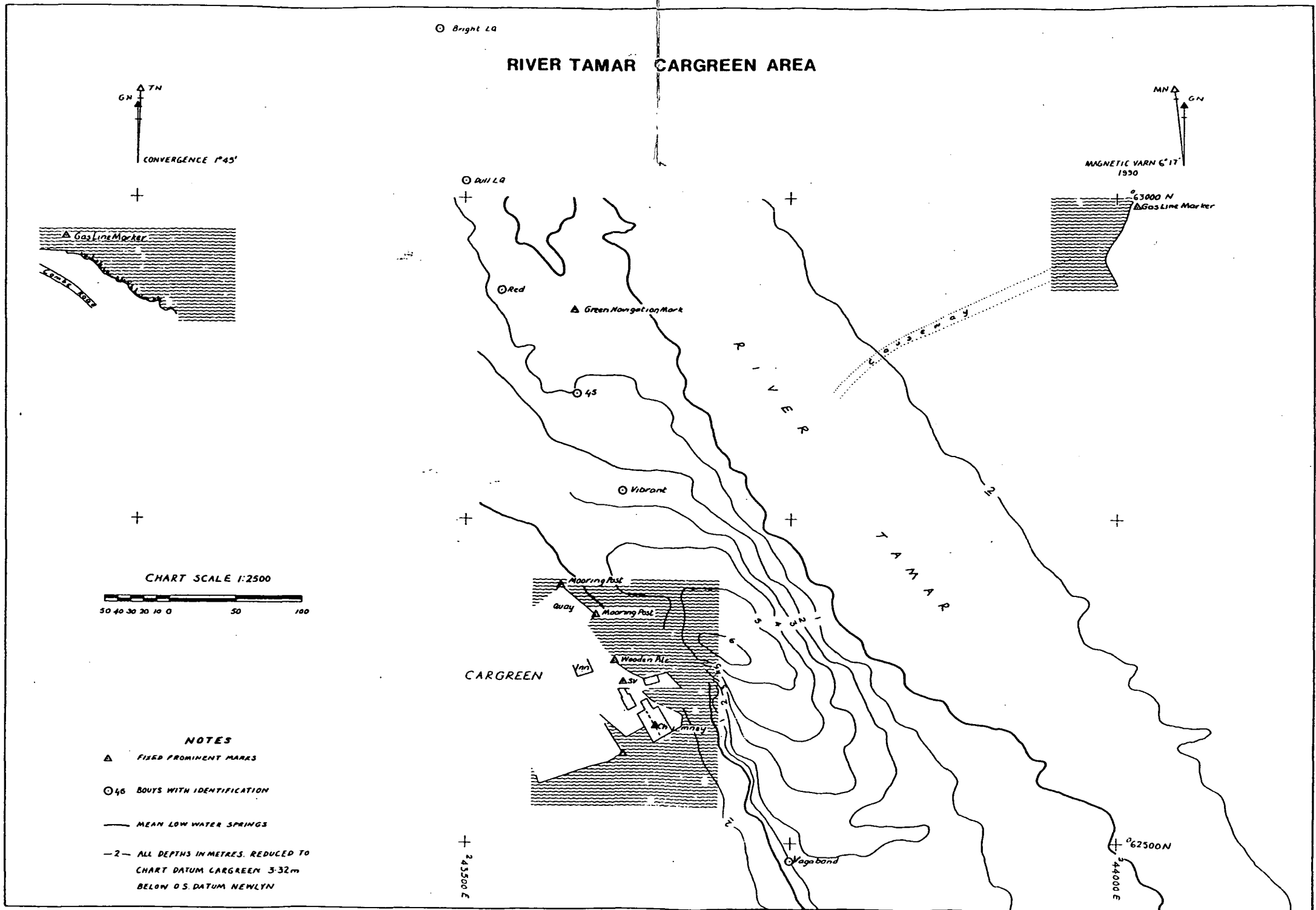


Figure 3.4: A schematic diagram of the bathymetry at Cargreen, showing the relative positions of the buoys and landmarks used to "fix" the position of *RV Catfish* in the longitudinal transects.

numerical model and early surveys showed that the ebb stream was the most interesting time, and that wave and mixing structures could linger for a short while at the beginning of the flood stream.

Due to constraints such as weather, lack of daylight in winter (the time of year with the largest runoff, and hence enhanced stratification), and the logistics of working at Cargreen with two launches and crew, it was not possible to survey for longer than about 7 or 8 hours continuously.

3.2.1 T-S Bridge

The instrument used was an MC-5 in-situ temperature and salinity bridge (Electronic Switch Gear Ltd.). The salinity is measured by balancing the resistance (or conductivity) of the water in a Wheatstone bridge. The temperature is obtained by balancing the resistance of a semiconductor thermistor in the same device. The bridge measures salinity to an accuracy of $\pm 0.1ppt$ and the temperature to $\pm 0.1^{\circ}C$.

Depth was calculated from wire length out and angle. A typical error in the estimation of depth might be 5–10% between metre marks (or 20–40cm overall).

3.2.2 Current Meter

The direct reading current meter, NBA model DNC-3, measures and displays current velocity in the range $0 - 2.5ms^{-1}$ with an accuracy of $\pm 2\%$ and direction in the range $0 - 360^{\circ}$ (magnetic) with an accuracy of $\pm 10^{\circ}$. This impeller type current meter has a typical stall speed of a few cms^{-1} .

3.2.3 Echosounder

The echosounder was a Raytheon DE-719B Portable Precision Survey Type Fathometer. The instrument provides a detailed recording in up to 60m of water depth. The transducer is an 8° (wide beam) angle type and was mounted in the hull of *RV Catfish*. The depth range was set to 0 – 16.5m and the echogram paper speed at 2.5cm per minute. The temporal scale on the echograms is then approximately 10cm = 240s. Small indentations are also present on the echograms at one minute intervals. The echogram paper is lined horizontally. These lines indicate a 0.5m spacing in the vertical.

3.3 Estuarine Thermistor Spar

The Estuarine Thermistor Spar was designed and built for the purpose of making fine temperature measurements in the top few metres of the water column with small vertical resolution and with fast time response. As temperature and salinity can be well correlated in the Tamar Estuary over periods of a few hours it was thought that one could infer salinity from other measurements made in conjunction with the Spar. The problem of detecting internal waves and subsequent mixing required an instrument capable of this performance. During the period between November 1987 and February 1989 the Spar was conceived, constructed, tested and made fit for use. The design characteristics are presented in Sturley & Dyer (1990) (see Appendix I). The Spar's performance is summarised in table 3.3.

Because of low runoff during the summer of 1989 there was insufficient

Table 3.3: The performance characteristics of the Estuarine Thermistor Spar.

Characteristic	Performance
Working temperature range	0 – 20.48°C
Temperature resolution	Theoretically, $\geq 0.005^\circ\text{C}$
Temperature accuracy	$\leq 0.1^\circ\text{C}$
Maximum depth of bottom sensor	3.75m
Minimum depth of top sensor	0.05m
Number of sensors	15 thermistors and 1 dummy
Vertical separation of sensors	0.25m
Sampling rate	10Hz
Anti-aliasing filter	Nyquist frequency 5Hz 2nd order roll off
Total Spar length	6m (4m in water)
A to D conversion	12 bits (0 – 4095)
Size of data samples	Virtually any size but typically 4096, 6144, 8096, ..., per sensor stored as a block

stratification for use of the Spar until November of that year. The Tamar river flow for the period of interest is depicted in figure 3.5 with the dates of the two most extensive surveys (6 November 1989, 15 November 1989) indicated.

3.4 Survey dates

There have been 12 surveys at Cargreen overall. The early surveys consisted of echosounding and Eulerian measurements, and the later ones included the deployment of the Spar. Table 3.4 shows the dates, tides, equipment deployed and which phenomena, if any, were observed.

Additional surveys were performed at an alternative depression in the Tamar bed which was thought to be a promising site for the generation of

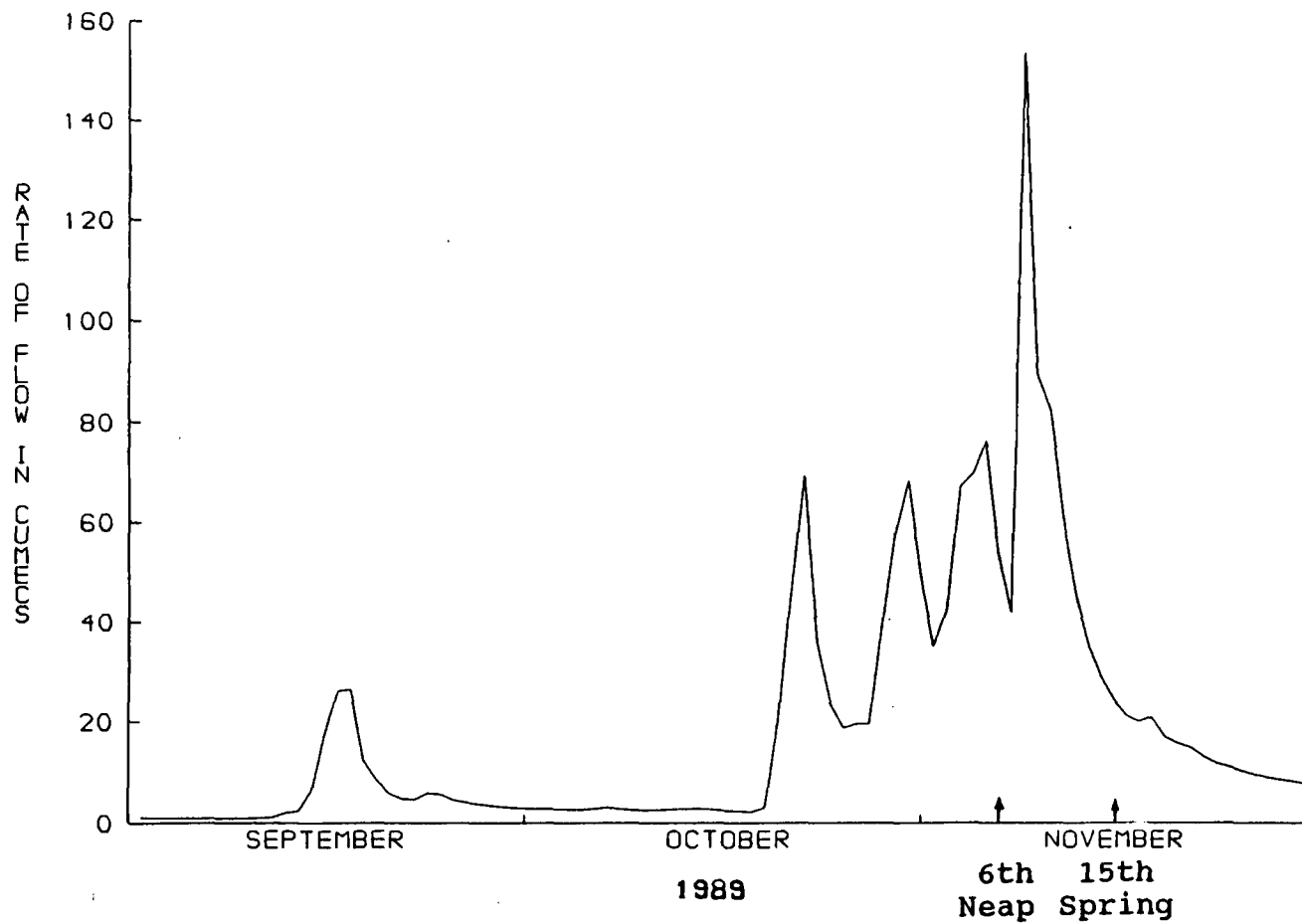


Figure 3.5: River flow data for the Tamar (Gunnislake) from September to November, 1989 (Courtesy of the National Rivers Authority, South West Region).

Table 3.4: A summary of the surveys conducted at Cargreen.

Date	Tide	Equipment deployed	Observations
1/10/87	Neaps Ebb stream	Echosounder T-S Bridge	No stratification No waves
16/11/87	Neaps Ebb stream	Echosounder T-S Bridge Current meter	Strong stratification (2 layers) Large group of small amplitude internal waves
30/11/87	Moderate stratification (2 layers) with a thick thermocline Lee wave and smaller internal waves
14/12/87	Weak stratification and a few internal waves
15/1/88	Strong stratification Lee wave
26/2/88	Weakly stratified at surface Lee wave
15/6/88	Neaps, Ebb and Flood stream	..	No stratification No waves
17/10/88	Neaps Ebb stream	Echosounder T-S Bridge 2 Self-recording Current meters	Strong stratification Lee wave and evolution into solitary internal waves
17/4/89	Neaps Ebb stream	Echosounder T-S Bridge Current meter Spar	Weak stratification No waves
19/4/89	Springs Ebb stream	..	Weak stratification Kelvin-Helmholtz billows on interface at low tide
6/11/89	Neaps Ebb stream	..	Strong stratification Lee wave and mixing
15/11/89	Springs Ebb stream	..	Moderate stratification Collapsed lee wave

Table 3.5: A summary of the surveys performed at Beggar's Island in the mouth of the River Lynher.

Date	Tide	Equipment deployed	Observations
15/12/87	Neaps Flood stream	Echosounder	Strong stratification Lee wave and internal waves
12/2/88	Neaps Ebb stream	Echosounder T-S Bridge Current meter	Moderate stratification A few internal waves
31/10/89	Springs Flood stream	Echosounder T-S Bridge Current meter Spar	Moderate stratification Internal waves

internal waves and mixing. This site is at Beggar's Island in the mouth of the River Lynher, a tributary of the Tamar, which joins the Hamoaze near Devonport. The behaviour at this site may be useful for comparison with that at Cargreen in future studies. These surveys are similarly summarised in table 3.5.

Chapter 4

Observations of an internal wave during a neap tide

This chapter describes a conceptual model of stratified tidal flow over topography and a set of observations made in the Tamar at Cargreen on 6 November 1989. The data sets, collected by different means, are discussed qualitatively in separate sections, and then combined quantitatively in the last section. The data consists of Eulerian measurements of salinity, temperature, current velocity and direction, at station "45", and echosoundings and Spar data collected on longitudinal transects. The observations show the formation of an internal wave by interaction of the tidal ebb stream with the topographic depression. The wave evolved with the varying stream, and intense shear across the thermocline at the seaward end of the wave resulted in vigorous vertical mixing. Estimates are made of the energies in the wave and mixing.

4.1 The Maxworthy (1979) model

A conceptual model of lee wave formation has been derived from Maxworthy (1979) and Lee & Beardsley (1974), but is referred to in this thesis as the Maxworthy (1979) model. The model is described at the beginning of this chapter to aid the reader trying to 'visualise' this neap tide behaviour. Maxworthy's and Lee & Beardsley's main concern was the evolution of lee waves, formed from stratified tidal flow over a submarine ridge, into solitary waves. Maxworthy used a simple laboratory model to reproduce the tidal flow of a stratified fluid over a three-dimensional obstacle. The model results, the observations of Halpern (1971b), and the mathematical theory and laboratory experiments of Lee & Beardsley, were combined in Maxworthy's "Discussion". Maxworthy's analysis was for a topographic ridge and sinusoidal tidal flow, analogous to Stellwagen Bank in Massachusetts Bay, but the model is equally applicable to other topographic forms:

As the ebb tide proceeds a lee wave field is built up behind the ridge by the supercritical flow at that location. The magnitude of this depressed region, i.e., length, height, shape, depends on many factors: the basic stratification, the magnitude and direction of the tidal current as a function of time, and the topographic shape.

As the ebb tide slackens the depression that has developed a large phase velocity in order to remain stationary in the supercritical flow over the ridge now moves upstream against the tide. As this front propagates, and is also convected, away from the ridge it evolves into a series of solitary waves the number and magnitude of which depend on the characteristics of the depression and the stratification.

Equivalently, Lee & Beardsley proposed the following:

Our overall picture of the generation mechanism contains three distinct phases. Phase 1 is the formation of an initial warm front due to partial blocking of the stratified flow ... Phase 2 is the nonlinear steepening of this internal front, and Phase 3 is the formation of new waves due to the interplay of dispersion and nonlinearity.

Unlike Maxworthy, Lee & Beardsley stressed the importance of the nonlinear steepening of the wave in Phase 2 as an evolutionary process. In particular, the balance between nonlinear steepening and dispersion seems to govern the formation of new waves from the initial wave form in Phase 3.

In the observations described in this chapter it is apparent that a lee wave formed over the landward slope of the Cargreen depression (Phase 1), as described by Maxworthy and Lee & Beardsley. Nonlinear steepening seemed to play an important role in the waves evolution (Phase 2), but fission into solitary waves was not observed (Phase 3).

These two descriptions, and the authors observations, can be combined into one conceptual model. The stages in this model are depicted schematically in figure 4.1 (note that a bed depression is shown). In figure 4.1 (a),(b) and (c) depict the formation and growth of a lee wave over a bed depression in an accelerating stratified tidal flow. After maximum stream the lee wave, as Maxworthy proposed, propagates into the slackening ebb, (d),(e). In doing so it undergoes nonlinear steepening, as proposed by Lee & Beardsley, (d). Finally, as the tidal stream slackens beyond some critical value, if steepening and dispersive effects become comparable, fission into solitary waves may occur, (e),(f).

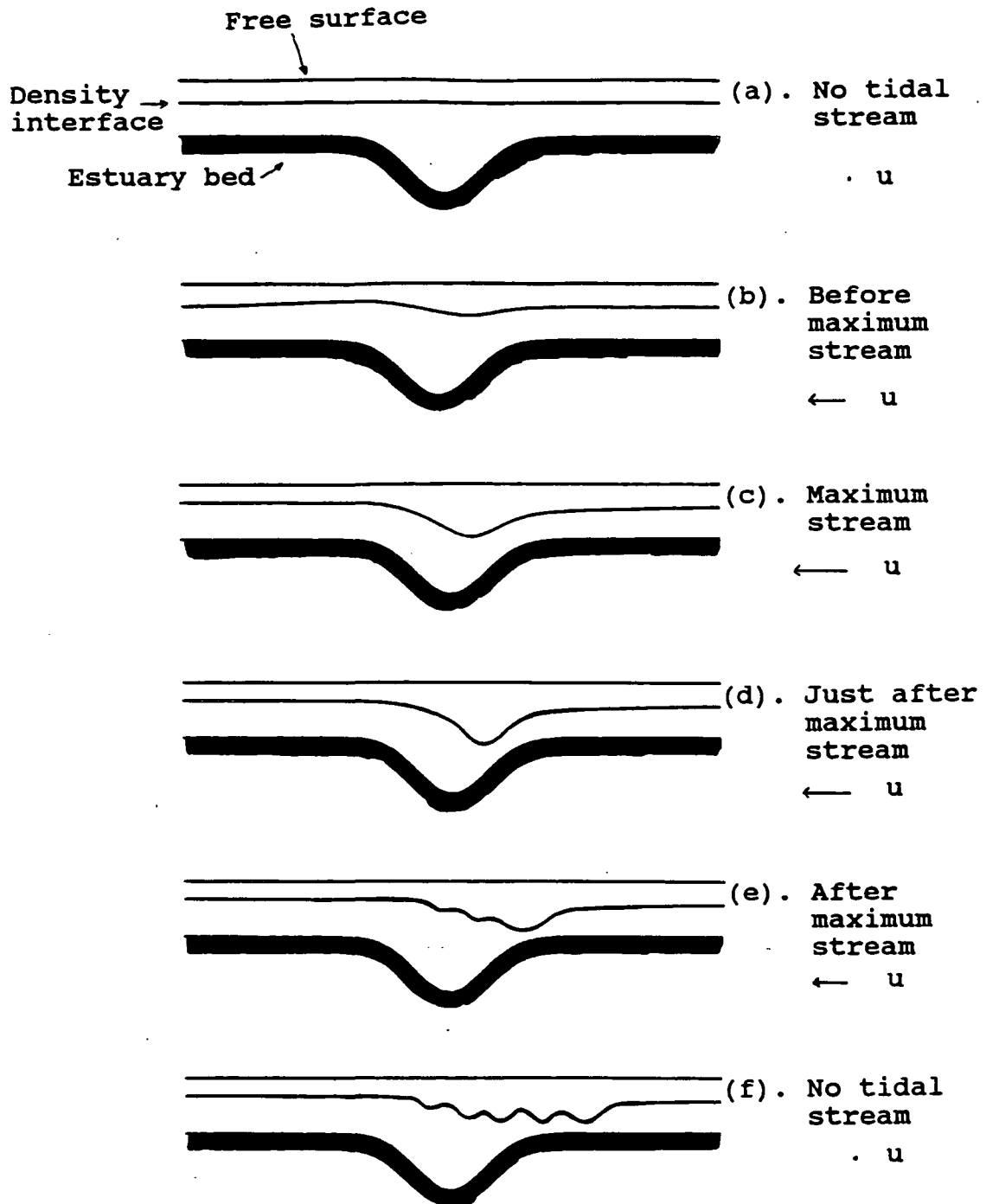


Figure 4.1: The stages which form the conceptual model of lee wave formation. (a),(b),(c) The wave grows over the landward slope of the bed depression in the accelerating tidal stream. (d) After maximum tide the wave steepens nonlinearly. (d),(e) The wave propagates into the slackening stream. (e),(f) The wave may fission into solitary waves through a balance between dispersion and nonlinear steepening.

Table 4.1: Predicted times of tides for Cargreen (and Devonport) on 6 November 1989 (Admiralty Tide Tables, 1989).

Slack Water	Time (GMT)	Tide height above C.D.
High Water	09:59 (09:49)	4.7m (4.6m)
Low Water	16:38 (16:18)	2.1m (2.1m)

4.2 Ancillary data

The predicted tides for Cargreen and Devonport are shown in table 4.1 (Admiralty Tide Tables, 1989). *RV Bass* was moored at position "45" (see figures 3.3 and 3.4) taking vertical profiles of temperature, salinity, current velocity and direction, at twenty minute intervals from 11:20 to 15:40. The profiles are presented in figures 4.2 to 4.5. Figure 4.6 shows the magnitude of the depth averaged velocity, \bar{u} .

The salinity and temperature profiles show that the estuary was stratified into two layers, separated by a region of strong gradient in temperature and salinity. This gradient weakened toward the end of the exercise as the thermocline, and halocline, thickened vertically, and as less saline and less stratified water was advected down the estuary. However, the mean layer density difference was around 16kgm^{-3} throughout the study period.

The station "45" was landward (upstream) of the wave trough for most of the period, until the wave propagated landward in the latter stages. However, as figures 4.2 to 4.5 show, the profiles from "45" were still greatly influenced by the wave presence. The profiles show a change with time in the depth of both the thermocline and halocline, reflecting the formation

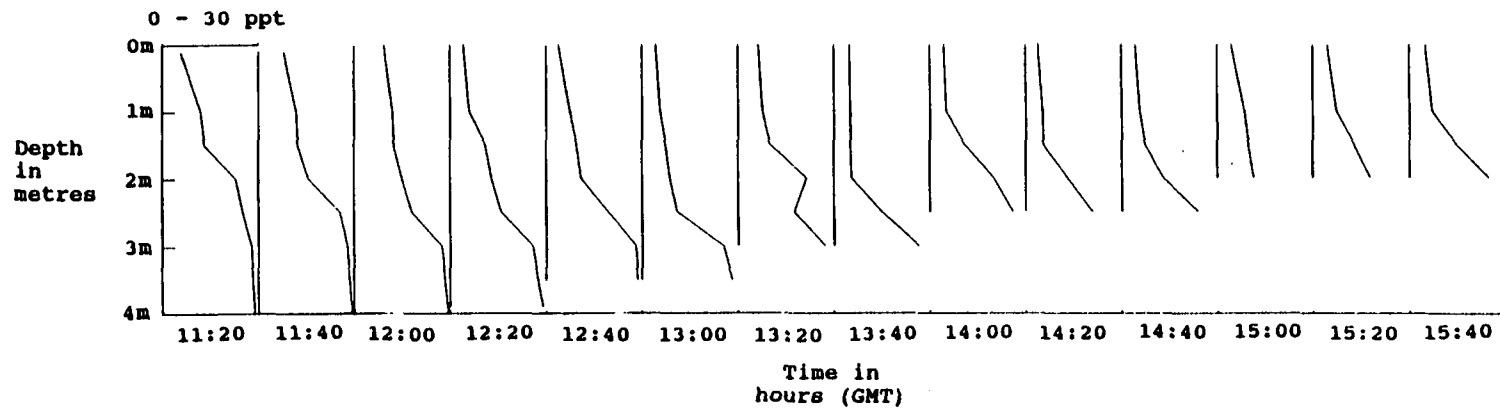


Figure 4.2: The vertical profiles of salinity at "45" on 6 November 1989, made every 20 minutes, as indicated on the horizontal time axis. The depth is in metres, and the scale for salinity is indicated in the top left hand corner, in ppt.

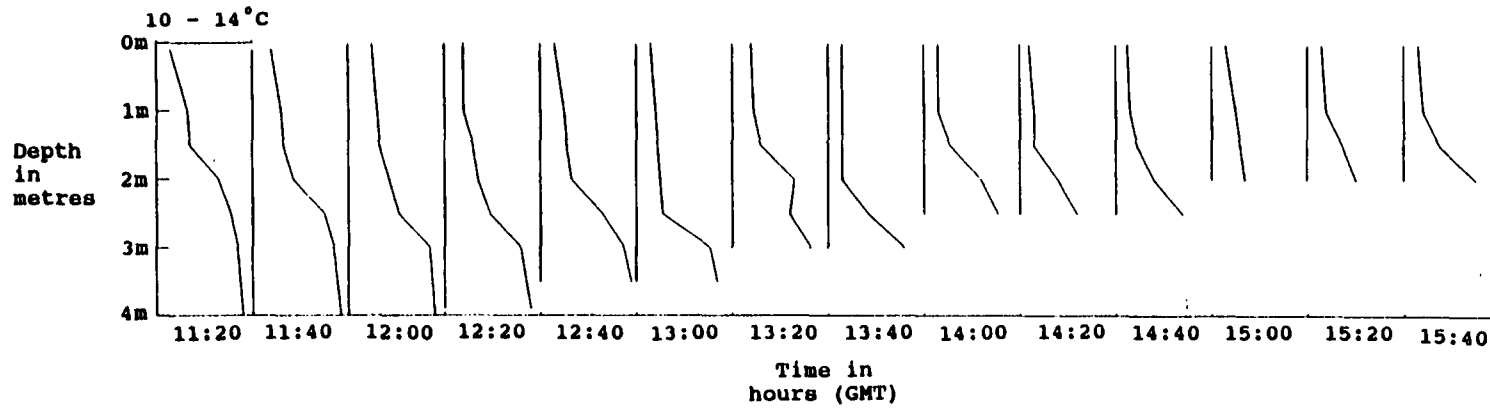


Figure 4.3: The vertical profiles of temperature at "45" on 6 November 1989, made every 20 minutes, as indicated on the horizontal time axis. The depth is in metres, and the scale for temperature is indicated in the top left hand corner, in celsius.

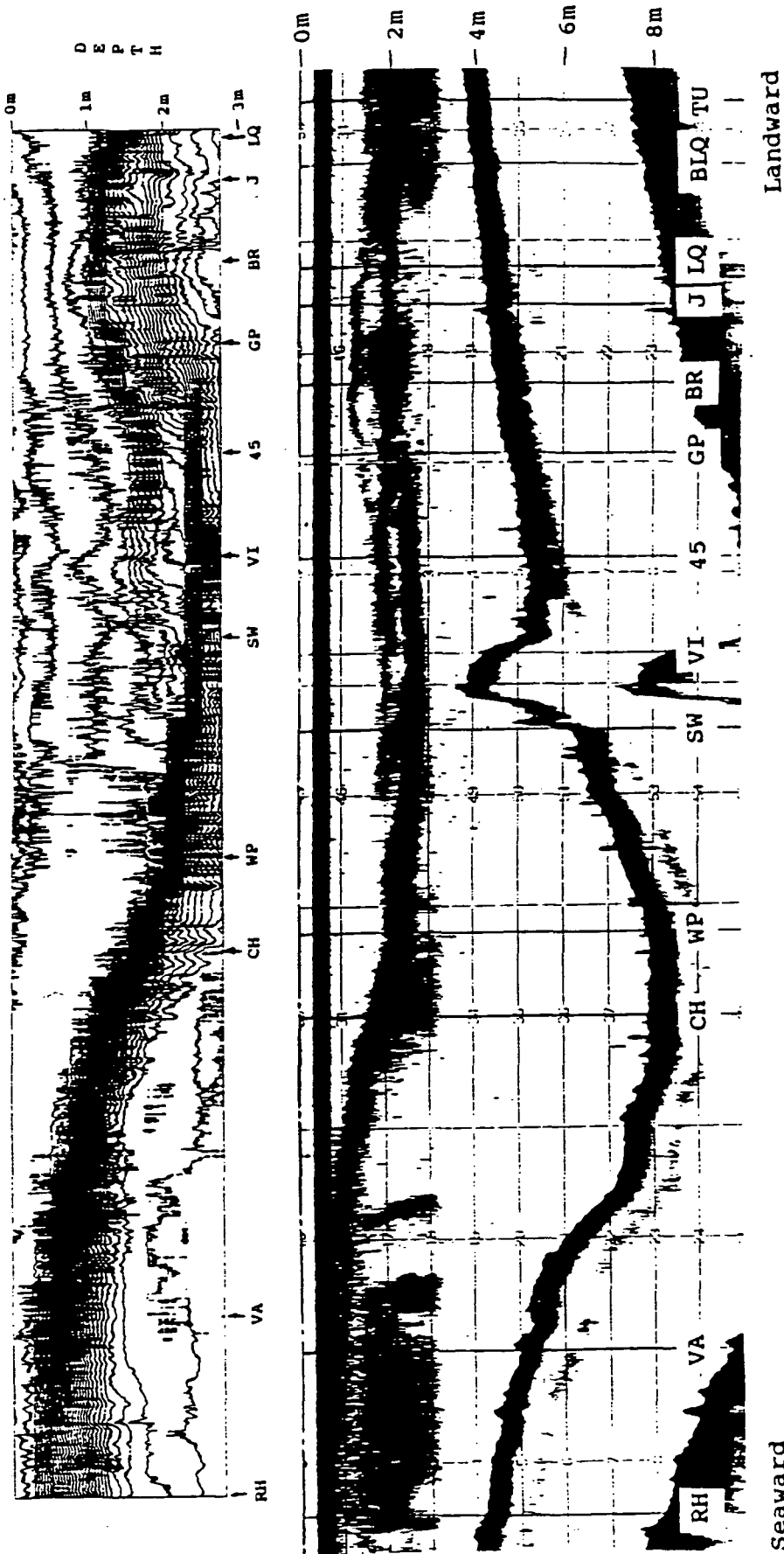


Figure 4.15: Transect 12 at 15:15 on 6 November 1989.

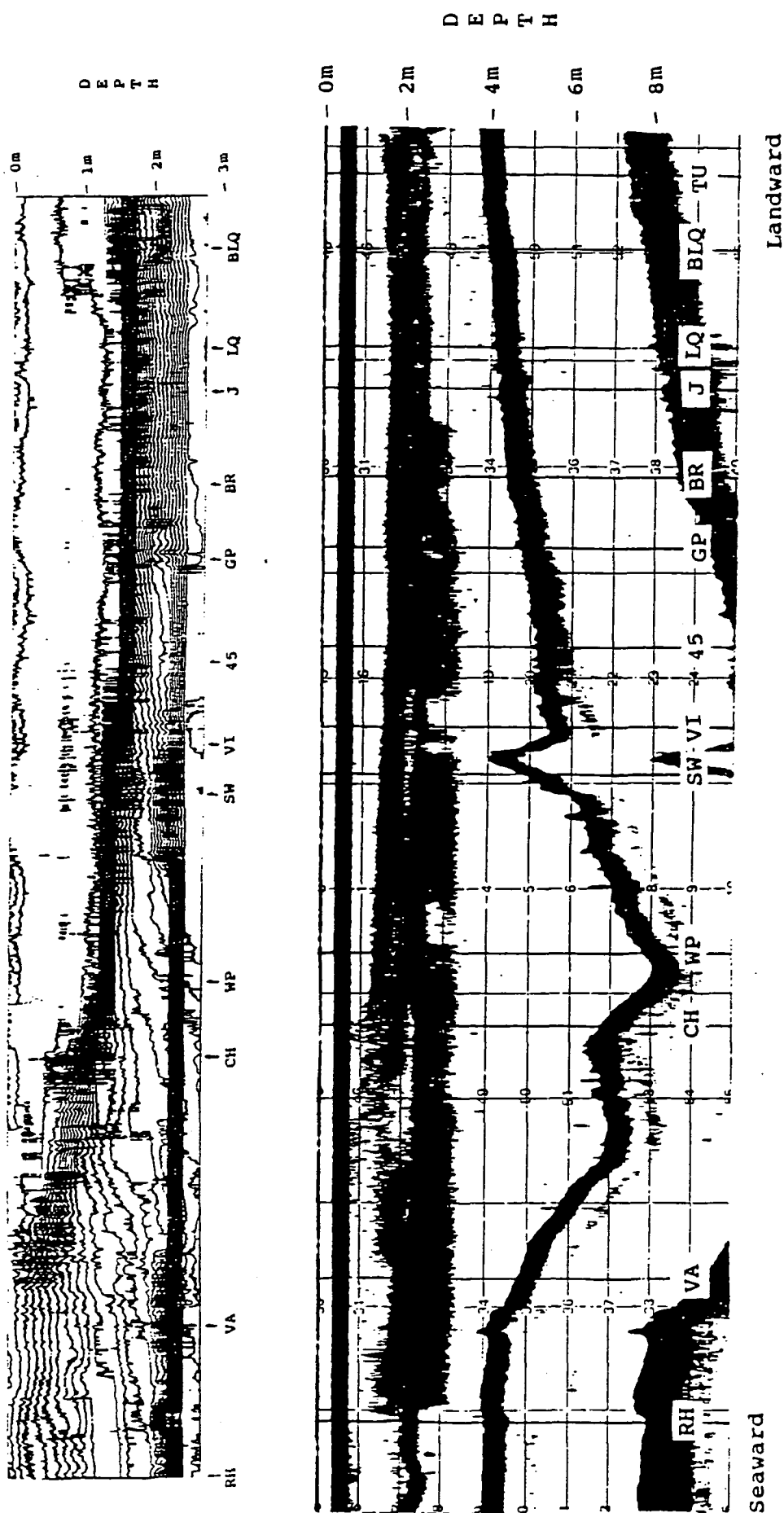


Figure 4.21: Transect 18 at 16:45 on 6 November 1989.

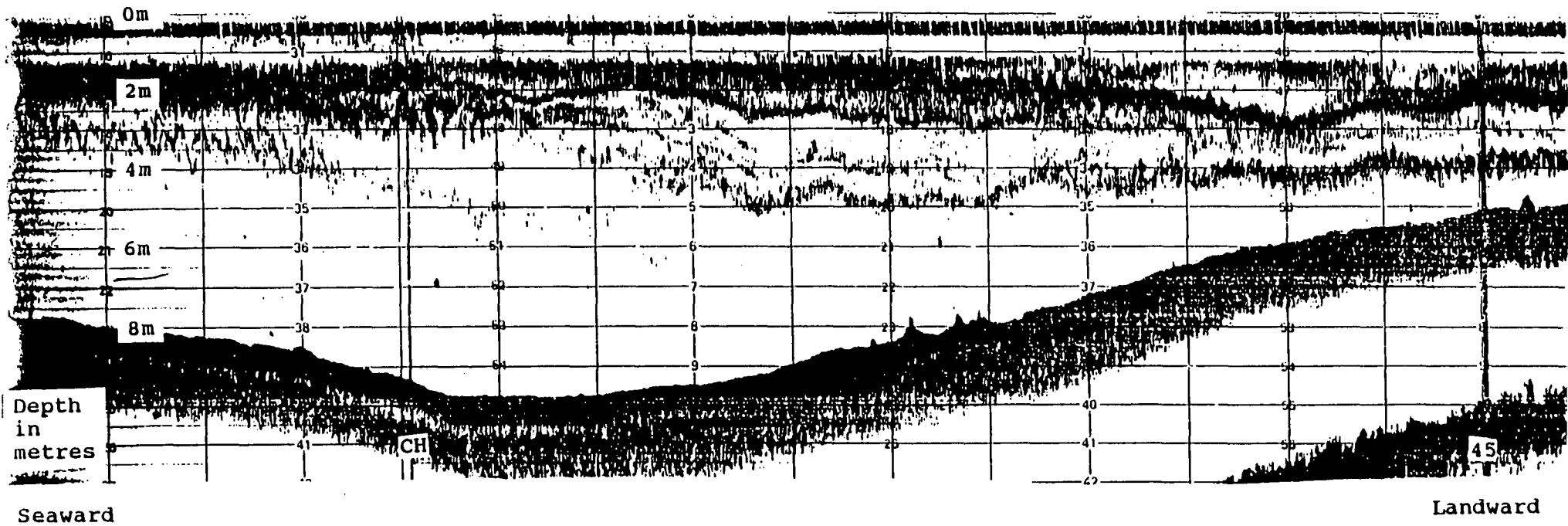


Figure 6.3: Longitudinal transect made at 3.5 hours after high water on 30 November 1987, at Cargreen.

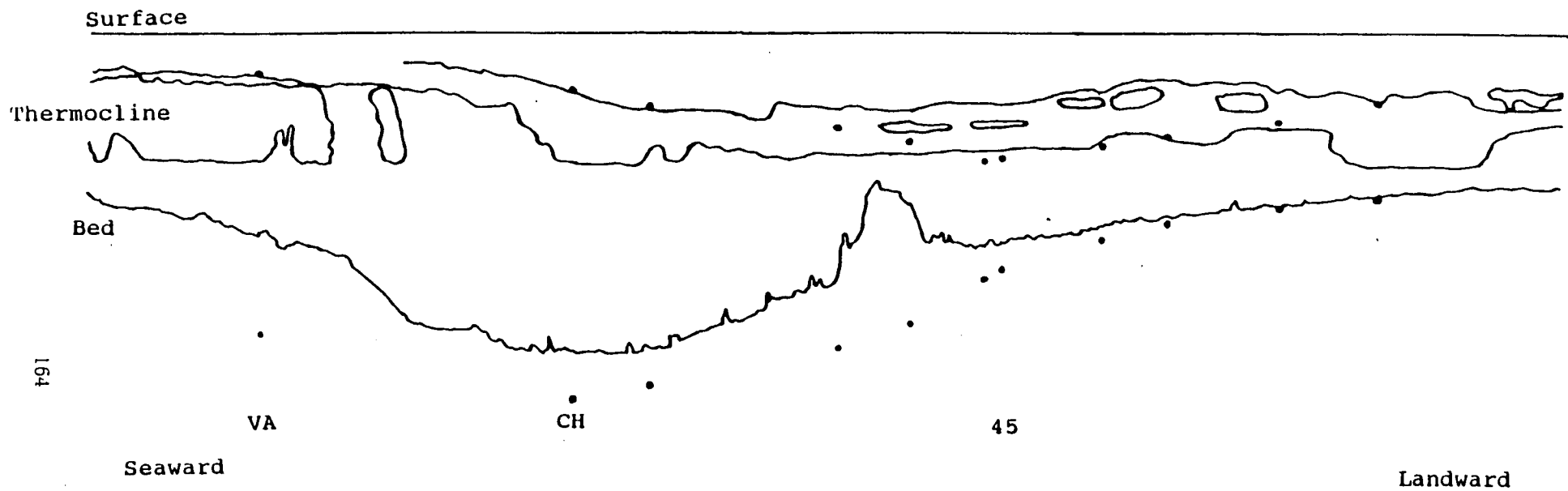


Figure 8.3: The schematic diagram of acoustic backscatter and model predictions, from transect 12 at 15:15 on 6 November 1989.

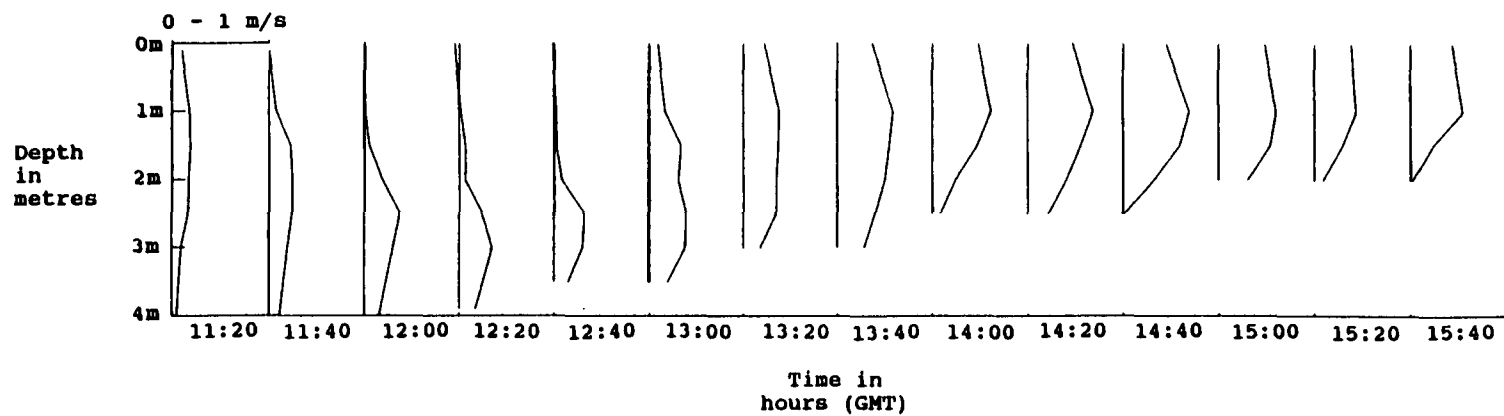


Figure 4.4: The vertical profiles of longitudinal velocity at "45" on 6 November 1989, made every 20 minutes, as indicated on the horizontal time axis. The depth is in metres, and the scale for velocity is indicated in the top left hand corner, in metres per second.

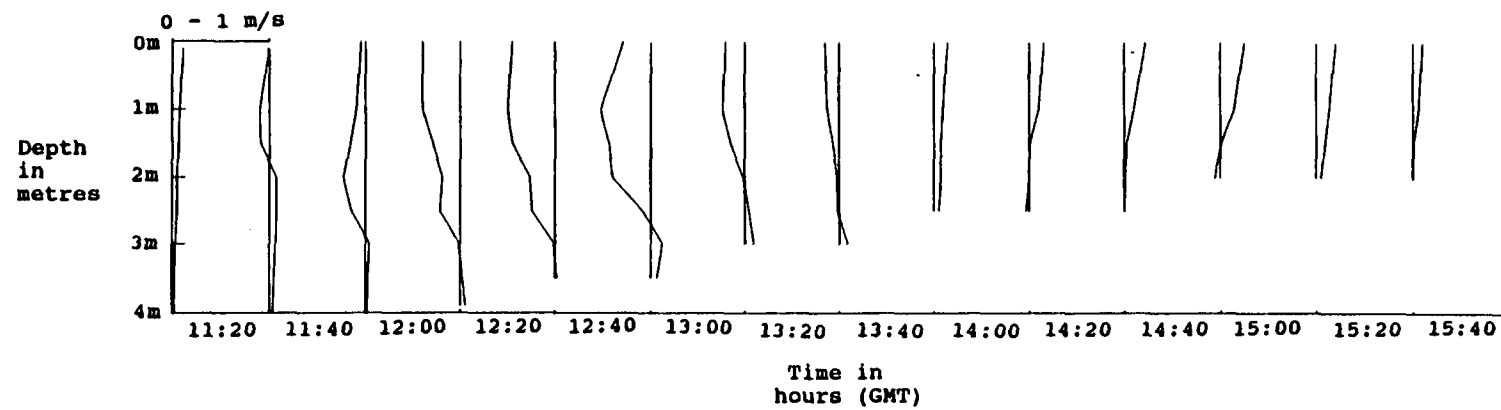


Figure 4.5: The vertical profiles of transverse velocity at "45" on 6 November 1989, made every 20 minutes, as indicated on the horizontal time axis. The depth is in metres, and the scale for velocity is indicated in the top left hand corner, in metres per second.

Depth
averaged
velocity
in m/s

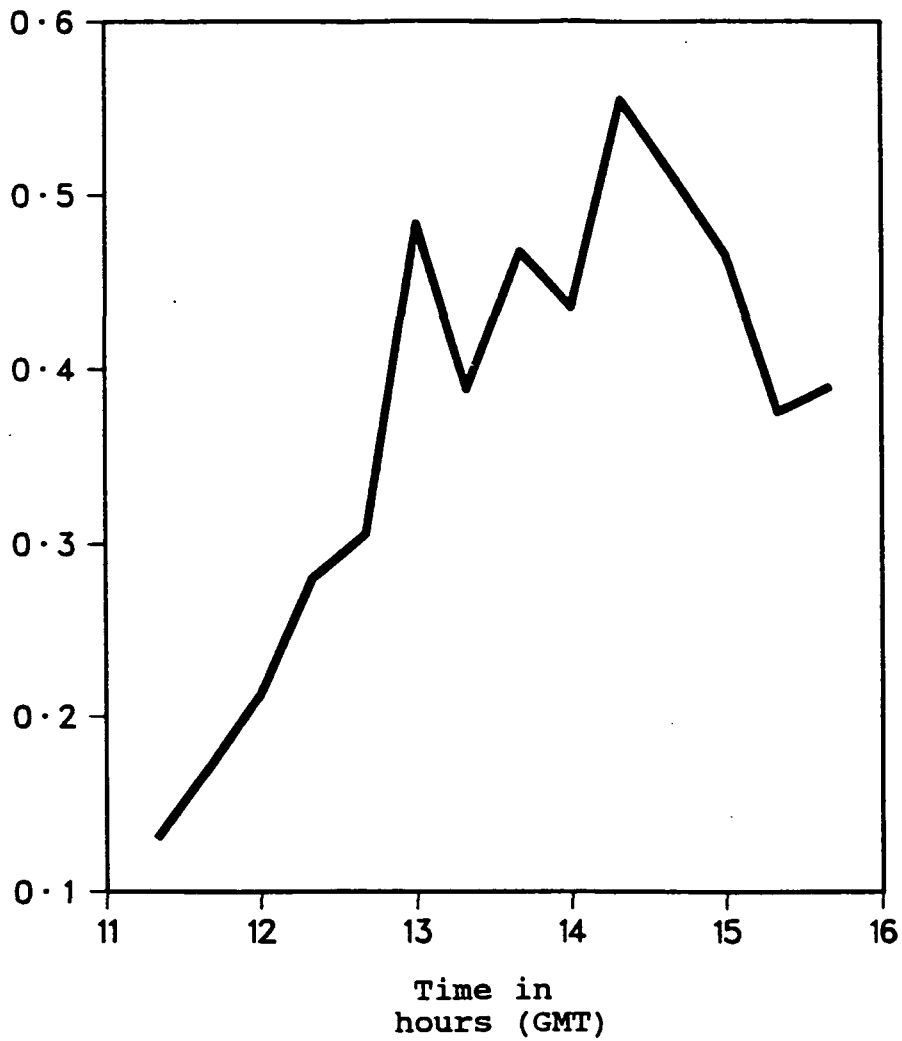


Figure 4.6: The magnitude of the depth averaged velocity at "45" on 6 November 1989.

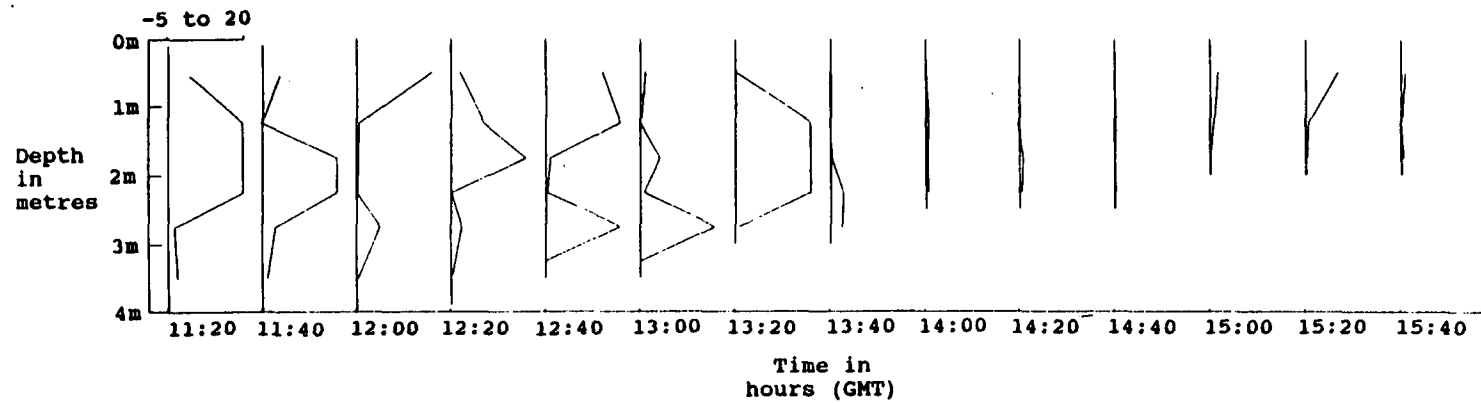


Figure 4.7: The vertical profiles of longitudinal Richardson number at "45" on 6 November 1989, made every 20 minutes, as indicated on the horizontal time axis. The depth is in metres, and the scale for Ri is indicated in the top left hand corner. The vertical lines show $Ri=0.25$.

and evolution of a leewave. The echograms and thermal maps discussed later support this data from "45", showing the same changes in thermocline depth and thickness.

The velocity profiles show a similar but more subtle effect. The ebb stream was already progressing at the start of the measurements (High Water + 1:20), and at their conclusion (High Water + 5:40) was still strong. Figure 4.6, which depicts the magnitude of the depth averaged velocity, suggests a long ebb stream, perhaps up to 7 hours in duration, with a double peak in velocity. This behaviour is common in the middle and upper Tamar (George, 1975).

Figure 4.4 shows the axial velocity component. The maximum seaward flow was at mid-depth at, or slightly above, the level of the thermocline. The level of this maximum flow evolved in exactly the same way as shown by the T and S profiles. It was expected that the seaward flow would be enhanced in the upper layers of the water column. That it should so closely follow the thermocline is noteworthy.

Figure 4.5 shows the cross-estuary flow and its evolution during the exercise. The figure indicates the velocity in the direction 90° to the local estuary axis (aligned to 142° from chart North), with negative values showing flow toward the Devon bank and positive values flow toward the Cornish bank. The figure shows at times a strong transverse component to the flow in the upper layers with negligible transverse flow in the lower water column. The cross-estuary flow had its maximum above the thermocline. The level at which the flow became zero coincided with the bottom of the thermocline,

and evolved with it in time. The two Eulerian velocity profiles together indicate a strong three dimensional flow associated with the growth and evolution of the wave.

There are a number of possible explanations for the strong transverse flow in the upper layer, weak transverse flow below and the strong longitudinal flow along the thermocline:

- Station "45" was landward of the deepest part of the bed depression and slightly to the Devon side of the main channel. It means that the wave trough was likely to have been mostly seaward of "45" and more westward, in the main channel. Also "45" was positioned over topography with isobaths which locally run across the estuary (see figures 3.3 and 3.4).
- There is a slight bend in the estuary at Cargreen suggesting the possibility of a secondary circulation due to centripetal forces.
- During the growth of the wave the flow at "45" was largely seaward with little cross-estuary flow. Assuming that cross-isotherm flow did not occur, as the wave grew to its maximum size and shape the flow through the wave structure would have been diverted along isotherm surfaces. This would make water approaching from above the thermocline diverge horizontally over the depressed thermocline (there is a large proportional change in upper layer thickness) enhancing the transverse shear, and perhaps producing a transverse flow. As the wave approached its maximum size and later propagated upstream

past "45" the cross-estuary flow would have diminished as water no longer needed to divert along isotherm surfaces.

The echograms and thermal maps do not show the full transverse structure of the wave. The velocity profiles, and the topography suggests that this wave must have considerable cross-estuary structure.

Calculations of the gradient Richardson number (Pond & Pickard, 1983),

$$R_i = -\frac{g}{\rho} \frac{\delta\rho}{\delta z} \left(\frac{\delta u}{\delta z}\right)^{-2} \quad (4.1)$$

from the profiles at "45" show that before 13:20 there was no indication that extensive mixing generated by shear driven overturning might be possible. Figure 4.7 depicts these results. After 13:20 the value of R_i is uniformly small with depth (< 2) and was often close to or less than the traditionally accepted critical value 0.25. Basically the thermocline was stable until 13:20 despite large shears.

4.3 Echosounding data

RV Catfish made axial transects of the estuary over the depression from 11:18 to 16:45. The echosounder was left on for the whole period providing a near continuous record of acoustic backscatter. The echograms consist of seaward and landward transects interleaved. The seaward transects have generally shorter echograms because of the strong ebb stream.

Figures 4.8 to 4.21 show 14 of the echograms in a natural temporal

sequence starting at 12:45 and finishing at 16:45. On the same pages are the synchronous Spar data contoured as isotherms. The thermal maps are discussed later in this chapter. Notice that the apparent bed shape changes, depending on which course was steered over the depression.

The echograms depict the formation of a wave in the manner described by Maxworthy (1979), as a disturbance of the thermocline in the lee of the landward slope of the depression. As the ebb stream slackened the wave was observed to progress slowly landward. At about 14:45, the approximate time of maximum stream, but well after the onset of the period of low R_i , the thermocline immediately to seaward of the wave thickened vertically, reducing the temperature gradient across it. This thickening increased with time, suggesting mixing in the thermocline, and the region affected spread landward engulfing the wave trough itself. At 16:00, seaward of the wave trough, the upper 3m of the water column had become mixed, and a new thermocline had developed at 2.3m depth, about the level of the wave trough.

The wave trough itself underwent a similar transition, starting as a well defined thermocline, which thickened gradually after 14:45. The echograms show large patches of backscatter below the thermocline, around the wave trough and seaward of it, which do not appear to be caused by large temperature gradients in the Spar data. These were evident in nearly all the echograms but markedly so at 15:30 (figure 4.16), 16:00 (figure 4.18) and 16:25 (figure 4.20) and it is suggested that these were due to the presence of temperature finestructure, below or in the thermocline. They coincide with regions where the isotherms in the Spar data diverge vertically. These

patches were not observed landward of the wave, or above the thermocline.

There are also vertically aligned patches of strong backscatter which have a correspondence in the Spar data, and these are attributed to vigorous mixing across the thermocline produced by the propellers of *RV Catfish*. These were caused at the ends of the transects, when turning. These patches do not obscure the temperature and backscatter structures of main interest, but are an indicator of the likely importance of vessel activity as a contributor to mixing in estuaries.

4.4 Spar data

During each transect made in *RV Catfish* the Estuarine Thermistor Spar collected temperature data. These data sets also alternate between transects collected in the seaward and the landward directions.

From the Eulerian observations it was possible to correlate T against S, and to regress linearly S on T showing the relationship between the two variables. The regression coefficients were used to infer salinity and hence density from the Spar data using the Millero-Poisson equation (Pond & Pickard, 1983). Plots of S against T show a strong linear relationship and the correlation coefficients were never below 0.99.

From the raw data it has been possible to reconstruct the thermal field in the form of a map of isotherms, representing a longitudinal vertical section of the estuary. These maps are contained in figures 4.8 to 4.21, with the corresponding echograms, and are annotated in the same way. The maps

show temperature increasing with depth, and have the isotherms plotted at 0.1°C intervals. From these maps some general observations can be made:

- The wave presence is preserved through all the maps, with an evolution in its size, shape and position.
- Each map represents thousands of data points in the horizontal, but only 9; 12 or 15 points in the vertical (according to the number of sensors in the water). Due to the method of interpolation and contouring, and because there are some very steep temperature ramps in the data, the isotherms often take on a stepped structure. This results in artificial jumps in the contours of heights corresponding to the spacing between sensors. Similar behaviour is presented in Thorpe et al. (1977).
- The sequence of thermal maps reinforces the Maxworthy (1979) model of an evolving lee wave, evidenced by the echograms.
- There are regions where isotherms strongly diverge vertically, suggesting that some mixing event is causing the water to destratify. These regions have associated patches of acoustic backscatter in the echograms. In these cases the backscatter is attributed to finestructure in the water rather than to strong temperature gradients.
- There is a strong resemblance between the thermal maps and the echograms, suggesting that regions with large vertical temperature gradients are good acoustic reflectors.

- Individual features on the thermocline, such as multiple layers, ripples and undulations often have an exact correspondence in the echograms. E.g. In figure 4.10 at "SW" the thermocline was composed of 3 distinct layers. In figure 4.14 halfway between "CH" and "VA" the thermocline had an undular structure, which on closer inspection revealed billows.
- In some thermal maps it is possible to see the effect of propellor mixing across the thermocline. E.g. In figure 4.10 seaward of "RH" the isotherms were tangled and vertically aligned in a patch of mixed water.
- Figure 4.12 represents the situation at 14:15. This transect was made with only 9 sensors in the water, (the Spar was re-deployed after grounding), and depicts only the top 2m of the water column. This transect was to the Devon side of the main channel. Hence the wave shape shown is not in the region of maximum displacement. For these reasons the data from this echogram and thermal map does not appear in the following analyses where wave amplitude is an important parameter. However, this figure does show that the wave has transverse extent and structure.

4.5 Quantitative comparison of data sets

Qualitatively the Eulerian measurements, echograms and thermal maps complement each other. Some small differences are accounted for by conservative error estimates.

4.5.1 Maximum thermocline displacement

The maximum thermocline displacement, or wave trough, has been measured from each echogram and thermal map and these are presented as time series in figure 4.22. In measuring a maximum displacement it was necessary to define the undisturbed thermocline in each case. Previous observations by the author, and exercises with the numerical model presented in Chapters 7 and 8, have shown that the downstream (in this case, seaward) level of the thermocline is a good indicator of the undisturbed level, (or rather, the level remote from the depression in the bed), and this convention has been adopted. In each transect the thermocline has a finite thickness. The point of maximum gradient, or alternatively, vertical mid point of the thermocline, was chosen to represent the boundary between the upper and lower layers. Where the thermocline appeared to thicken, or bifurcate, vertically seaward of the trough, in the latter stages of the exercise, the upper thermocline depth was adopted as the undisturbed level.

There is good agreement between the maximum thermocline displacements obtained from these two sources. Since the course of *RV Catfish* may have deviated transversely from the most displaced region of the thermocline, in this undoubtedly three dimensional feature, the maximum is a local one in space, but serves as an estimate for the whole wave.

Figure 4.22 shows that the wave was already quite well developed at 12:45 with a displacement of about 1.75m, in response to the increasing ebb stream. Between 12:45 and the end of the study the depth of the wave trough

varied in response to the variable ebb stream. The maximum thermocline displacement and the magnitude of the depth averaged velocity measured at "45" show this. To remain stationary in the accelerating seaward flow the wave developed a landward phase velocity, continually evolving to match the ebb stream. Between 11:20 and 13:00 the magnitude of the depth averaged velocity, \bar{u} , increased and the wave height increased in response. From 13:00 to 13:20, \bar{u} decreased slightly, but the wave continued to grow through nonlinear steepening. \bar{u} increased again from 13:20 to 14:20, but the response was a decrease in wave height over this period. This may have been due to increased attenuation at the wave crest, through diffusion and dissipation. From 14:20 to 15:20 \bar{u} decreased again. The initial response, from 14:45 to 15:15, was an increase in height, again as a result of nonlinear steepening. From 15:20 to 15:40 \bar{u} increased by a small amount, and there is a suggestion that the wave height also increased at this time. The general trend from 15:15 to 16:15 was a decline in the wave height as it propagated landward losing energy.

At 16:45 the thermocline still appeared to be displaced by about 1.3m - 1.4m, but the wave structure and the level of the undisturbed thermocline were difficult to define.

The error incurred in measuring the size of the wave trough is estimated to be of the order $\pm 0.2m$. This error is roughly equivalent to a 10% uncertainty in the largest thermocline displacement, and is a result of making essentially subjective judgements about the level of the thermocline. It ignores instrumental and computational errors, which are felt to be small in

comparison.

4.5.2 Position of wave trough

The position of the wave trough was measured as a positive distance landward from the centre of the bed depression, taken as "CH". In the echograms there was not always an easily defined single point of maximum displacement. Figure 4.23 shows the wave trough position in metres landward of "CH".

The trough movement, due to wave steepening in response to the variable ebb stream, cannot be inferred from figure 4.23. In fact between 13:00 and 13:30 when it was expected that the trough might move landward, in order to steepen the wave in response to the decreased ebb flow, the observations show a seaward movement, and between 13:30 and 14:30 when a seaward movement was expected, a landward movement occurred. The reason for this is unclear, but the error in determination of a wave trough position is high. The values obtained might be as much as $\pm 60m$ in error where the wave trough is broad, equivalent to a 20 - 25% uncertainty, in the distance from "CH". The only time when expected and observed behaviour matched was between 15:30 and the end of the exercise, when the ebb stream diminished enough to allow the wave to propagate landward.

Unfortunately the measurements at "45" stopped at 15:45, so from 15:45 until 16:45 the behaviour of the wave can only be described with conjecture.

The behaviour of $(\bar{u} - c_0)$ was examined, assuming that the linear shallow

water wave phase speed (Pond & Pickard, 1983)

$$c_0 = \sqrt{g \frac{\Delta\rho}{\rho} \frac{h_1 h_2}{h_1 + h_2}} \quad (4.2)$$

for the shallow water upstream of the depression was a first order estimate for the phase speed of this wave trough. h_1 and h_2 are the upper and lower layer depths respectively, H is the total water depth, ρ is the mean water density, $\Delta\rho$ is the density difference between the layers, and g is the gravitational constant. $(\bar{u} - c_0)$ was calculated for the period 11:30 to 16:45, with the values of \bar{u} from 15:45 to 16:45 assumed to be those indicated by the sinusoidal approximation shown in figure 8.1. The gross behaviour of $(\bar{u} - c_0)$ in time follows closely that of \bar{u} .

From 11:30 to 12:45 $(\bar{u} - c_0)$ is negative, from 13:00 to 15:30 it is positive, and from 15:30 on it is negative again. The first period of negative $(\bar{u} - c_0)$ is a growth phase of the wave, the positive period has its value never larger than $0.15ms^{-1}$ and the behaviour of \bar{u} describes this phase well. After 15:45 $(\bar{u} - c_0)$ drops rapidly from $0ms^{-1}$ to $-0.2ms^{-1}$ at 16:45. The thermal maps indicate a change in wave trough position of $248m$ during this time. This movement is equivalent to a mean value of $-0.07ms^{-1}$ for $(\bar{u} - c_0)$, in rough agreement with the above calculations.

For the same topographic feature, also on an ebbing neap tide, New & Dyer (1987b) found that an internal wave progressed upstream between 5.25 and 6.25 hours after high water, at a rate of $(\bar{u} - c_0) = -0.05ms^{-1}$.

4.5.3 Wavelength

No analysis of wavelength of the lee wave has been performed. Because of the lack of coverage of the estuary landward of the wave, where the water was too shallow for the Spar, the spatial extent of the wave was uncharted, though during the growth of the wave it had an axial length scale commensurate with that of the topography. The wave appeared about half as long as the bed depression itself, or at least as long as the the landward slope. Other authors have found a relationship between wavelength and topography length scale (e.g. Chereskin, 1983). There is a hint in the data that the wavelength increased as the wave propagated landward into shallower water after 15:30, (the model presented in Chapters 7 and 8 predicts that this should be so), but the echograms and thermal maps are ambiguous on this point. Choosing figure 4.10, the situation at 13:15, as representative of the wave during its growth, one can see that the wave existed as a disturbance from "J" to a position 40m landward of "VA", some 500m in all. The seaward end of the wave did not appear to move during the exercise, while the landward end was out of reach of the Spar perhaps as early as 12:45, but certainly long before 16:45. At 16:45 the wave trough appears to be some 350m landward of "CH". Assuming the wave was roughly symmetrical about its trough position, a wavelength of about 800m is indicated at that time.

4.5.4 Thermocline spreading and vertical extent

The thermocline thickness at the beginning of the observations, (see figure 4.8), was largest on the landward edge of the wave and at its trough. At "45", for example, the thermocline on the echogram was about $1.3m$ thick. The thermocline was considerably thinner along the seaward edge of the wave. At "CH" it was $0.7m$, and at "VA" $0.25m$ thick. This trend, of a thick thermocline to landward and thin thermocline to seaward continued until 13:15 (figure 4.10) despite some overall thermocline thickening. At 13:15 the thermocline at "CH" still showed a thinness ($0.43m$) relative to the landward edge, but at "RH", seaward of the wave, the thermocline had begun to spread vertically ($0.71m$). This spreading carried on until the end of the exercise with the region involved also spreading horizontally from "RH" landward along the thermocline.

At 16:00, (figure 4.18), the region had developed horizontally from "RH" to "CH" and the thermocline was some $2m$ thick vertically. At 16:15, (figure 4.19), the seaward end of the wave was composed of a vertically thick but poorly stratified thermocline, with a sharp temperature gradient at its base, at $2.3m$. The horizontal spreading had then gone from "RH" to "SW". At 16:25, (figure 4.20), the water column seaward of the wave had developed two distinct thermoclines according to the echograms. At 16:45, (figure 4.21), the thermocline seaward of the wave had spread vertically, occupying the water column from the surface to $2.3m$ depth. The horizontal region over which this expanded thermocline extended was from "RH" to "GP", a dis-

tance of some 500m. This gives a rate of horizontal spreading, landward, of $0.04ms^{-1}$. The rate of vertical spreading was $0.14mms^{-1}$ at "RH" and $0.13mms^{-1}$ at "CH".

The wave trough also thickened vertically during the period 15:30 to 16:45 at a rate of $0.22mms^{-1}$.

4.5.5 Potential energy excess

The mass 'excess' and potential energy 'excess' were calculated for the top 2.75m of the water column, for each position in each transect, from the Spar data. This 'excess' is the difference between the observed potential energy (or mass) of the Tamar water column and the energy (or mass) it would have if composed entirely of fresh water. This analysis concerns only the upper 2.75m of the water column, with the depth of 2.75m as the geopotential zero level. Changes in the potential energy excess measure fine changes in potential energy due to the vertical redistribution of density. Table 4.2 shows the potential energy excess and mass excess of the water column, at "45", "VA" and "RH", at 14:45 and 16:45. Figure 4.24 shows the vertical density profiles at "VA" and "RH", at 14:45 and 16:45. There are a number of ways in which changes in the vertical distribution of density might have come about:

- Seaward advection of less saline water down the Tamar.
- Seaward advection of less stratified water down the Tamar.
- Vertical mixing within the water column.

- Vertical migration of the thermocline due to wave activity.

The vertical migration of the thermocline, as an internal wave, accounts for very large differences in potential energy excess, between positions along the estuary. At 14:45 the values for "VA" and "45" were $554 Jm^{-2}$ and $169 Jm^{-2}$, respectively, a difference of $385 Jm^{-2}$, reflecting the large difference in thermocline height at these two places.

Between 14:45 and 16:45 mixing had the effect of thickening the vertical extent of the thermocline at "RH". It spread at the expense of the lower layer, rather than entraining lower layer water into it. With time the potential energy excess at "RH" was lowered. Vertical mixing at "RH" should have led to an increase in potential energy excess, but this was offset by the introduction of less saline water. The evidence for this is in table 4.2, which shows that the mass excess of the water column at "RH" fell over the period 14:45 to 16:45. Figure 4.24 shows how the density of the water column at "RH" was radically lowered, not just redistributed through mixing, between 14:45 and 16:45. The same occurred at "VA", but later in time, as the mixed region spread landward. The homogeneous layer above the thermocline seemed to have disappeared after 16:00 at "RH" and "VA" (figure 4.18). After 16:25 (figure 4.20) a second thermocline at about 2.3m depth formed and intensified, suggesting different interactions with the layers above and below the main thermocline.

It is reasonable to assume that water from above the thermocline mixed down across the top of the thermocline, mixing in the thermocline redis-

Table 4.2: The potential energy excess and mass excess at "45", "VA" and "RH" at 14:45 and 16:45.

Time	"45"	"VA"	"RH"
14:45	$169 Jm^{-2}$ $17.7kg$	$554 Jm^{-2}$ $50.8kg$	$546 Jm^{-2}$ $50kg$
16:45	$223 Jm^{-2}$ $26.9kg$	$296 Jm^{-2}$ $29.6kg$	$277 Jm^{-2}$ $27.7kg$

tributed water vertically, and lower layer water evacuated the bottom of the water column.

The loss of potential energy excess due to the supply of fresher water from above the thermocline, and the gain from mixing in the thermocline, were separated by calculating how much the potential energy excess should have changed, from the change in mass excess alone (i.e. changes in water salinity), and comparing this with the observed changes.

The following method was used to find those changes in potential energy excess at "VA" and "RH" due to the freshening of the water column and due to vertical mixing. At these two fixed positions there was negligible movement of the thermocline between 14:45 and 16:45. At the other fixed positions the behaviour of the potential energy excess was more complicated, because the thermocline height changed significantly with time.

The mass excess at "45", "VA" and "RH", at 14:45, was $17.7kg$, $50.8kg$ and $50kg$ respectively. At 16:45 these had changed to $26.9kg$, $29.6kg$ and $27.7kg$. The changes in mass excess were, respectively, $9.2kg$, $21.2kg$ and $22.3kg$ - an increase at "45" and decreases at "VA" and "RH". The dif-

ference in density between the surface and bottom waters was 20kgm^{-3} at "VA" and "RH", at 14:45 and 16:45. To displace 21.2kg of mass excess at "VA" required an exchange of 1.06m^3 of surface and bottom waters, of density difference 20kgm^{-3} . Similarly, at "RH", 1.12m^3 of water would have to have been supplied at the surface and lost from the bottom to account for the loss of 22.3kg of mass excess. The thermocline and centre of mass, in the absence of mixing, would have been lowered to accommodate these exchanges. Evidence for this is given by figure 4.24. The decreases in potential energy excess that should have occurred, due to this freshening of the water column, were calculated at 313Jm^{-2} (RH) and 302Jm^{-2} (VA). The observed decreases in potential energy excess were 269Jm^{-2} (RH) and 258Jm^{-2} (VA). The increases in potential energy excess attributed to mixing are 44Jm^{-2} (RH) and 44Jm^{-2} (VA).

Why this happened in the seaward edge of the wave is perhaps answered by a volume transport argument and by the numerical model. If the flow was strictly along the longitudinal axis of the estuary, and volume transport of water was roughly conserved, in the layers above and below the thermocline, then intense vertical shear in the horizontal velocities is predicted in regions where the two layer geometry was radically different from the landward shallow water configuration (upstream condition). For example, compression of the upper layer relative to the lower layer would have enhanced the upper layer velocities, and decreased the lower layer velocities, giving a sheared flow. The model predicts that two such regions exist, and that they migrate during the evolution of the wave. The model predictions are discussed in

more detail later. These regions are predicted to be a few hundred metres landward, and seaward, of "CH". This argument ignores the fact that the real estuarine flow itself was highly sheared, but this would serve to enhance the shear predicted seaward of the wave, and lessen it landward of "CH".

A region of large shear seaward of "CH", migrating landward toward it (as the wave evolved) is plausible and might explain why the mixed region developed seaward of "RH", and spread landward to "CH".

The spreading and mixing of the thermocline does not appear to have involved much entrainment of water from below, as evidenced by the behaviour of the isotherms. A homogeneous layer above the thermocline was not evident after 16:00, the isotherms again suggesting that considerable mixing in the thermocline had caused it to be eroded, and finally engulfed. Mixing within the thermocline also lead to a sharpening of the density gradient across its base, providing a 'new' thermocline on the echograms and thermal maps.

4.5.6 Wave energy

The total wave energy, E_T , was calculated from (Phillips, 1977)

$$E_T = \int \eta(x)^2 \Delta \rho g \delta x \quad (4.3)$$

over the domain defined by the stations "VA" and "BLQ", where the thermocline is displaced by a variable amount, $\eta(x)$, in the longitudinal direction, x , $g = 9.8ms^{-2}$, and a density difference of $\Delta\rho$ separates the two layers. The

assumptions are:

- The wave is on the thin interface in a two layer fluid.
- There is equipartition of potential and kinetic energy, which is true for linear waves, and good to first order for non-linear waves.

In making the calculations it was necessary to define a fixed horizontal domain over which to calculate the energy. Since landward coverage of the estuary was not long enough to define completely the upstream thermocline position, "BLQ" was chosen as the landward limit of the waveform. In the cases when the transect did not extend to "BLQ" the thermocline level was extrapolated from the most landward point of the transect. In all cases "VA" was more seaward than the seaward end of the wave. The undisturbed thermocline level was identified in the way already described. The integration was performed in sections, using the fixed station positions, and measuring a mean thermocline displacement between section ends. $\Delta\rho$ was kept at 16kgm^{-3} , which was the mean difference in layer densities over the period 12:45 to 16:45.

The method of dealing with the boundaries for the wave would, certainly for the latter stages of the study, cut off part of the landward edge of the wave. It is considered that the effects of this are not severe, and that the estimates are good to first order. The measurement errors are of the order 20 - 25% in the largest energy estimates.

Figure 4.25 shows the depth averaged speed, together with the energy measurements derived from the echograms and thermal maps. The energy

follows a similar pattern to the maximum thermocline displacement, but is more exaggerated in its fluctuations, reflecting the dependency on the square of the displacement.

The total wave energy is relatively high at 12:45, around $160-180kJm^{-1}$, before falling to $120-140kJm^{-1}$ at 13:00 in line with a sharp increase in the ebb stream. The reason for this is unclear, but as the energy had to be extrapolated to "BLQ" in the 12:45 data, in a rather confused and thick thermocline, it is possible that the energy indicated at that time is too high. Otherwise, the energy increased with an increasing ebb stream, and continued to increase for a while when the ebb slackened, due to the same non-linear steepening mechanism discussed earlier. The energy diminished when the ebb stream diminished significantly, especially from 14:45 on.

A peak wave energy of about $220kJm^{-1}$ was measured. From 14:45 to 16:45 the wave energy dropped by about $85kJm^{-1}$. Per metre of the length of the wave ($\simeq 500m$) this amounts to a fall in energy of $170Jm^{-2}$.

4.6 Conclusion

This set of observations, made on a neap tide at Cargreen, shows that the combination of a moderately large amplitude tidal flow, with highly stratified water, led to the formation of an internal wave over a bed depression. The mechanism of formation and evolution seems to be the same as that described by the Maxworthy (1979) model. The double peak in the ebb stream, and the waves response, are strong indicators that non-linear steep-

ening played a large role in its evolution.

The formation of a mixed region, to seaward of the wave trough, is best accounted for by examining the regions where largest shear above, below and in the thermocline might occur. The potential energy excess decrease, in the regions where significant mixing took place, was mainly due to a reduction in density of the water column, caused by advection and incorporation of less saline water from above the thermocline, and loss of denser water from below the thermocline. Once this is accounted for, vertical mixing was responsible for an energy increase of $44Jm^{-2}$.

The total wave energy reached a maximum of $220kJm^{-1}$ (per metre of crest length across the estuary). In the same period when the mixing at "RH" and "VA" occurred the wave energy diminished by $170Jm^{-2}$, averaged along the wave length. This wave energy must have been lost to dissipation and diffusion, and hence some to increased potential energy of the water column through mixing.

In the case of wave overturning it is usual to compare the subsequent increased potential energy of the water column to the total wave energy, in the form of a conversion efficiency. In this case, where the wave presence was undoubtedly responsible for enhanced mixing at "RH" and "VA", but energy for this mixing may have been extracted from the barotropic flow, such a comparison might not be strictly valid. Even if internal waves rarely 'break' by overturning, and instead mostly smear their energy out in the water column through enhanced shear, turbulence and diffusion, still giving rise to increased potential energy, the problem remains: How much of their

total energy works against gravity? The comparison is still useful, and here we have a loss of wave energy of $170Jm^{-2}$, and a $44Jm^{-2}$ gain in the potential energy of the water column, over a large region of the estuary ("RH" to "VA", at least). This gives a conversion efficiency of 26%. The estimated errors make this efficiency lie between 20% and 33%.

The barotropic tidal wave energy (Pond & Pickard, 1983)

$$E_B = \frac{1}{2}\rho g A^2 \quad (4.4)$$

is the source for the internal wave, and it is useful again to make a first order comparison of energies. A is the tidal amplitude, $1.3m$ for this neap tide, $g = 9.8ms^{-2}$, and ρ is the average water density, $1014kgm^{-3}$. In a tidal cycle this gives an energy density of $8.4kJm^{-2}$ over the whole estuary, or $4.2MJm^{-1}$ over the internal wave length. Assuming that there are two such internal waves generated in this cycle (one on the flood, and one on the ebb), the conversion efficiency from barotropic tide to internal wave in this case is about 10% (7.5% to 12.5%), and from barotropic tide to potential energy, a little over 2.5% (2% to 3.3%).

Figure 4.8 to Figure 4.21 The following 14 figures are the echograms, and thermal maps derived from the Spar data, for the longitudinal transects starting at 12:45 and ending at 16:45 on 6 November 1989, at Cargreen. The echograms and their corresponding thermal maps are presented in pairs for ease of comparison. Both diagrams in each figure are annotated with fixed positions and with a depth scale in metres. The Eulerian measurements were made at position "45". For a rough idea of the horizontal scale the distance between "VA" and "CH" is 144m, "CH" and "45" is 234m, and "CH" and "BLQ" is 560m. Isotherms and backscatter more seaward than "RH" must be ignored as this data was collected while the launch *RV Catfish* turned at the seaward end of the transects. In figure 4.10, for example, the Spar and echosounder recorded the mixing caused by the propellers of the launch as it turned. The isotherms are increasing in value downwards, and are plotted at 0.1°C intervals. Seaward and landward directions are indicated. The figures are explained and discussed in the text.

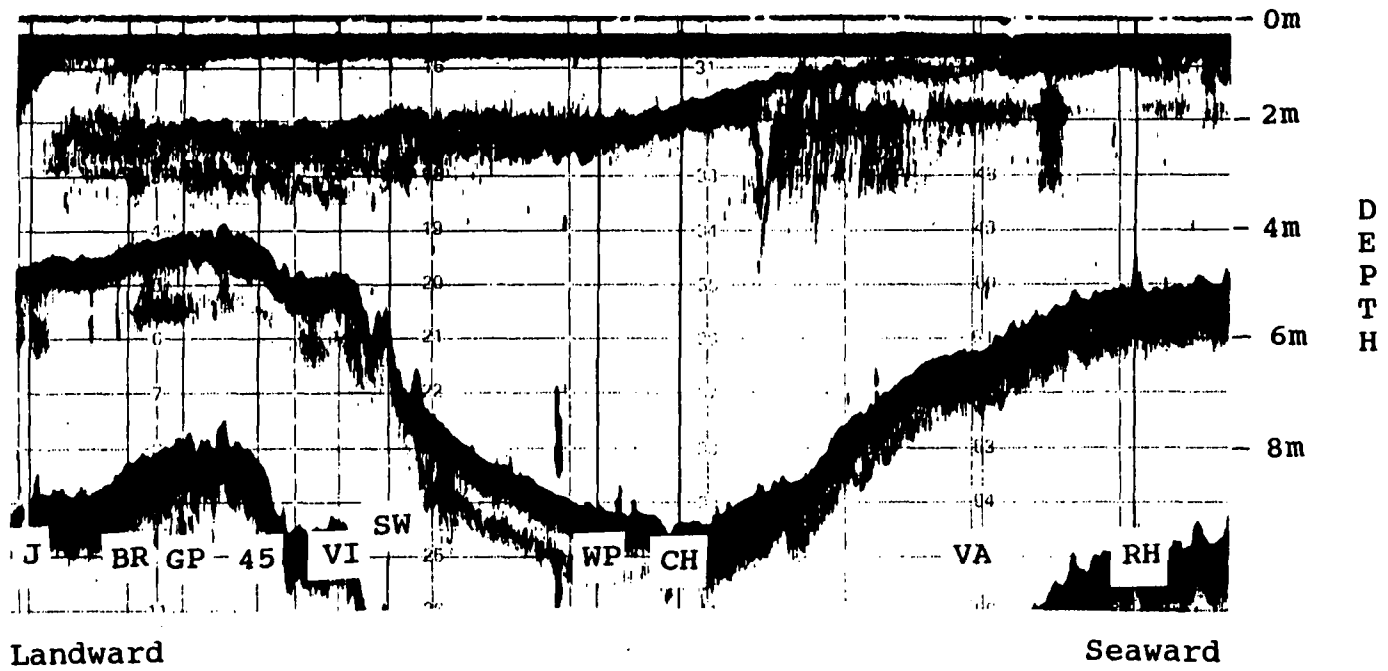
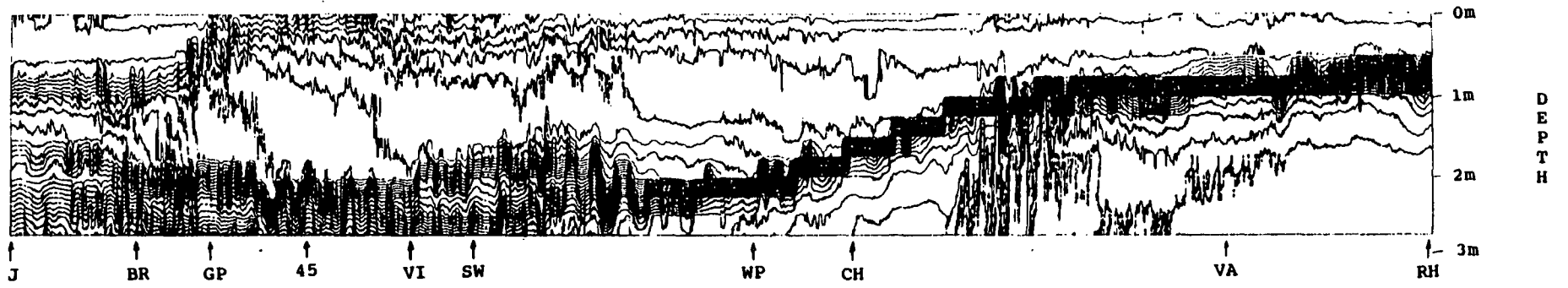


Figure 4.8: Transect 5 at 12:45 on 6 November 1989.

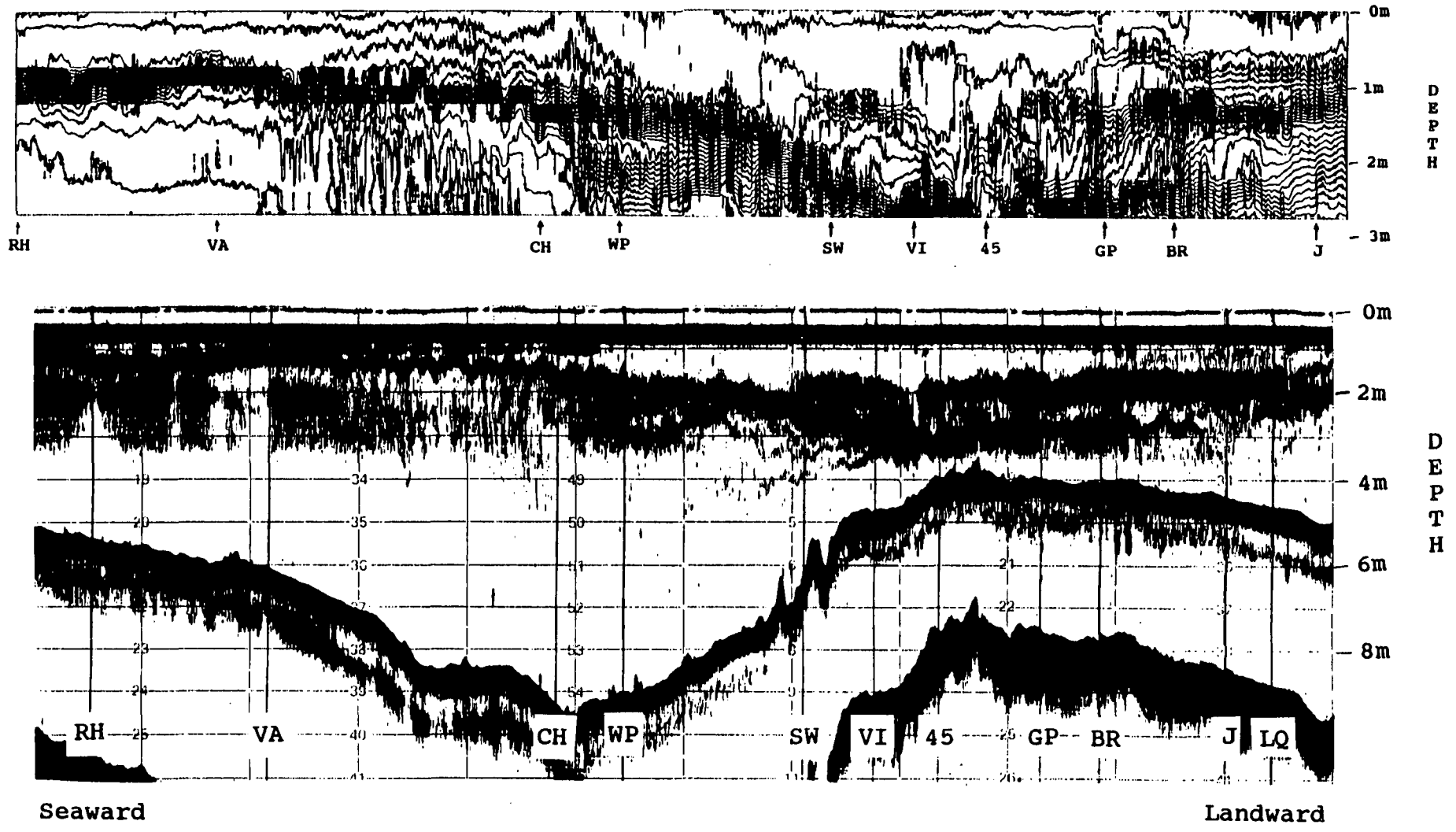
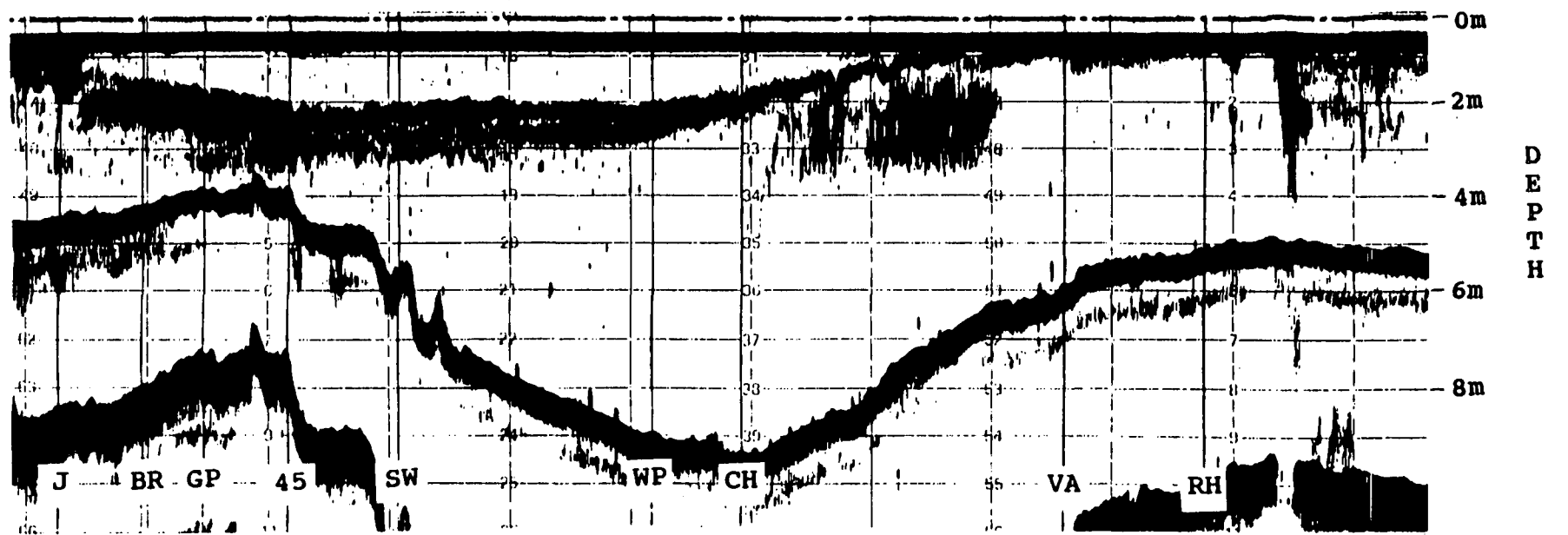
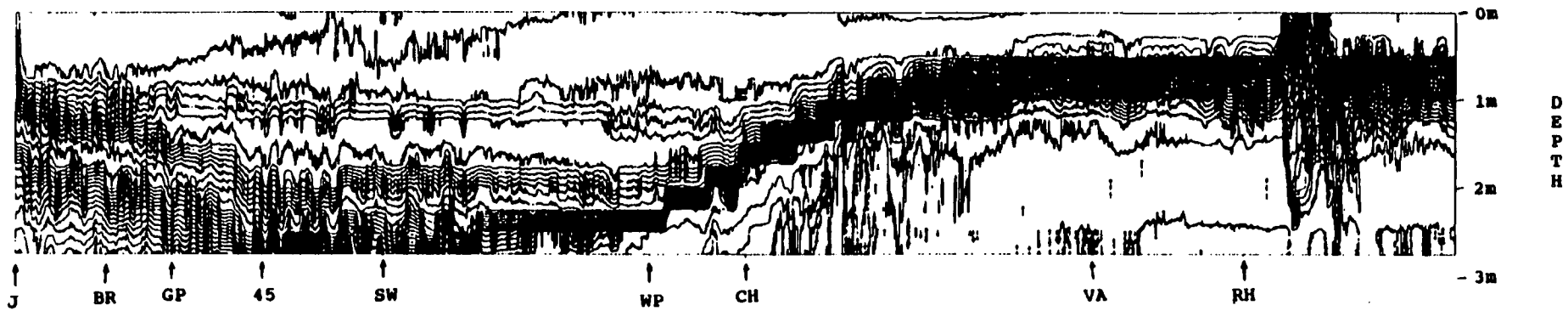


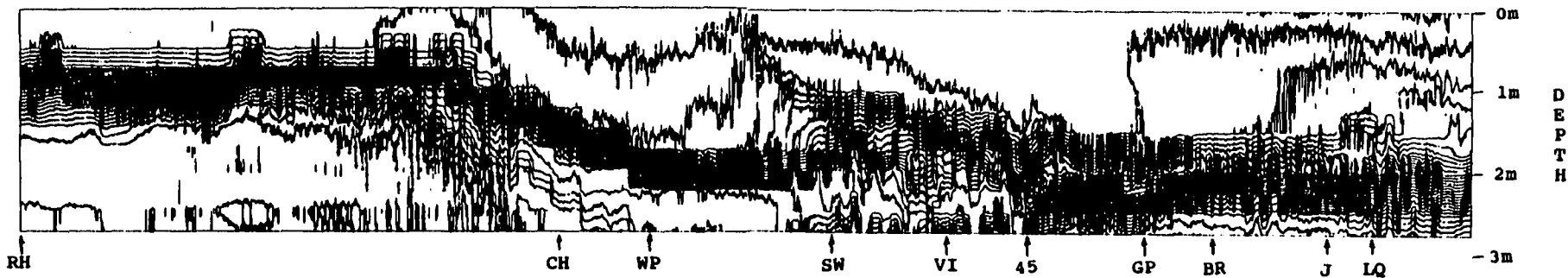
Figure 4.9: Transect 6 at 13:00 on 6 November 1989.



Landward

Seaward

Figure 4.10: Transect 7 at 13:15 on 6 November 1989.



68

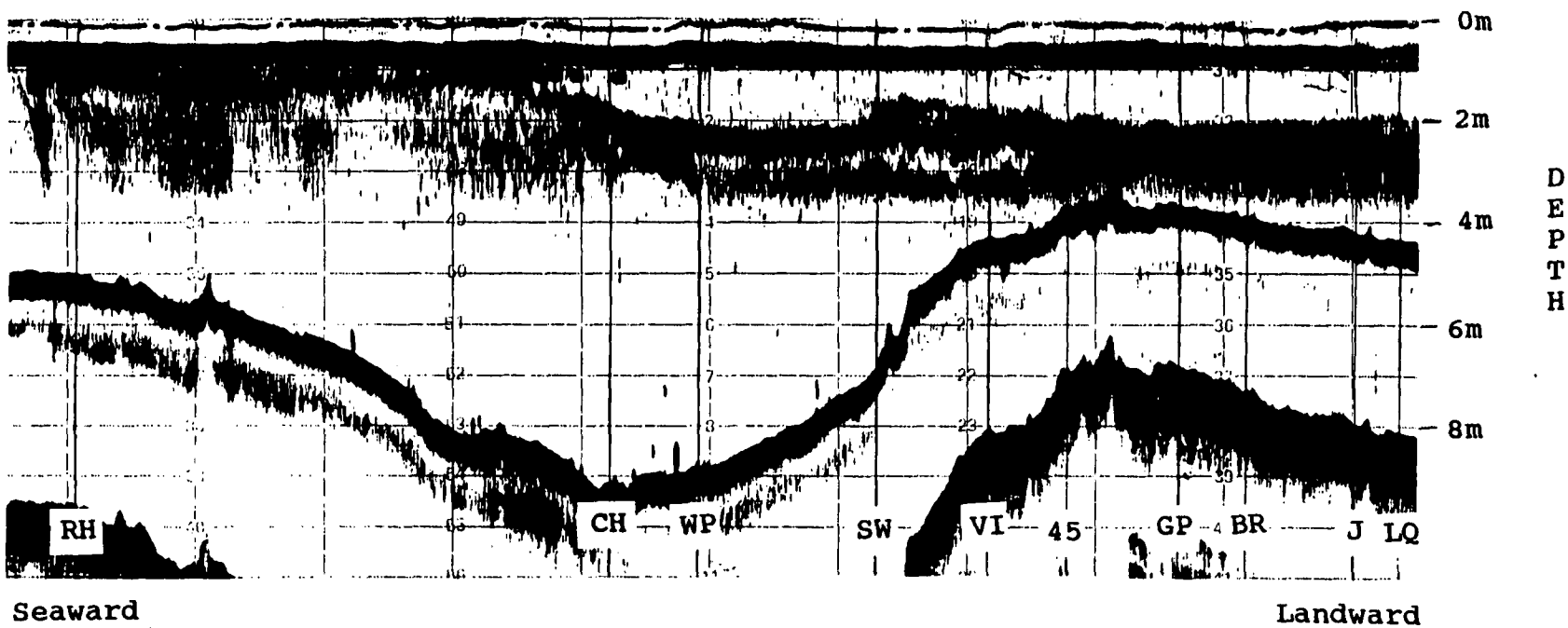
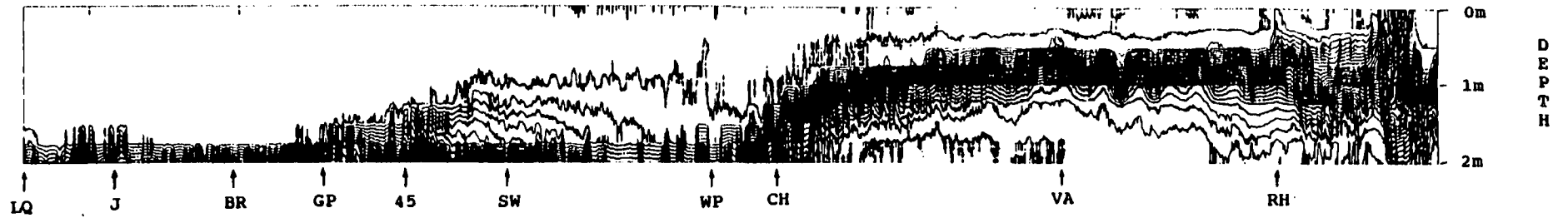


Figure 4.11: Transect 8 at 13:30 on 6 November 1989.



69

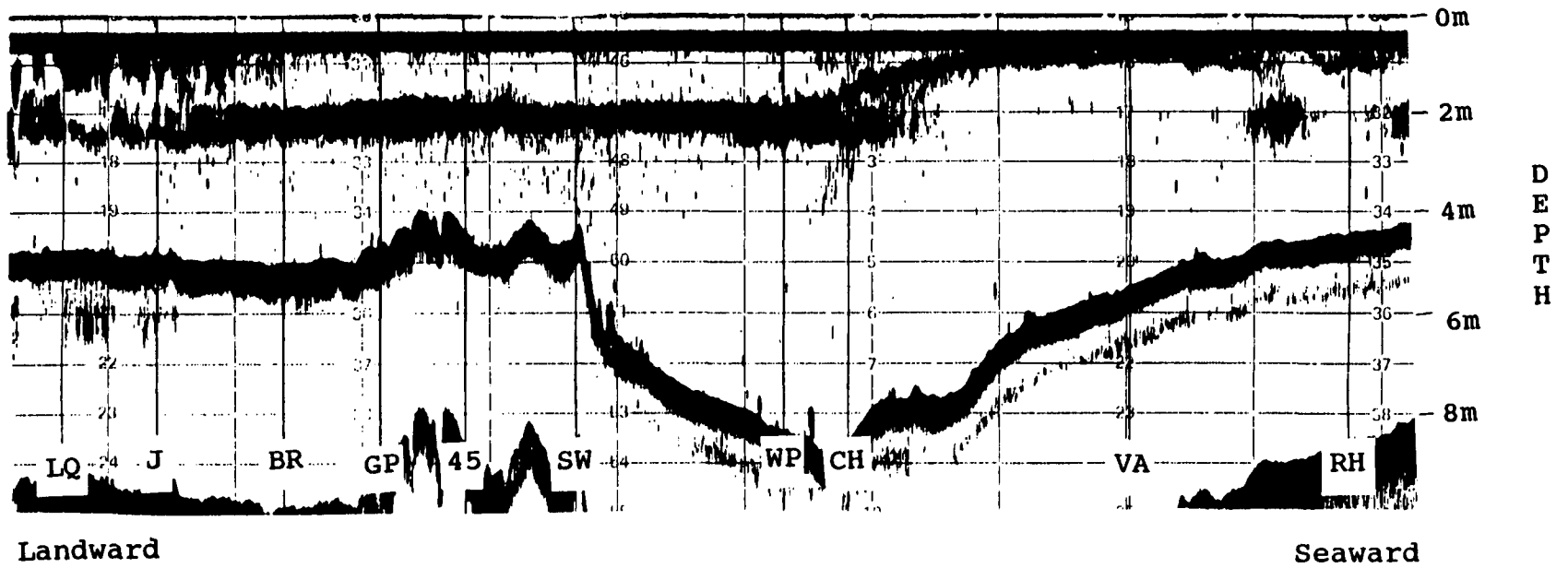


Figure 4.12: Transect 9 at 14:15 on 6 November 1989.

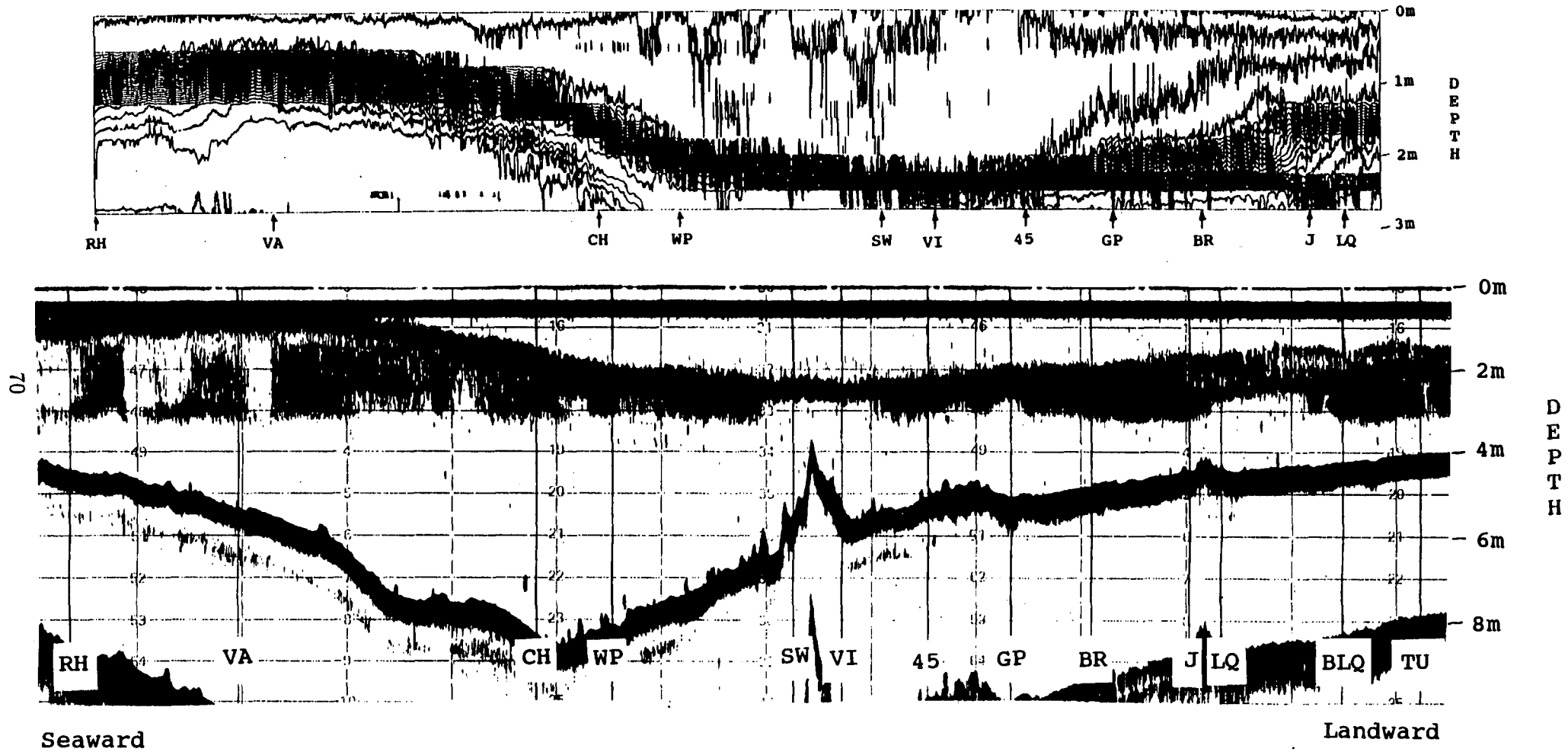
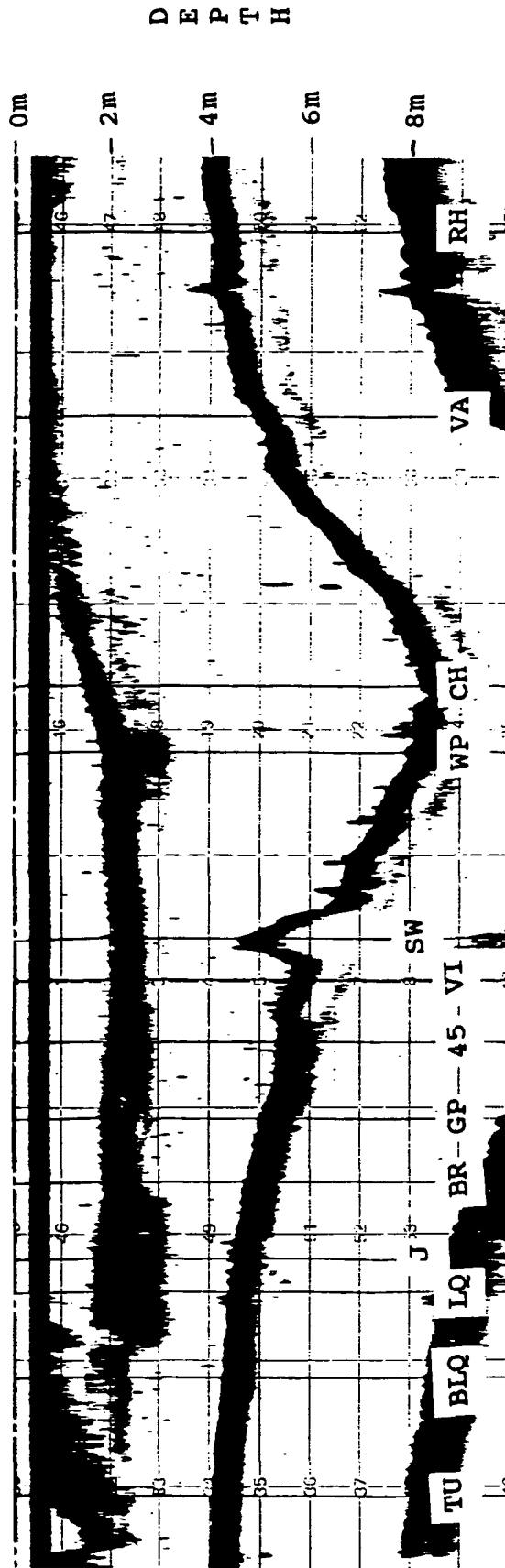
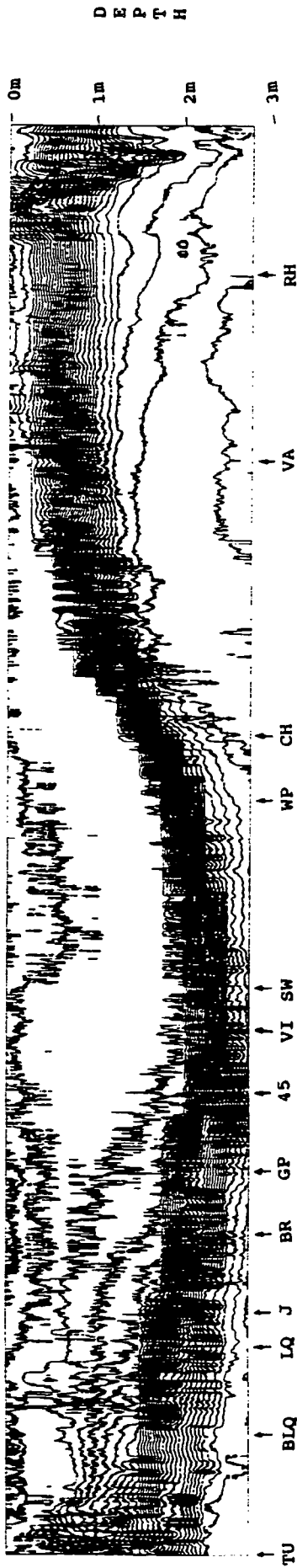


Figure 4.13: Transect 10 at 14:30 on 6 November 1989.



Landward

Seaward

Figure 4.14: Transect 11 at 14:45 on 6 November 1989.

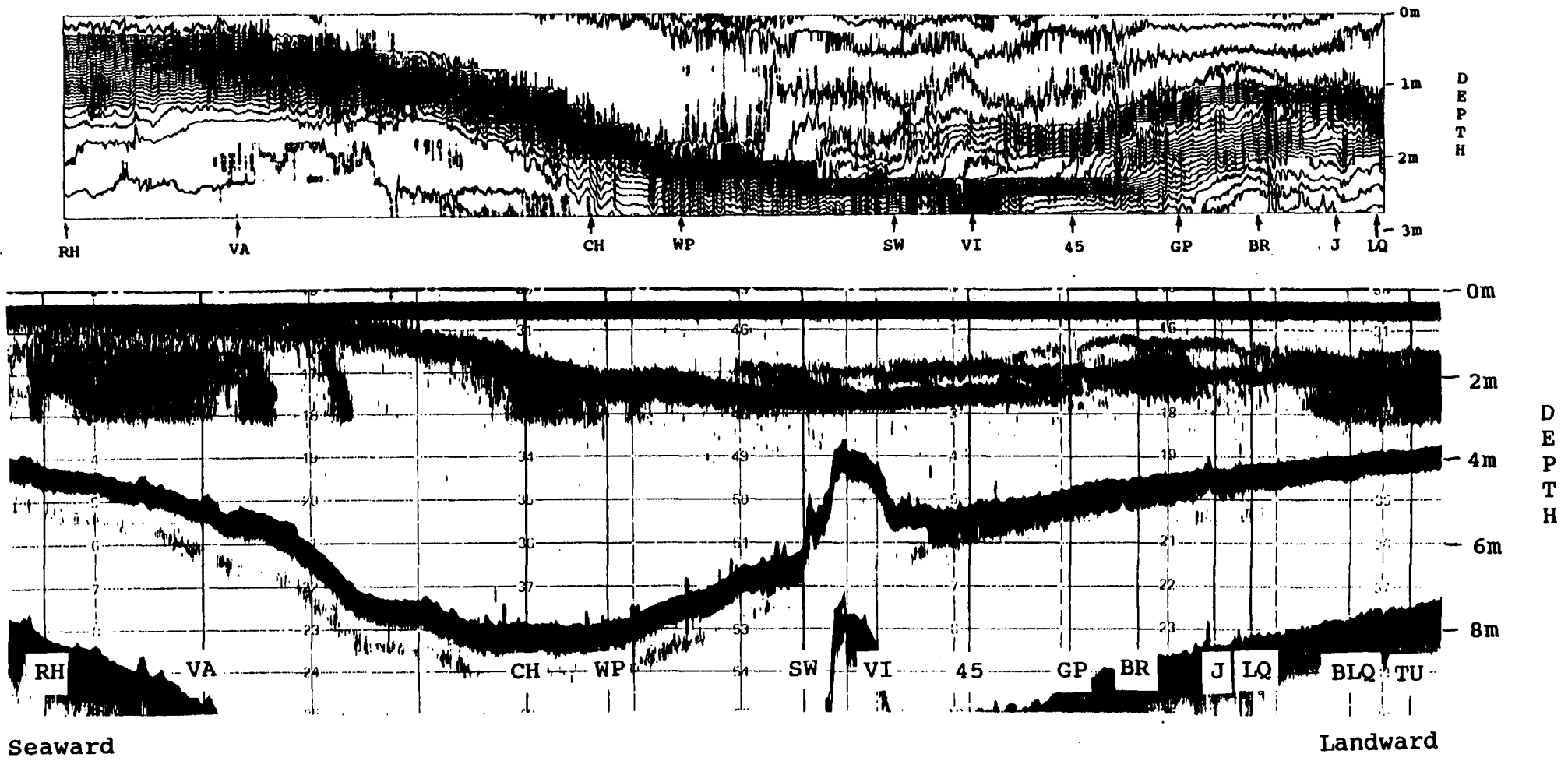


Figure 4.15: Transect 12 at 15:15 on 6 November 1989.

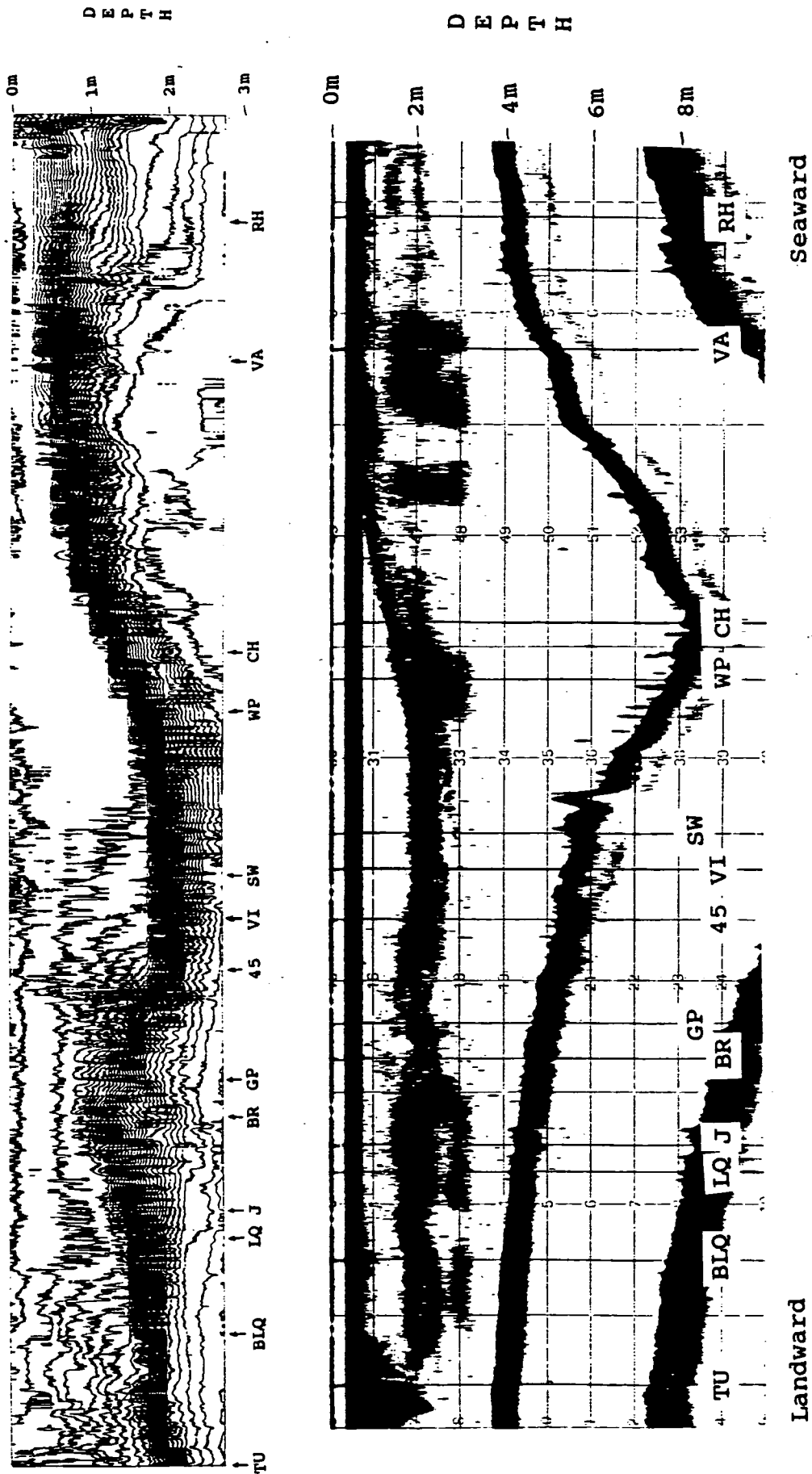
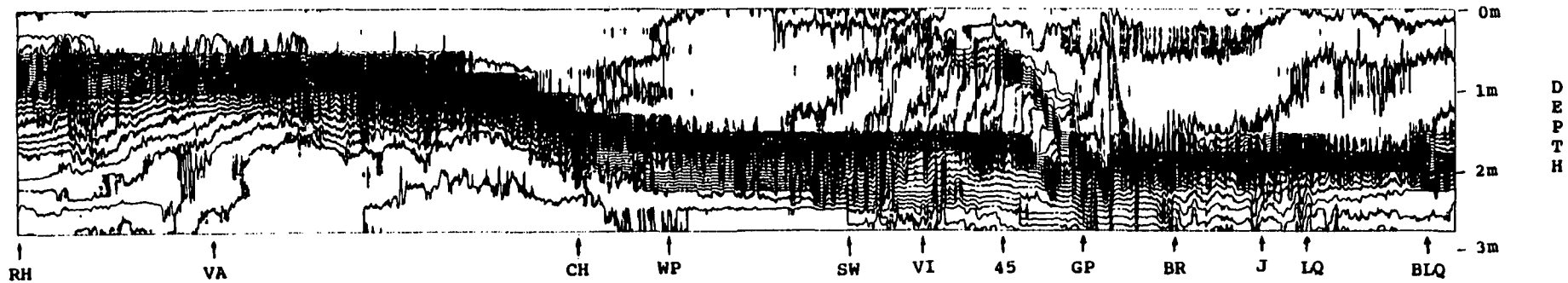
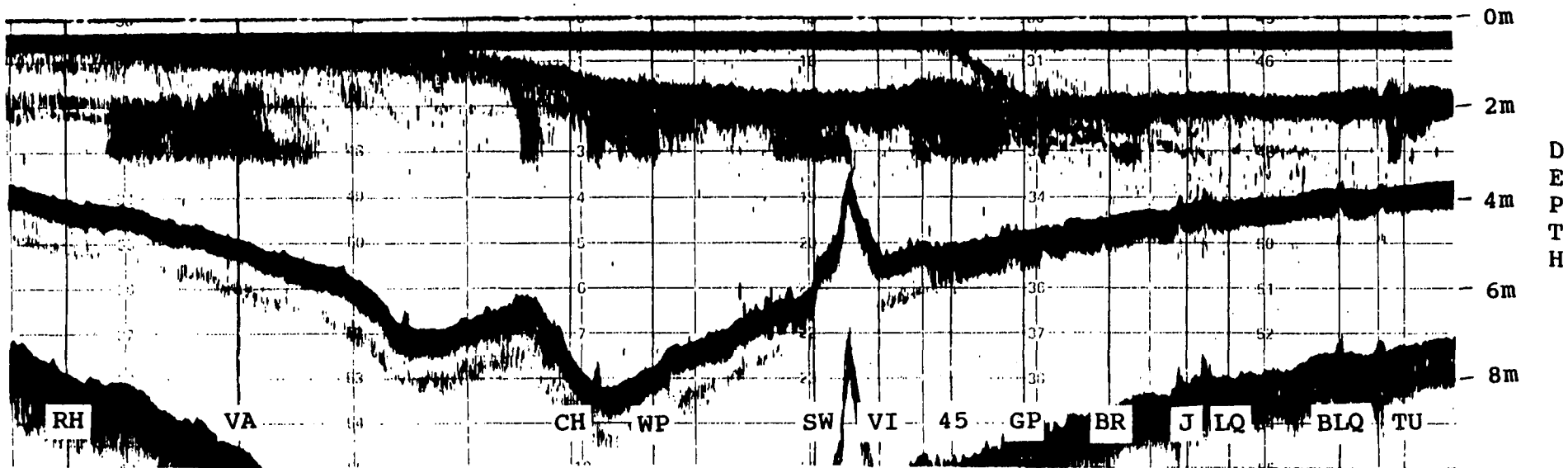


Figure 4.16: Transect 13 at 15:30 on 6 November 1989.



74



Seaward

Landward

Figure 4.17: Transect 14 at 15:45 on 6 November 1989.

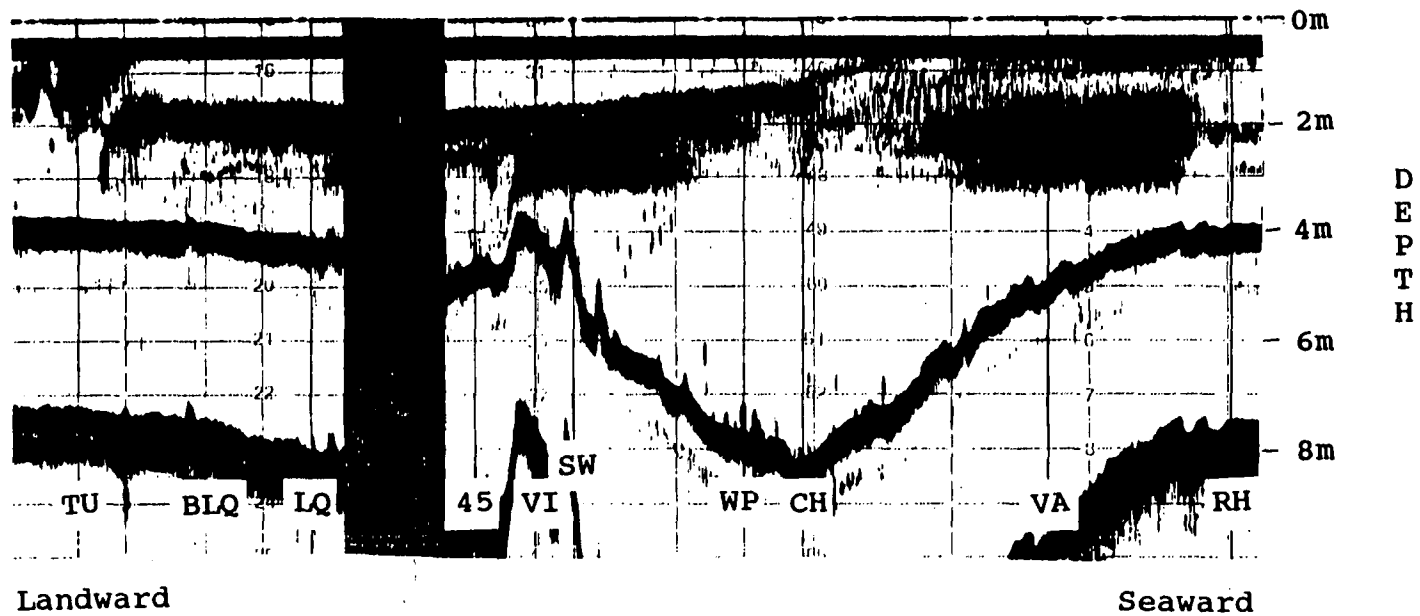
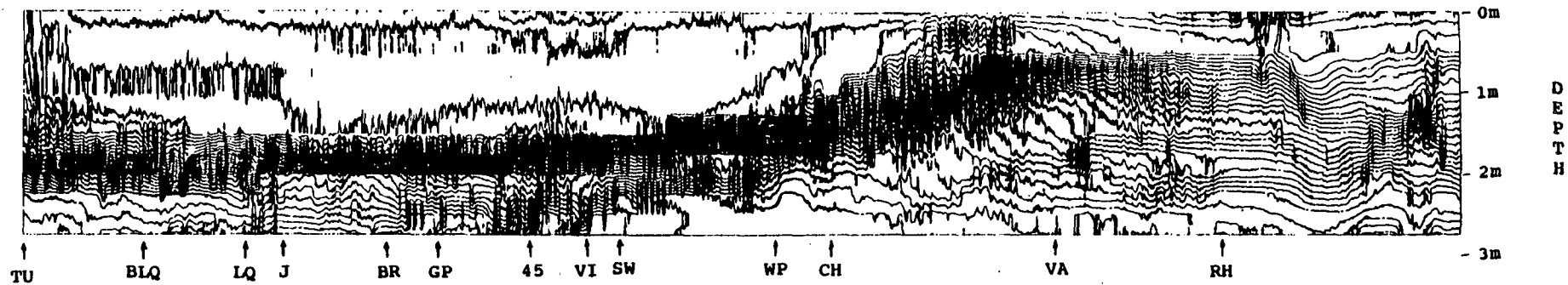
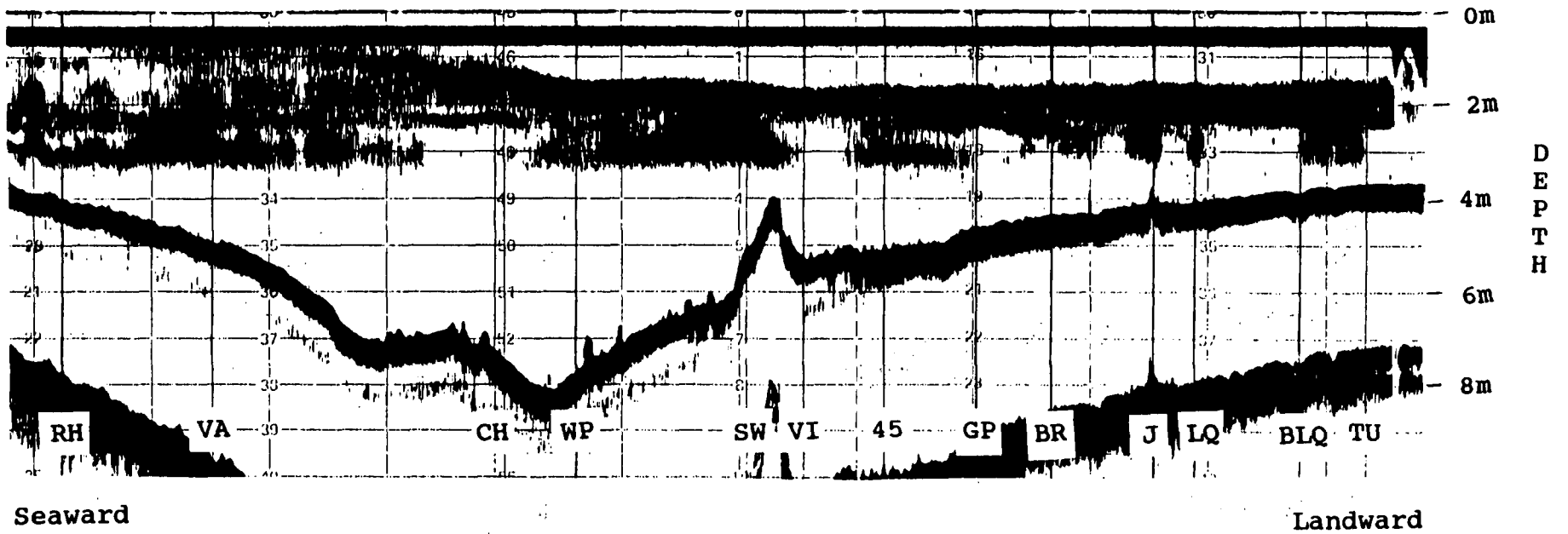
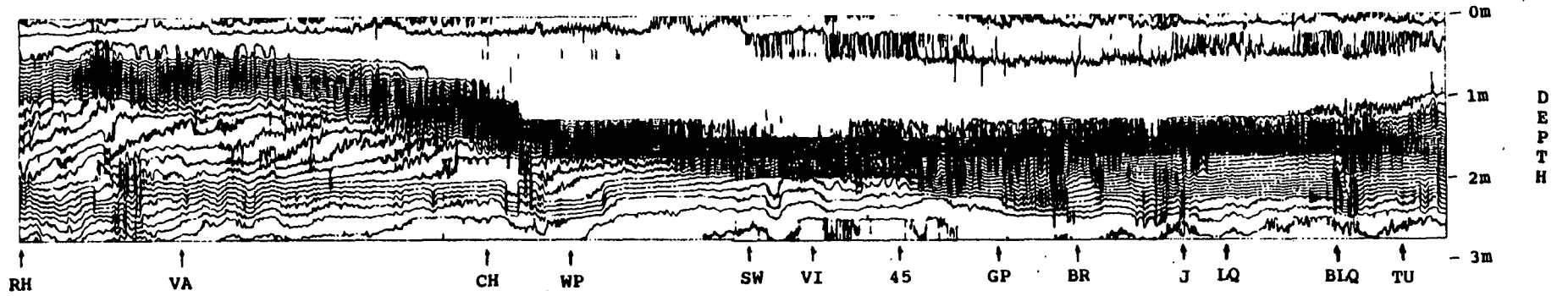


Figure 4.18: Transect 15 at 16:00 on 6 November 1989.



76

Figure 4.19: Transect 16 at 16:15 on 6 November 1989.

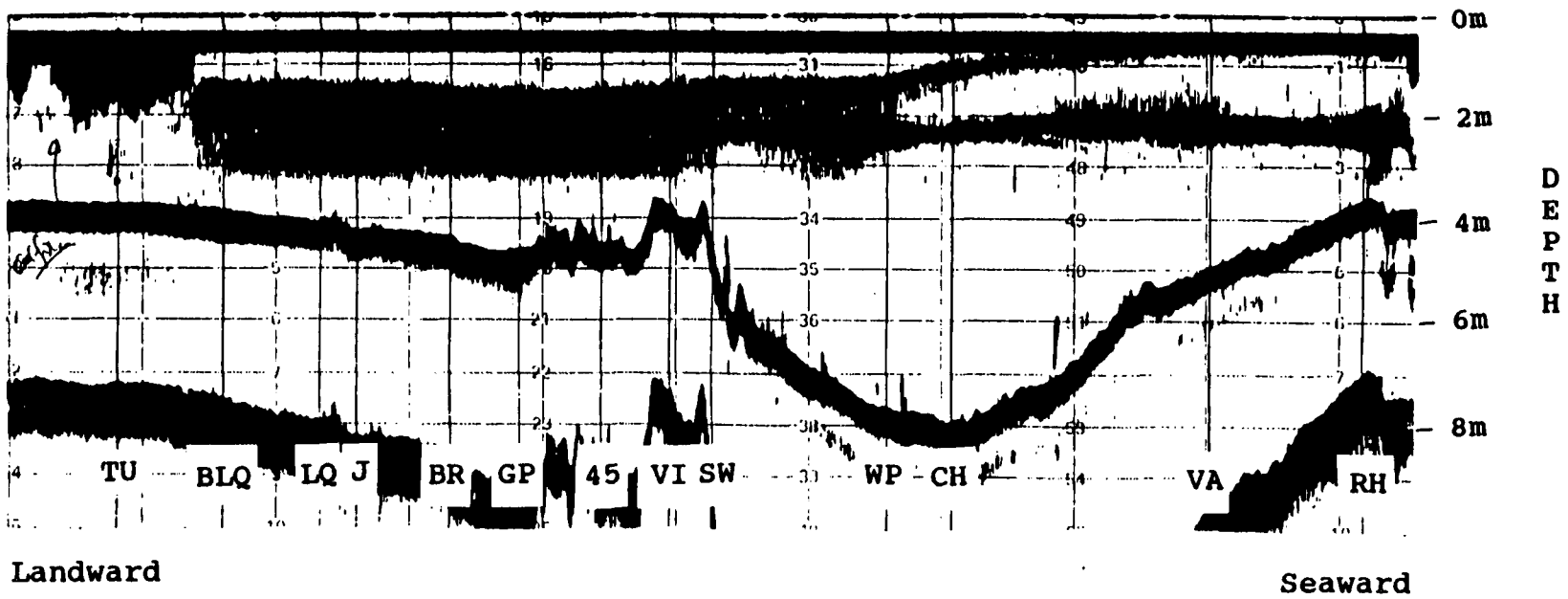
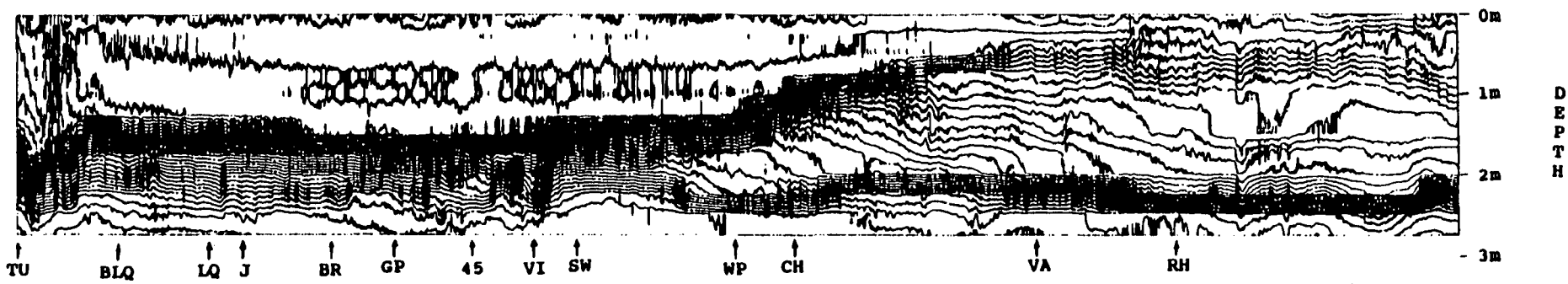


Figure 4.20: Transect 17 at 16:25 on 6 November 1989.

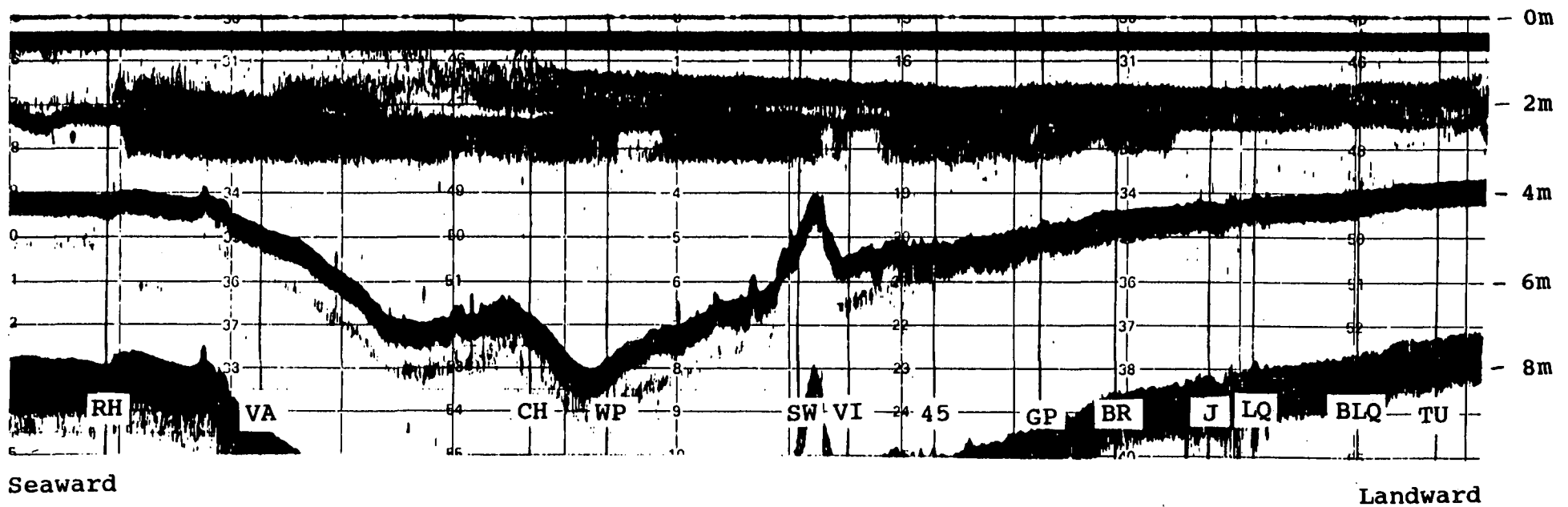
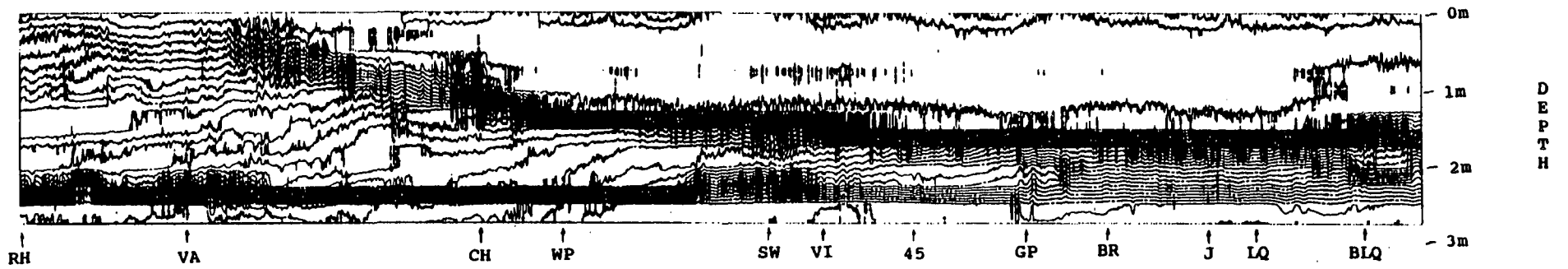


Figure 4.21: Transect 18 at 16:45 on 6 November 1989.

Maximum
thermocline
displacement
in metres
&
Depth averaged
velocity in m/s

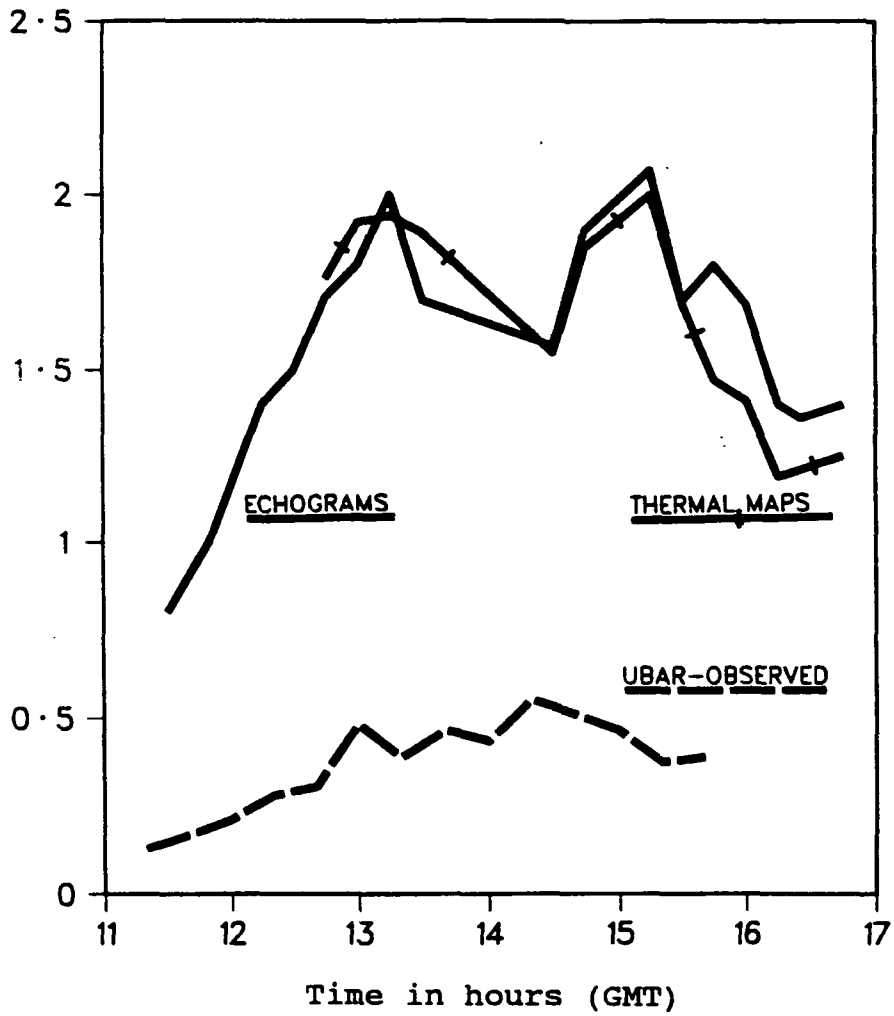


Figure 4.22: The size of the observed maximum thermocline displacement, in metres, plotted together with the depth averaged speed "45" in m/s, for 6 November 1989. The observations are derived from both echograms and thermal maps.

Wave trough
position
in metres
&
Depth averaged
velocity in cm/s

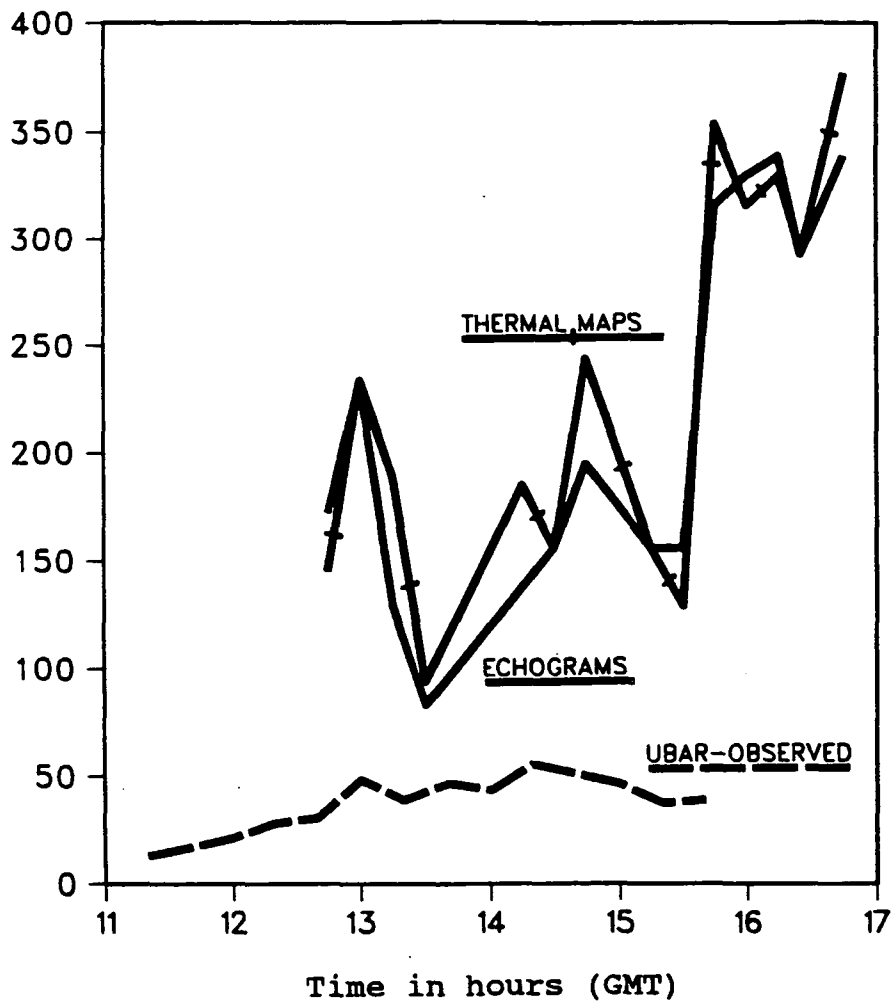


Figure 4.23: The observed position of the wave trough, in metres upstream from "CH", plotted with the depth averaged speed "45" in cm/s, for 6 November 1989. The observations are derived from both echograms and thermal maps.

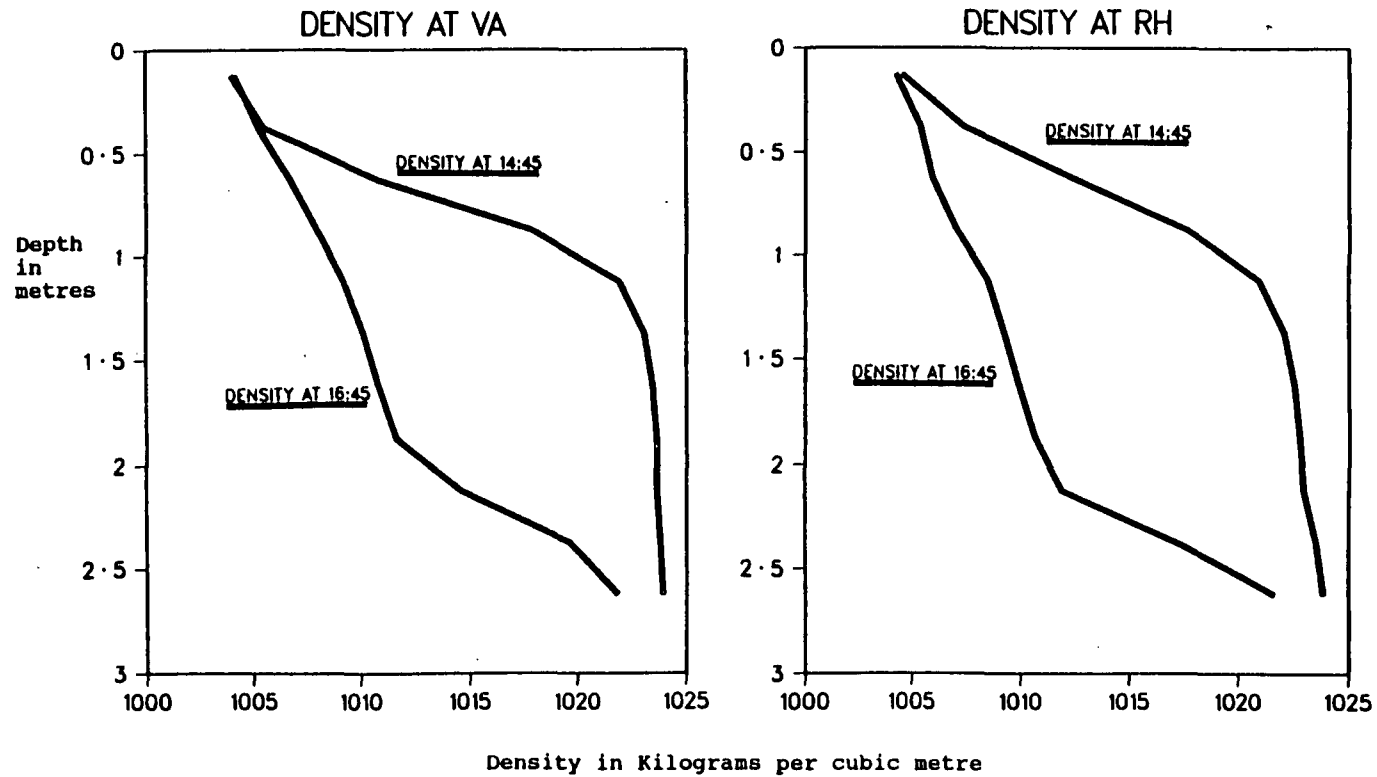


Figure 4.24: The density profiles at positions "VA" and "RH" at 14:45 and 16:45, showing the freshening of the watercolumn and the fall in height of the centre of mass. Density units are kilograms per cubic metre, and depth is in metres.

Total wave energy in Kilojoules per metre & Depth averaged velocity in cm/s

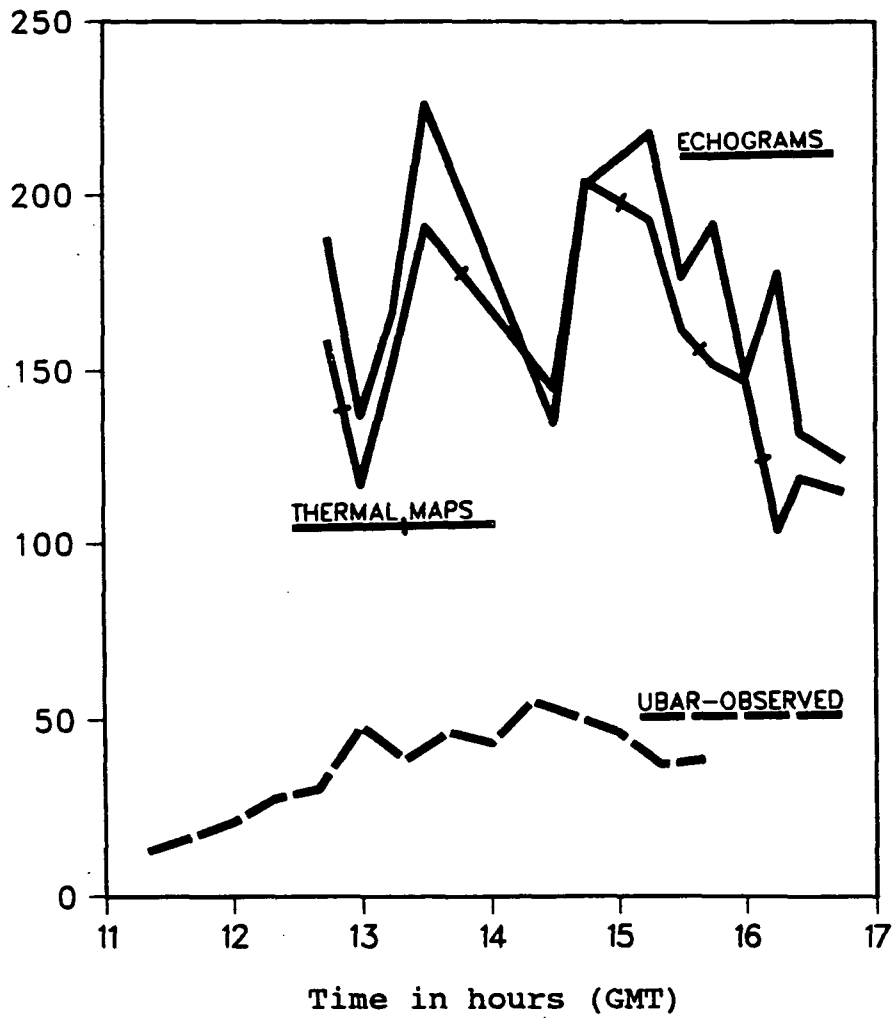


Figure 4.25: The observed total wave energy in kiloJoules per metre, with the depth averaged speed at "45" in cm/s, for 6 November 1989. The observations are derived from both echograms and thermal maps.

Chapter 5

Observations of an internal wave during a spring tide

This chapter describes a set of observations made in the Tamar at Cargreen on 15 November 1989. The data sets are discussed separately in qualitative terms, and then together quantitatively in the last section. The data consists of vertical profiles of temperature, salinity, current velocity and direction at station "45" and echosoundings and Spar data collected on longitudinal transects. The observations show the formation of an internal wave by interaction of the tidal ebb stream with the topographic depression. The wave grew with the rapidly increasing stream and decreasing stratification, until it interacted with the bed itself. Wave break-down and well-mixed conditions ensued. It is concluded that the flow underwent a hydraulic jump, and a Froude number analysis is presented, to show under what conditions this process might be expected.

Table 5.1: Predicted times of tides for Cargreen (and Devonport) on 15 November 1989 (Admiralty Tide Tables, 1989).

Slack Water	Time (GMT)	Tide height above C.D.
High Water	07:06 (06:56)	5.9m (5.8m)
Low Water	13:22 (13:02)	0.6m (0.7m)

5.1 Ancillary data

The predicted tides for Cargreen and Devonport are shown in table 5.1 (Admiralty Tide Tables, 1989). *RV Bass* was moored at position "45" taking vertical profiles of temperature, salinity, current velocity and direction, at twenty minute intervals from 10:00 to 12:40. The profiles are presented in figures 5.1, 5.2, 5.3, and 5.4. Figure 5.5 shows the time series of depth averaged speed, \bar{u} .

The salinity and temperature profiles show that the Tamar was weakly stratified at the beginning of the exercise, with well mixed upper (11.5ppt, 11.6°C) and lower (20ppt, 12.1°C) layers and a small temperature and salinity gradient separating them. During the exercise the thermocline, and halocline, weakened and then virtually disappeared. As the water depth fell to one metre, at "45", the water became nearly homogeneous in the vertical (3.8ppt, 10.8°C). These effects suggest seaward advection, past "45", of much less saline and less stratified water during the period 10:00 to 12:40. The difference in density between the surface and bottom waters is shown in table 5.2.

Figure 5.5, which shows the depth averaged speed, suggests a long ebb,

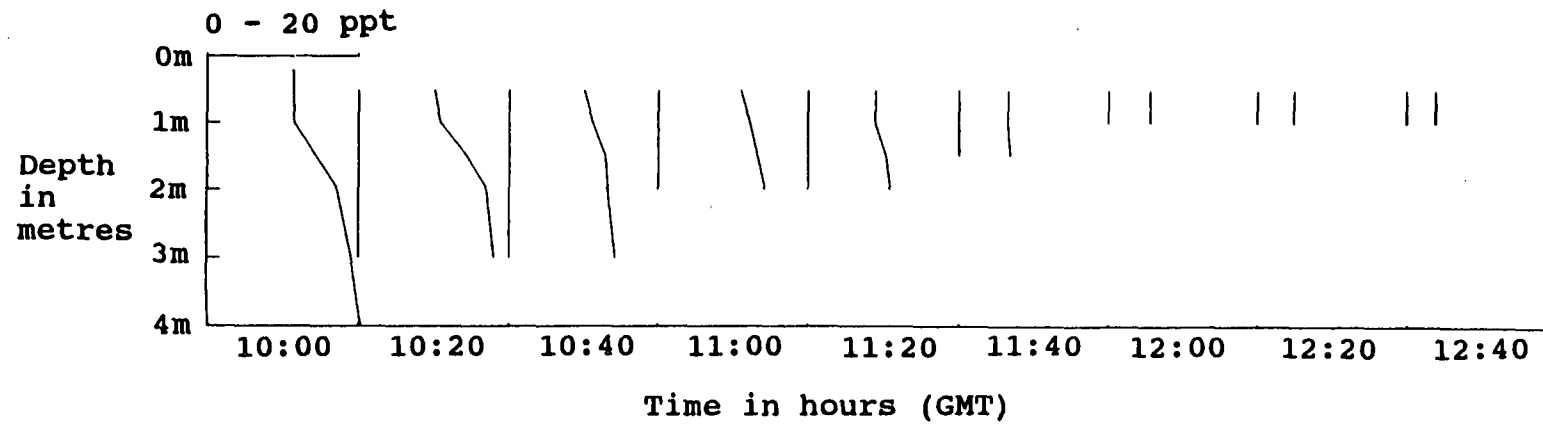


Figure 5.1: The vertical profiles of salinity at "45" on 15 November 1989, made every 20 minutes, as indicated on the horizontal time axis. The depth is in metres, and the scale for salinity is indicated in the top left hand corner, in ppt.

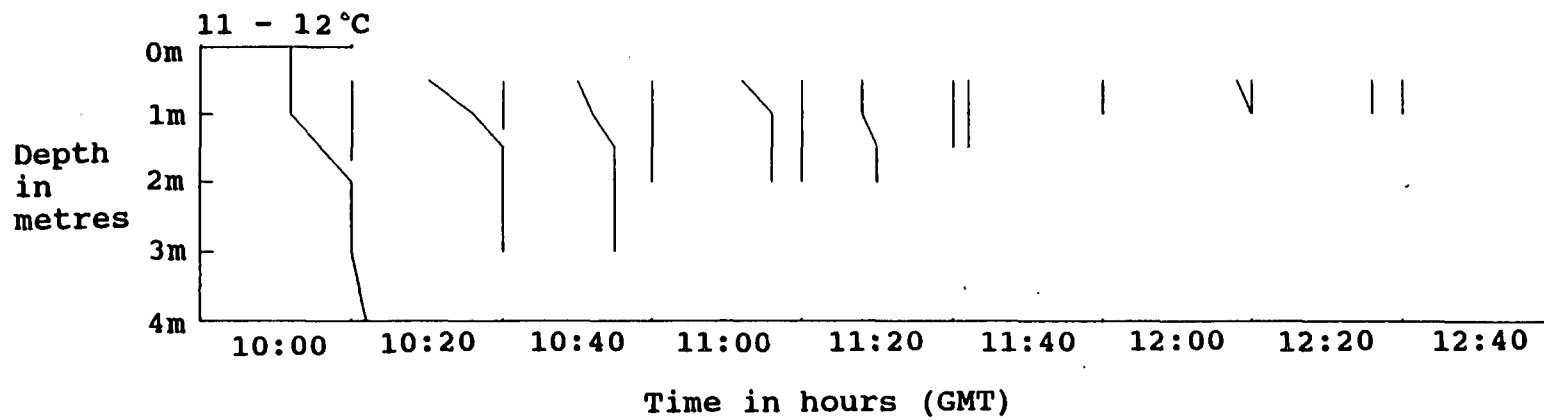


Figure 5.2: The vertical profiles of temperature at "45" on 15 November 1989, made every 20 minutes, as indicated on the horizontal time axis. The depth is in metres, and the scale for temperature is indicated in the top left hand corner, in celsius.

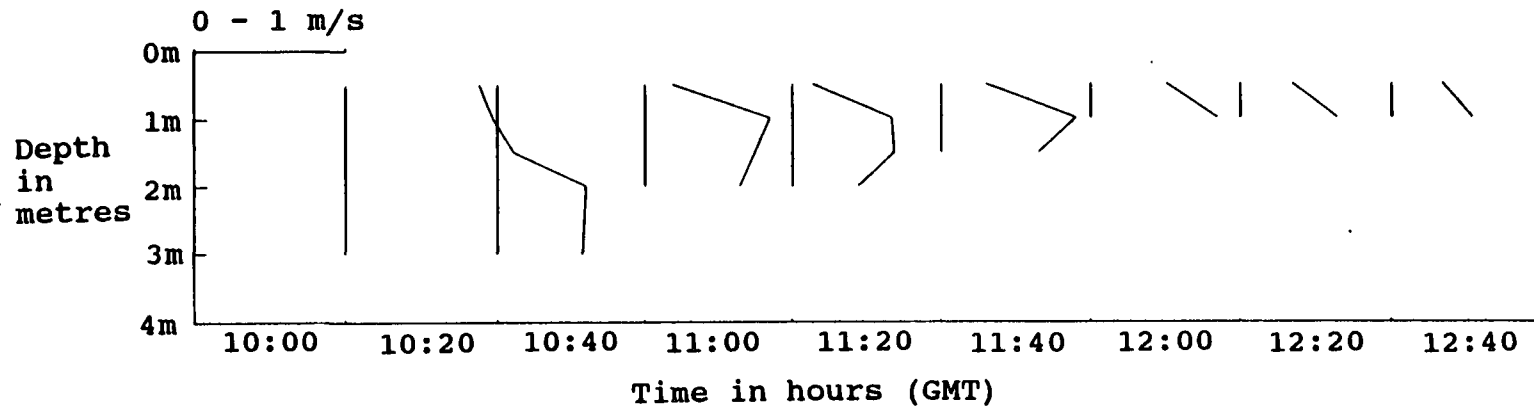


Figure 5.3: The vertical profiles of longitudinal velocity at "45" on 15 November 1989, made every 20 minutes, as indicated on the horizontal time axis. The depth is in metres, and the scale for velocity is indicated in the top left hand corner, in metres per second.

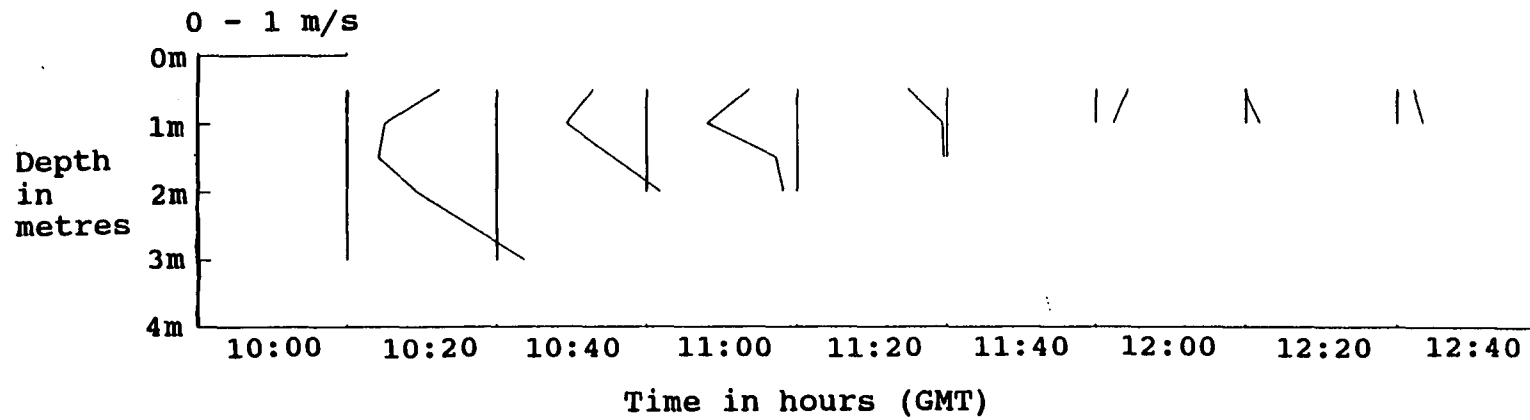


Figure 5.4: The vertical profiles of transverse velocity at "45" on 15 November 1989, made every 20 minutes, as indicated on the horizontal time axis. The depth is in metres, and the scale for velocity is indicated in the top left hand corner, in metres per second.

Depth
averaged
velocity
in m/s

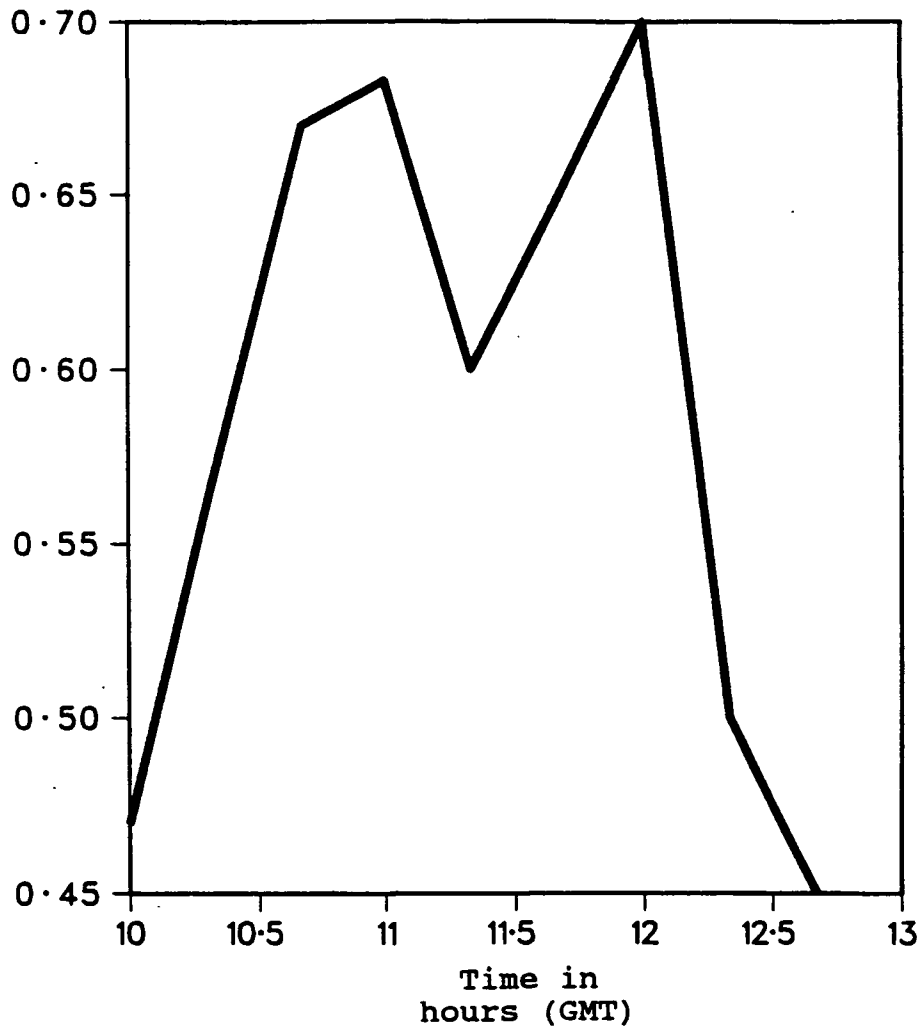


Figure 5.5: The magnitude of the depth averaged velocity at "45" on 15 November 1989. The velocity is in metres per second and the horizontal axis is in hours GMT.

Table 5.2: The surface to bottom water density difference in kilograms per cubic metre.

Time	$\Delta\rho$
10:00	6
10:20	6
10:40	3
11:00	2.5
11:20	2.5
11:40	0.25
12:00	0.25
12:20	0
12:40	0

perhaps up to 7 hours in duration, with a double peak in velocity. Like the neap case, this is a common feature (George, 1975). The current meter did not provide direction measurements until 10:40, when an electrical fault was corrected. Hence the early observations are omitted from the axial and transverse velocity figures.

Unlike the neap observations there did not appear to be much correspondence between the thermocline level and the velocity profiles. However, the behaviour of the transverse and axial components, in the two tidal states, was similar. Figure 5.4 indicates that before 11:20 there was a large transverse flow toward the Devon bank in the upper layer, which diminished near 12:00, and later became a small flow toward the Cornish bank. The axial velocities show a large seaward flow which increased up to 12:00, diminishing only slightly after that time, with a maximum at mid-depth. This maximum was possibly around the level of the thermocline, although this was hard to infer for the behaviour before 10:40. These profiles, like the

neap observations, indicate a strong three dimensional structure to the flow.

Correlating T against S , and regressing S on T , did not show as clear a relationship as for the neap case. With fewer profiles, fewer measurements in the profiles, and such small temperature and salinity ranges, the statistical error bounds were also large. The gradient Richardson number profiles show that the whole water column, at "45", was near to or below the critical value, 0.25, from 10:40 to 12:40.

5.2 Echosounding data

RV Catfish made axial transects of the estuary over the depression from 09:50 to 13:02. The echosounder provided a continuous record of acoustic backscatter. Figures 5.7 to 5.18 show the echograms in sequence, together with the Spar data as thermal maps. The pattern of mid-water acoustic backscatter was very different to that of the neap study, for a number of reasons.

- In figure 5.7 to figure 5.10 there is an acoustic return from a constant 1.2m – 1.4m depth. This is attributed to a scattered signal from the Spar itself. The acoustic return is absent from the echograms after the Spar was raised due to the falling water depth.
- In order to help identify the regions with most finestructure, due to turbulence, the gain sensitivity of the echosounder had to be reduced during the exercise when the echograms "blacked out". This was due to the water column becoming saturated with acoustic backscatterers.

These reductions in sensitivity were made between figure 5.10 and figure 5.11 and between figure 5.12 and figure 5.13.

- In figure 5.7, which depicts the situation at 10:00, there was an acoustic return from mid-depth, which was identifiable as a wave - a depression of the thermocline over the landward slope of the bed depression, with the maximum thermocline displacement near "WP". The wave was present at least from "RH" to "BR", and perhaps more landward of this.
- There was no obvious stable (non-breaking) waveform after 10:20 (figure 5.8). At 10:40 (figure 5.9) and 11:00 (figure 5.10) the flow had depressed the thermocline down to the bed. From 11:40 (figure 5.11) on there is no identifiable wave structure.
- In figure 5.13 to figure 5.18 there are triangular regions of backscatter over the landward slope of the depression, in the top 2m of the estuary. In the same figures there are patches of backscatter from the bottom 2m of the water, over the seaward slope and the deepest part of the bed depression. These two features may give clues to the flow regime. It is conceivable that a separation of the flow, from the bed, occurred over the seaward slope of the depression, and that a hydraulic jump was responsible for strong downward vertical motion in the water column over the landward slope. Whether rotors or eddies formed in these two regions is open to question. Figure 5.14 shows these effects most clearly.

The overall impression given by the echograms is that a wave formed over the bed depression at 10:00 in a rapidly increasing ebb stream and decreasing stratification. It grew until about 10:20 when the thermocline reached the estuary bed. After 10:40 the wave had given way to a highly turbulent flow, which had followed the wave break-down. The exact mechanism of wave break down is not known although a "hydraulic jump" seems most likely.

5.3 Spar data

During each transect made in *RV Catfish* the Spar collected temperature data simultaneously with the echograms. The resulting thermal maps are presented together with the echograms. The maps show temperature increasing with depth and have the isotherms plotted at 0.1°C intervals. Some general observations can be made.

- During this spring tide the water level fell rapidly, and the Spar was run aground twice in attempts to get full coverage of the estuary temperature structure. It was necessary to raise the Spar from the water, and this occurred at 10:30 and 11:30, and accounts for a change in size of the thermal maps which are plotted with essentially no change in vertical scale.
- The thermocline, when present, was below the lowest sensor on the Spar for a large portion of the transects.
- Superimposed on the isotherms, but not obscuring the data, is a harmonic ripple of electronic origin, perceptible in some of the figures.

- In some figures (e.g. figure 5.11 near 1m depth) there is an apparent temperature inversion. This "inversion" rose in the water column with adjustments in the depth of Spar deployment, and was almost definitely not real. It is felt that this was either due to a faulty sensor, or poor calibration of the same sensor against the others.
- The thermal maps in figure 5.8 and figure 5.10 are elongated, because of the strong ebb stream. They each represent some 26 minutes of data.
- The thermal map for figure 5.18 is absent because the data was partially corrupt.
- In figure 5.8 the vertical line near "VA", is a spike caused by a surge in the electrical supply to the Spar.

Overall, the Spar data shows the same qualitative behaviour as the echograms, but for the top few metres of the water column only.

5.4 Quantitative comparison of data sets

5.4.1 Froude number analysis

An analysis similar to that performed for the neap tide case is not appropriate for these spring conditions. The destratification of the estuary near the Cargreen depression made the spring tide hydraulics very different to those on the neap tide studied.

It would appear that wave formation is possible but not sustainable at

Table 5.3: The internal Froude number evolution over the bed depression at Cargreen, on 15 November 1989.

Time	$F_{i,s}$	$F_{i,d}$	Wave present ?
10:00	2.0	1.1	✓
10:20	2.5	1.2	✓
10:40	4.3	2.0	?
11:00	4.9	2.3	?
11:20	4.7	1.9	?
11:40	14	5.7	x
12:00	21	7.7	x
12:20	∞	∞	x
12:40	∞	∞	x

a high internal Froude number, F_i .

$$F_i = \frac{\bar{u}}{c_0} \quad (5.1)$$

where \bar{u} is the depth averaged current speed and c_0 is the linear long wave phase speed, (equation 4.2). Table 5.3 shows how the shallow water Froude number, $F_{i,s}$, estimated for the flow outside the depression, and the deep water Froude number, $F_{i,d}$, estimated for the flow over the deepest part, evolved with time on 15 November 1989. The depth averaged speed, \bar{u} , was estimated, for each Froude number, by assuming horizontal volume continuity along the estuary using the velocity data observed at "45".

It is clear that as the internal Froude number increased beyond some critical value, the wave response of the estuary broke down as a hydraulic jump formed over the depression. For this to have happened there had to be a transition, from supercritical flow upstream of the depression to subcritical

flow over the centre of the depression. A critical value of F_i near 2 or 3 is indicated by table 5.3, for this particular stratification and topographic feature. After the critical value had been reached the flow continued to be everywhere supercritical, and no further wave activity was observed.

5.4.2 Internal wave height

The wave height measured from the echograms is shown in figure 5.6. The measurement error in the wave height is $\pm 20\%$. The wave grew rapidly from slack water to a height of about $3m$ at 10:00, then to $5.6m$ at 10:20 and remained about this height until 11:00, after which it broke *in situ*. \bar{u} increased from $0.47ms^{-1}$ at 10:00 to $0.68ms^{-1}$ at 11:00. By 11:20 \bar{u} had fallen to $0.6ms^{-1}$. The echograms suggest that from 10:20 to 11:00 the wave was strongly interacting with the bed. The wave did not break until after 11:00, when the echograms became completely saturated with backscatter. Nonlinear steepening, and growth of the wave, in the temporarily slackening ebb stream between 11:00 and 11:20 might have provided the specific mechanism for wave breaking.

5.4.3 Internal wave energy

The total internal wave energy was estimated for easily identifiable wave structures. Calculated in the same way as for the neap tide wave, the estimates from the echograms were $164kJm^{-1}$ at 10:00 (figure 5.7), $320kJm^{-1}$ at 10:20 (figure 5.8), and $89kJm^{-1}$ at 10:40 (figure 5.9). The error in the estimation was about 30% in the first two energies, and about 50% in the 10:40

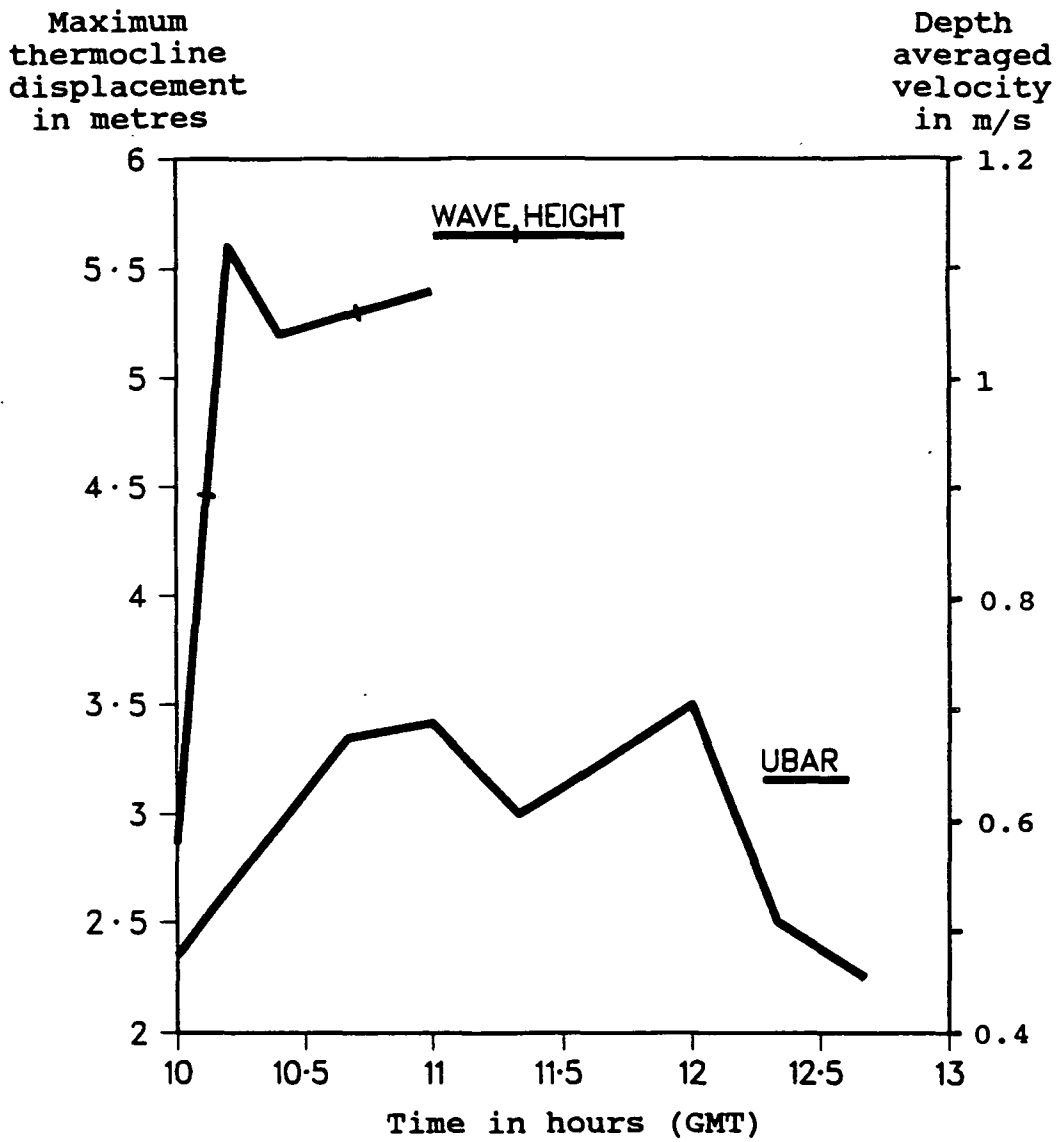


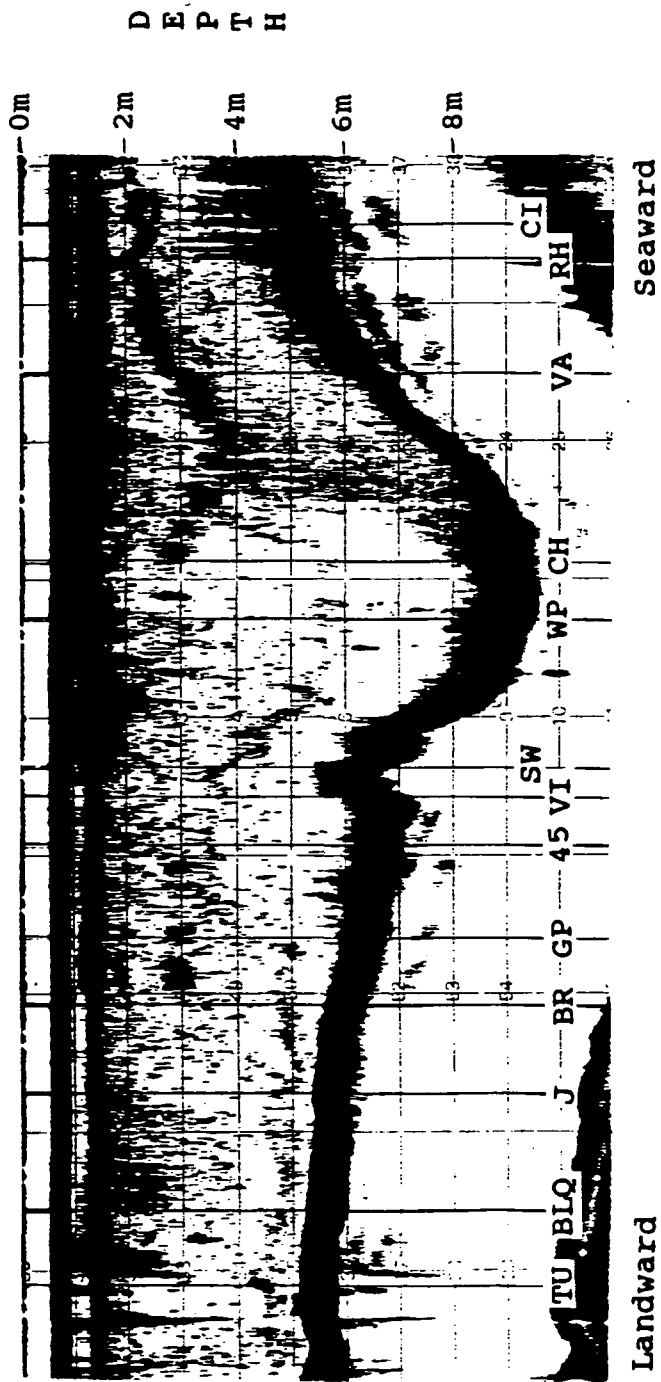
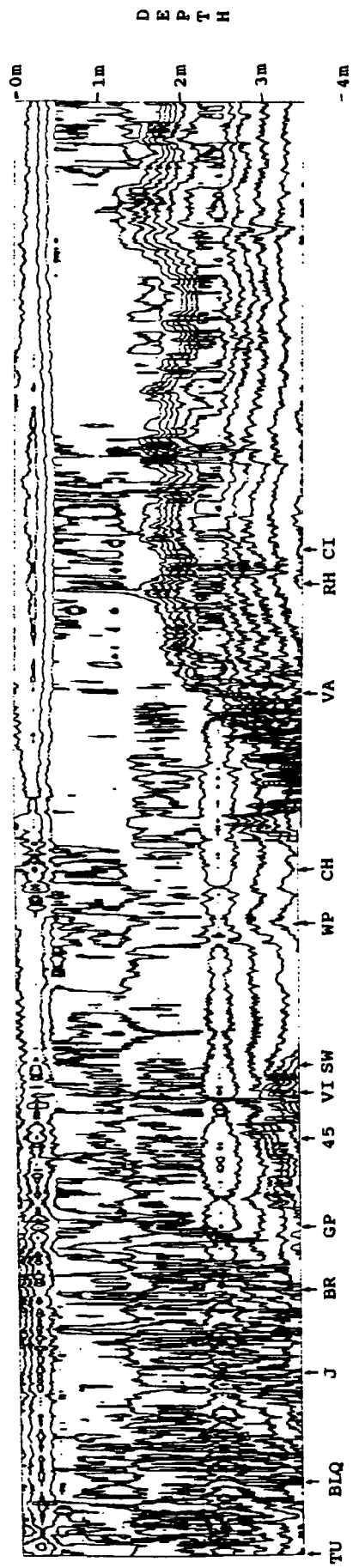
Figure 5.6: The wave height and magnitude of the depth averaged velocity at "45", on 15 November 1989. The wave height is in metres and the velocity is in metres per second.

estimate. The sharp reduction in energy between 10:20 and 10:40 appears to be solely due to the water over the depression becoming less stratified, through advection and mixing upstream. The wave height did not change much in the same period, but the thermocline was close to the bed.

The barotropic tidal wave energy for this half tide, averaged over the landward slope of the depression, was 8.7 MJ m^{-1} . Thus about 2.5% to 5% of the available barotropic tidal energy was accountable for by the internal wave at 10:20. Unlike the neap case, the initial fate of the internal wave energy cannot even be partially accounted for.

The formation of an internal wave, as a precursor to violent vertical mixing in such conditions, may be interesting and curious, but not particularly important. The estuary on 15 November 1989 seemed to be destined to destratification, through the action of the strong tidal stream, and associated shears, across the thermocline and at the bed. The presence of the bed topography at Cargreen may have helped increase mixing locally, but as vigorous mixing was already apparent throughout the upper Tamar, its relative contribution was probably small.

Figure 5.7 to Figure 5.18 The following 12 figures are the echograms, and thermal maps derived from the Spar data, for the longitudinal transects starting at 10:00 and ending at 13:00 on 15 November 1989, at Cargreen. The echograms and their corresponding thermal maps are presented in pairs for ease of comparison. Both diagrams in each figure are annotated with fixed positions and with a depth scale in metres. The Eulerian measurements were made at position "45". For a rough idea of the horizontal scale the distance between "VA" and "CH" is 144m, "CH" and "45" is 234m, and "CH" and "BLQ" is 560m. Isotherms and backscatter more seaward than the most seaward station indicated, and more landward than the most landward one, must be ignored, as this data was collected while the launch *RV Catfish* turned at the end of the transects. The isotherms are increasing in value downwards, and are plotted at 0.1°C intervals. Seaward and landward directions are indicated. The figures are explained and discussed in the text.



Landward Seaward

Figure 5.7: Transect 1 at 10:00 on 15 November 1989.

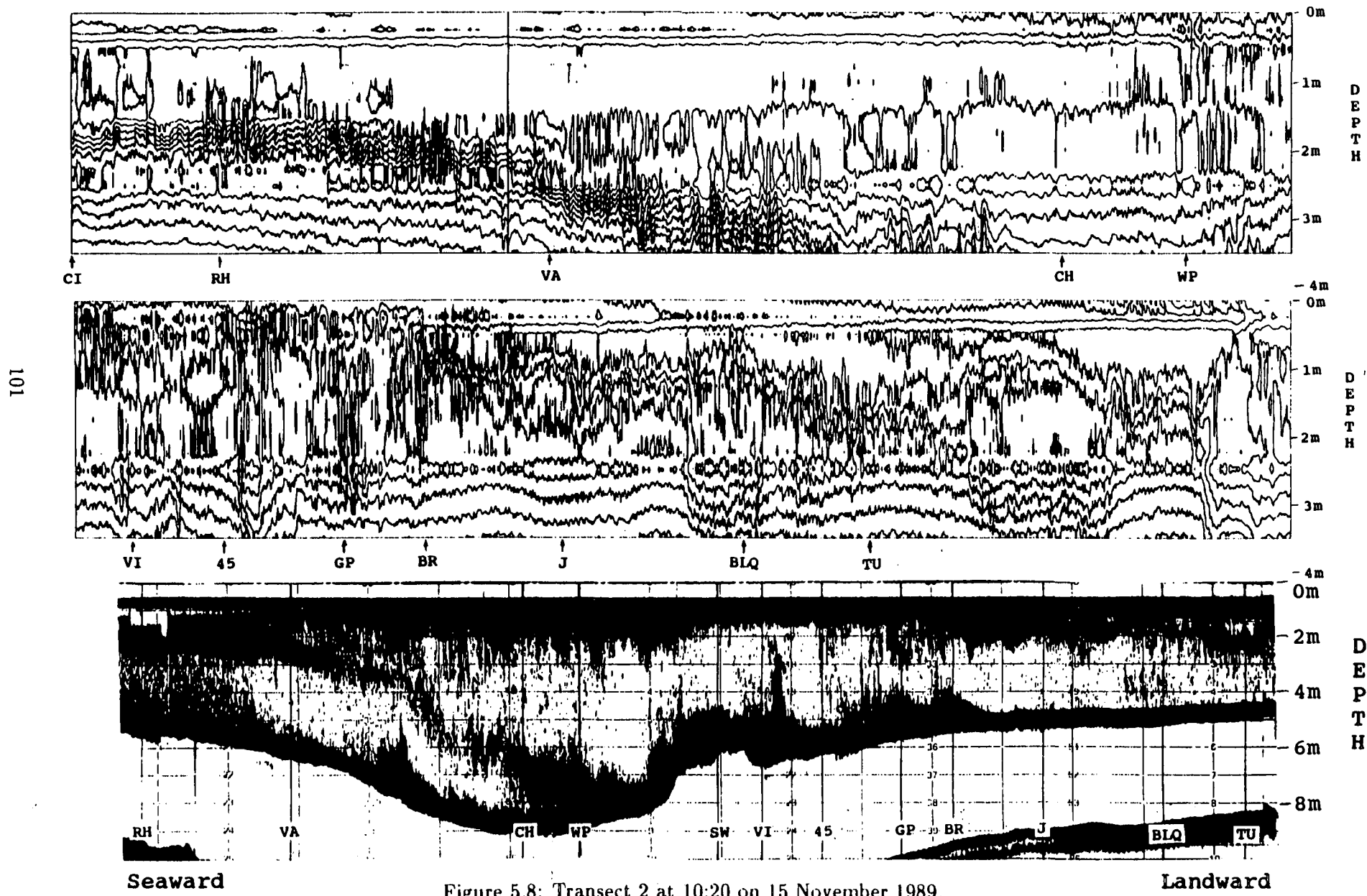


Figure 5.8: Transect 2 at 10:20 on 15 November 1989.

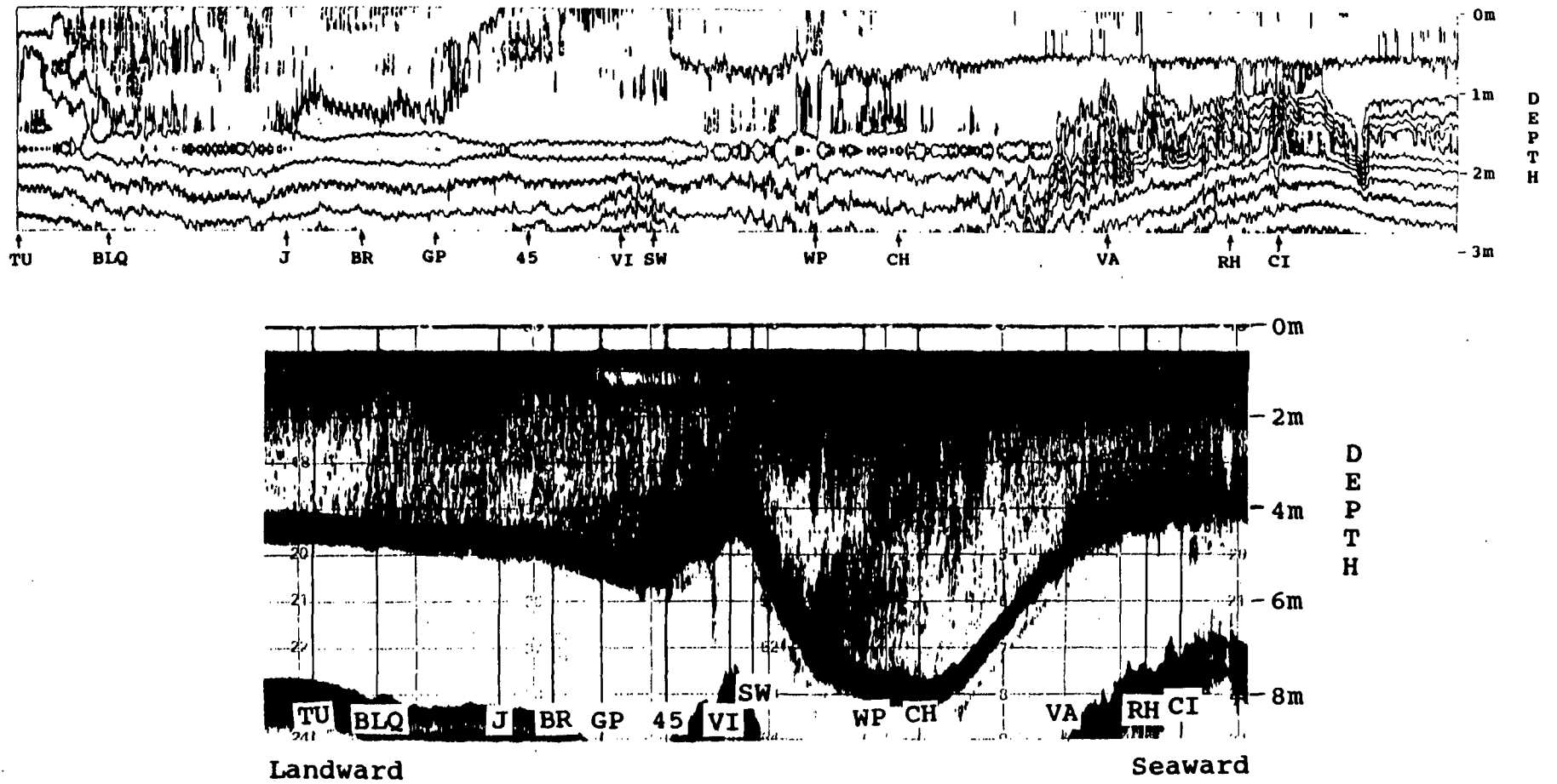


Figure 5.9: Transect 3 at 10:40 on 15 November 1989.

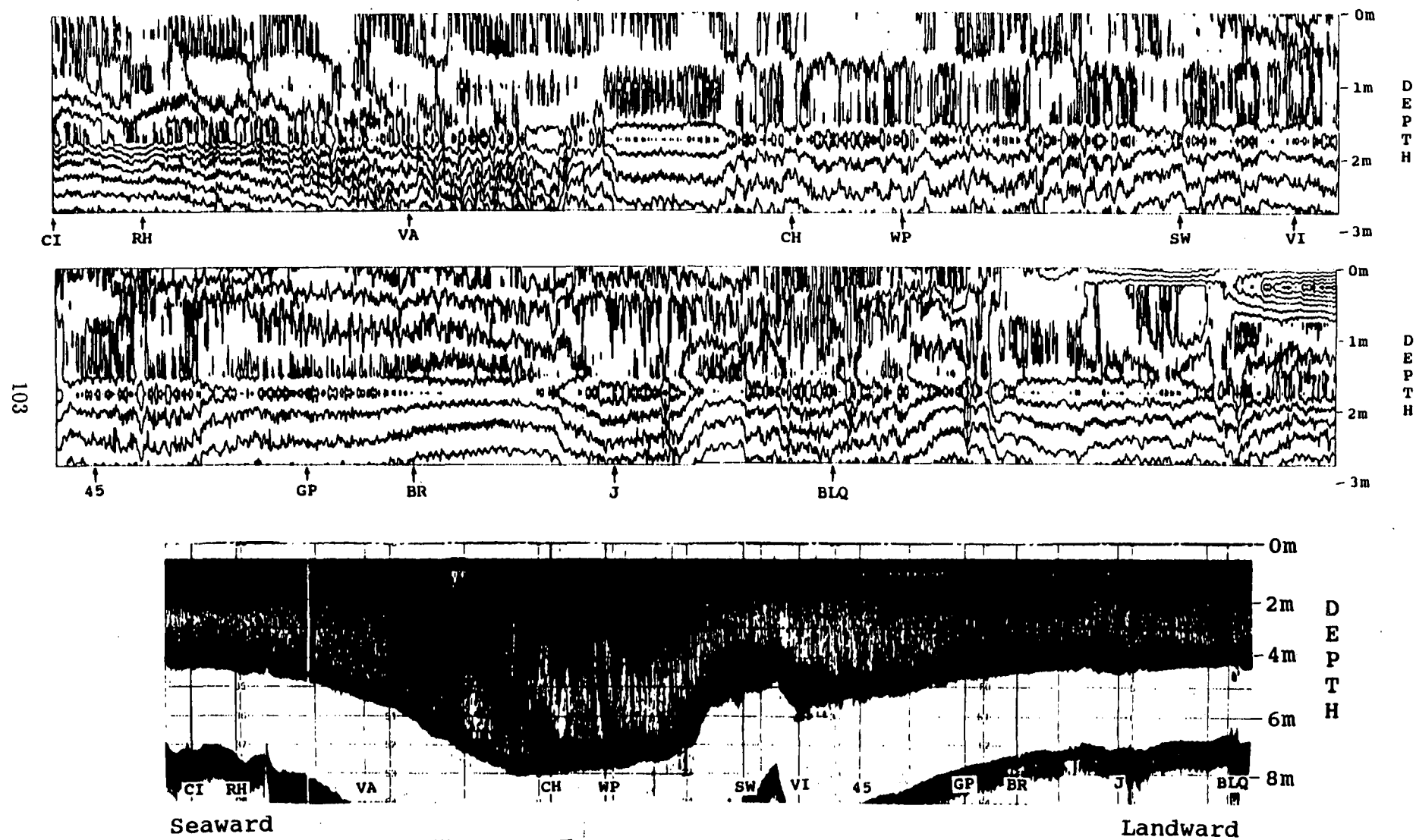


Figure 5.10: Transect 4 at 11:00 on 15 November 1989.

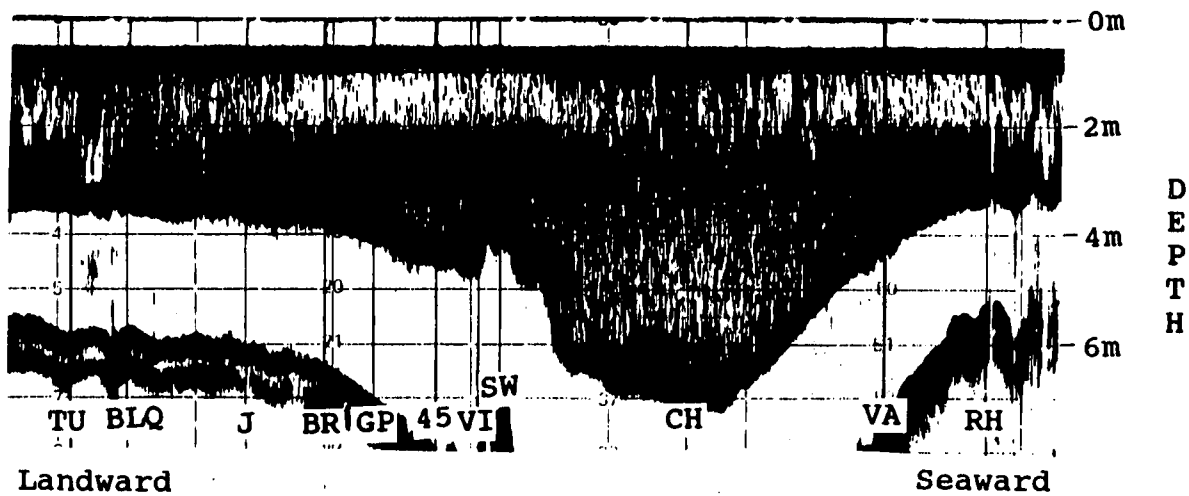
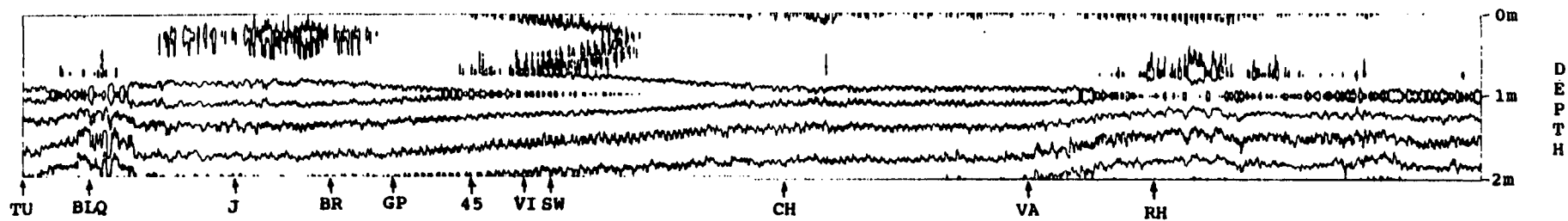


Figure 5.11: Transect 5 at 11:40 on 15 November 1989.

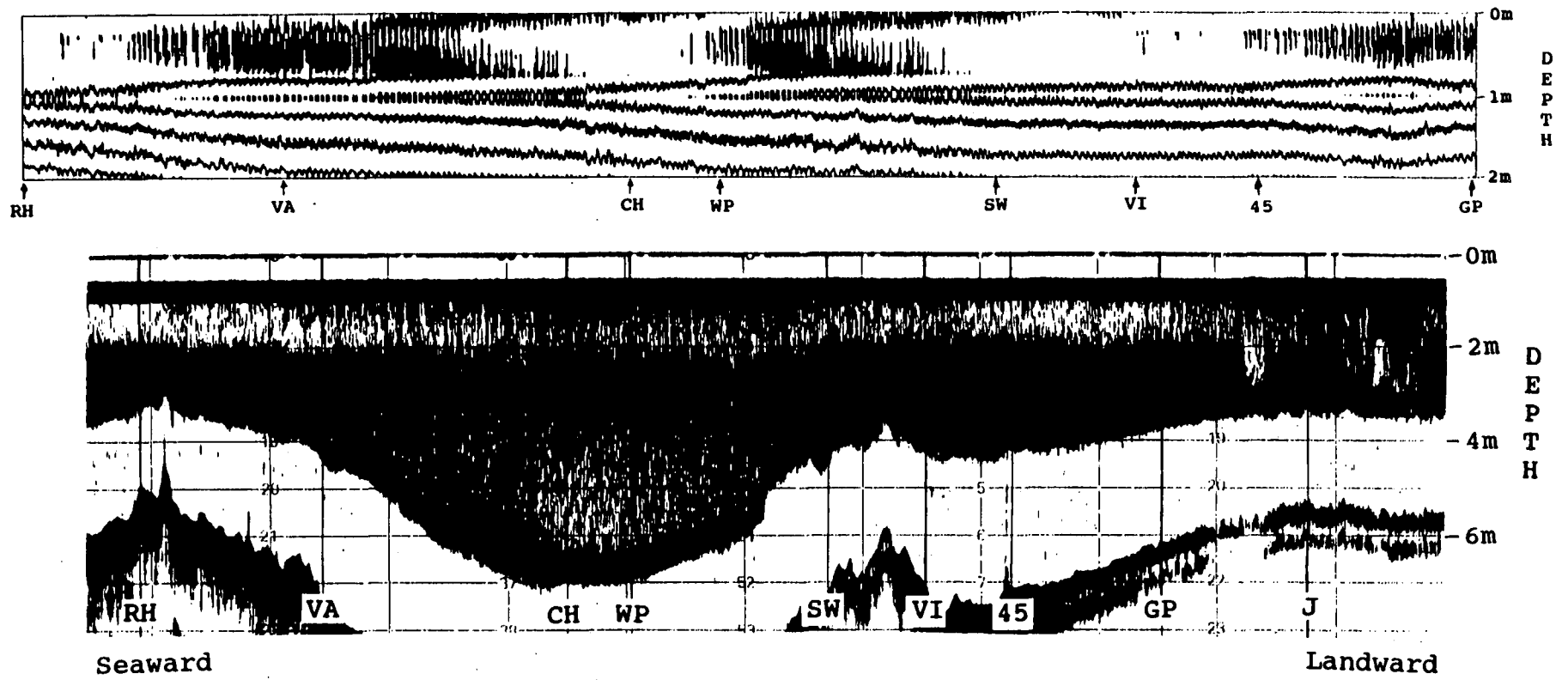


Figure 5.12: Transect 6 at 11:50 on 15 November 1989.

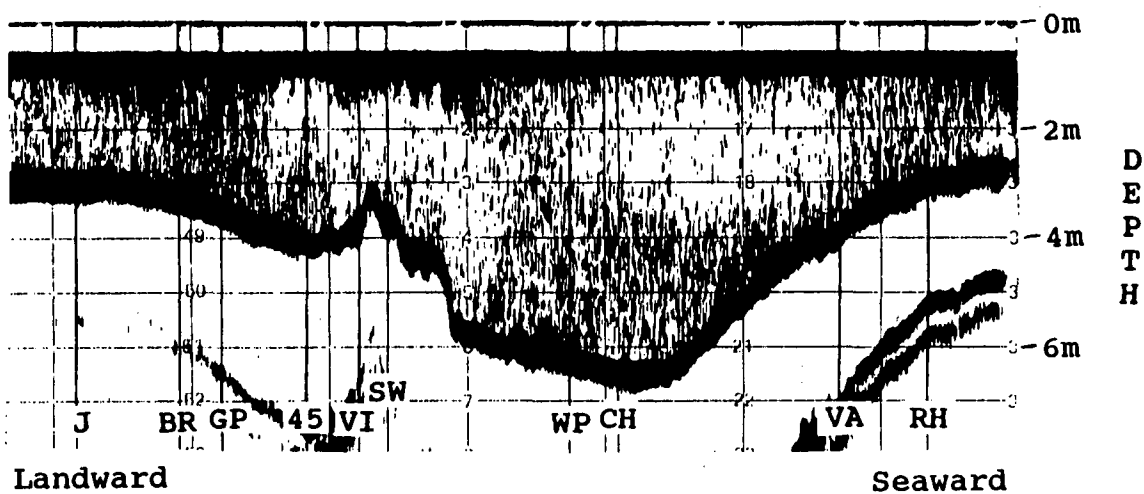
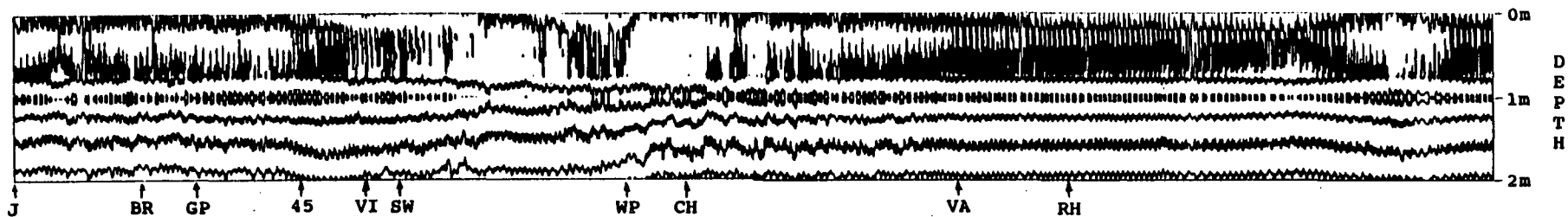


Figure 5.13: Transect 7 at 12:00 on 15 November 1989.

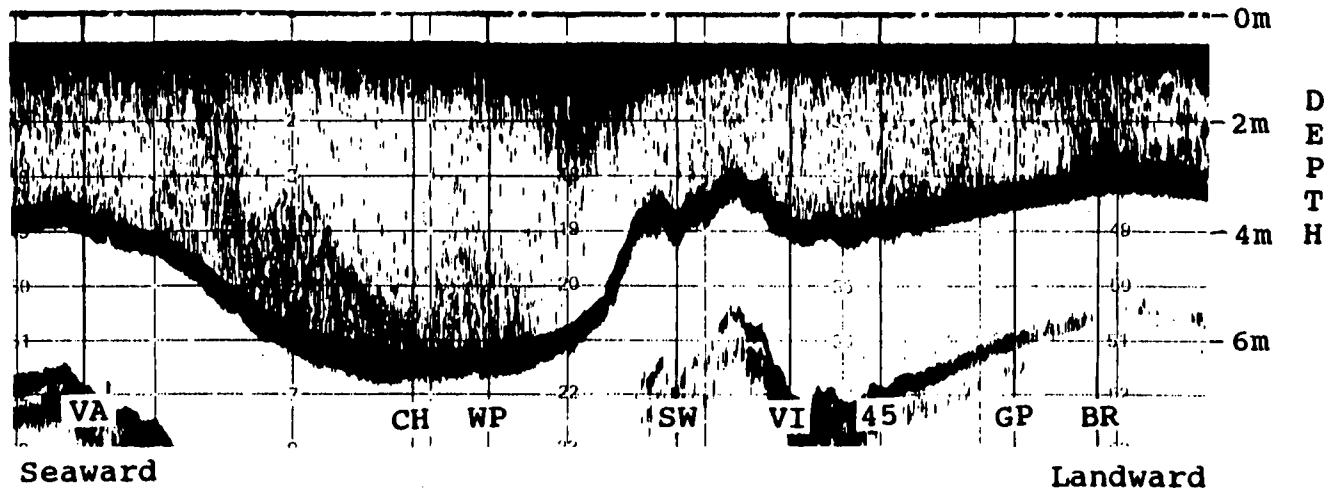
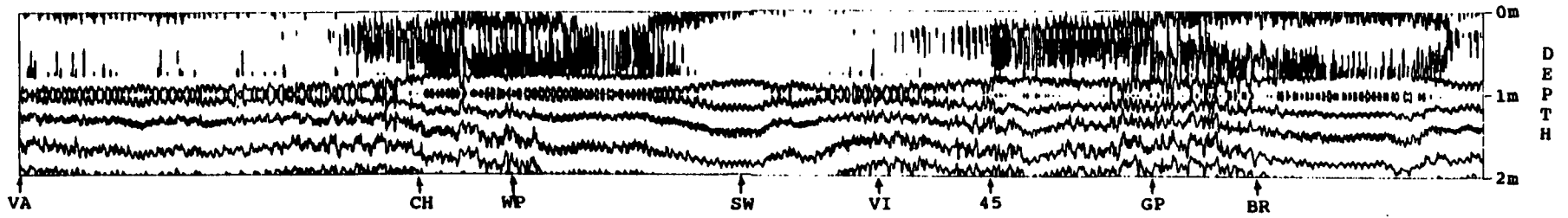


Figure 5.14: Transect 8 at 12:10 on 15 November 1989.

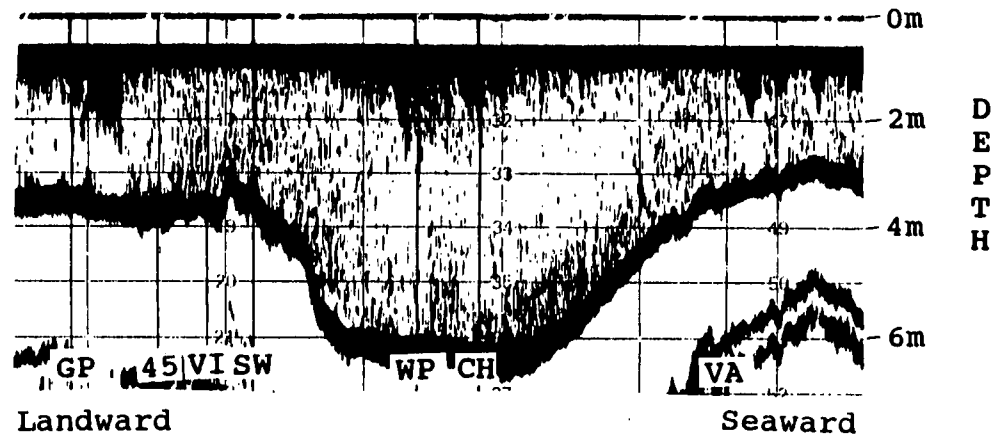
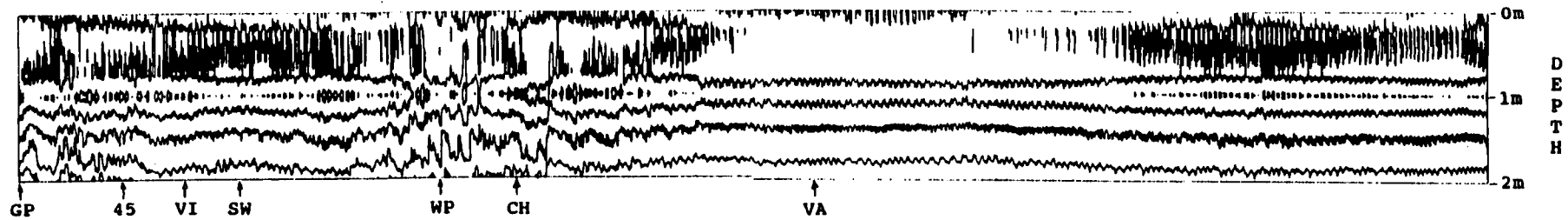


Figure 5.15: Transect 9 at 12:20 on 15 November 1989.

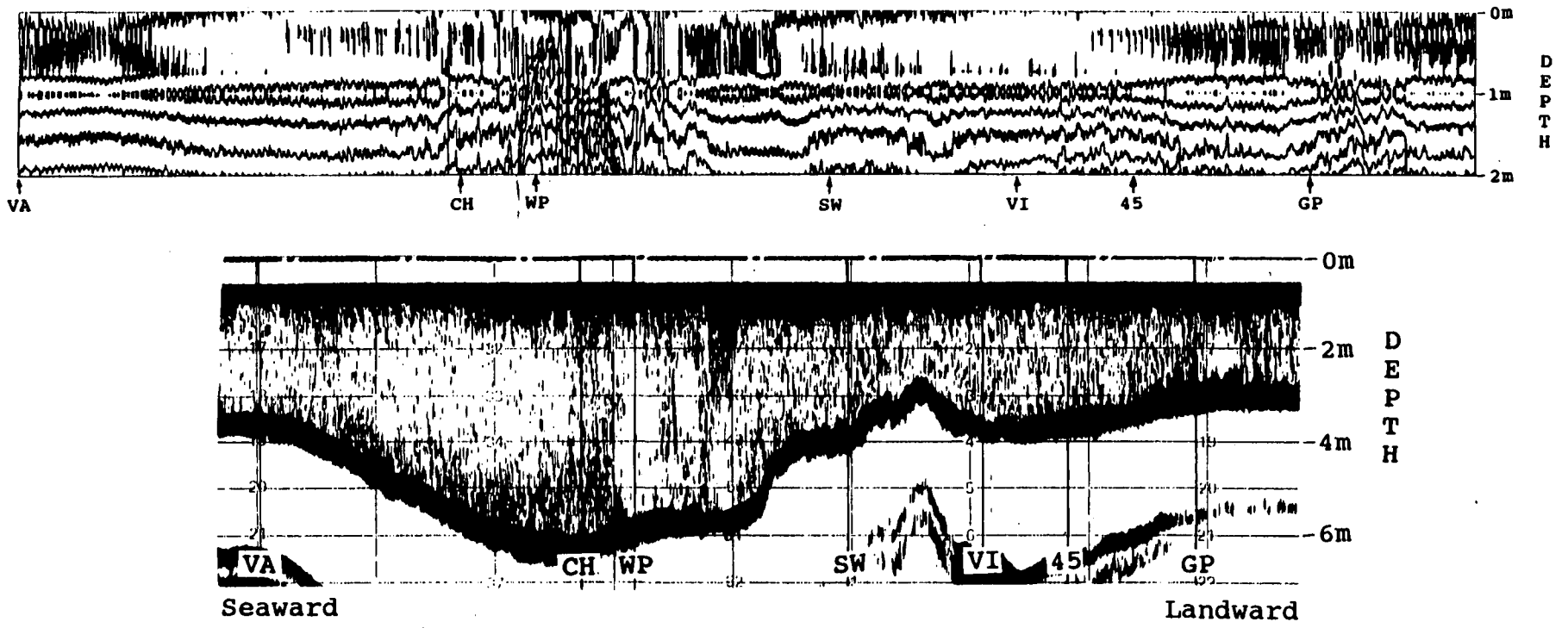


Figure 5.16: Transect 10 at 12:35 on 15 November 1989.

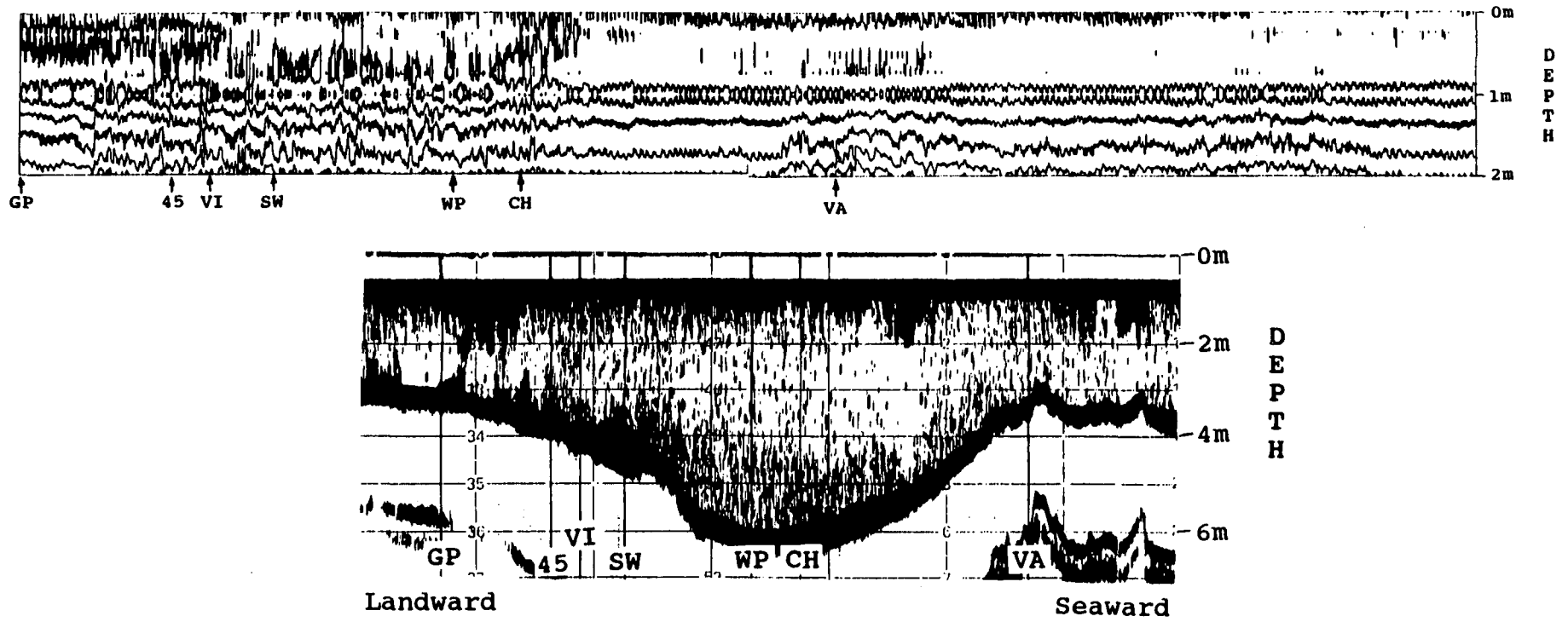


Figure 5.17: Transect 11 at 12:45 on 15 November 1989.

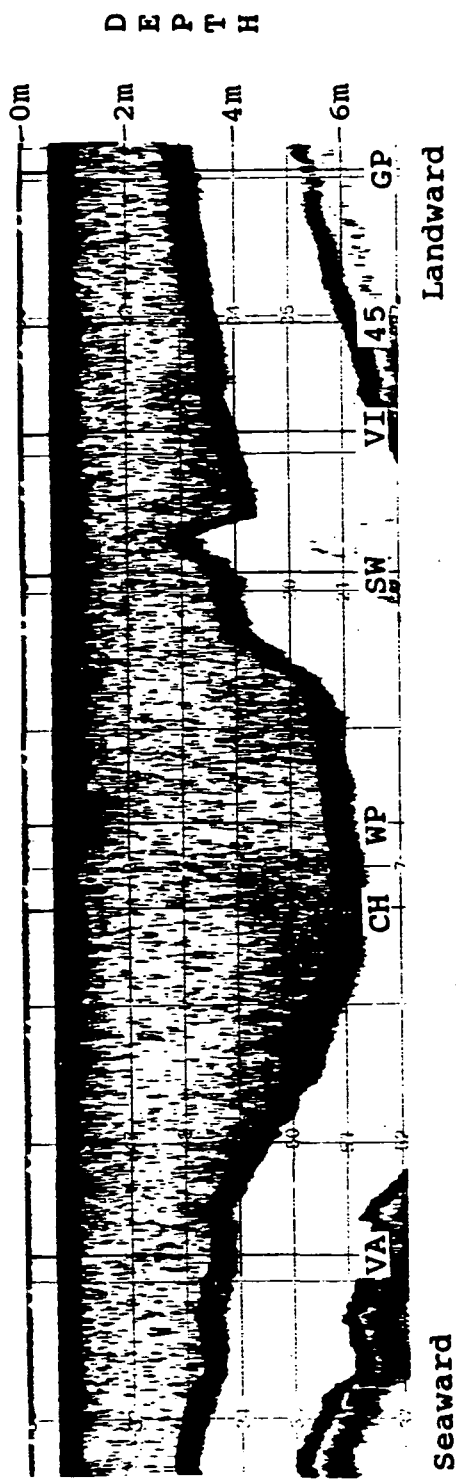


Figure 5.18: Transect 12 at 13:00 on 15 November 1989.

Chapter 6

Other observations at Cargreen

As indicated in Chapter 3, the author has conducted 12 surveys at the Cargreen site. Only two of these have been discussed in depth, due to the wealth of detail revealed in the Spar data. Some of the other observations are here given a brief presentation, to show the rich variety of hydrodynamic behaviour that is possible in the Tamar. From these results two further estimates of energy conversion, from barotropic tide to internal wave, have been made. The Tamar at Cargreen was explored under the conditions, and with the equipment, listed in table 3.4.

6.1 16 November 1987

The predicted tidal range for Cargreen was 2.4m (Admiralty Tide Tables, 1987). Two vertical profiles, made at 2.5 and 3 hours after high water at

station "45", showed that the estuary was highly stratified, forming two distinct layers, with a thin ($< 0.5m$ thick) thermocline separating them. The upper layer ($6ppt, 10^{\circ}C$) and lower layer ($30ppt, 11.8^{\circ}C$) had a density difference of $18kgm^{-3}$. The flow was seaward at all depths, and indicated a depth averaged velocity, at maximum stream, of about $0.5ms^{-1}$, with maximum flow in the upper layer.

Figure 6.1 shows the echograms for 2 and 3 hours after high water. A small amplitude internal wave formed over the landward slope of the bed depression. Embedded on the seaward end of this wave was a sequence of undulations of the thermocline. These undulations appeared to be a train of waves distinct from the main leewave. They did not seem to migrate during the observation period. The point at which they formed coincided with the position at which vigorous vertical mixing took place in the 6 November 1989 study.

It is conjectured that they too are a product of intense shear across the thermocline. The density gradient in this feature was so high that internal waves resulted initially rather than mixing. In the echograms there was a suggestion that, from 2 to 3 hours after high water, the thermocline around, and seaward, of the waves, thickened vertically. Acoustic backscatter appeared below the thermocline. The most landward undulation, or wave, has a length of about $25 - 30m$. At the time of writing the author has not been able to find a report of other examples of this class of behaviour in the marine environment.

Using the same techniques as in Chapter 4 energy estimates were made.

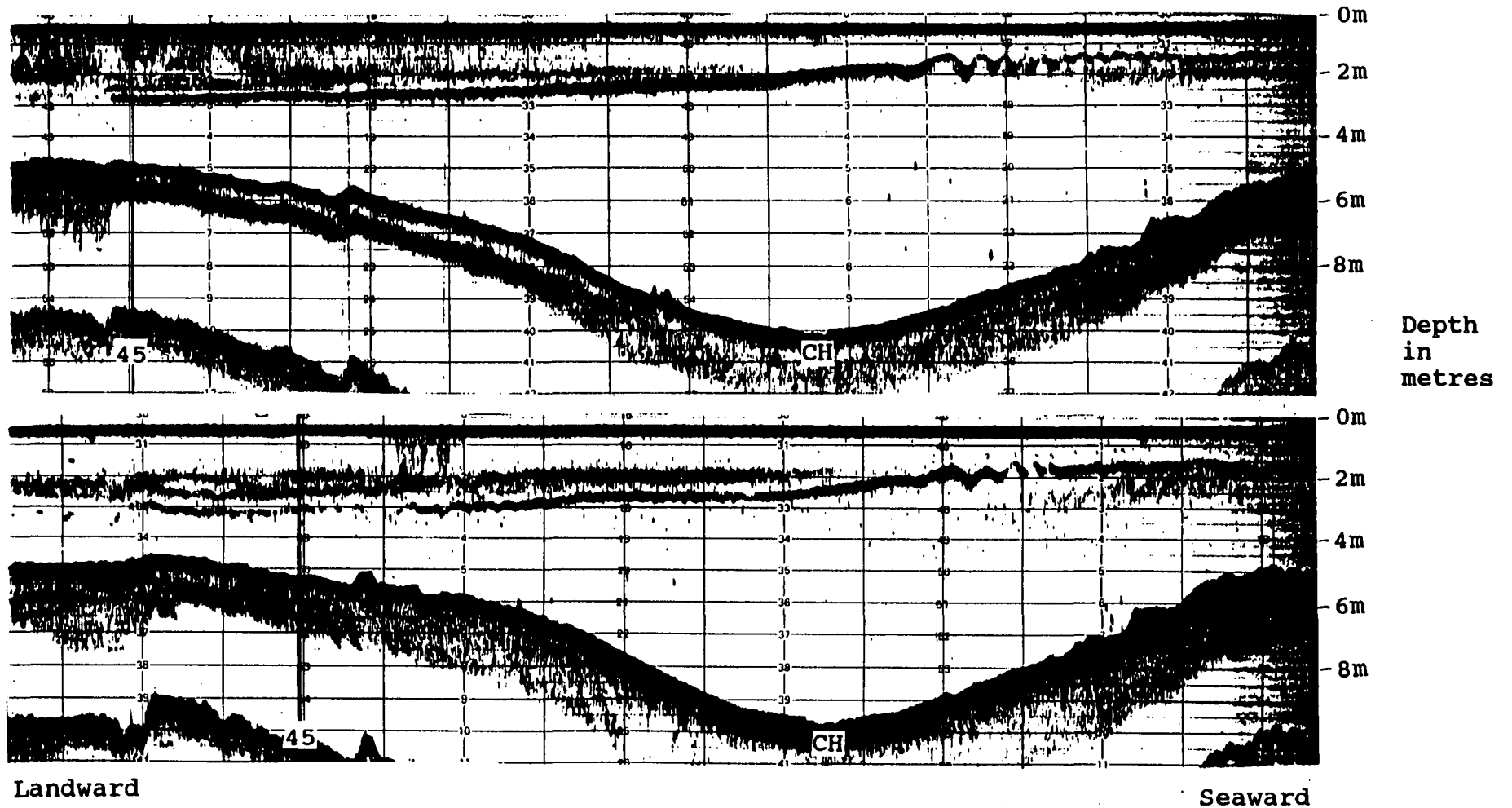


Figure 6.1: Longitudinal transects made at 2 hours (top) and 3 hours (bottom) after high water on 16 November 1987, at Cargreen.

The barotropic tidal energy density for the ebb stage was about $3.6kJm^{-2}$. Over the landward slope of the bed depression, assumed to correspond to the internal wave length ($500m$), this amounts to $1.8MJm^{-1}$. The total internal wave energy is about $150 - 200kJm^{-1}$. The conversion efficiency, from barotropic tidal energy to total internal wave energy, is then 8% to 10%.

6.2 30 November 1987

On 30 November 1987 the predicted tidal range for Cargreen was $3.3m$ (Admiralty Tide Tables, 1987). Two vertical profiles made at 1.5 and 2.5 hours after predicted high water, at "45", showed that the estuary was composed of two homogeneous layers, separated by a rather thick thermocline. At 1.5 hours after high water the density difference between the layers was $12kgm^{-3}$ and the thermocline was $3m$ thick, and at 2.5 hours after high water the density difference was $16kgm^{-3}$ and the thermocline was $4m$ thick.

Figure 6.2 shows the echograms for 2 and 2.5 hours after high water. The thermocline in both cases appeared to be composed of about 4 layers, each of which gave rise to acoustic backscatter. The wave itself was manifest as a downward vertical displacement of these layers, over the landward slope of the bed depression. On the thermocline there were undulations, or smaller waves, embedded. At 2.5 hours after high water the lowest scattering layer, to seaward of "CH" and landward of "SB", appeared to have been formed of Kelvin-Helmholtz billows. The height of these billows was about $1 - 1.5m$

and their length was approximately 5 – 6m.

Figure 6.3 depicts the echogram for 3.5 hours after high water. It is rather elongated due to the launch movement against the ebb stream. This echogram suggested that the leewave may have been evolving into a train of solitary waves. These were larger in wavelength and amplitude than the undulations which were earlier observed to be embedded on the leewave, and it is not clear what the relationship was between them. There were possibly 6 solitary waves forming at 3.5 hours after high water.

Observations of the formation of solitary waves, from tidal flow over topographic features, have been presented, for example, by Maxworthy (1979) and Lee & Beardsley (1974) in laboratory experiments; Sandstrom & Elliott (1984) and Holloway (1987) near the shelf-break region; Haury et al. (1979) in Massachusetts Bay; and Farmer & Smith (1978) in a Fjord.

Djordjević & Redekopp (1978) made a theoretical examination of the fission of an initial solitary internal wave propagating into shallow water. The fission products are themselves dispersive solitary waves. These authors give an approximate fission law for two layer fluids:

$$N \leq 1 + \left(\frac{(\frac{32}{3})(\frac{h_1}{h_{2s}})(1 - \frac{h_1}{h_{2s}})}{(\frac{\eta_0}{h_1})} \right)^{\frac{1}{2}} \ln \left(\frac{6}{\pi} \frac{\eta_0}{h_1} \frac{h_{2d}}{h_1} \right) \quad (6.1)$$

where N is the number of fission products appearing in the shallow water, h_1 is the upper layer depth, h_{2s} is the shallow water lower layer depth, h_{2d} is the deep water lower layer depth, and η_0 is the wave height of the initial wave form. Approximating the 30 November 1987 conditions gives

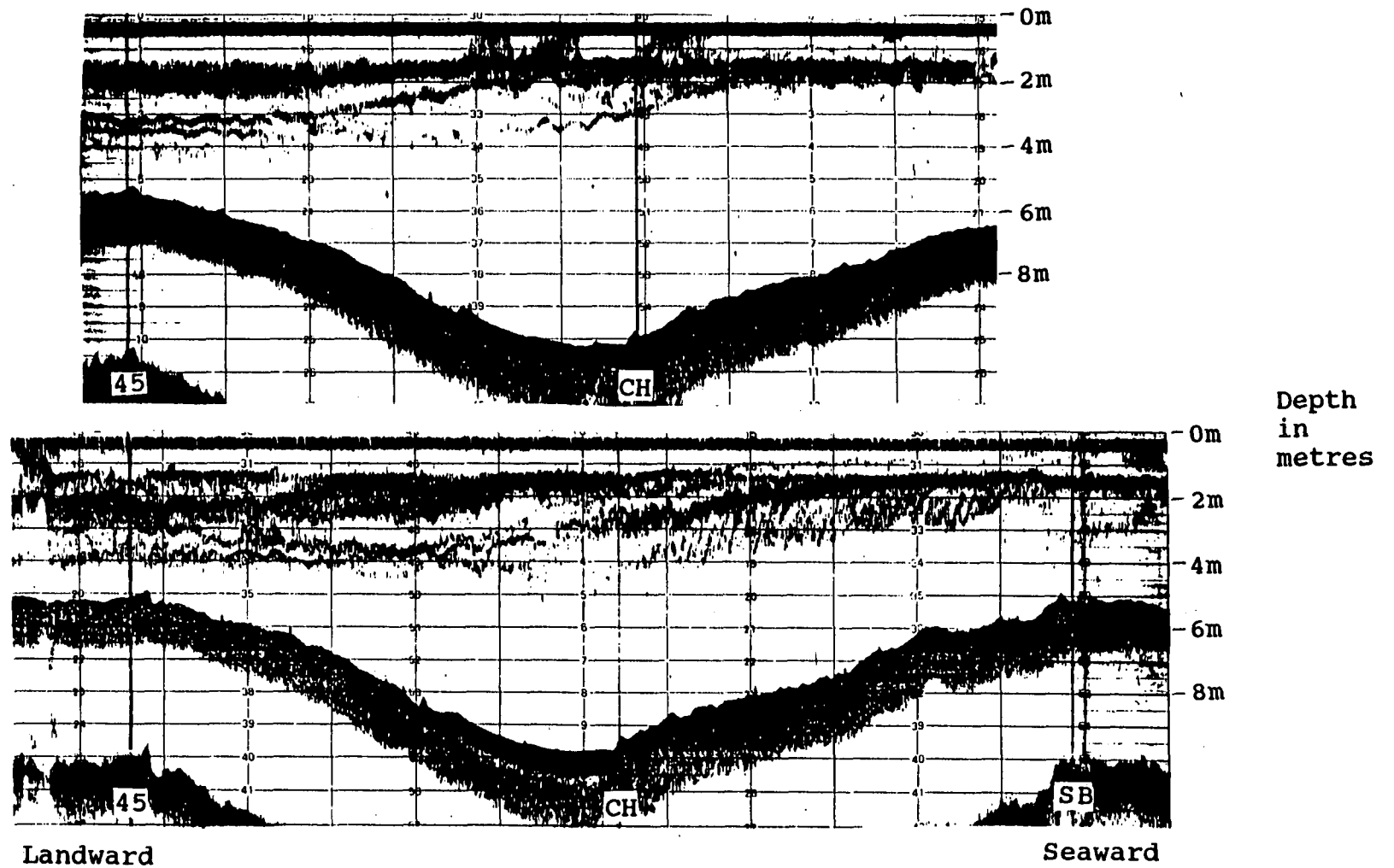


Figure 6.2: Longitudinal transects made at 2 hours (top) and 2.5 hours (bottom) after high water, at Cargreen, on 30 November 1987.

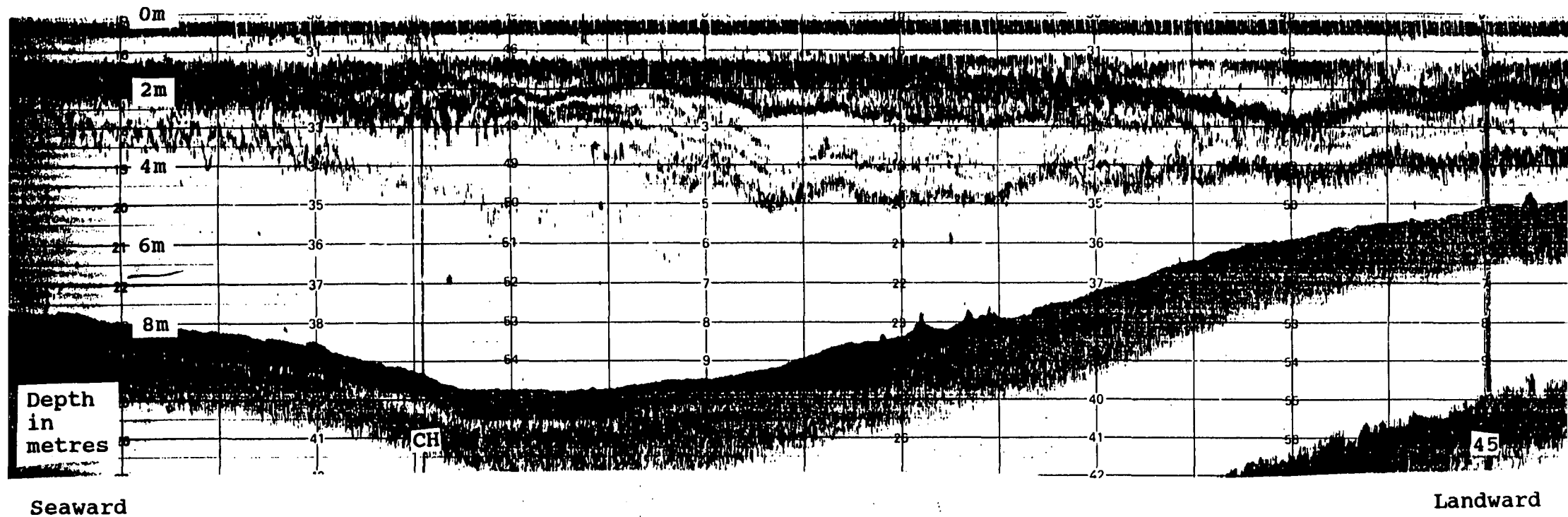


Figure 6.3: Longitudinal transect made at 3.5 hours after high water on 30 November 1987, at Cargreen.

$N \leq 4.69$. A prediction of four to five fission products is in good agreement with the observations, given that this fission law loses some validity in the case of a thick thermocline in shallow water.

The barotropic tidal energy for the ebb stream was $3.4 MJm^{-1}$ over the internal wave length. The total internal wave energy, at 3.5 hours after high water, is estimated as $250 - 300 kJm^{-1}$, leading to a conversion efficiency of 7% to 10%.

6.3 19 April 1989

As a test for the Estuarine Thermistor Spar, early in 1989, during a spring tide, Eulerian measurements were made at Cargreen, over the bed depression. *RV Catfish* was moored between "45" and "CH" for seven hours starting at predicted high water. The Spar worked perfectly, yet there was poor thermal stratification, and no internal wave activity. However, at the time of predicted low water, Kelvin-Helmholtz billows became apparent on the echograms.

Figure 6.4 depicts a time series of acoustic backscatter at the mooring. The vertical scale is indicated, and the vertical lines are spaced 60s apart. The Spar was deployed in the top 4m of the water, and its coverage of these events was restricted to the tips of the billows. The poor temperature stratification and the 0.25m sensor spacing allowed only rough resolution. Despite this the Spar data (not presented here) roughly agrees with the echograms. The mechanism for formation is conjectured as the following.

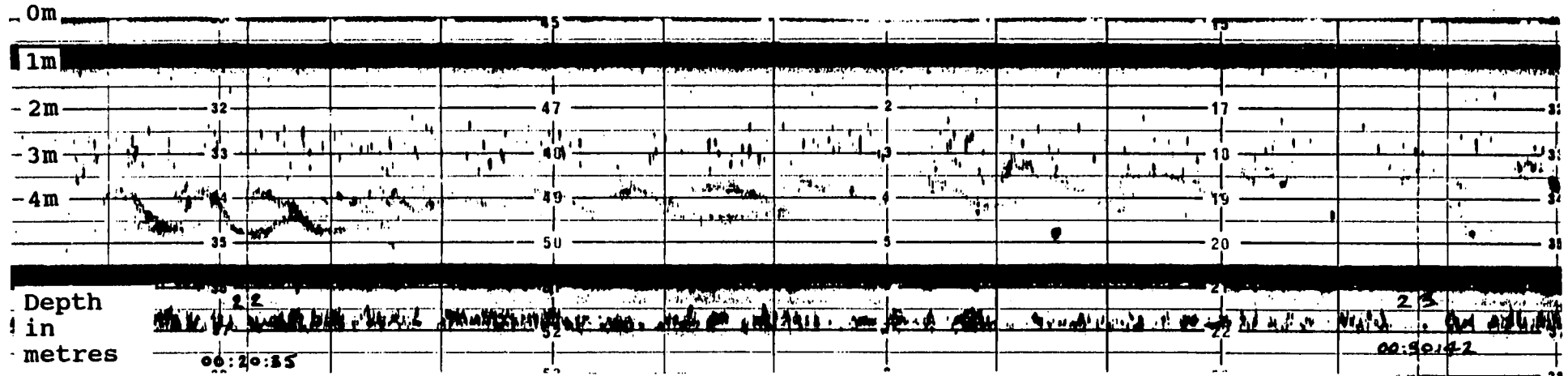


Figure 6.4: Time series of acoustic backscatter made at the mooring over the bed depression at Cargreen on 19 April 1989, at about low water. Time is increasing to the right. The vertical lines are spaced 60 seconds apart.

The bottom metre of the water column was more saline (17.6ppt, 10.6°C) and started to flood before the surface waters (8.7ppt, 10.4°C) had finished ebbing. In consequence a shear was developed across a small density gradient at some 4 – 5m depth. The orientation of the billows on the echogram (time is increasing to the right) suggests that they were forced to migrate seaward, while the layer below them moved landward. Their heights are 1 – 1.5m. It took each billow about 60s to pass the launch, so a horizontal length of the order of 10m is suggested. The echograms show that the height of the base of the billows rose in time, as the lower layer intruded landward.

It was impossible to detect exactly how many billows formed, but these beautiful and exotic features were present on the echograms for over 40 minutes. No measurements were performed that enable calculation of their likely contribution to mixing. Future studies aimed at quantification of this process should prove interesting.

Woods (1968) presented observations of similar instabilities on the summer thermocline in the Mediterranean Sea, as well as a simple theoretical description. Thorpe et al. (1977) and Thorpe & Hall (1977) have shown billows on the thermocline in Loch Ness, evidenced in thermistor array data. Thorpe (1987a) comprehensively discussed laboratory experiments of this class of behaviour in his review paper on transitional phenomena in stratified fluids.

Table 6.1: Values of the internal Froude number for the five conditions described in the text.

	16/11/87	30/11/87	19/4/89	6/11/89	15/11/89
F_{is}	1.5	1.5		1.7	21
F_{id}	0.5	0.53	0.4	0.87	7.7

6.4 Froude number analysis

The three phenomena described above, and those occurring on 6 November and 15 November 1989, can be categorised in terms of an internal Froude number, F_i , for the flow, using the method described in Chapter 5. Table 6.1 shows the estimates of F_i for these five events.

The shallow water Froude number, F_{is} , refers to that estimated for the flow outside of the bed depression, and the deep water Froude number, F_{id} , is for the flow over the deepest part. In calculating F_i the assumption has been made that the estuary behaved like a two-layer fluid.

Chapter 5 contains a description of events on a spring tide, when a hydraulic jump occurred. The flow underwent a transition from supercritical F_i upstream of the depression to subcritical F_i over the centre of the depression. A critical value of F_i between 2 and 3 was indicated. All five events are discussed in the following, in terms of a critical Froude number lying between 2 and 3.

16/11/87. At maximum stream the shallow water flow was characterised by $F_{is} = 1.5$ and the deep water flow by $F_{id} = 0.5$. This flow was subcritical everywhere. The formation of an internal wave which did not break *in situ*

at maximum stream is entirely in keeping with this Froude number regime.

30/11/87. At maximum stream the flow was again everywhere subcritical ($F_{is} = 1.5$, $F_{id} = 0.53$). An internal wave formed which also did not break *in situ*. In this event the water behaved least like a two-layer fluid - the thermocline was a large proportion of the shallow water depth. An evolution into solitary waves is a highly nonlinear process, which cannot be described in a simple Froude number analysis.

19/4/89. The Froude number presented here, $F_{id} = 0.4$, is for the flow at about low water at one station only. The flow was subcritical at this point. To describe effects like Kelvin-Helmholtz billows, which are local instabilities in the flow, requires a more detailed and local analysis. A gradient Richardson number analysis would be of more interest. Lack of adequate velocity data precludes this.

6/11/89. At maximum stream both the shallow and deep water flows were subcritical ($F_{is} = 1.7$, $F_{id} = 0.87$). An internal wave was formed, with small undulations and ripples on the thermocline which did not evolve. The internal wave did not break during the observations.

15/11/89. At maximum stream the flow was highly supercritical ($F_{is} = 21$, $F_{id} = 7.7$) along the bed depression. As already described in Chapter 5, an initial waveform grew until it interacted with the bed and broke in the form of a hydraulic jump, when the flow upstream was supercritical ($> 2-3$) and the flow over the centre of the depression was subcritical (< 2). The flow continued to be supercritical during the study period and no further waves were formed.

Behaviourally these events fall into different categories, depending on the flow regime at Cargreen, determined by F_{i_s} and F_{i_d} . It would be improper to suggest that in such a complex fluid, F_i is the only parameter which controls or describes the flow, but it provides a gross interpretation. Long (1953,1954,1955) pursued the problem of stratified flow, over an obstacle, in multi-parameter space, but found that for fixed obstacle and layer geometry F_i was a key parameter.

The following categories are suggested in the light of these five observations.

- For large F_{i_s} and F_{i_d} (greater than 2 or 3 perhaps), as on 30 November 1987, the flow appears not to favour the stable evolution of internal waves, and a hydraulic jump may form if there is a transition from supercritical to subcritical flow along the bed topography.
- For more moderate values of F_{i_s} and F_{i_d} (0.5 to 2.0 perhaps), internal waves are formed which do not break *in situ*. Within this category there must be subcategories of behaviour, depending on the relationship between F_{i_s} and F_{i_d} , and their absolute values. For example, under what conditions do solitary waves form?
- There might also be conditions of small F_{i_s} and F_{i_d} for which no internal waves are detectable, but this is probably not achieved in the Tamar at Cargreen.

More observations are required for a better understanding in terms of F_i .

Chapter 7

A model of oscillatory flow in an idealised estuary

In conjunction with the observations of lee wave formation in the Tamar Estuary at Cargreen a numerical model was developed to simulate interfacial displacement and evolution in an idealised two layer fluid, representing an estuary. The feature of most interest in both of these studies was the energy associated with lee waves on the disturbed interface, produced when stratified tidal flow interacts with bed topography. To be able to predict the energy in the lee waves by numerical modelling, and to then associate this energy with changes in the potential energy and stratification of the estuary, was the major aim of this work.

Many models exist which predict the behaviour of stratified flow over topography. The most notable, and relevant to the Tamar environment, are those of Lee & Su (1977) and Pingree et al. (1983). Heathershaw

et al. (1987) extended the Pingree et al. model by adding sediment flux calculations and Wilmott & Edwards (1987) extended the Heathershaw et al. model to 3 layers.

The simplest of these is that of Pingree et al. (1983), which shall from now on be referred to as "the model". This model was adopted in preference to writing a new one or adapting others because of its proven success in predicting internal tide formation and evolution over the continental shelf break, and because its two layer geometry was felt to be adequate in representing the most often encountered stratification in the Tamar at Cargreen.

This chapter describes the model in general terms - e.g. its physics, numerical scheme, and non-dimensionalised behaviour - and sets the scene for the next chapter, which examines the models ability to reproduce observed wave activity in the Tamar.

7.1 Physics of the model and the governing equations

The model geometry is depicted in figure 7.1. The coordinate system has x as the along estuary direction, z as the vertical coordinate, and y in the cross-estuary direction. Variations in y are ignored. The horizontal momentum equations which govern the flow in the two layers are, after making the hydrostatic approximation,

$$u_{1t} + u_1 u_{1x} = -g\zeta_x + K u_{1zx} \quad (7.1)$$

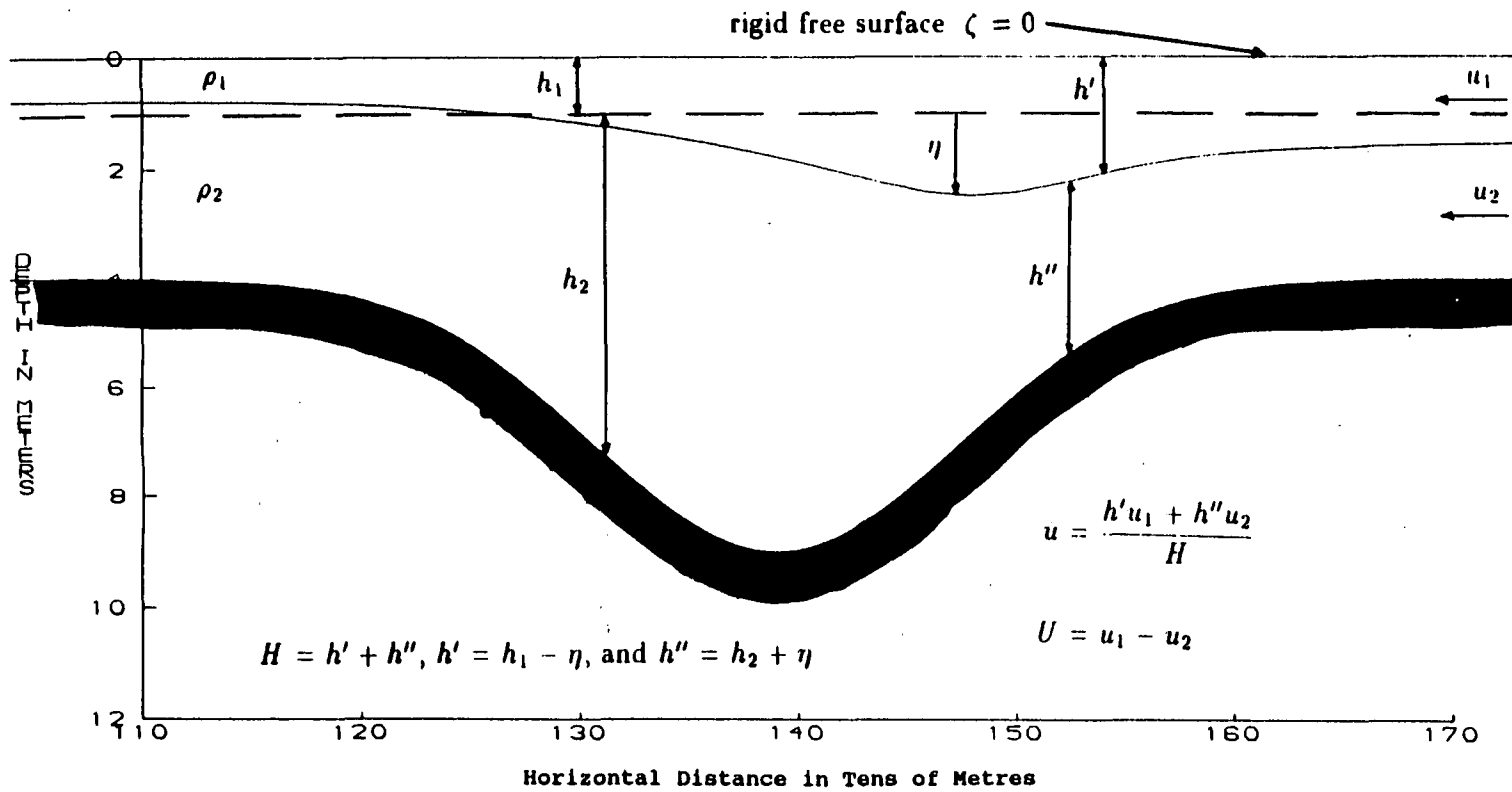


Figure 7.1: The model geometry, showing the relative depths of the two layers and the disturbed and undisturbed interface.

and

$$u_{2t} + u_2 u_{2x} = -\frac{\rho_1}{\rho_2} g(\zeta_x - \eta_x) - g\eta_x + K u_{2xx} \quad (7.2)$$

where u_1 and u_2 are the upper and lower layer velocities, respectively, ζ is the elevation of the free water surface, and η is the elevation of the internal interface. We have also assumed that h_1 is constant with x .

The continuity equations are, under the same assumptions,

$$((h_1 + \zeta - \eta)u_1)_x + (\zeta - \eta)_t = 0 \quad (7.3)$$

and

$$((h_2 + \eta)u_2)_x + \eta_t = 0 \quad (7.4)$$

Defining the *barotropic tide* u as the vertically integrated tidal current such that

$$u = \frac{h'u_1 + h''u_2}{H} \quad (7.5)$$

where $H = h' + h''$, $h' = h_1 - \eta$, and $h'' = h_2 + \eta$ and the *baroclinic tide* U as a vertical shear such that $U = u_1 - u_2$ means that the horizontal momentum equations can be rewritten, with $\Delta\rho = \rho_2 - \rho_1$, as

$$U_t + (uU)_x + \left(U^2 \frac{(h'' - h')}{2H}\right)_x = g \frac{\Delta\rho}{\rho_2} \eta_x + K U_{xx} \quad (7.6)$$

These further assumptions have been applied making the free surface rigid:

$\eta \gg \zeta$, $\eta_t \gg \zeta_t$, $\eta_x \gg \zeta_x$. g is the gravitational constant, $9.81ms^{-2}$.

The term KU_{xx} represents attenuation by viscous or turbulent diffusion

and also provides help with numerical stability in the model. The diffusion selectively damps out regions of high spatial gradients but still allows waves to propagate a long way, albeit at the expense of attenuation. It also has the effect of limiting finite amplitude shallow water steepening, thus effectively limiting the possibility of wave breaking.

The continuity equations undergo a similar transformation to become

$$\eta_t = (h'u)_x + \left(\frac{h'h''}{H}U\right)_x \quad (7.7)$$

Equations 7.6 and 7.7 are two equations in two unknowns, U and η , and define completely the physics of the model. U and η are functions of x and t only, and are uniform in the y direction.

7.2 Numerical scheme and radiation conditions

The equations of motion and continuity are integrated forward in time using finite difference approximations employing the central differences approach. For a model grid spacing of size Δx the spatial derivatives of a function f at position i in the grid are given by

$$f_{ix} = \frac{f_{i+1} - f_{i-1}}{2\Delta x} \quad (7.8)$$

and

$$f_{ixx} = \frac{f_{i+1} - 2f_i + f_{i-1}}{(\Delta x)^2} \quad (7.9)$$

In a model domain consisting of $N + 1$ points the spatial derivatives of f_i can be determined in this way only for points $i = 2, \dots, N$. For the end points the one sided derivative rule is applied.

The derivative with respect to time also employs central differences giving the so called "leap frog" method

$$f_t(t_0) = \frac{f(t_0 + \Delta t) - f(t_0 - \Delta t)}{2\Delta t} \quad (7.10)$$

where Δt is the time step in the model. In addition η and U are evaluated at alternate positions giving a spatially staggered grid. The numerical scheme has η and U stored in two arrays at three time levels: old, present, and new. η is evaluated when i is odd at the new level, and U when i is even, and then linear interpolation is used to fill in the grid.

The diffusive term, KU_{xx} , is always evaluated at the old time step to avoid complicated one sided interpolation or integration.

For more precise details on the numerical scheme the reader is referred to Heathershaw et al. (1987). The numerical processes in the present model are no different to the ones presented by those authors. The main difference between their model and this is in its application and scaling for shallow water.

To help prevent reflection and distortion of waves propagating toward the ends of the model, a special "radiation" condition is applied near the end points, which should allow the waves to leave the model domain. If at the ends of the model one assumes that disturbances behave as steady

long linear waves over a horizontal bottom then the linearised equations of motion give their phase speed as

$$c_0 = \sqrt{g \frac{\Delta \rho}{\rho_2} \frac{h_1 h_2}{H}} \quad (7.11)$$

and a radiation condition of

$$U = \pm \frac{c_0 H \eta}{h' h''} \quad (7.12)$$

for waves travelling to the left (+) and right (-). Disturbances should then effectively propagate out of the model at each end, without reflection as though they were long linear waves.

7.3 Stability criteria

There are two criteria that have to be satisfied when choosing variable values for this model. The first is the well documented "Courant-Friedrichs-Lewy" criterion (Hirsch, 1988), that Δx and Δt should satisfy

$$\frac{\Delta x}{\Delta t} > c \quad (7.13)$$

where c is the maximum phase speed of disturbances in the model. The second criterion is that of Simons (1980)

$$\frac{(\Delta x)^2}{2K} > \Delta t \quad (7.14)$$

Ideally one would like to choose Δx , Δt , and K such that the diffusive term is small in comparison to the other terms. The author has found that in practice there is a lower bound to K consistent with numerical stability, about $30 - 50m^2s^{-1}$, but no upper bound. To satisfy both these criteria and to keep the computations stable requires the following values: if $c = 0.5ms^{-1}$, a typical long wave phase speed, and if $K = 50m^2s^{-1}$, then $\Delta x = 10m$ and $\Delta t = 0.1s$. A value of $\Delta x = 10m$ means that the bed depression in the model is adequately resolved, as are any internal waves formed. Heather-shaw et al. (1987) resorted to a value of $K = 40m^2s^{-1}$, quite close to the above choice. However, their choice of $\Delta x = 250m$ and $\Delta t = 155s$ reflects the very different scales of the shelf break region and the estuary.

7.4 Model configuration for the Tamar Estuary

At time $t = 0$ suppose the two layers are at rest with the interface undisturbed. i.e. $u, U, \eta = 0$ for all x . The barotropic tide u is then forced from one end of the model by the function $u = -u_0 \sin(\omega t)$. The value of u at all other points in the model is calculated from $(uH)_x = 0$, thus preserving total mass transport.

The undisturbed depth of the lower layer h_2 and the total water depth H are functions of x . To represent a typical depression in the estuary bed (e.g. Cargreen, see figure 7.2) H was assumed constant throughout the domain, except for a region in the middle. Here the depth varies like

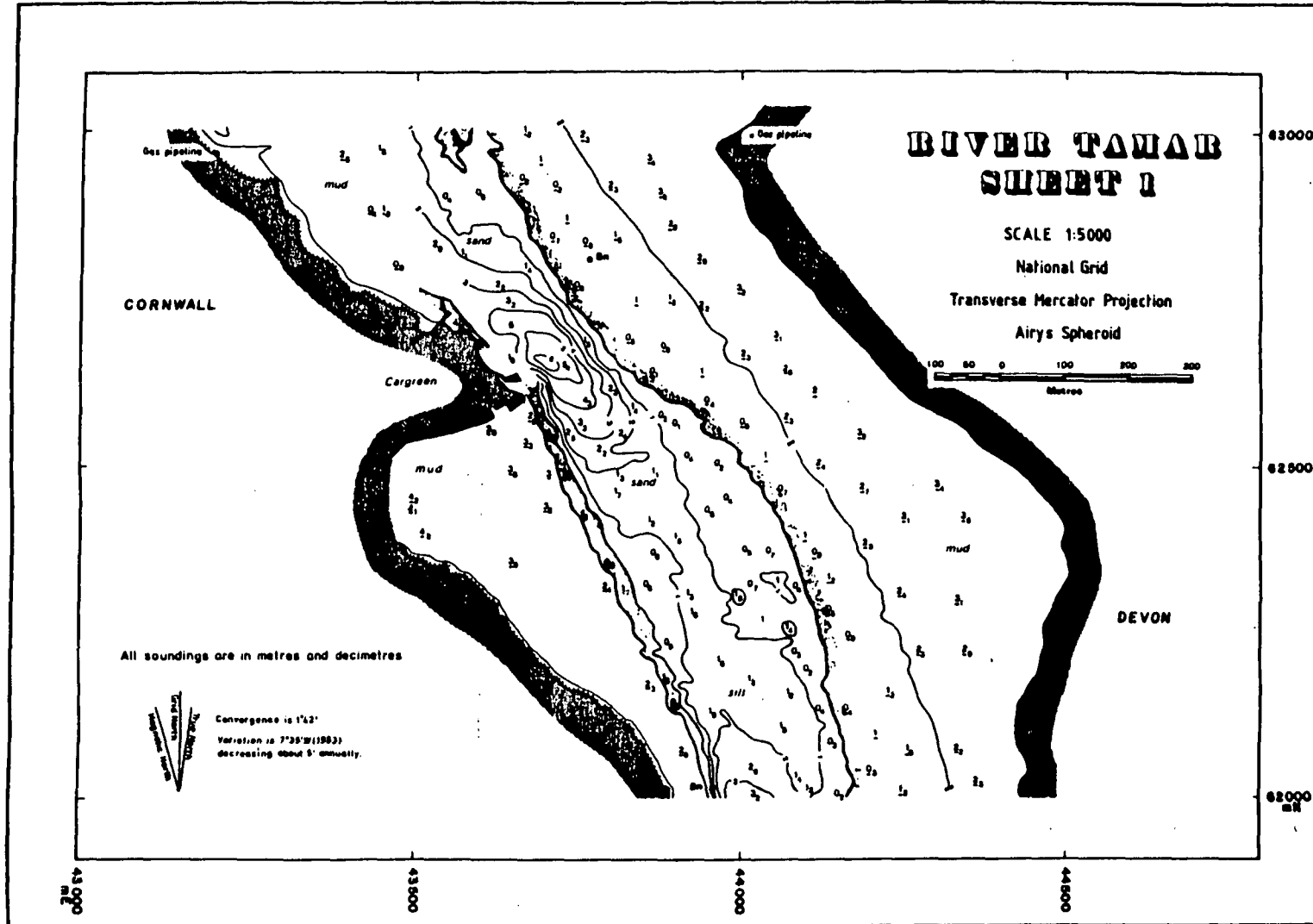


Figure 7.2: The bathymetry at Cargreen. The depression in the bed takes the form of a long ragged ellipse whose axis is aligned in the along estuary direction. Note that at this part of the estuary there is a slight constriction of the flow.

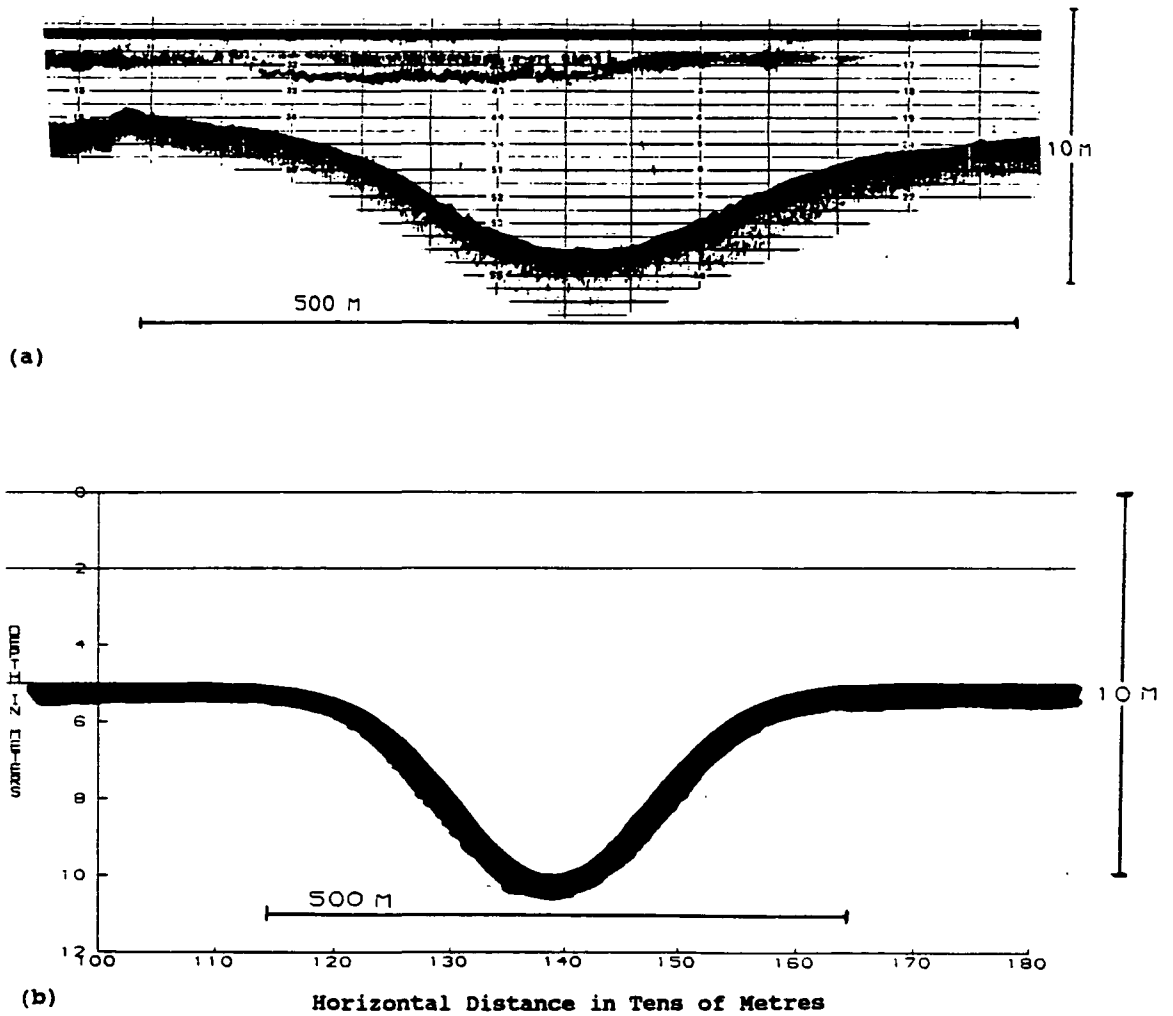


Figure 7.3: (a): A 200kHz echosounding of the estuary bed at Cargreen made along the axis of the estuary. (b): The model analogue to the axial section above, but not to the same scales. The rigid surface, the interface and the bottom are all depicted.

$$H(x) = H + B \exp(-\alpha(x - \frac{x_L}{2})^2) \quad (7.15)$$

where $x = 0$ defines one end of the domain and x_L is the other end. This is then a model with a flat bottom, of depth H , which has a smooth Gaussian depression, of depth B , in the middle, whose horizontal length scale can be varied through α . The undisturbed upper layer depth h_1 is constant with x . We can define an effective depression length in the along estuary direction as $2L = \frac{2B}{\alpha}$. Figure 7.3 depicts an axial survey of the Cargreen depression made using a 200kHz echosounder, and the idealised bedform used in the model. Note that $B = 5m$ and $\alpha = 0.02$ (i.e. $2L = 500m$) give a fair two dimensional analogue to the Cargreen depression and that this function has the added attraction of being mathematically "smooth" - differentiable and continuous.

7.4.1 The choice of other variables

In all of the model runs the variables are dimensional. The reasons for the choice of some of the variables have already been discussed.

The model domain as defined by $N + 1 = 281$ and $\Delta x = 10m$ represents some 2810m of flat bottomed estuary with a Gaussian depression in its centre (i.e. $x_L = 2810m$). This allows for a long fetch of water either side of the topography but, unlike the shelf break model of Heathershaw et al. (1987), does not allow for waves to survive in the model long after the tidal stream which created them. They quickly propagate and are advected out of the domain after mid-tide. The sinusoidal barotropic tidal frequency ω

was set at a value corresponding to a period of 12.4 hours, representing the dominant M_2 tidal constituent, but ignoring estuarine effects.

For the purposes of examining model behaviour and intratidal variations, a standard configuration was adopted corresponding to a "typical" stratification and geometry. This was based on data from a survey at Cargreen conducted on 30th November 1987. The values used were: $\frac{\Delta\rho}{\rho_2} = 0.010$, $u_0 = 0.5\text{ms}^{-1}$, $h_1 = 2\text{m}$, $H = 5\text{m}$, $B = 5\text{m}$ and $\alpha = 0.02$.

7.5 Transients in the model

The model was run in the standard configuration for four half-tidal cycles (four times 6.2 hours, or two ebbs and two floods) to examine its transient behaviour. It was found that transient motion on the interface quickly leaves the model domain and that the important feature is the growth, evolution and decay of lee waves.

The model predicts a repetitive, symmetric formation of lee waves each half-tidal cycle (6.2 hours). The maximum amplitude of the wave formed on the first half-tidal cycle was slightly smaller (10%) than the following waves, whose maxima settled down to a constant amplitude. It was further found that after a certain number of hours of model time (this number being dependent on K) instabilities grew at the ends of the model domain and the model failed. The reason for this is not obvious, but one suspects that the radiation condition is inadequate in allowing waves to freely vacate the model and a build up of energy occurs at the ends, producing quickly

growing disturbances: Increasing K helps to attenuate these disturbances in the short term, and increasing the length of the model domain also helps by giving the waves further to propagate and attenuate before reaching the ends.

7.6 Model results for the standard configuration and an examination of intratidal behaviour

The intratidal behaviour for the standard configuration reveals interesting and typical features in the model, which are present in many of the other parameterisations, and is therefore a good introduction to the model. To describe the intratidal behaviour for all parameterisations would be long and tedious and also irrelevant.

A graphical representation of the wave formed is presented in figures 7.4 7.5, 7.6 and 7.7. The development of the internal wave is shown as a depression of the interface in a time sequence. Each plot in the sequence consists of a pair of axes showing depth and horizontal distance, and the three curves show, from the top, the rigid water surface, the internal density interface and the estuary bottom. The first and last of these are invariant in time. At "High Water" plus 0 hours (HW+0), i.e. $t = 0$, there is no distortion of the interface - it is in its relaxed initial position. The next three plots, depicting the growth phase, are at $\frac{12.4}{12} = 1.03$ hours apart, and the following ones are at $\frac{12.4}{60} = 0.21$ hours apart. "Upstream" is on the right of each plot, or equivalently, the barotropic ebb tide "flows" from right

to left.

From HW+0.0 to HW+3.10, the time of maximum stream, the wave develops such that its maximum departure from the relaxed position, (its "trough") is positioned over the upstream slope of the depression, and not over its centre. When fully developed, between HW+3.1 and HW+4.55, the interface immediately upstream of the wave is considerably lowered from its undisturbed level and the interface immediately downstream is raised. The growth of the wave up to HW+3.1 is relatively rapid as evidenced in figure 7.8, which shows the change in non-dimensionalised wave height $\frac{\eta_0}{H}$ with time. η_0 is the wave height and H is the shallow water depth, i.e. $H(x = 0)$. The wave seems to remain unchanged from HW+3.1 to HW+4.55, but then as the flow slackens substantially it is allowed to propagate upstream, slowly until HW+5.17, then more rapidly. The wave height diminishes greatly from HW+4.75 onwards and finally propagates away from the depression in the form of a long internal wave, which is just observable in plots HW+5.37 to HW+5.99. The maximum barotropic ebb tide occurs at HW+3.1 but examining figure 7.8 the maximum wave height occurs at approximately HW+4.01. This is attributed to nonlinear steepening in the model as the wave adjusts to the slackening flow. The maximum non-dimensionalised wave height, during the half tidal cycle, is computed as $\frac{\eta_m}{H} = 0.62$.

The wavelength is calculated as being that horizontal distance which spans the region where the interface is disturbed by more than 10% of the maximum departure. The model examines the grid for the maximum interfacial departure from the initial state, at each time step, and then scans

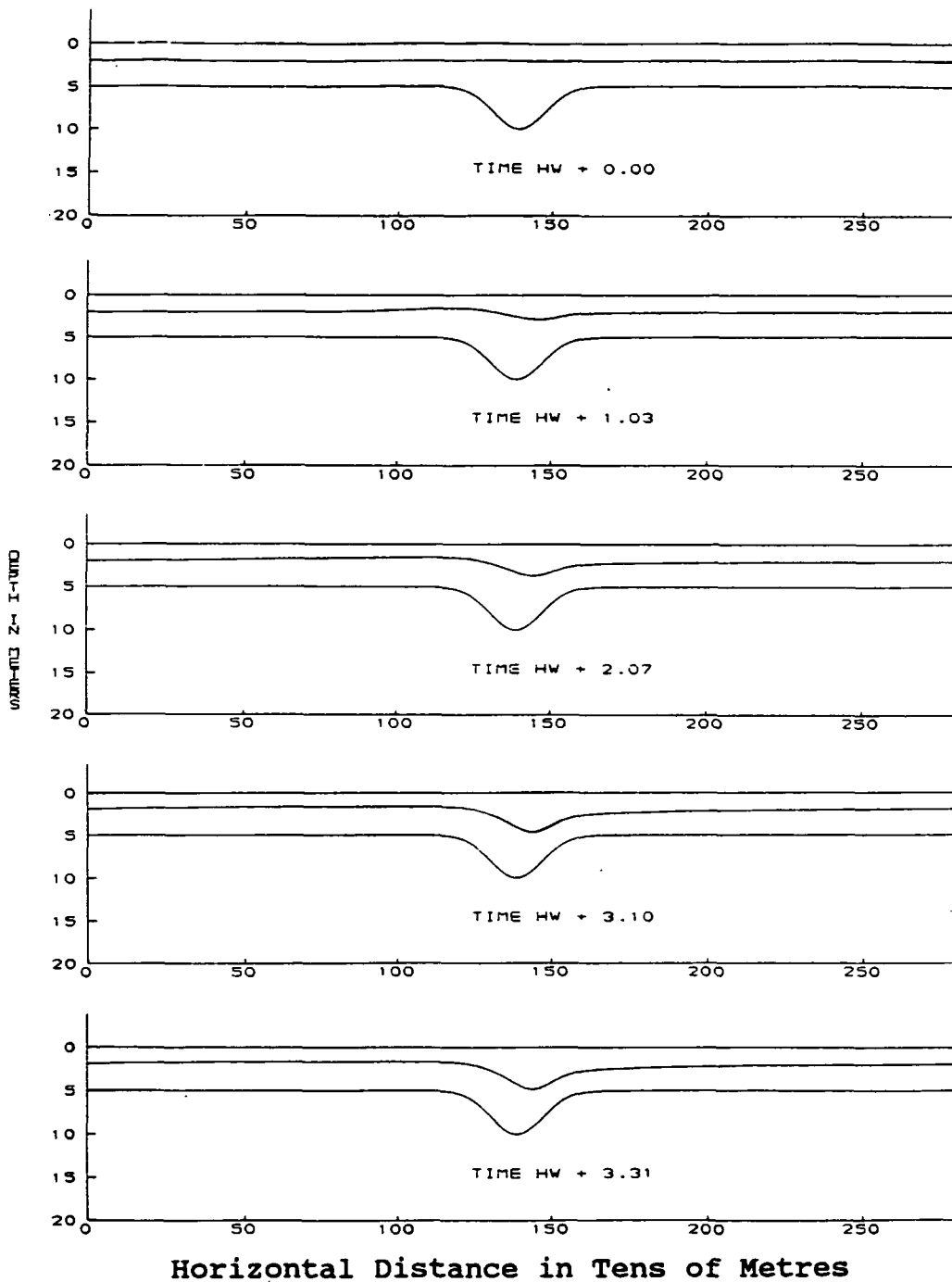


Figure 7.4: A time sequence of model output for the standard configuration. Results from HW+0.0 to HW+3.31 are shown, see text for explanation.

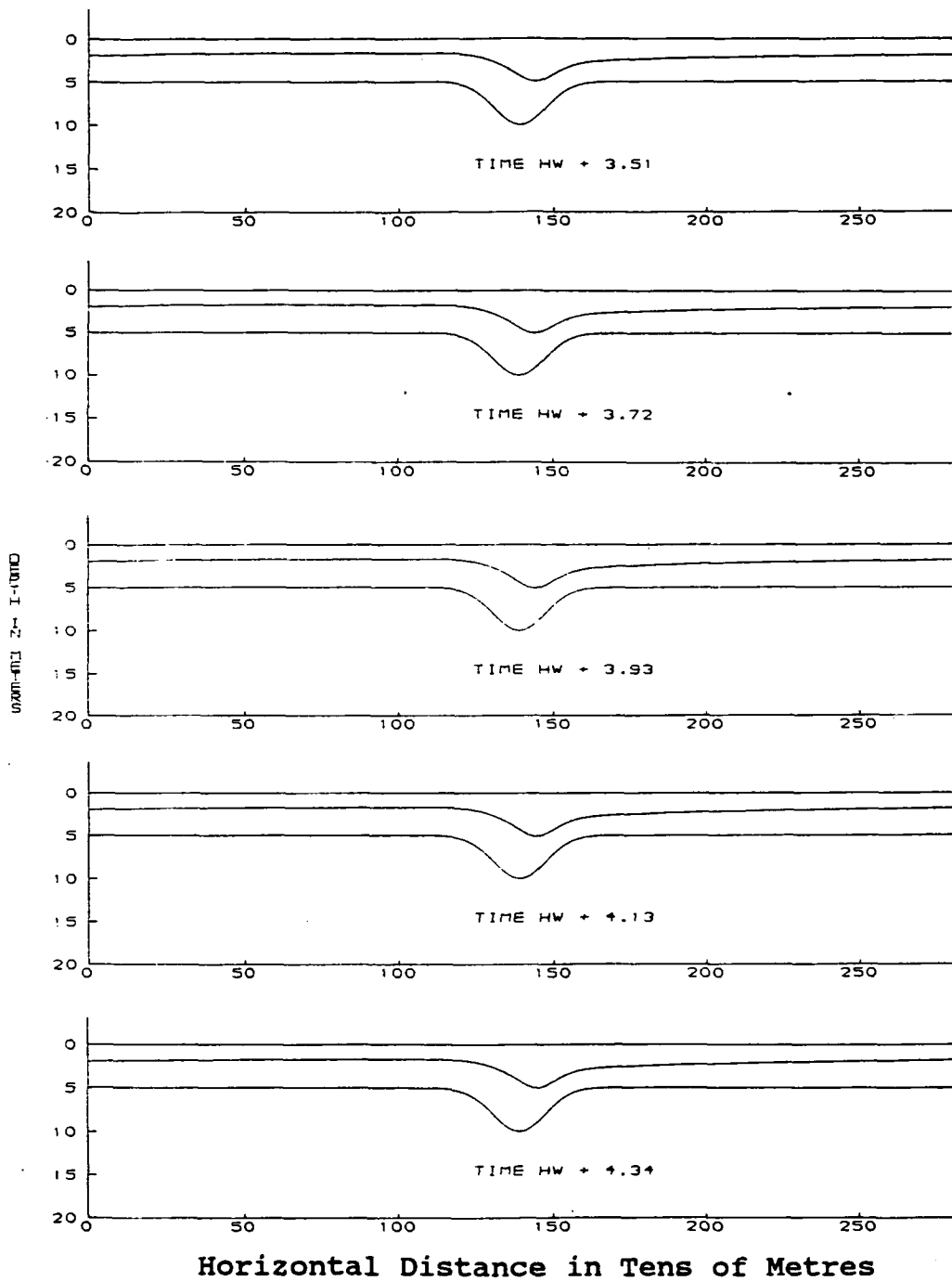


Figure 7.5: Model output for the standard configuration. Results from HW+3.51 to HW+4.34 are shown.

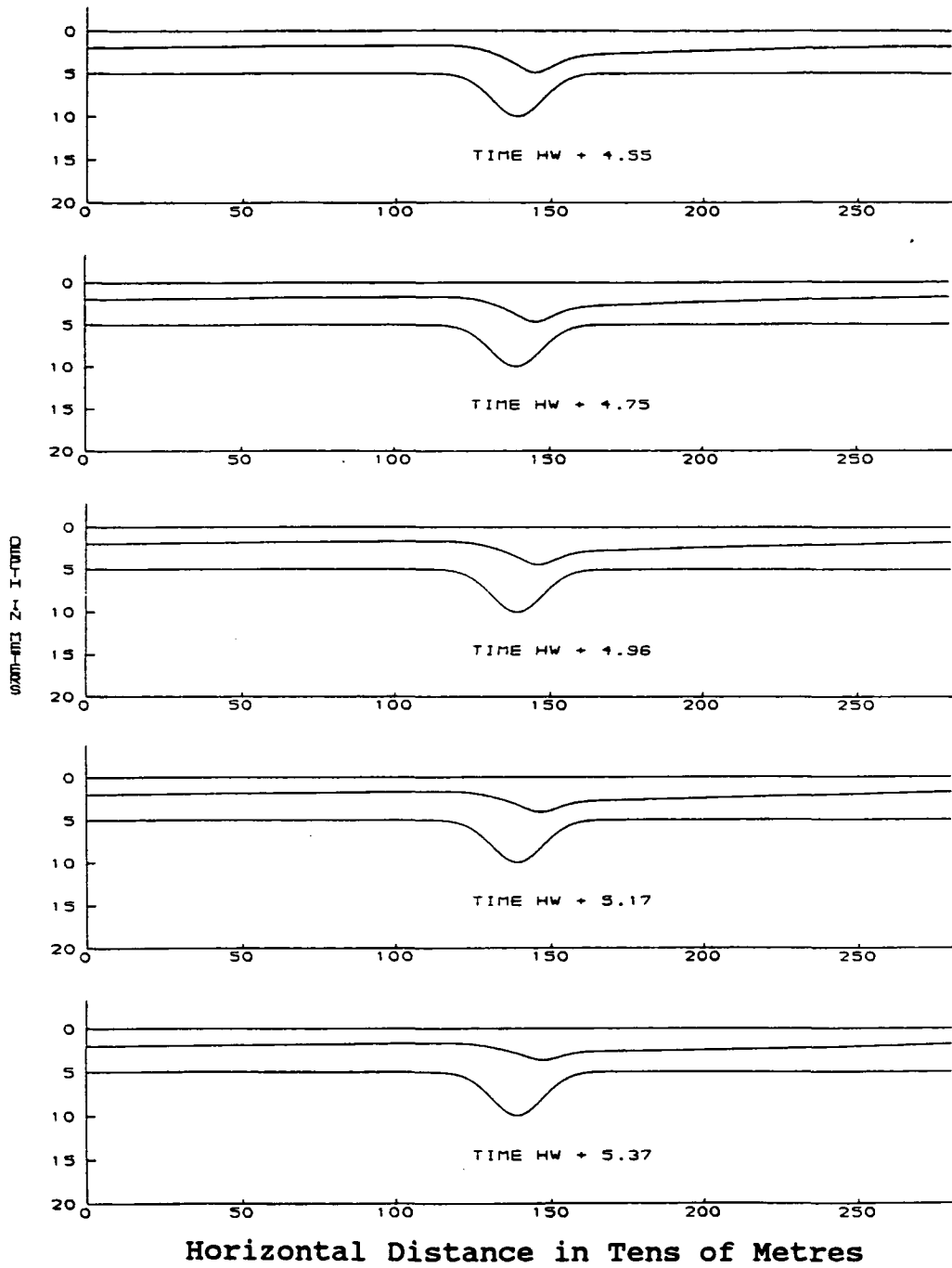


Figure 7.6: Model output for the standard configuration. Results from HW+4.55 to HW+5.37 are shown.

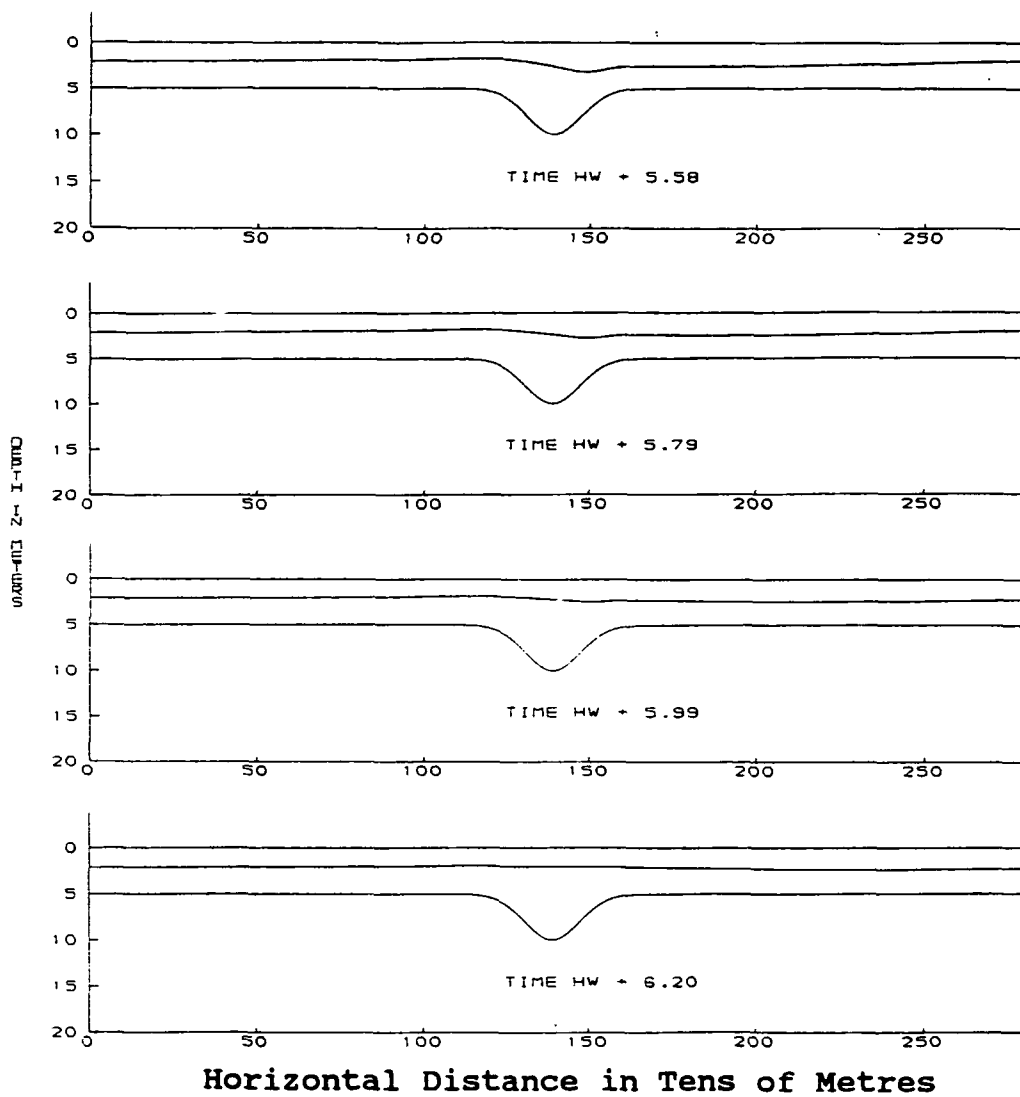


Figure 7.7: Model output for the standard configuration. Results from HW+5.58 to HW+6.20 are shown.

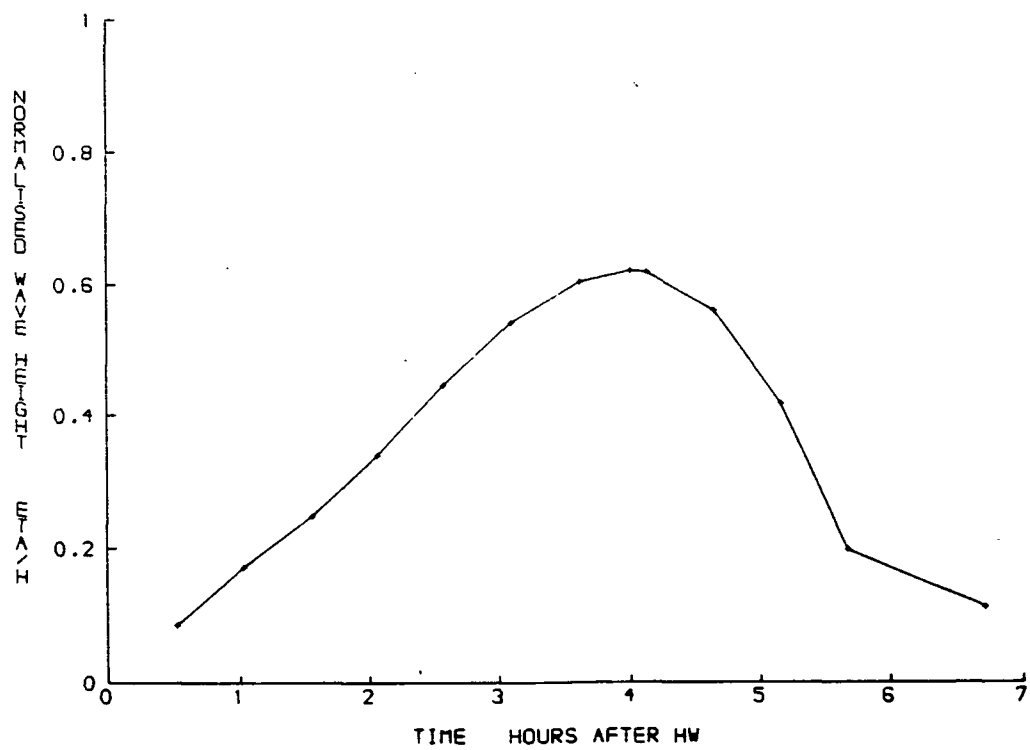


Figure 7.8: Wave height non-dimensionalised by the shallow water depth, H , plotted against time for the standard configuration.

the grid either side to see where it falls to less than 10% of this value. The intervening area is designated a wave and its length is computed. The wavelength changes with time also and its behaviour is represented in figure 7.9. In association with the steepening of the wave crest at HW+4.0 there is an adjustment of the wavelength, although the overall tendency is for the wavelength to grow with time. From HW+0 to about HW+2.0 a wave grows and appears to attain a length scale commensurate with the topography. The wavelength remains relatively unaltered until about HW+4.0, after which it increases dramatically, presumably in association with the release of a long internal wave upstream. After about HW+5.5 the wave begins to leave the model domain at the upstream end. In figure 7.9 this is evidenced by a smaller growth in wavelength, up to HW+7.0.

The total energy density, E , associated with an internal wave is computed as due to the departure of the interface from the initial state over the whole domain, i.e. the whole model grid. Assuming equipartition of potential and kinetic energy the total energy density is (Phillips, 1977)

$$E = \sum_{domain} \Delta \rho g \eta^2 \Delta x \quad (7.16)$$

E is plotted against time in figure 7.10. The maximum energy in the wave also occurs after maximum barotropic flow, at HW+4.03, close to the time of the wave height maximum. Like η_m , E also seems to diminish rapidly in the model after its maximum. The maximum wave energy is computed as $E_m = 144 \text{ kJ m}^{-1}$ for this model run. (This would be energy contained in

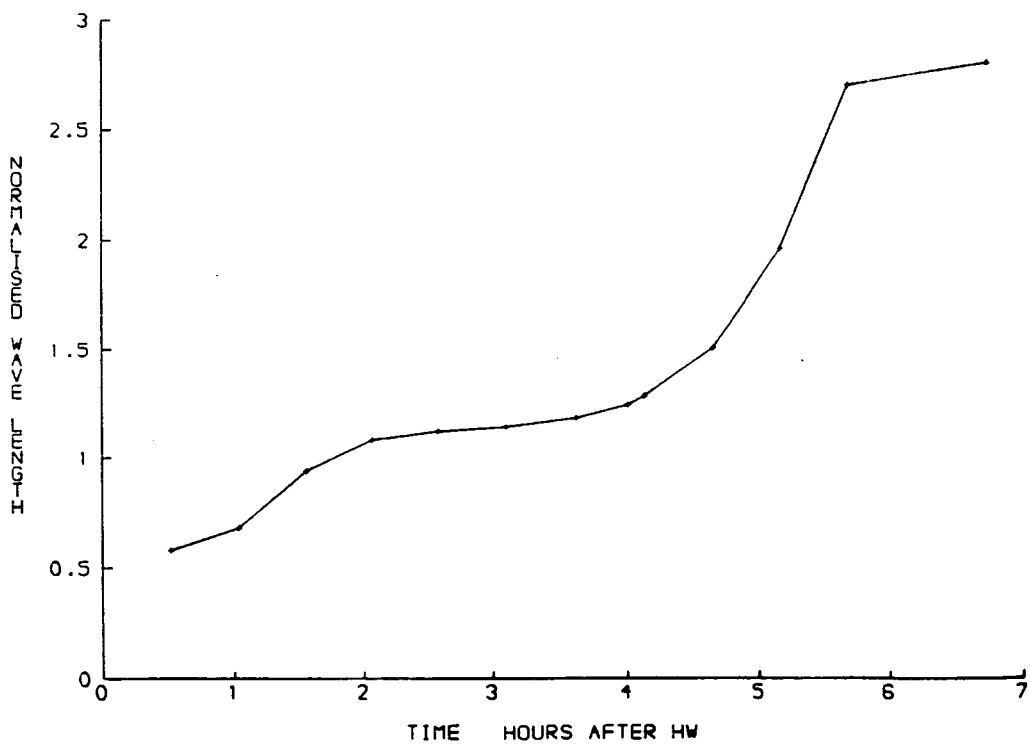


Figure 7.9: Wavelength non-dimensionalised by the depression length, $2L$, plotted against time for the standard configuration.

the entire wave per unit length in the y direction, assuming that the wave had some meaningful presence in the y direction - across the estuary).

The source of energy for the internal wave is the barotropic tide. In a real estuary this would be associated with a wave like motion, resulting in a rise and fall of the free surface, and total water depth, H . In the model the tidal stream is represented by a sinusoidal motion, in water of constant depth. The fate of the model internal wave energy is diffusive attenuation, and radiation through the ends of the model domain.

7.7 A non-dimensional analysis and an examination of general behaviour

In order to devise a strategy to examine the model behaviour under varying hydrographic regimes a non-dimensional analysis was performed. This analysis highlighted certain model parameters which are important in characterising its behaviour.

The two equations (7.6, 7.7) on which the model is based can be non-dimensionalised using the following scaling relationships: $U, u \sim u_0$; $\frac{\delta}{\delta x} \sim \frac{1}{L} = \frac{\alpha}{B}$; $\eta \sim H$; $h', h'' \sim H$; $\frac{\delta}{\delta t} \sim i\omega$. Using a tilde to denote a non-dimensionalised variable equation 7.6 becomes

$$(i\omega u_0)\tilde{U}_{\tilde{t}} + \frac{u_0^2}{L}(\tilde{u}\tilde{U})_{\tilde{x}} + \frac{u_0^2}{2L}\left(\frac{\tilde{h}'' - \tilde{h}'}{\tilde{H}}\tilde{U}^2\right)_{\tilde{x}} = \left(g\frac{\Delta\rho}{\rho_2}\frac{H}{L}\right)\tilde{\eta}_{\tilde{x}} + \left(K\frac{u_0}{L^2}\right)\tilde{U}_{\tilde{x}\tilde{x}} \quad (7.17)$$

**ENERGY IN
kJ PER METRE**

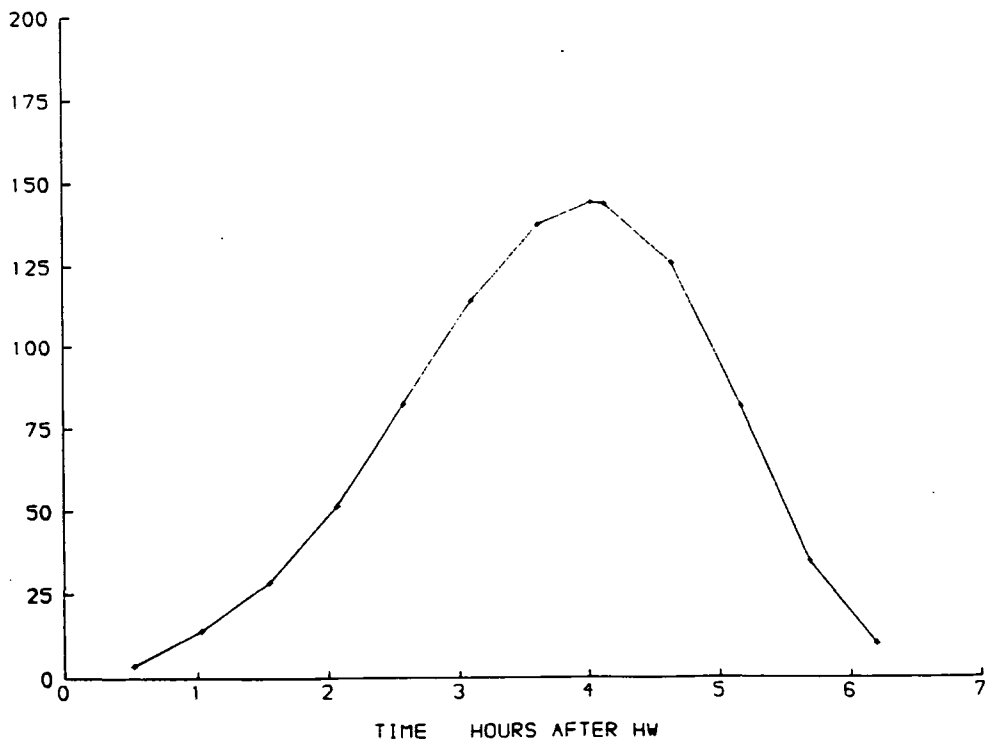


Figure 7.10: Wave energy in the standard configuration plotted against time. The vertical axis is scaled in kJoules per metre.

and dividing by $\frac{u_0^2}{L}$ gives

$$\left(\frac{i\omega L}{u_0}\right)\tilde{U}_t + (\tilde{u}\tilde{U})_{\tilde{x}} + \frac{1}{2}\left(\frac{(\tilde{h}'' - \tilde{h}')\tilde{U}^2}{\tilde{H}}\right)_{\tilde{x}} = \left(g\frac{\Delta\rho H}{\rho_2 u_0^2}\right)\tilde{\eta}_{\tilde{x}} + \left(\frac{K}{Lu_0}\right)\tilde{U}_{\tilde{x}\tilde{x}} \quad (7.18)$$

Equation 7.18 shows that the non-dimensionalised nonlinear terms - advective acceleration by the barotropic tide, and advective acceleration by the baroclinic tide - scale as 1 and $\frac{1}{2}$ respectively. This indicates the great importance of the nonlinear terms in this model, and since these terms represent real physics in the Tamar Estuary, further indicates the importance of nonlinear acceleration in the observed behaviour.

The other coefficients for the terms in this equation are scaling parameters.

$$R = \frac{i\omega L}{u_0} \quad (7.19)$$

relates the importance of the Eulerian acceleration to the advective acceleration. Then

$$F' = g\frac{\Delta\rho H}{\rho_2 u_0^2} \quad (7.20)$$

is the inverse square of an internal Froude number (F_i), and

$$S = \frac{K}{Lu_0} \quad (7.21)$$

is a diffusion scaling parameter.

Performing the same analysis on equation 7.7 gives

$$\left(\frac{i\omega L}{u_0}\right)\tilde{\eta}_t = \left(\tilde{h}'\tilde{u} + \frac{\tilde{h}'\tilde{h}''\tilde{U}}{\tilde{H}}\right)_{\tilde{x}} \quad (7.22)$$

Equation 7.22 yields no new scaling parameters, but it does express the notion that for variable values in the standard configuration (i.e. $u_0 = 0.5ms^{-1}$, $L = 250m$, $\omega = \frac{2\pi}{12.4hours}$) $R = 0.07$. This suggests that in the continuity equation (equation 7.7) maintenance of horizontal mass continuity might dominate over growth in η with time.

The relative importance of the terms in equations 7.6 and 7.7 is governed by the scaling parameters listed above. The balance or imbalance in these terms determines classes of behaviour in the model. Considering the non-dimensional terms of equations 7.18 and 7.22 to be of order one, it should be possible to examine the behaviour of the model just in terms of R , F' , and S .

In retarding the growth of the baroclinic tide the relative importance of the diffusive term to the pressure gradient derived term can be examined through F' and S .

7.7.1 Model results for $\frac{h_1}{H} = 0.4$, in the F', S plane

For this set of model results the undisturbed upper layer depth, h_1 , was fixed at $2m$, and the shallow water depth, $H(x = 0)$, was fixed at $5m$, i.e. $\frac{h_1}{H} = 0.4$. The model was run for a large variety of parameters varying only $\frac{\Delta\rho}{\rho}$, u_0 and K . The other parameters were held constant as in the

standard configuration. R was not held constant, but was always smaller than F' and S , e.g. $\frac{S}{R}$ ranged from about 4 to 10, and was typically 6. The model results are presented in the F', S plane. Figure 7.11 shows the maximum normalised wave height per model half tide plotted in this plane, and $\frac{\eta_m}{H}$ values are contoured from 0.2 to 1.0 in steps of 0.1. The following are interesting points to note about this figure, and the results.

- The figure was constructed from 50 separate model runs.
- For $F' < 1$ (i.e. for $F_i > 1$, an internally supercritical mode), the model failed inside the domain due to numerical instability, (Δ), runaway growth in η or U , or there was more than one maximum wave height, (\circ), due to wave steepening after maximum stream. $F' < 1$ implies that nonlinearities are important in the momentum equation (7.6).
- The model fails inside the domain, due to numerical instability, or there is runaway growth in η or U , for $F' \leq 0.5$ (i.e. for $F_i \geq 1.4$), and small S ($S < 0.3 - 0.4$). Model failures are depicted with a Δ . This behaviour could be interpreted as a hydraulically unstable situation which may have an analogue in the real world in the form of a hydraulic jump. Another Δ appears at $F' \simeq 1.7$ and $S \simeq 0.2$, for the same reasons.
- For $F' \geq 1$ (i.e. for $F_i \leq 1$, an everywhere internally subcritical mode), the model produces stable computations and internal waves with only one maximum wave height.

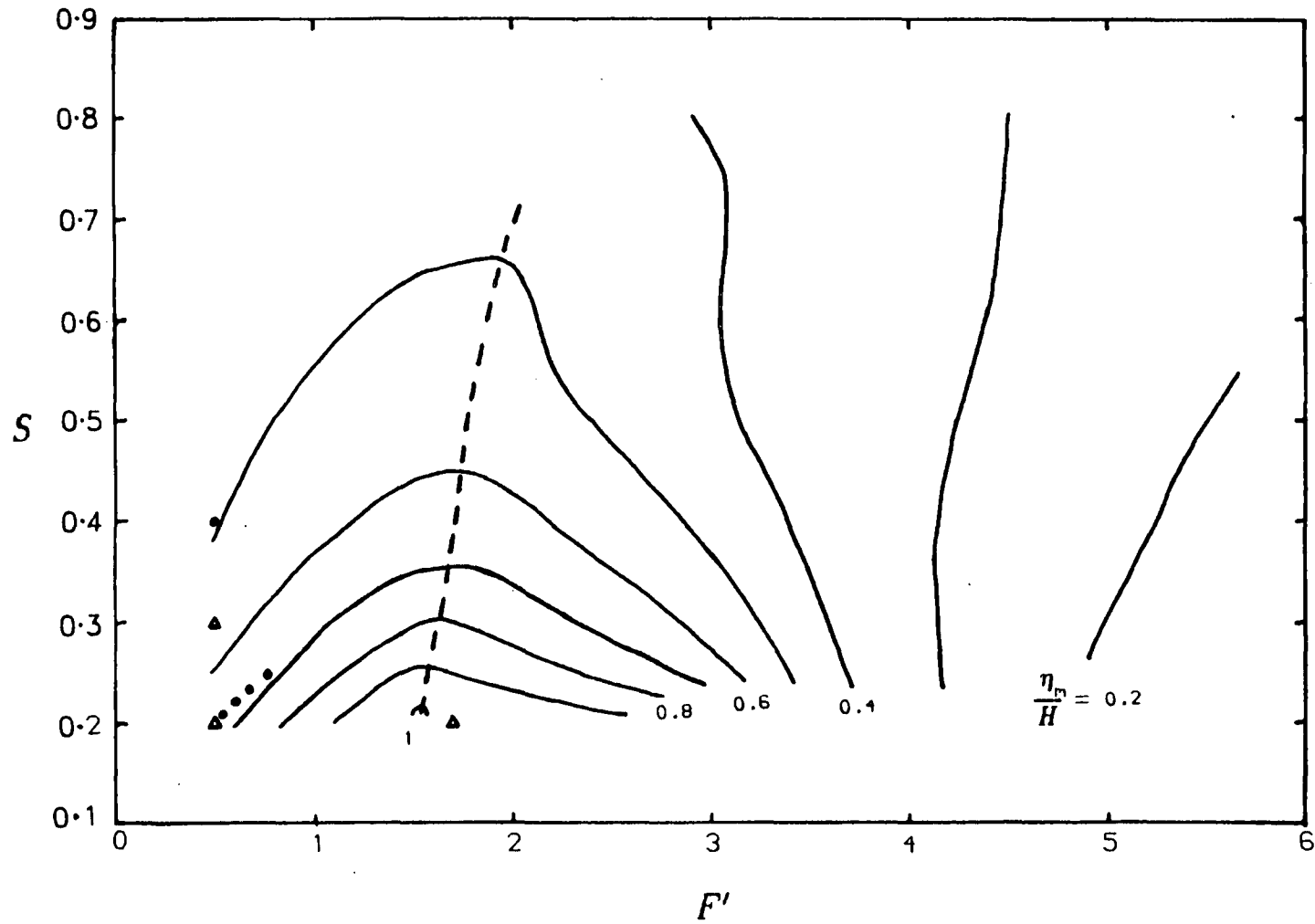


Figure 7.11: The normalised maximum wave heights plotted in the F' , S plane, for $h_1/H=0.4$. A circle refers to a wave with two height maxima per half tidal cycle, and a triangle refers to a complete model failure.

- For the purposes of making complete smooth contours the quasi-steady solution, or first wave maximum, is plotted in figure 7.11, so that the graph depicts behaviours from $F' = 0$ to 6 and from $S = 0.1$ to 0.9.
- The dashed curve indicates the values of F' and S which produce the largest maximum wave heights. As $S \rightarrow 0$ this curve tends to $F' = 1.5$. The curve slopes to the right for increasing S due to the need for a larger pressure gradient to overcome diffusive effects.
- Figure 7.11 is composed of several zones of behaviour. For a given value of F' , below 4, smaller maximum wave heights are formed with increasing S (increasing diffusion). To the right of the dashed curve, for fixed S , smaller maximum wave heights are formed for increasing F' , (corresponding to increasing $\Delta\rho$ or decreasing u_0). For fixed F' , above 4, marginally larger maximum waves heights are obtained by increasing S , and to the left of the dashed curve, for fixed S , maximum wave heights decrease with increasing F' . These effects can be summarised in the following way.
- For the largest waves to form the necessary condition seems to be a balance between a tendency for growth and retardation in the model. More specifically this might be a gross balance between non-linear steepening as represented in the advective acceleration terms and inhibition of growth due to the development of a wave and subsequent pressure gradient, with the other terms playing minor rôles.

7.7.2 Model results for $\frac{h_1}{H} = 0.2$ in the F', S plane

The ratio of undisturbed upper layer depth, h_1 , to shallow water depth, $H(x = 0)$, was fixed at $\frac{h_1}{H} = 0.2$, and $\Delta\rho$, u_0 , and K were varied as described in the last section. The maximum normalised wave height produced in each case was plotted in the F', S plane, shown in figure 7.12. Values of $\frac{\eta_m}{H}$ are contoured from 0.2 to 0.6 in steps of 0.1, with the addition of the $\frac{\eta_m}{H} = 0.25$ contour. The following points are of interest.

- This figure was constructed from 49 separate model runs.
- For $F' < 1$ ($F_i > 1$) and small S ($S < 0.4$), there was more than one maximum wave height, due to steepening after maximum stream. These are depicted with a \circ .
- The model did not fail or show numerical instability in any of the model runs used to construct figure 7.12.
- For $F' > 1$ and for $S > 0.4$ the model produces stable computations and internal waves with only one maximum wave height during the ebb stream.
- Figure 7.12 shows the same general pattern as figure 7.11 and so the same general conclusions regarding the model behaviour for $\frac{h_1}{H} = 0.4$ apply for $\frac{h_1}{H} = 0.2$.
- The maximum wave heights produced when $\frac{h_1}{H} = 0.2$ are smaller than for $\frac{h_1}{H} = 0.4$, by about 60%, for the same F' and S values.

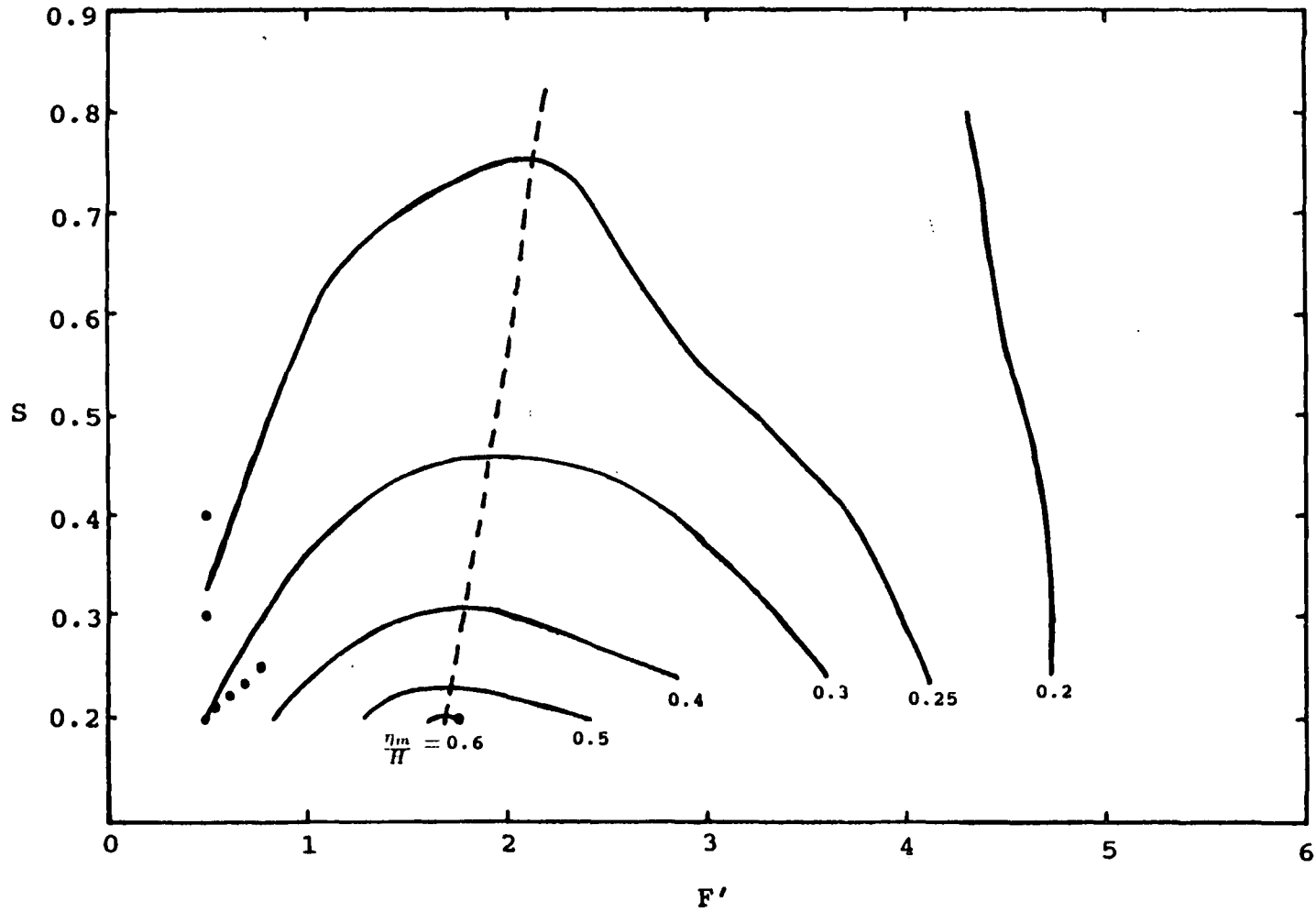


Figure 7.12: The normalised maximum wave heights plotted in the F' , S plane, for $h_1/H=0.2$. A circle refers to a wave with two height maxima per half tidal cycle.

Figures 7.11 and 7.12 show that the model is sensitive to changes in S when $1 < F' < 3$. Thus, care must be taken in choosing K for certain model parameterisations.

7.8 Energy in the model

As already described the model computes, at each time step, the total energy associated with the internal waves (equation 7.16). Unlike η_m there is no clear and obvious behaviour for maximum E in the F', S plane due to its strong dependence on the square of the maximum wave height and the density difference between the two layers $\Delta\rho$. For the purposes of comparing real wave energies, as observed in the Tamar, and those predicted by the model it is simplest to resort to individual model parameterisations.

Chapter 8

Modelling observed phenomena

The phenomena described in Chapters 4 and 5 were very different. The neap tide observations depicted the formation and evolution of a non-breaking internal wave, while the spring tide observations described an internal wave which grew until it interacted with the bed, and then broke *in situ*. An attempt has been made to reproduce these behaviours using the numerical model described in general terms in Chapter 7.

The numerical simulations are in general agreement with the observations, but there are some differences. The model shows an ability to predict maximum wave heights and energies, in particular, but cannot reproduce fully the nonlinear behaviour present in the Tamar, manifest as wave growth through steepening.

The general response of the model is discussed first, for each observation

set, with a brief direct comparison of observations and predictions for the neap case only. Individual wave attributes are discussed in detail. A set of concluding remarks are included.

8.1 Modelling the neap tide observations

8.1.1 Model configuration

The model configuration corresponding to the set of conditions, measured on 6 November 1989, is as follows: $\Delta\rho = 16\text{kgm}^{-3}$, $h_1 = 1\text{m}$, $H = 4\text{m}$, $\Delta t = 0.1\text{s}$, $\Delta x = 10\text{m}$, $K = 40\text{m}^2\text{s}^{-1}$, $B = 5\text{m}$ and $\alpha = 0.01$. Note that $\alpha = 0.01$ gives a topographic length scale of $2L = 1000\text{m}$ in this case. After the November 1989 fieldwork the Cargreen site was more extensively surveyed. It was found that although the seaward slope of the bed depression had a length scale of $250 - 300\text{m}$, as previously assumed, the length of the landward slope was nearer to $500 - 600\text{m}$. Since it is felt that on an ebb stream the landward slope is the dominant feature in determining wave size and shape, α was fixed at $\alpha = 0.01$.

Changes in water depth with tidal motions are not included in this model and so $H = 4\text{m}$ reflects the mean shallow water depth between high water and low water. Similarly, $h_1 = 1\text{m}$ reflects the estimated mean depth of the upper layer.

The barotropic tidal flow was modelled in two ways. Firstly, a sinusoidal function $u = -u_0 \sin \omega t$ was used. Figure 8.1 shows the fit of this sinusoidal tide to the observed magnitude of the depth averaged velocity, \bar{u} . u_0 was

set to 0.5ms^{-1} and ω was fixed at a value corresponding to a 12.4 hour tidal period. The time of predicted high water on 6 November 1989 was 10:00, but the sinusoidal approximate has $u = 0$ at 11:00. There was a lack of observations before 11:20 and after 15:40. (The results show that this approximation is adequate in representing \bar{u}). Secondly, the model was run using \bar{u} itself as the barotropic tidal forcing. \bar{u} was extrapolated linearly from the first observation to $\bar{u} = 0$ at 10:00, and from the last observation to $\bar{u} = 0$ at 17:00.

8.1.2 General description

The behaviour of the model, for both forcing modes, can be summarised in general terms.

From the initial state of no barotropic flow, and an undisturbed interface, a wave grows over the bed depression, with increasing tidal current. This is manifest as a downward displacement of the density interface over the landward shelf and slope of the bed depression.

During this growth phase the level of the interface upstream of the bed depression is lowered from the relaxed position, and in the downstream direction is raised.

The wave attains its maximum height at 15:04 (real forcing) and 15:10 (sine forcing) - about 1 hour after maximum barotropic flow. The model wave continues to grow in height after maximum stream through nonlinear steepening as an adjustment to the slackening barotropic flow.

When the barotropic forcing falls to a sufficiently low level the wave

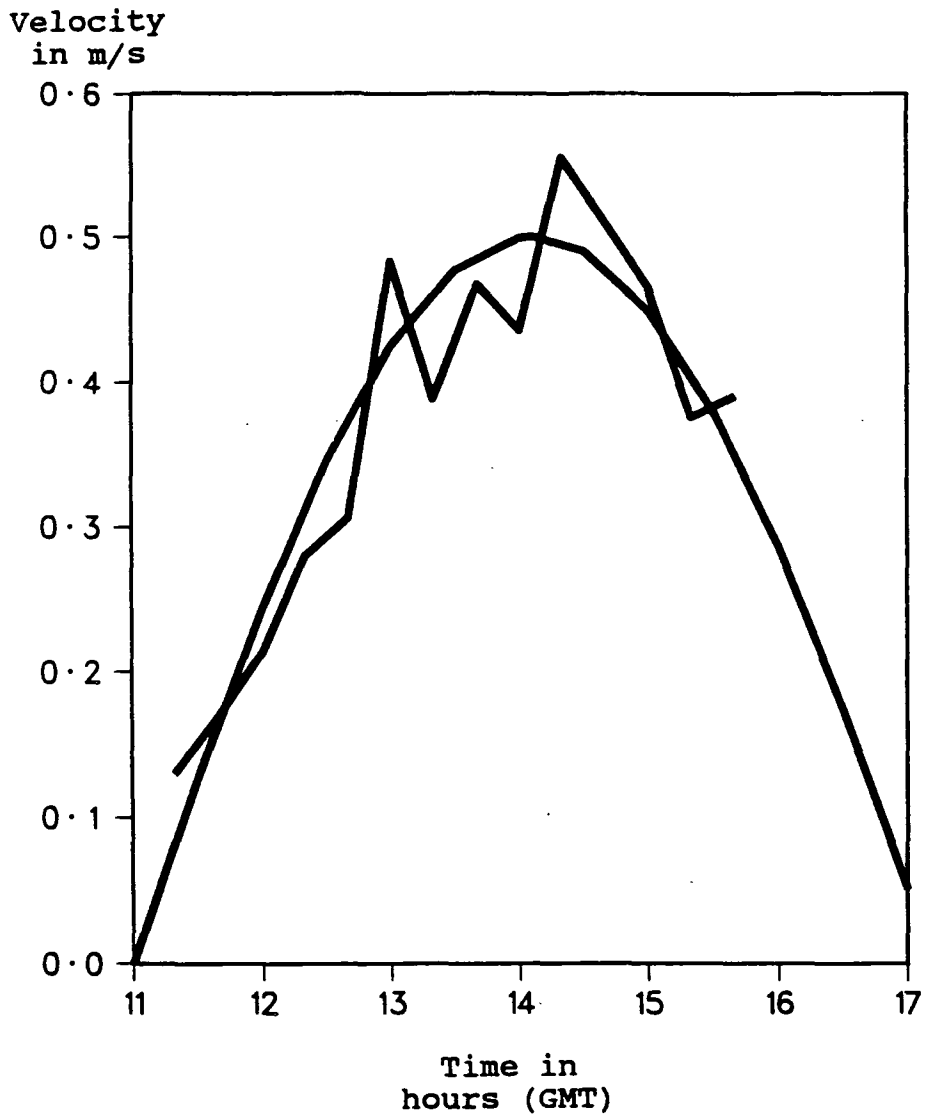


Figure 8.1: The magnitude of the depth averaged velocity, measured at "45" on 6 November 1989, plotted with the sinusoidal approximation used in the model.

propagates upstream - away from the bed depression. In doing so the wave amplitude is attenuated and the wavelength increases considerably. This occurs at 16:00 - 16:45.

Qualitatively this behaviour matches the observations. The model predicts the formation and evolution of a leewave in the manner described by Maxworthy (1979) and Lee & Beardsley (1974) (without fission into solitary waves). Quantitatively there are some differences between the model and observations. The model wave attributes are discussed separately in the following sections.

8.1.3 Direct comparison with observations

Direct comparisons of the model predictions of the position of the interface, and the observed position of the thermocline, are presented for three different times. The echograms provide the observed behaviour. These show the bed and the "raw" thermocline, i.e. not one that has been reconstructed. The three times chosen reflect different phases in the waves evolution. The first, at 13:15, corresponds to the first observed maximum in the wave height. The second, at 15:15, corresponds to the second observed maximum in the wave height, after maximum stream. The third, at 16:45, corresponds to the final observation, when the wave height in the model, and in reality, has decayed. For this comparison, only the sine forcing mode results are used. The comparison using the real forcing mode results is very similar.

13:15 - the time of the first observed maximum wave height.

Figure 8.2 shows a schematic diagram of acoustic backscatter for the 13:15

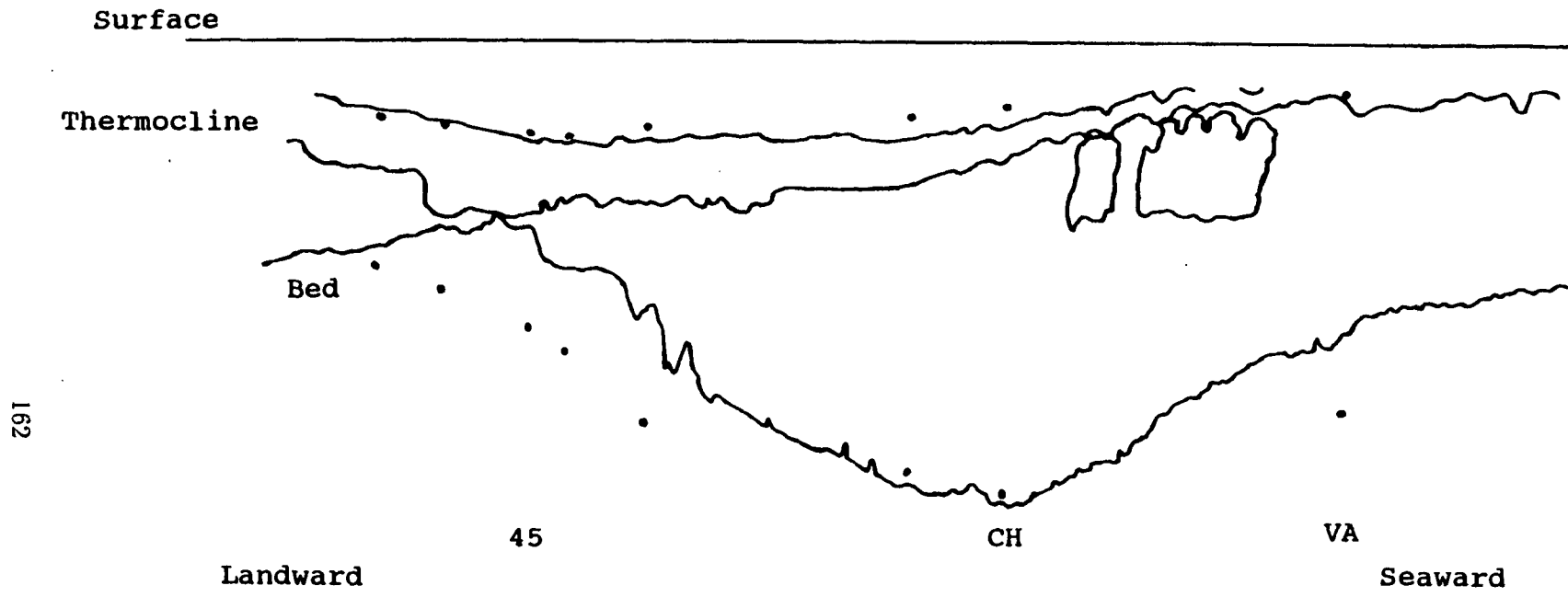
transect. The echogram for this transect was traced showing the outline of midwater backscatter events, the bed and the water surface. Included in this figure, as small circles, are the model predictions of the interface level, and the position of the idealised bed, at the fixed stations (e.g. "CH", "VA", and "RH" etc.). Note that in this figure the horizontal scale is linear with time, and not distance. Subsequently the smooth model bed seems distorted.

The model topography is a good representation of the bed near the centre of the depression, but does not match the observed bed either landward or seaward of this centre. The model bed is symmetrical longitudinally about the centre of the depression. Because the bed at Cargreen is not symmetrical, as discovered in the survey, a match is only possible on the landward slope. However, since the Tamar bed also varies considerably transversely in the main channel, (there being a ridge that sticks out from the Devon bank), there are echograms in which the idealised model bed does not match even the landward slope. This is one such echogram.

Nevertheless, the model predicts an internal wave which is in qualitative agreement with the observations. The model underpredicts the thermocline displacement, in the region of maximum displacement (for reasons discussed later) by about 50%. The position of the wave trough is predicted to be in approximately the same position as that observed. The observed wave trough was rather broad and its position was hard to locate exactly.

15:15 - the time of the second observed maximum wave height.

Figure 8.3 shows the schematic diagram of acoustic backscatter and model predictions for the 15:15 transect. The model predictions for thermocline



162

Figure 8.2: The schematic diagram of acoustic backscatter and model predictions, from transect 7 at 13:15 on 6 November 1989.

displacement are much better than at 13:15. The small circles (model) lie mostly on or around the region indicated as being the thermocline. The wave trough in reality is broader than the prediction, along the estuary axis. This leads to a more easily defined wave trough position in the model. Overall the agreement is very good.

16:45 - the final observation.

Figure 8.4 depicts the model predictions and the schematic acoustic backscatter at 16:45 on 6 November 1989. The thermocline displacement is again underpredicted for most of the length of the wave by about 50%, and the wave trough position is predicted to be much further landward than actually occurred (in fact more landward than the region depicted in figure 8.4). This suggests that the model allows the wave to progress too quickly upstream, at the expense of attenuation. At this stage the model wave trough is also very broad, in the longitudinal direction, but still not as broad as the real trough.

8.1.4 Results and comparison

The model predictions, for the whole of the period of the 6 November 1989 study, are separated into various wave attributes and discussed in detail separately.

Wave height

Figures 8.5 and 8.6 depict the maximum thermocline displacement (or wave height), η_0 , derived from the echograms and thermal maps, together with the model predictions for the sine forcing and real forcing modes, respectively.

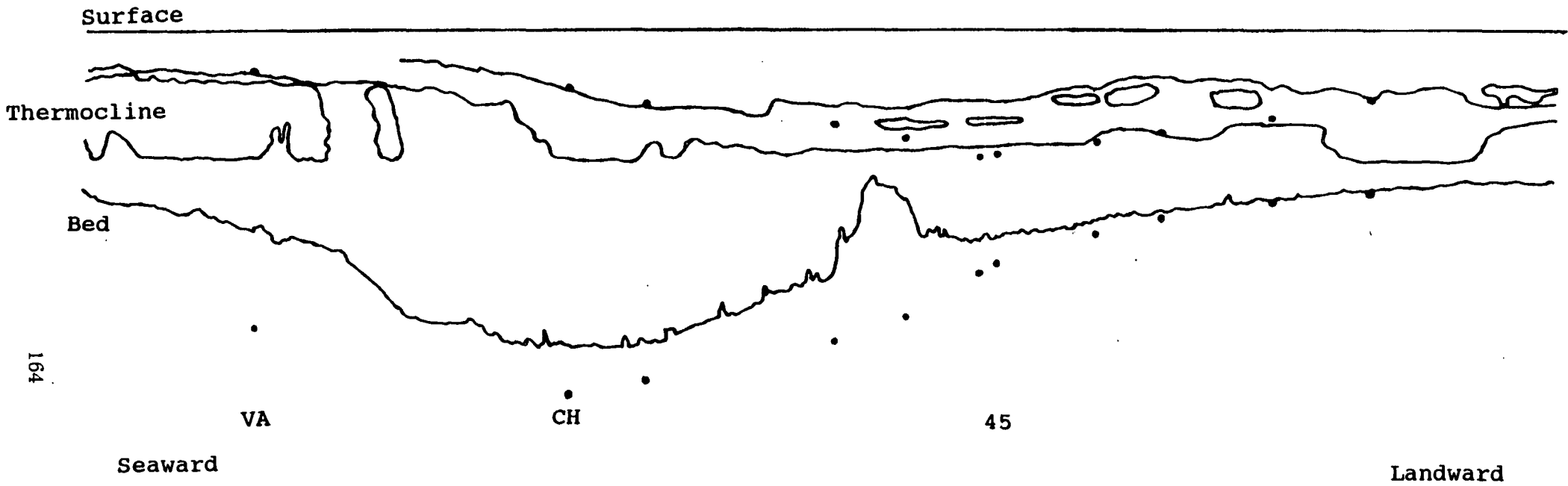


Figure 8.3: The schematic diagram of acoustic backscatter and model predictions, from transect 12 at 15:15 on 6 November 1989.

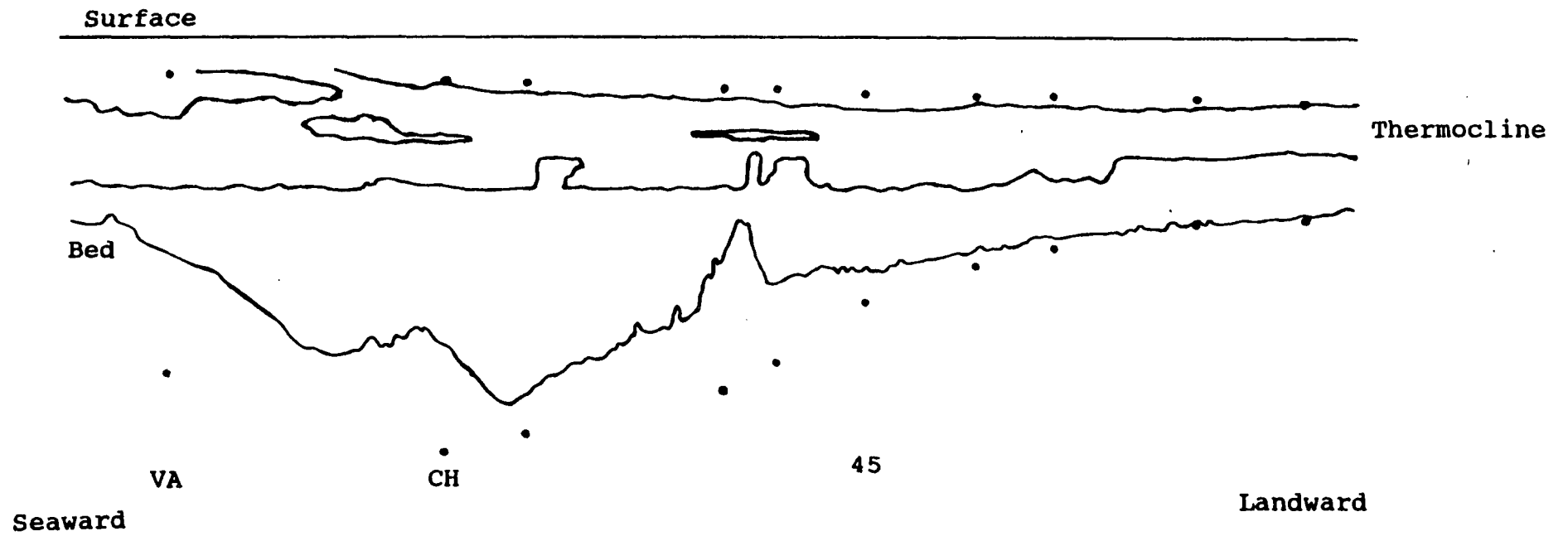


Figure 8.4: The schematic diagram of acoustic backscatter and model predictions, from transect 18 at 16:45 on 6 November 1989.

Maximum
thermocline
displacement
in metres

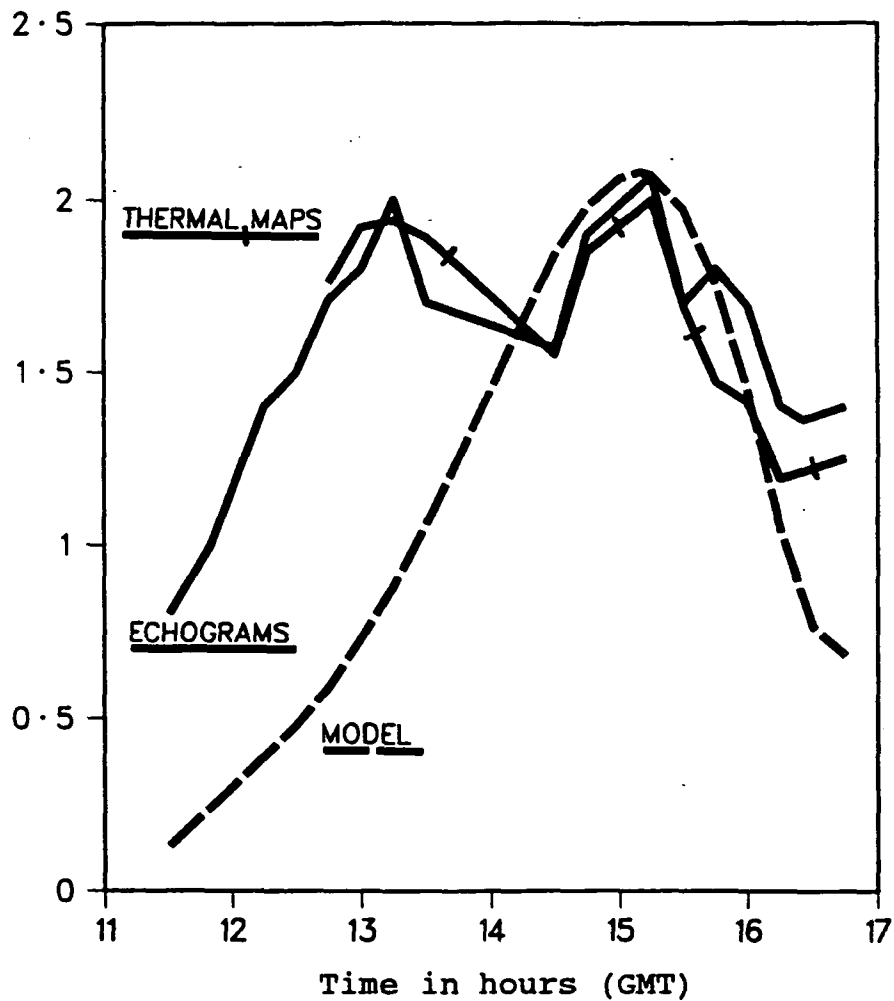


Figure 8.5: Observed maximum thermocline displacement and interfacial displacement from the model forced with a sinusoidal barotropic tide, for 6 November 1989.

Maximum
thermocline
displacement
in metres

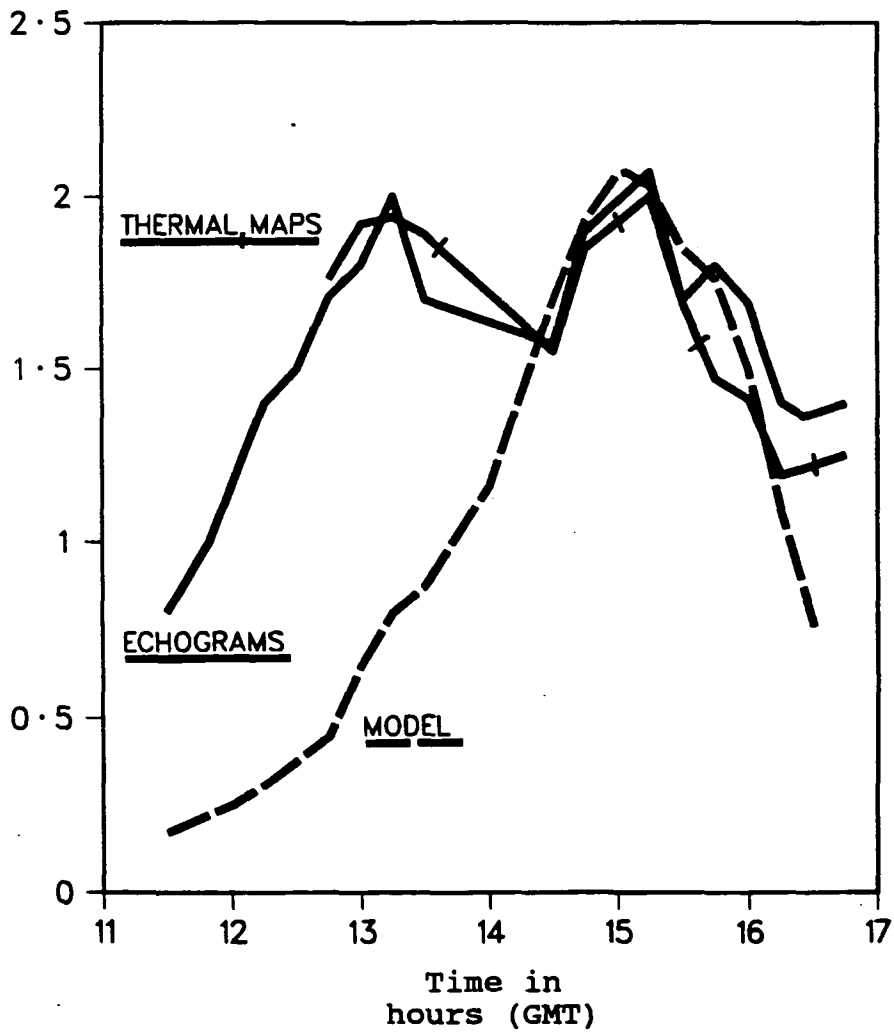


Figure 8.6: Observed maximum thermocline displacement and interfacial displacement from the model forced with the real barotropic tide, for 6 November 1989.

Overall there is good qualitative agreement between the model and observations, after 14:30, and between the model results for the two forcing modes. The model predicts a growth in η_0 from zero at time $t = 0$ to a maximum ($\eta_0 \simeq 2.1m$) at approximately 15:10 (sine forcing) and 15:04 (real forcing), ($\frac{\delta\eta_0}{\delta t} \simeq 0.45mhour^{-1}$). After the maximum is attained the wave height decays rather rapidly, for both forcing modes, to $\eta_0 \simeq 0.67m$ at 16:45. In the case of the sinusoidal tide the maximum stream is at 14:06, yet the wave grows up to and beyond this time. The reason for this is nonlinear steepening of the wave in the slackening stream. The same is true for the real forcing, despite there being two maxima in the tidal stream.

The model predicts the second observed maximum wave height well, for both forcing modes, (given the $0.2m$ uncertainty in the observed η_0). There is a large discrepancy between the model and the observations before 14:30. The observed wave growth was rapid, even at low barotropic tidal flow, ($\frac{\delta\eta_0}{\delta t} \simeq 0.67mhour^{-1}$). At low tidal stream the model wave is not allowed to steepen rapidly, as the diffusive attenuation is too large. At large tidal stream the balance between steepening and attenuation was realistic. The diffusion problem will be referred to again later in this chapter, and solutions and alternatives will be discussed.

The differences in the model results from the two modes of forcing are subtle. The sine forcing gives a marginally larger wave, about $0.2m$ larger, from 12:00 to 15:05. The predicted time of maximum wave height and the maximum height itself are in close agreement, and the wave decay after 16:00 is virtually identical.

At about 13:00 to 13:15 there is a slight increase in wave height, for the real forcing case, which is attributable to the first dramatic peak in \bar{u} . Obviously the model is trying to respond to this change in \bar{u} . At 15:45, after the model wave starts decaying, \bar{u} undergoes another increase and the model responds by slowing the rate of decay. This also corresponds to a "shoulder" in the observations curve.

The model overpredicts the final decay rate of the wave from 16:00 to 16:45.

In summary, the first observed maximum wave height is not represented in the model, but the second maximum wave height, after the time of maximum stream, is represented very well (certainly within the measurement error in η_0). The real forcing mode replicates some of the more subtle behaviour in the observed η_0 .

Wave energy

Figures 8.7 (sine forcing) and 8.8 (real forcing) show the wave energy observations and model results. There is good qualitative agreement between the model and observations, after 14:30, and between the results from the two forcing modes. The wave energy behaviour is similar to that of wave height, as would be expected due to its dependence on η_0^2 .

The model results from the two modes reproduce the second observed energy maximum ($\simeq 220 \text{ kJ m}^{-1}$), after maximum stream, but fail to replicate the first observed maximum.

The model results from the two modes of forcing are essentially the same, but have slight differences. The real forcing mode, as in the case of

Total wave energy in kiloJoules per metre

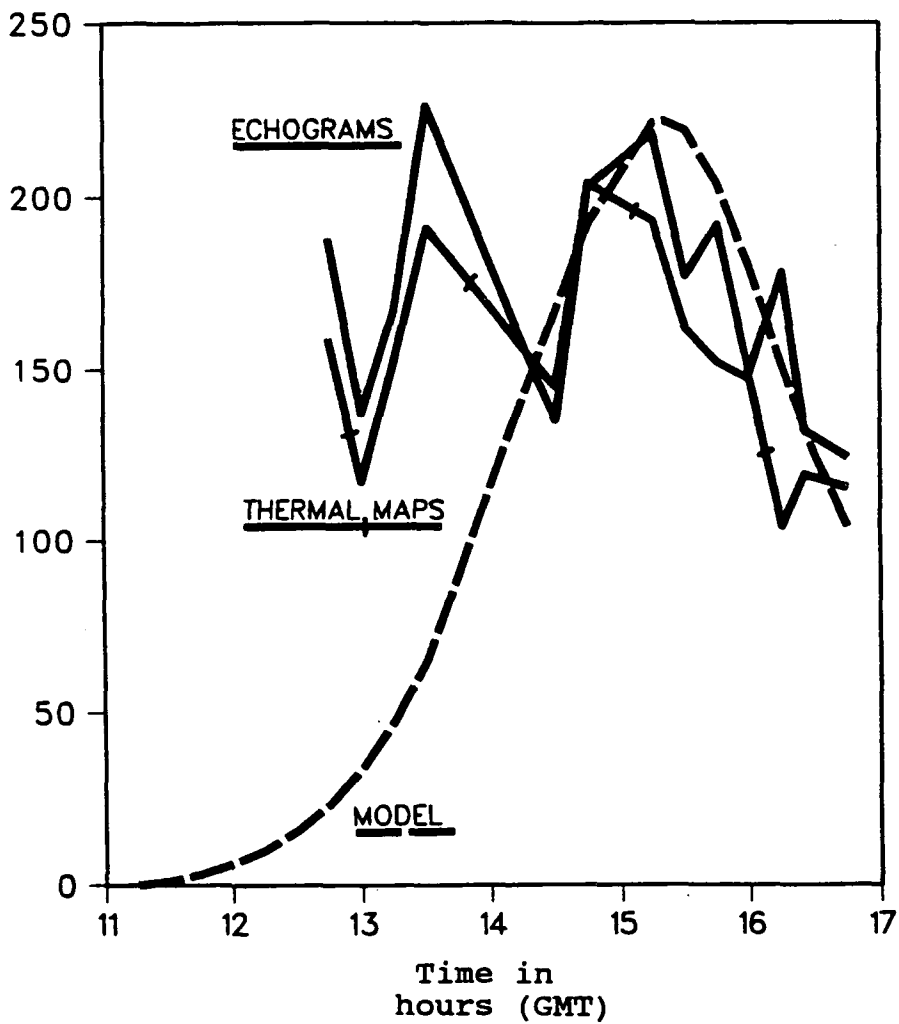


Figure 8.7: Observed wave energy on 6 November 1989, together with the predictions from the model in the sine forcing mode.

Total wave energy in kiloJoules per metre

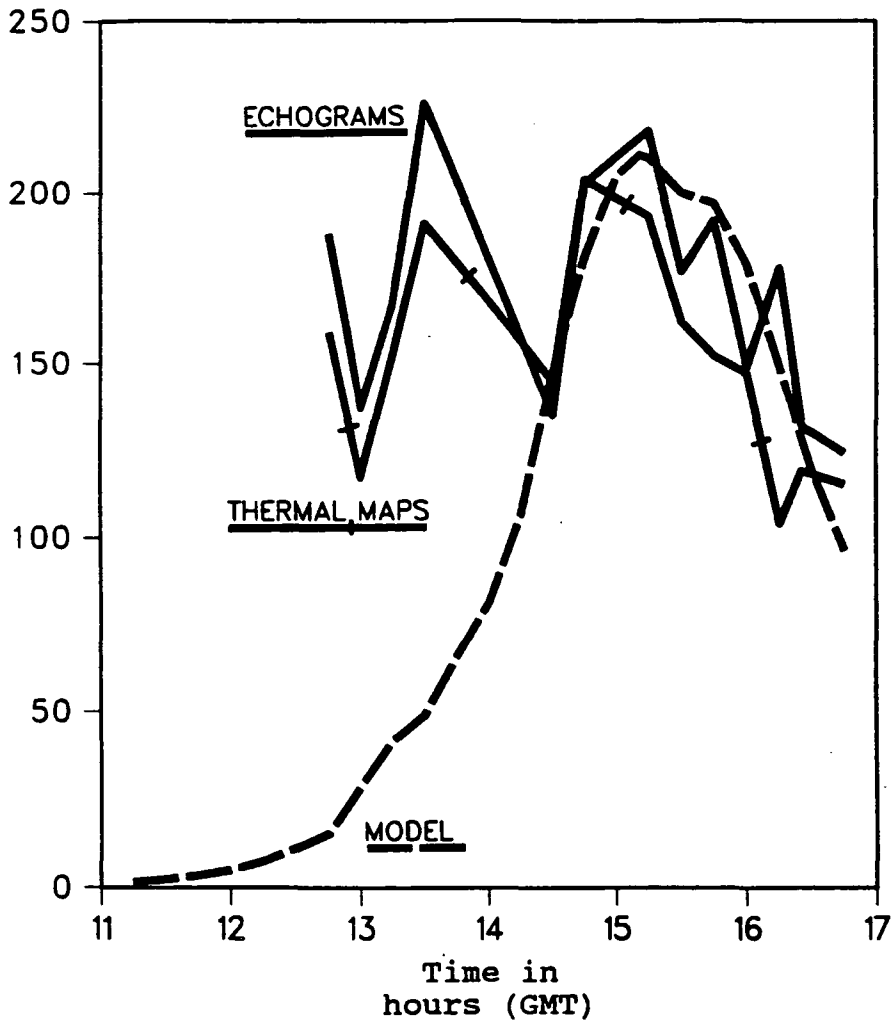


Figure 8.8: Observed wave energy on 6 November 1989, together with the predictions from the model in the real forcing mode.

η_0 , produces small variations in wave energy which are linked to variations in \bar{u} . The most notable of these is the lessening of the wave energy decay at 15:45, which also seems to occur in the observations.

After 14:30 both model results give a very good fit to the data, with the real forcing mode performing better. The observed wave energy has an uncertainty of the order of $\pm 50 kJm^{-1}$ at its maximum value.

Wave trough position

Figures 8.9 (sine forcing) and 8.10 (real forcing) show the observed wave trough position plotted against the model predictions. The trough position is measured in metres landward of "CH". The uncertainty in the observations is $\pm 60m$.

Up to about 16:15 there is very good agreement between both model modes and between the model and the data. The wave trough holds a steady position 200 – 250m landward of "CH". After 16:15 the model predicts that the wave should propagate landward from "CH", in response to the rapidly slackening ebb. From 16:15 to 16:45 the model wave propagates about 800m upstream - a speed of about $0.44ms^{-1}$. In the same period the observed wave remained between 300m and 400m upstream of "CH".

The reasons for this difference are not obvious. In reality the water depth dropped to about 3m outside the bed depression and 8m over the depression, at 16:45. This behaviour is absent from the model. Also, the model overpredicts the decay of the wave height from 16:00 to 16:45. This may be linked to the predicted propagation speed. The (KU_{xx}) formulation of the diffusive attenuation allows waves to exist and propagate in the model

Wave Trough
position
in metres
landward of
"CH"

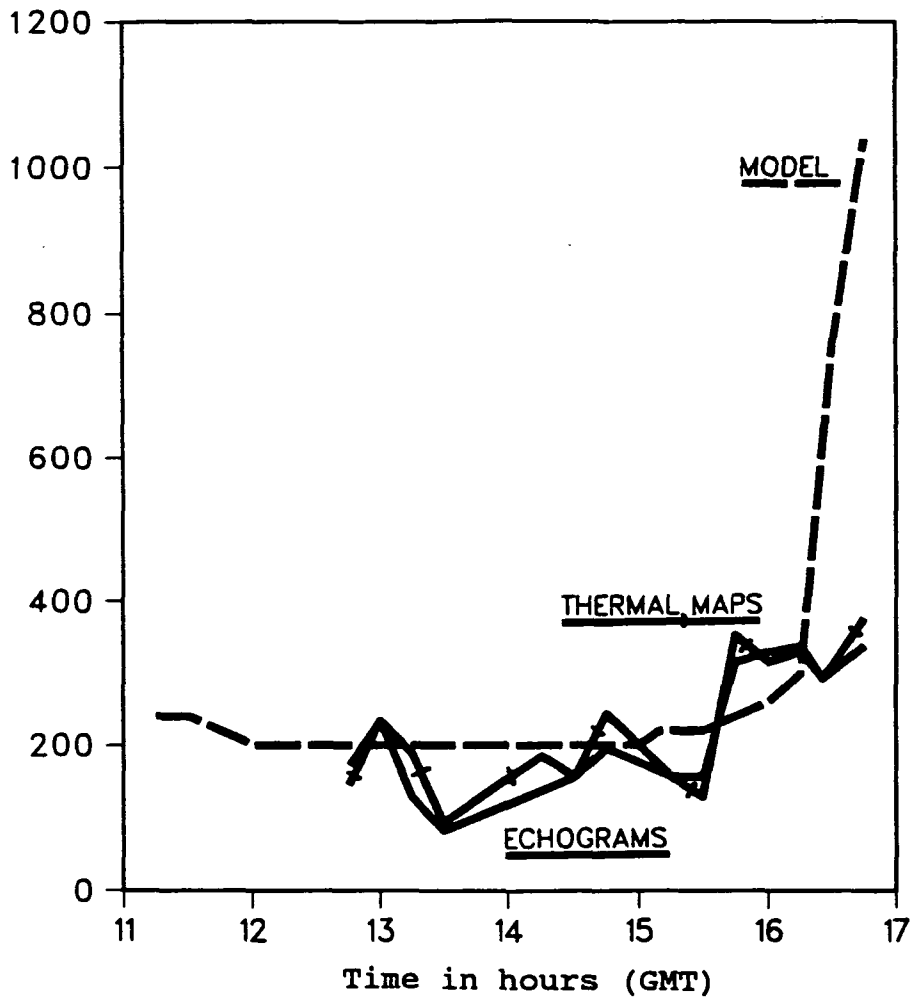


Figure 8.9: Observed wave trough position, on 6 November 1989, together with the results predicted by the model in the sine forcing mode.

Wave trough
position
in metres
landward of
"CH"

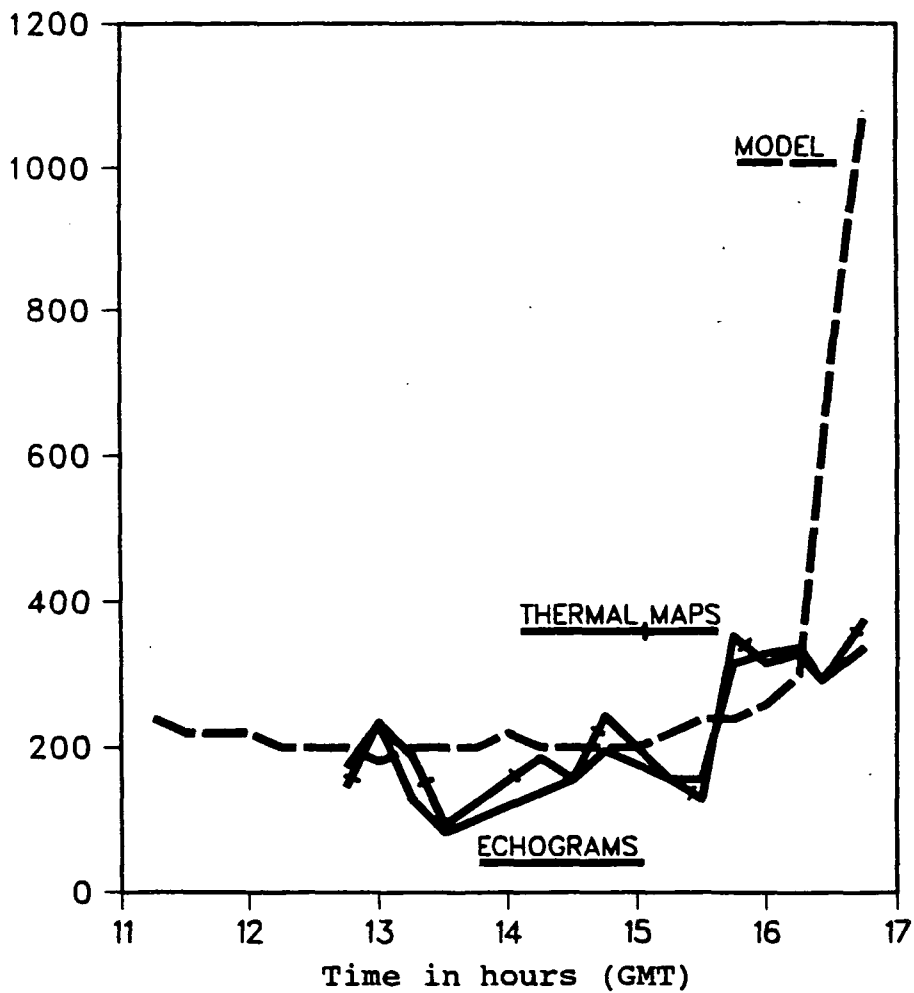


Figure 8.10: Observed wave trough position, on 6 November 1989, together with the results predicted by the model in the real forcing mode.

at the expense of attenuation. The behaviour from 16:00 to 16:45 may be a manifestation of this. The observed wave height did not decay so rapidly after 16:00, and may not have been able to move away quickly from "CH".

Maximum baroclinic tide (shear)

Between 14:45 and 16:45 the maximum baroclinic tide, $(u_1 - u_2)$, is predicted to be 400m to 500m seaward of "CH", for both forcing modes. At 14:45 $(u_1 - u_2) = 0.16ms^{-1}$, and this increases to its maximum of $(u_1 - u_2) = 0.2ms^{-1}$ at 16:45. The thermocline thickening, which was first observed near "RH" ($\approx 250 - 300m$ seaward of "CH"), and which spread landward to engulf the whole wave trough by 16:45, was a direct result of enhanced shear across the thermocline. That the model should predict the area near "RH" to be the region of largest shear is encouraging.

Wavelength

The model predictions for wavelength are very similar in the two forcing modes. The model calculates the 10% wavelength - the length of the interface which is disturbed from its initial level by more than 10% of the maximum displacement. The wavelength is predicted to be about 1000m up to 15:30 when it reaches 1200m. It then grows rapidly to 1500m at 16:00, 2100m at 16:30 and 2400m at 16:45. The rapid growth in wavelength in the latter stages is associated with the decay in wave height and movement of the wave trough landward, i.e. the wave in the model propagates out of the bed depression as a long wave of small amplitude after 16:00.

The observations indicated a wavelength of about 500m for most of the survey period, with an increase to 800m at 16:45. However, there was little

observational coverage landward of the bed depression, because of the falling water depth and fear of damaging the Spar. The observed wavelength is almost definitely a gross underestimate (see Chapter 4, Section 4.5.3). This wavelength cannot be compared to the models prediction of 2400m, as the observed wave did not evolve and progress far upstream.

8.1.5 Summary

For the configuration corresponding to the set of neap tide observations, the numerical model is able to predict successfully the maximum wave height, maximum energy and position of the wave trough, for most of the observed period. The behaviour of the model at the beginning of the tidal stream, and toward the end of the tide are at odds with the observations. Specifically, the model underpredicts the wave height, for both forcing modes. This is almost certainly due to the way in which diffusive attenuation is parameterised. The model does not allow rapid wave growth and forces waves to decay quickly after the tidal stream relaxes sufficiently.

Nonlinear steepening appears to be an important process in governing wave growth immediately after the maximum tidal stream has been reached.

The wavelength predicted by the model is at least twice as large as that estimated from the observations, but the observed wavelength was almost certainly grossly underestimated, because of the lack of landward coverage with the echosounder and Spar.

The predicted position of maximum shear is in agreement with the observed location of the onset of vigorous vertical mixing.

The non-dimensional variable set corresponding to this configuration, with sinusoidal forcing, is: $\frac{h_1}{H} = 0.25$, $F' = 2.51$, $S = 0.2$ and $R = 0.113$. The maximum non-dimensional wave height achieved from this configuration was $\frac{\eta_m}{H} = 0.52$. The two non-dimensional analyses presented in Chapter 7 had $H = 5m$, $\frac{h_1}{H} = 0.2$ or 0.4 , R small compared to S and F' , and $\alpha = 0.02$. Nevertheless, those analyses predicted that the value of $\frac{\eta_m}{H}$ should lie between 0.4 and 0.9. The non-dimensional analyses, and this neap configuration, predicted that the model should produce only one wave height maximum with time. The observations clearly showed that there were two. This difference is thought to be linked to the diffusive attenuation, and is discussed later in this chapter.

8.2 Modelling the spring tide observations

8.2.1 Model configuration

Modelling the spring tide observations is quite different to the neap case, in one important aspect. The spring observations indicated a wave breaking *in situ* over the topography. The model has no physics in it which allows for wave breaking. The nearest state that this model can achieve is runaway growth in η or U , and model failure.

A model configuration which adequately represents the spring observations is hard to define. The stratification especially changed dramatically during the spring tide study. The Tamar did not resemble a two layer fluid and the density difference between bottom and surface waters, $\Delta\rho$, was not

constant. In addition, the upper layer depth, h_1 , varied and the overall water depth, H , decreased considerably with time. A compromise is achieved in the following set of variables: $\Delta t = 0.1s$, $\Delta x = 10m$, $K = 40m^2s^{-1}$, $B = 5m$, $\alpha = 0.01$, $h_1 = 2m$ and $H = 4m$. The model was run for different values of $\Delta\rho$.

As in the neap case the model was tidally forced, using both the magnitude of the depth averaged velocity observed at "45" and a sinusoidal approximation (see figure 8.11). The sine function, $u = -u_0 \sin \omega t$, was evaluated with $u_0 = 0.68ms^{-1}$, ω corresponding to a tidal period of 12.4 hours, and $u = 0$ at 08:00 (i.e. 1 hour after predicted high water).

In the real forcing mode \bar{u} was extrapolated to $\bar{u} = 0$ at 07:00 and 14:00.

8.2.2 General description

The behaviour of the model, for both forcing modes and for all values of $\Delta\rho$, can be summarised in the same way as for the neap case. A wave grows over the bed depression with the increasing barotropic tidal current. The level of the interface is lowered on the upstream side of the depression and raised on the downstream side. The wave attains its maximum height around 13:30 - about 2.5 hours after maximum barotropic flow, ($\frac{\delta\eta_0}{\delta t} \simeq 0.9mhour^{-1}$ from zero stream to 13:30). The model wave continues to grow in height after maximum stream through nonlinear steepening, as an adjustment to the slackening barotropic flow. When the barotropic forcing diminishes sufficiently the wave propagates upstream, out of the region of the bed de-

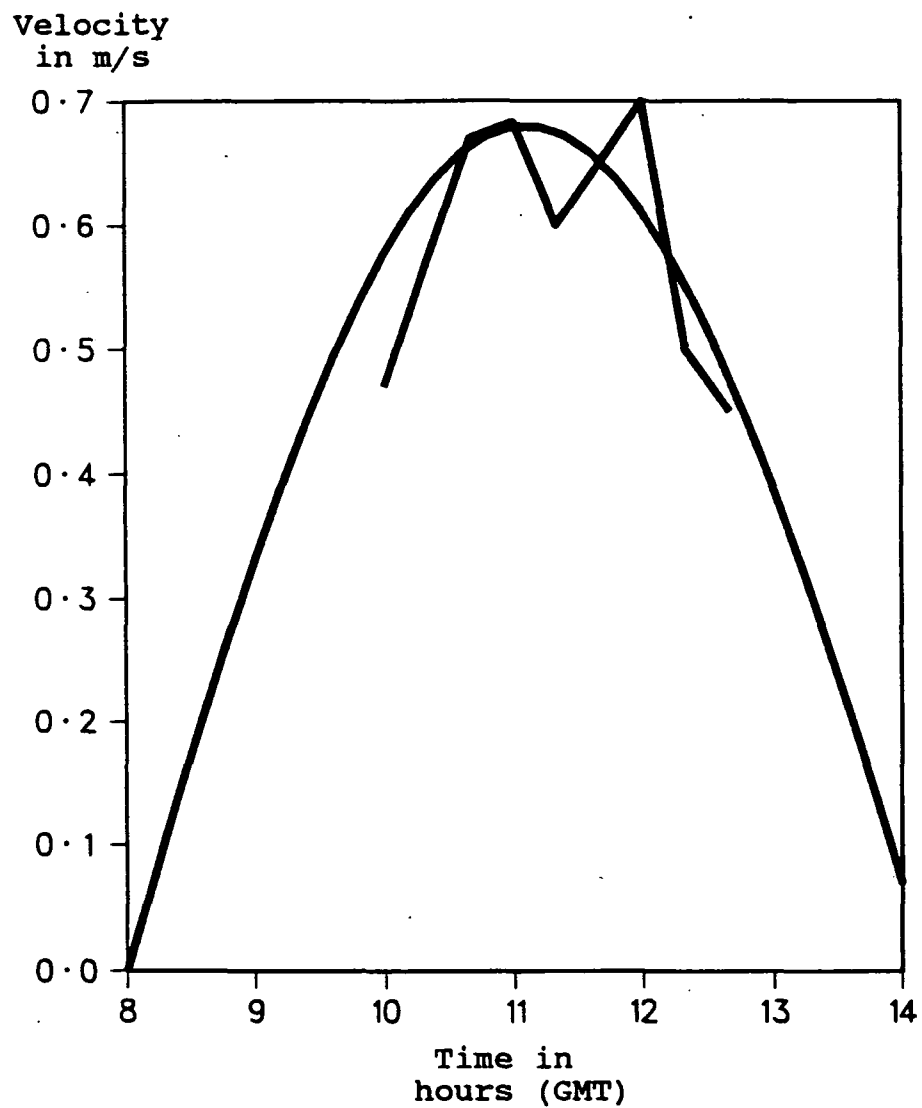


Figure 8.11: The magnitude of the depth averaged velocity, measured at "45" on 15 November 1989, and the sinusoidal approximation used in the model.

pression. In doing so the wave amplitude is attenuated and the wavelength increases considerably. Unlike the neap case, there is relatively rapid growth in wave height with time, and a large wave height (near the level of the maximum) is maintained for a larger portion of the tidal stream. There is a more pronounced nonlinear response in the wave growth, than in the neap case.

Qualitatively this matches the observations, up to 11:00. After this the wave was observed to break via a hydraulic jump. Runaway growth in U or η is not observed in any of the numerical simulations. In each case a wave is formed which is allowed to evolve and propagate upstream, as in the conceptual model of Maxworthy (1979). Therefore only the observed wave height is discussed below in relation to the model results.

8.2.3 Results and comparison

There are not enough clear observations to make a direct comparison of interfacial position between the model and the echograms. Instead, it is more rewarding to concentrate on the wave height. From the echograms the wave heights have been measured at twenty minute intervals, from 10:00 to 11:00. There is a 20% error in these measurements. The modelled wave heights are depicted in figures 8.12 (sine forcing) and 8.13 (real forcing) with the observations. The model results for $\frac{\Delta\rho}{\rho} = 0.003, 0.006, 0.008$ are shown. It is important to note that the two layer approximation became less appropriate during the period of observations. At 10:00 and 10:20 $\frac{\Delta\rho}{\rho} = 0.006$, at 10:40 $\frac{\Delta\rho}{\rho} = 0.003$ and at 11:00 $\frac{\Delta\rho}{\rho} = 0.0025$. The observations show that a wave grew on a thermocline whose structure itself was evolving.

Maximum
thermocline
displacement
in metres

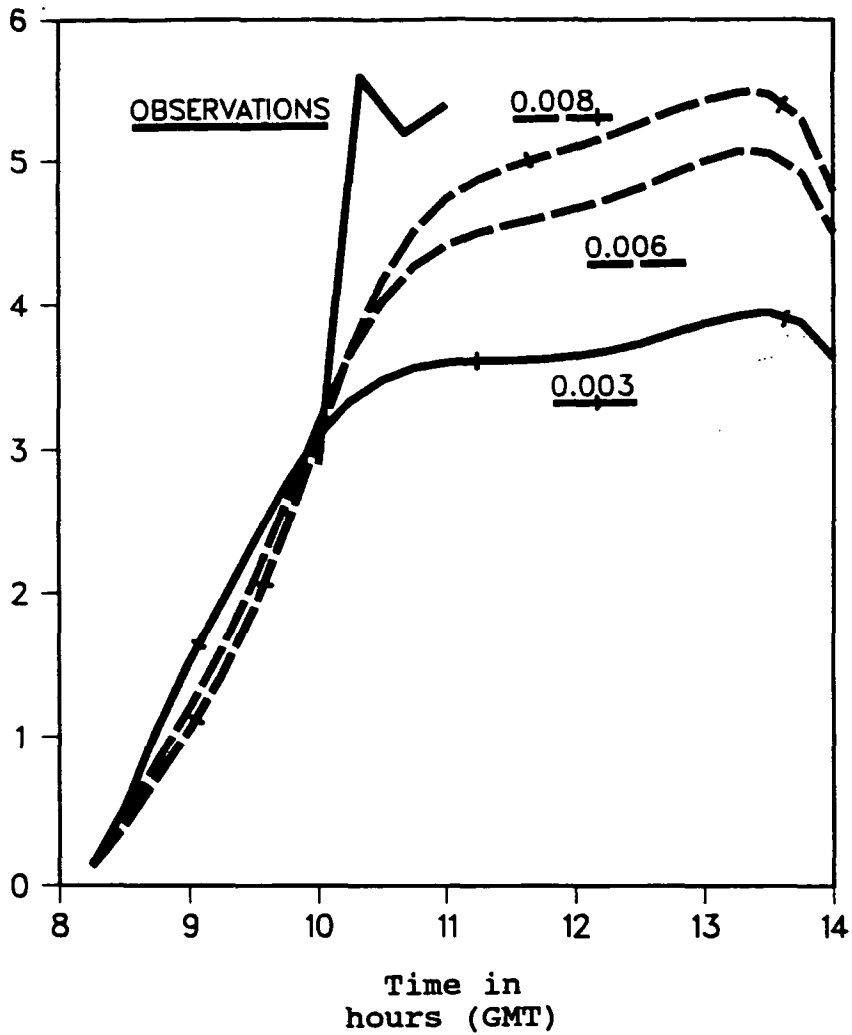


Figure 8.12: Observed maximum thermocline displacement on 15 November 1989, together with the predictions from the model in the sine forcing mode.

Maximum
thermocline
displacement
in metres

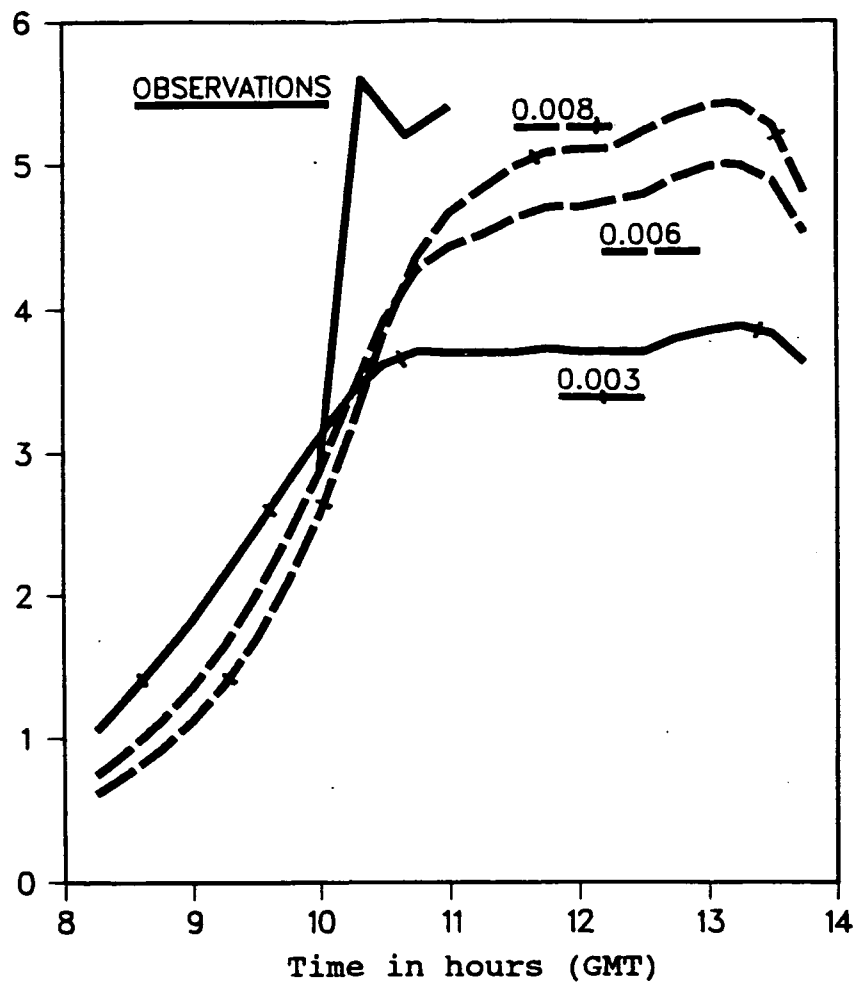


Figure 8.13: Observed maximum thermocline displacement on 15 November 1989, together with the predictions from the model in the real forcing mode.

Figure 8.12 shows that the observed wave grew rapidly from high water to a height of about $3m$ at 10:00 ($\frac{\delta\eta_0}{\delta t} \simeq 1\text{hour}^{-1}$), then to $5.6m$ at 10:20 ($\frac{\delta\eta_0}{\delta t} \simeq 8\text{hour}^{-1}$), $5.2m$ at 10:40 and finally $5.4m$ at 11:00 - the time of the first maximum in the ebb stream. Nonlinear steepening and growth of the wave in the decreasing stream after 11:00 may have caused the wave to interact with the bed and break. The results from the model with sine forcing show a rapid growth in wave height from the time of zero stream, 08:00. The lower values of $\frac{\Delta\rho}{\rho}$ give the most rapid initial growth in wave height, but the larger values of $\frac{\Delta\rho}{\rho}$ lead to the largest maximum wave heights. The time at which all values of $\frac{\Delta\rho}{\rho}$ produced the same wave height is about 10:00. $\frac{\Delta\rho}{\rho} = 0.008$ provides the best overall fit to the observations, by producing a maximum wave height of $5.5m$. Unlike the neap case the model produces rapid wave growth early in the tidal stream. At 10:00 all values of $\frac{\Delta\rho}{\rho}$ give realistic values of η_0 . From 10:00 to 11:00 the model does not match the observed growth in η_0 , for any $\frac{\Delta\rho}{\rho}$. Again excessive attenuation in the model is believed to retard rapid growth, and presumably removes any tendency to runaway growth in U or η .

Figure 8.13 depicts the observations and model results with real tidal forcing. This forcing mode gives similar predictions for the wave heights after 09:00.

For both forcing modes, the same problem with attenuation, as occurred in the neap model, is in evidence after 10:00. At the maxima in the tidal stream, and after, the model indicates that nonlinear steepening is again an important feature. In particular there is sustained and gradual wave growth

from 10:30 to 13:30.

8.2.4 Summary

In this spring tide configuration the model is able to reproduce the observed behaviour well up to the time when the wave was observed to break. The rapid early growth of the wave in particular is included in the predictions. The observations are equally well reproduced by both barotropic forcing modes. In both forcing modes $\frac{\Delta\rho}{\rho} = 0.008$ predicts the nearest η_m to that observed, even though in reality the maximum height was associated with smaller values of $\frac{\Delta\rho}{\rho}$. The effect achieved by having a wave grow on a thermocline of large and time dependent density difference, cannot be replicated in the present model.

The non-dimensional variables which characterise the model, for the sine forcing mode, were $\frac{h_1}{H} = 0.5$, and:

- $\frac{\Delta\rho}{\rho} = 0.003$, $F' = 0.25$, $S = 0.15$, $R = 0.083$, giving $\frac{\eta_m}{H} = 0.99$.
- $\frac{\Delta\rho}{\rho} = 0.006$, $F' = 0.51$, $S = 0.15$, $R = 0.083$, giving $\frac{\eta_m}{H} = 1.27$.
- $\frac{\Delta\rho}{\rho} = 0.008$, $F' = 0.68$, $S = 0.15$, $R = 0.083$, giving $\frac{\eta_m}{H} = 1.37$.

These non-dimensional variables were not represented in the earlier analyses. However, with $\frac{h_1}{H} = 0.5$ and such small values of F' and S , the large maximum wave heights produced are hardly surprising. The model does not produce, in these configurations, any double wave maxima with time, or failure through runaway growth in η or U .

8.3 Conclusions

8.3.1 Neap tide

The model is able to predict the observed second maximum in wave height and energy, wave trough position and the location of most intense shear. It is unable to reproduce the observed first maximum in wave height and energy. The reason for this is the models inability to produce rapid growth in wave height, especially at low barotropic tidal flow.

8.3.2 Spring tide

The model is able to predict the observed rapid growth in wave height up to 10:00, but fails to match the more rapid growth after 10:00. The observed maximum wave height is reproduced when the assumption $\frac{\Delta\rho}{\rho} = 0.008$ is made.

8.3.3 Strengths and Deficiencies

This model is a first order numerical model. The intention was that it should provide a first attempt at reproducing the hydrodynamic behaviour at Cargreen, by treating the estuary as a simple hydraulic channel, enclosing a two layer fluid.

This model was chosen because of its success in reproducing internal tides at the larger scales of the continental shelf-break region (Pingree et al., 1983; Heathershaw et al., 1987). It is also successful in this Tamar configuration, in that it predicts the gross behaviour of the internal density

interface well, under two extremely different conditions.

The two most obvious successes are the prediction of maximum wave heights and the position of the region of most intense shear (at neaps). The two most obvious inadequacies are the failure to reproduce rapid growth in wave heights and the wave breaking at springs (although these can be viewed as part of the same problem).

The parameterisation of diffusive attenuation is highlighted as being particularly weak. This should be no surprise. At the small scales of the Tamar Estuary at Cargreen, with its extremely nonlinear baroclinic behaviour, and small scale but vigorous mixing mechanisms, there is no physical justification for using (KU_{xx}) , with constant K , to represent turbulent diffusion. More realistic behaviour might be achieved by assuming a relationship between K and U , for example, or as some authors have suggested, a Richardson number dependency on K (Hamilton & Rattray, 1978). Wilmott & Edwards (1987) suggest making K a function of x thus linking the degree of diffusive attenuation to topography. As yet there is no physical justification for any parameterisation of diffusive attenuation.

The numerical model described in Chapter 7 is based on the nonlinear finite amplitude shallow water equations. These equations have depth integrated velocity and pressure variations and are thus hydrostatic. Frequency dispersive effects are not included in these equations. (Frequency dispersion describes the effect of different frequency components moving with different phase speeds). Some authors (e.g. Lee & Beardsley, 1974; Lighthill, 1978; and Baines, 1982) have suggested that the important physics, in rapid wave

growth and evolution, is a balance between nonlinear steepening (amplitude dispersion) and frequency dispersion. Equations such as the Korteweg-de Vries equation and the Boussinesq equations include frequency dispersion, with a term which has the form of (\bar{u}_{xxt}) , where \bar{u} is a depth integrated layer velocity (Whitham, 1974).

Frequency dispersion is not likely to have a large role at the beginning of wave development, while it has small amplitude and is not steepened. So, nonlinear growth and steepening may be initially rapid. As a wave steepens the dispersive effect will increase and eventually may balance the steepening, (as well as other effects, such as diffusion and dissipation). In the present model the balance is between diffusion and nonlinear steepening alone. The inclusion of frequency dispersion may have the effect of producing more realistic behaviour in wave growth.

Future extensions to this model may be the inclusion of dispersive effects, a new formulation for diffusion, and the specification of more realistic topography.

Future models might also need to include some or all of the following: 3-dimensional topography and vertical and lateral variations in velocity and density, a more realistic thermocline (i.e. finite thickness), a scheme for introducing buoyancy, tidal range, and vertical diffusion of density.

The addition of tidal range in the model by having either (a) a rigid surface which rises and falls sinusoidally in parallel with the oscillating barotropic tide, or (b) a rigid surface which oscillates vertically, and in so doing drives a barotropic current through a pressure gradient, might be

an interesting future extension to the equations and model used here. For simplicity these effects were not included in the current model, but the data suggest that they may be important, especially at spring tides.

Chapter 9

Discussion

9.1 Observations

9.1.1 Neap tide study

The observations made on 6 November 1989 depicted the formation and evolution of an internal wave, through the interaction of the stratified tidal flow of the Tamar with the bed depression at Cargreen. The variability in the ebb stream had a profound effect on the wave height, causing nonlinear steepening and wave growth twice in the slackening ebb, after a maximum in seaward velocity had passed. The generation mechanism was essentially the same as that proposed by the Maxworthy (1979) conceptual model described in Chapter 4, and similar to the many observations of internal wave formation on the shelf edge, in fjords and in estuaries, described in Chapter 2.

The wave did not propagate far upstream in the observation period, as

may have been expected. Rather, the wave maintained a position over the landward slope of the bed depression, dissipating energy through enhanced turbulent diffusion along the length of the thermocline, but mostly at the trough and in its seaward end. The most similar large scale topographic feature to this, Hudson Canyon (Hotchkiss & Wunsch, 1982), also seems to concentrate internal wave energy dissipation at the head of the landward slope.

The maximum internal wave energy density during the study period was 220 kJm^{-1} , along the trough length. This accounted for $10(\pm 2.5)\%$ of the energy density of the barotropic tide. This is in good agreement with estimates for the shelf edge (see Chapter 2, Section 2.1). At stations "VA" and "RH" internal wave induced mixing was observed to increase the potential energy of the water column by 44 Jm^{-2} in 2 hours. The loss of internal wave energy density at the same time was 170 Jm^{-2} . The efficiency of conversion of internal wave energy to potential energy, was then $26(\pm 6)\%$. This estimate is in excellent agreement with those obtained from laboratory and theoretical studies, presented in table 2.2. The rate of internal wave energy dissipation was 170 Jm^{-2} in 2 hours, or $\sim 2.4 \times 10^{-2} \text{ Wm}^{-2}$. This estimate is in good agreement with the estimates from the shelf edge, presented in table 2.1. The efficiency of transfer from barotropic tidal energy density to increased potential energy density was 2% to 3.3%. This is about half of the average 5.6% transfer quoted by Stigebrandt & Aure (1989), (see Chapter 2, Section 2.3), for Norwegian fjords.

These estimates, which the author believes to be the first of their kind

for an estuary, indicate that the internal wave observed on 6 November 1989 had the same essential hydrodynamic behaviour as internal tides at the shelf edge and in fjords. Although of a smaller scale, it appeared to extract energy from the barotropic tide and dissipate energy to mixing at the same rate as internal tides on the shelf edge. The 6 November 1989 internal wave does not seem comparable to fjord internal tides in this respect. The reason for this may lie in the very different stratification, topography and tidal range of the fjord environment. More estimates are required in estuaries for a fairer comparison.

The internal wave induced mixing was only evident for 2 to 3 hours during the ebb stream. This phenomenon must be regarded as an intermittent contributor to mixing, but its longevity was remarkable. The mean depth averaged water speed from 14:45 to 16:45 was 0.4ms^{-1} . Thus, $\sim 3\text{km}$ of the estuary might have been affected by this enhanced mixing event.

9.1.2 Spring tide study

Initially the response of the thermocline to the tidal forcing over the Car-green bed depression, on 15 November 1989, was similar to that of the neap tide study - a wave grew on the thermocline over the landward slope of the bed depression. However, in a rapidly increasing ebb stream and decreasing stratification, the wave grew until it interacted with the bed. In the slackening flow, after the first maximum in the ebb stream, the wave grew in amplitude through nonlinear steepening, perhaps causing the observed hydraulic jump. Hydraulic jumps have similarly been observed in fjords and

estuaries (see Chapter 2, Sections 2.3, 2.4). The maximum energy density of the internal wave, although not fully developed, was, before breaking *in situ*, $320(\pm 96)kJm^{-1}$, along the trough length. Compared to the barotropic tidal energy density, this represents a conversion efficiency of 2.5% to 5%. This is much less than in the neap tide case. It has been observed in fjords that internal hydraulic jumps are relatively inefficient in extracting energy from the barotropic tide compared to internal waves (see Chapter 2, Section 2.3, e.g. Stacey, 1985). Presumably this is because hydraulic jumps are waves which break *in situ*, unable to propagate upstream into a strong and increasing flow.

There was no estimate of the transfer of energy density to mixing on this occasion. The action of the strong tidal stream, and associated shear produced at the bed, led to destratification throughout the middle and upper Tamar. The relative contribution to mixing from this internal wave/hydraulic jump might therefore have been small.

9.1.3 Summary and future directions

The observations (presented in Chapters 4,5 and 6) show that there are a variety of hydrodynamic responses possible at the Cargreen bed depression. The main difference between the neap and spring observations was that in one case (neap) a waveform was sustained over the depression during the whole of the study period, thus allowing for the possibility of continued extraction of energy from the barotropic tide, for mixing, while in the other case (spring) a waveform was not sustainable, because of the strong tidal

flow. As described in Chapter 2, Section 2.4, Dyer & New (1986) found a similar qualitative difference in hydrodynamic behaviour in the Test Estuary, between a neap and spring tide.

Neap-spring modulations in stratification are common in estuaries (Haas, 1977; Griffin & LeBlond, 1990) and the baroclinic response of an estuary must vary as a result. To what extent internal waves and hydraulic jumps contribute to these neap-spring modulations is as yet not known, but in the case of neap tides, it may be that they make a larger relative contribution to local mixing. From only a few data sets it is hard to generalise.

The 16 November 1987 and 30 November 1987 studies, both neap tides, yielded estimates of the conversion efficiency of barotropic tidal energy density to internal wave energy density. These were 8% to 10% and 7% to 10%, respectively, again in good agreement with the shelf edge estimates.

The 19 April 1989 observations highlighted what may be an important process, and a possible future direction for estuarine research. The billows detected by the echosounder were of height 1 – 1.5m and length $\sim 10m$. The potential for mixing of these overturning instabilities may be high. Their presence on the thermocline, shown by many of the echograms in Chapter 4, suggests that they play some transitional role in the development of internal shear driven turbulence and mixing (Thorpe, 1987a).

The 30 November 1987 observations show that solitary wave formation, by fission from an initial lee wave, is possible, and may also play a transitional role. This further shows that dispersion may be an important part of the physics in lee wave development.

The analysis performed in Chapter 6 attempts to unify some of the observed phenomena, in terms of an internal Froude number, F_i . The suggestion is made that a critical value of $F_i = 2 - 3$ is appropriate, for the depression at Cargreen. Knowledge of variations in F_i , in the neap-spring cycle, would allow estimates to be made of the varying importance of internal wave induced mixing, for a particular stretch of estuary, associated with a topographic feature. Performing such an analysis for all the topography in an estuary would perhaps yield an estimate for the overall importance of these phenomena. How often F_i will exceed the critical value, thus allowing waves to break *in situ*, depends on stratification and the magnitude of the tidal velocities, which in turn affect stratification. (The amplitude of the depth averaged speed is typically 0.5ms^{-1} at neaps and 0.8ms^{-1} at springs). At present there is not sufficient data to estimate how often F_i exceeds the critical value at Cargreen. As Thorpe (1987a) points out, there is the ...

... fundamental difficulty of estimating the probability of conditions favoring the development of any particular kind of instability.

More measurements of individual wave events have to be made to confirm the critical value of F_i , perhaps mid way between neaps and springs, and more estimates of energy conversion efficiencies need to be made, to add to the very encouraging results presented here.

The Tamar Estuary has over 20 topographic pits and ridges (George, 1975), which may be capable of interacting with the flow, to produce intense

mixing, in stratified conditions. Given that the distances between them are of order less than the tidal excursion, it is conceivable that on a flood or ebb stream, conducive to wave formation, nearly the whole stratified portion of the estuary may be affected by enhanced mixing.

The survey method adapted for this research has worked well. In particular, the Estuarine Thermistor Spar developed for this purpose, has proved invaluable. However, there are refinements that could be made in making future observations. More landward and seaward coverage of the waves, if possible, would give better estimates of energy, the undisturbed level of the thermocline, and the exact location of maximum shear and onset of vigorous mixing. Making velocity shear measurements on the longitudinal transects would provide essential additional information on Richardson number variations across and in the thermocline.

The phenomena observed so far at Cargreen have had considerable 3-D structure. Future fieldwork may include an examination of transverse effects, flood streams, other topographic features (e.g. Beggars Island depression), the tides between neaps and springs, and eventually other estuaries.

9.2 Modelling

9.2.1 Neap tide study

For the neap tide study the numerical model is able to predict successfully the maximum wave height and energy, and position of the wave trough. The predicted position of maximum shear is in agreement with the observed

location of the onset of vigorous vertical mixing. The observed behaviour of the wave height with time is explainable in terms of variations in the depth averaged tidal velocity. The double maximum in wave height is not reproduced in the model and this is thought to be due to the particular parameterisation of diffusive attenuation, (KU_{xx}) , where K is held constant. Diffusive attenuation may be equally as strong at low and high tidal streams, which is probably not physically justifiable.

9.2.2 Spring tide study

In the spring tide study the model is able to predict the observed behaviour of the wave height more successfully than in the neap case. The rapid early growth of the wave is clearly predicted, but the subsequent steepening and more rapid growth, after which the wave was observed to be in contact with the bed, is not reproduced. Diffusive attenuation is again indicated as being particularly weak. The observed wave broke *in situ* in the form of a hydraulic jump and the model is unable to simulate this realistically, again due to the inclusion of (KU_{xx}) as the diffusive term.

9.2.3 Summary and future directions

To first order the model is successful at predicting maximum wave heights and energies. The latter was the primary aim of the modelling exercise. To be able to predict the maximum total internal wave energy density, associated with any topography, layer geometry, stratification and tidal stream, now seems possible, to first order. (How that energy is dissipated and dis-

tributed through mixing cannot be predicted by this model). This may be a useful tool for modellers of estuary circulation, who wish to estimate the energy associated with internal waves generated at any individual topographic feature. The secondary aims of the modelling, namely the reproduction of the more subtle observed behaviour, the wave trough position, wavelength, nonlinear steepening etc., have not been fully achieved.

The problems encountered by using a constant coefficient of diffusion, K , might have been overcome by a different parameterisation, (see Chapter 8, Section 8.3.3), but these are often not justifiable in physical terms. For a first order model the simple approach is the most appropriate.

The inclusion of dispersion to balance nonlinear steepening may be the most interesting extension to the model equations. This may allow solitary wave formation (given a small enough grid spacing, Δx) and wave "breaking" - in model terms a runaway growth in η or U for realistic forcing conditions.

In future models the 3-D nature of the flow must be taken into account.

9.3 Implications for estuarine circulation

The flow over the depression at Cargreen has proved capable of generating vigorous mixing for at least 2 - 3 hours, during an ebb stream, on a neap tide. Presumably this may also be possible on a flood stream. On a spring tide the estuary destratified, through the action of the tidal stream and bottom shears, and mixing from internal waves was not observed. The Tamar has

many bed depressions and ridges, and under stratified conditions may be prone to mixing and partial destratification, via internal wave mixing. A transfer of barotropic tidal energy to increased potential energy, via internal waves, is almost certainly not included in current models of the Tamar, or other estuaries.

9.3.1 Comparison with externally generated mixing

Externally generated mixing, resulting from large shears, primarily arising from the interaction of tidal velocities with the bed, dominates the vertical turbulent salt flux in well mixed and partially mixed estuaries. A comparison between bottom generated mixing and internal wave mixing, establishes the relative importance of the latter in estuarine circulation. A precise calculation of the rate of energy dissipated by the barotropic tide by frictional drag of the bed, E_F , is not possible for any of the data collected so far. However, an estimate can be made by making two assumptions: (i) the depth averaged barotropic tide is sinusoidal with amplitude u_0 , (ii) the friction at the bed can be characterised by a constant drag coefficient, C_D . The rate of energy dissipation to turbulence is (Pugh, 1987)

$$E_F = \frac{4}{3\pi} C_D \rho u_0^3 \quad (9.1)$$

per unit area. C_D , the drag coefficient, is assumed to be $\sim 2 \times 10^{-3}$ (e.g. Holloway, 1987; Sandstrom & Elliott, 1984), and ρ is the mean water density. For the neap tide study (6 November 1989), where $\rho = 1014 \text{ kg m}^{-3}$ and

$u_0 = 0.5ms^{-1}$, the barotropic tidal dissipation rate, to friction, is $E_F = 0.11Wm^{-2}$. The energy density associated with the barotropic tide (see Chapter 4, Section 4.6), $8.4kJm^{-2}$, is presumed dissipated in 12.4 hours, representing a total dissipation rate of $0.19Wm^{-2}$. The portion of the total tidal energy dissipated through friction with the bed is 58%. The portion estimated to be converted to internal wave energy density is 10%. Thus internal waves produced over topography are probably not the primary sink for tidal energy in this environment, but are still significant.

For the observed spring conditions (Chapter 5, Section 5.4), $u_0 = 0.68ms^{-1}$, $\rho = 1016kgm^{-3}$ and $E_F = 0.64Wm^{-2}$. The tidally averaged total barotropic tidal dissipation rate is estimated to be $0.78Wm^{-2}$. The ratio of the tidal energy dissipation rate, caused by frictional drag, to the total dissipation rate, is 82%. It is thought that the internal wave, and subsequent hydraulic jump, accounted for little of the barotropic tidal energy (certainly relatively less than in the neap case). The above analysis indicates, that in the spring tide example, dissipation by interaction of the tide with the bed was the dominant process, and was relatively more important than in the neap case. The Tamar at Cargreen was destined to destratification by externally generated mixing, and any mixing arising from baroclinic motions was probably far less than that from bed generated shear.

9.3.2 The final word

It is intuitive that stratified flow over estuary bed topography should lead to increased mixing. This thesis provides estimates that show the energy

transfer from the barotropic tide to mixing, via internal waves, may be more important than previously assumed.

The current wisdom in 1983 was summarised by the Natural Environment Research Council (NERC, 1983) in the following words:

By using the largest available computers, models employing up to 10^5 grid points can be developed. With, say, 10 vertical layers a horizontal resolution of 200×50 grid boxes is therefore possible, representing a resolution of less than 1 km for UK estuaries. With this level of resolution the dependence on empirical coefficients is minimised and a realistic simulation should be achieved of most significant processes with the exception of wind waves, internal waves and fronts.

For meso-tidal or macro-tidal stratified estuaries with irregular topography, intermittent internal wave induced mixing may be an important process, whose effects are currently being aliased or underestimated. Many more estimates need to be made, especially of the difference in the neap-spring response, so that models can incorporate these effects, perhaps as a sub-grid scale process.

References

Abraham G., 1980, "On internally generated estuarine turbulence." in Proceedings of the 2nd I. A. H. R. International Symposium on Stratified flows, Trondheim 344-353.

Admiralty Tide Tables, 1987, "Vol. 1: European Waters including Mediterranean Sea." The Hydrographer of the Navy.

Admiralty Tide Tables, 1989, "Vol. 1: European Waters including Mediterranean Sea." The Hydrographer of the Navy.

Admiralty Tide Tables, 1990. "Vol 1: European Waters including Mediterranean Sea." The Hydrographer of the Navy.

Baines P. G., 1982, "On internal tide generation models." Deep Sea Research 29, 307.

Blackford B. L., 1978, "On the generation of internal waves by tidal flow over a sill - a possible nonlinear mechanism." Journal of Marine Research 36,529.

Blackford B. L., 1984, "Effect of a tidal stream on internal wave observations and predictions." Atmospheres and Oceans 22,125.

Chereskin T. K., 1983, "Generation of internal waves in Massachusetts Bay." Journal of Geophysical Research 88,2649-2661.

Djordjevic V. D., Redekopp L. G., 1978, "The fissional disintegration of internal solitary waves moving over 2-D topography." Journal of Physical

Oceanography 8,1016-1024.

Dyer K. R., 1973, "Estuaries: a physical introduction."
J. Wiley & Sons Ltd. pp140.

Dyer K. R., New A. L., 1986, "Intermittency in Estuarine Mixing." in "Estuarine Variability" Proceedings of the Eighth Biennial International Estuarine Research Conference, University of New Hampshire, Durham, July 28 - August 2, 1985. pp509, ed. Wolfe D. A. 321-339. Academic Press, Inc.

Farmer D. M., 1983, "Stratified flow over sills." in "Coastal Oceanography" Proceedings of a NATO Advanced Research Institute Workshop on Coastal Oceanography, June 6 - 11, 1982, Oslo, Norway,
ed. Gade H. G. et al. 337-362, Plenum Press (New York). pp582.

Farmer D. M., Denton R. A., 1985, "Hydraulic control of flow over the sill in Observatory Inlet." *Journal of Geophysical Research* 90,9051.

Farmer D. M., Freeland H. J., 1983, "The physical oceanography of fjords." *Progress in Oceanography* 12,147-219.

Farmer D. M., Smith J. D., 1978, "Nonlinear internal waves in a Fjord." in "Hydrodynamics of Estuaries and Fjords." ed. Nihoul J. C. J. Elsevier Oceanography Series 23, Elsevier (Amsterdam).

Farmer D. M., Smith J. D., 1980, "Tidal interaction of stratified flow with a sill in Knight Inlet." *Deep Sea Research* 27,239-254.

Fischer H.B., List E. J., Koh R. C. Y., Imberger J., Brooks N. H., 1979, "Mixing in Inland and Coastal Waters." Academic Press (New York) pp483.

Fu L. L., Holt B., 1984, "Internal waves in the Gulf of California; observations from a spaceborne radar." *Journal of Geophysical Research* 89,2053.

Gardner G. B., 1984, "Internal hydraulics and mixing in highly stratified estuaries." PhD Thesis, University of Washington pp241.

Gardner G. B., Smith J. D., 1978, "Turbulent mixing in a salt wedge estuary." in "Hydraulics of Estuaries and Fjords." ed. Nihoul J. C. J. Elsevier Oceanography Series 23, Elsevier (Amsterdam). 79-106.

Gargett A. E., 1976, "Generation of internal waves in the Strait of Georgia, British Columbia." *Deep Sea Research* 23,17-32.

George K. J., 1975, "Tides and tidal streams in the Tamar Estuary." PhD. Thesis, University of London.

George K. J., 1979, "Tides in the Tamar." *Tamar Magazine* Vol 2,6-20.

Griffin D. A., LeBlond P. H., 1990, "Estuary/Ocean exchange controlled by spring-neap tidal mixing." *Estuarine, Coastal and Shelf Science* 30,275-297.

Haas L. W., 1977, "The effect of the spring-neap tidal cycle on the vertical structure of the James, York and Rappahannock Rivers, Virginia, U.S.A." *Estuarine, Coastal and Shelf Science* 5,485-496.

Halpern D., 1971a, "Semi-diurnal internal tides in Massachusetts Bay." *Journal of Geophysical Research* 76,6573.

Halpern D., 1971b, "Observations on short-period internal waves in Massachusetts Bay." *Journal of Marine Research* 29,116-132.

Hamilton P., Rattray M., 1978, "A numerical model of the depth dependent wind-driven upwelling circulation on a continental shelf." *Journal of Physical Oceanography* 8,437-457.

Haury L. R., Briscoe M. G., Orr M. H., 1979, "Tidally generated internal wave packets in Massachusetts Bay." *Nature* 278,312-317.

Heathershaw A. D., New A. L., Edwards P. D., 1987, "Internal tides and sediment transport at the shelf break in the Celtic Sea." *Continental Shelf Research* 7,485-517.

Hibiya T., 1986, "Generation mechanism of internal waves by tidal flow over a sill." *Journal of Geophysical Research* 91,7697-7708.

Hibiya T., 1988, "The generation of internal waves by tidal flow over Stellwagen Bank." *Journal of Geophysical Research* 93(C1),533-542.

Hirsch C., 1988, "Numerical computation of internal & external flows." Wiley Interscience series in numerical methods in engineering; 1.

Vol 1: Fundamentals of numerical discretization. J. Wiley & Sons Ltd. pp515.

Holligan P. M., Pingree R. D., Mardell G. T., 1985, "Oceanic solitons, nutrient pulses and phytoplankton growth." *Nature* 314,348.

Holloway P. E., 1987, "Internal hydraulic jumps and solitons at a shelf break region on the Australian North West Shelf." *Journal of Geophysical Research* 92,C5,5405-5416.

Holloway P. E., 1988, "Climatology of internal tides at a shelf break location on the Australian N. W. shelf." *Australian Journal of Marine and Freshwater Research* 39(1),1-18.

Hotchkiss F. S., Wunsch W., 1982, "Internal waves in Hudson Canyon with possible geological implications." *Deep Sea Research* 29A,415.

Huthnance J. M., 1981, "Waves and currents near the continental shelf edge." *Progress in Oceanography* 10,193.

Huthnance J. M., 1989, "Internal tides and waves near the continental shelf edge." *Geophysical and Astrophysical Fluid Dynamics* 48,81-106.

Imberger J., 1987, "Introduction to papers from the IUTAM symposium on mixing in stratified fluids." *Journal of Geophysical Research* 92,C5,5229.

Koop C. G., 1976, "Instability and turbulence in a stratified shear layer." NSF and ONR Report, Dept. of Aerospace Engineering, University of Southern California pp134.

Lambeck K., 1988, "Geophysical Geodesy." Clarendon (Oxford).

Lansing F. S., Maxworthy T., 1984, "On the generation and evolution of internal waves." *Journal of Fluid Mechanics* 145,127-149.

Lee C., Beardsley R. C., 1974, "The generation of long nonlinear internal waves in a weakly stratified shear flow." *Journal of Geophysical Research* 79,3,453-462.

Lee J. D., Su C. H., 1977, "A numerical method for stratified shear flows

over a long obstacle." *Journal of Geophysical Research* 82(3),420-426.

Lighthill Sir James, 1978, "Waves in Fluids."

Cambridge University Press, pp504.

Long R. R., 1953, "Some aspects of the flow of stratified fluids: I. A theoretical investigation." *Tellus* 5,42-58.

Long R. R., 1954, "Some aspects of the flow of stratified fluids: II. Experiments with a two-fluid system." *Tellus* 6,97-115.

Long R. R., 1955, "Some aspects of the flow of stratified fluids: III. Continuous density gradients." *Tellus* 7,341-357.

Maxworthy T., 1979, "A note on the internal solitary waves produced by tidal flow over a 3-D ridge." *Journal of Geophysical Research* 84,C1-6,338-346.

Maze R., 1987, "Generation and propagation of nonlinear internal waves induced by the tide over a continental slope." *Continental Shelf Research* 7,1079.

McDowell D. M., O'Connor B. A., 1977, "Hydraulic Behaviour of Estuaries." The MacMillan Press Ltd. (London) pp292.

McEwan A. D., 1983a, "The kinematics of stratified mixing through internal wavebreaking." *Journal of Fluid Mechanics* 128,47-57.

McEwan A. D., 1983b, "Internal mixing in stratified fluids." *Journal of Fluid Mechanics* 128,59-80.

NERC, 1983, "Research on Estuarine Processes." Report of a multidisciplinary workshop held at the University of East Anglia, 14-17 Sept 1982, pp31, Natural Environment Research Council.

New A. L., 1988, "Internal tidal mixing in the Bay of Biscay." *Deep Sea Research* 35,5,691-709.

New A. L., Dyer K. R., 1987a, "On the generation of lateral internal waves by a surface seiche in a partially mixed estuary." *Estuarine, Coastal and*

Shelf Science 24,557-566.

New A. L., Dyer K. R., 1987b, "Internal waves and mixing in stratified estuarine flows." in "Proceedings of International Symposium on Physical Processes in Estuaries." ed. Dronkers J., van Leussen W. Noordwijkerhout, The Netherlands, Sept 1986.

New A. L., Dyer K. R., Lewis R. E., 1986, "Predictions of the generation and propagation of internal waves and mixing in a partially stratified estuary." Estuarine, Coastal and Shelf Science 22,199-214.

New A. L., Dyer K. R., Lewis R. E., 1987, "Internal waves and intense mixing periods in a partially stratified estuary." Estuarine, Coastal and Shelf Science 24,15-33.

Nihoul J. C. J. (ed.), 1978, "Hydrodynamics of Estuaries and Fjords." Proceedings of the 9th International Liege Colloquium on Ocean Hydrodynamics, Elsevier Oceanography Series: 23, Elsevier (Amsterdam).

Nihoul J. C. J., Jamart B. M. (eds.), 1987, "3-D Models of Marine and Estuarine Dynamics." Elsevier Oceanography Series: 45, Elsevier (Amsterdam).

Osborn T. R., 1980, "Estimates of the local rate of vertical diffusion from dissipation measurements." Journal of Physical Oceanography 10,83-89.

Osborne A. R., Burch T. L., 1980, "Internal solitons in the Andaman Sea." Science 208,4443,451-460.

Partch E. N., 1981, "Time dependent mixing in a salt wedge estuary." PhD Thesis, University of Washington, 165pp.

Partch E. N., Smith J. D., 1978, "Time dependent mixing in a salt wedge estuary." Estuarine, Coastal and Marine Science 6,3-19.

Phillips O. M., 1977, "The Dynamics of the Upper Ocean." 2nd Ed. Cambridge University Press, pp336.

Pietrzak J. D., Kranenburg C., Abraham G., 1990, "Resonant internal waves in fluid flow." Nature 344,6269,844-847.

Pingree R. D., Griffiths D. K., Mardell G. T., 1983, "The structure of the internal tide at the Celtic Sea shelf break." *Journal of the Marine Biological Association of the U.K.* 64,99-113.

Pingree R. D., Mardell G. T., Holligan P. M., Griffiths D. K., Smithers K., 1982, "Celtic Sea and Armorican current structure and the vertical distributions of temperature and chlorophyll." *Continental Shelf Research* 1,99.

Pond S., Pickard G. L., 1983, "Introductory Dynamical Oceanography." 2nd Ed. Pergamon Press (Oxford), pp329.

Pugh D. T., 1987, "Tides, Surges and Mean Sea-level." J. Wiley & Sons Ltd. (Chichester) pp472.

Sandstrom H., Elliott J. A., 1984, "Internal tide and solitons on the Scotian shelf: A nutrient pump at work." *Journal of Geophysical Research* 89,C4,6415-6426.

Sandstrom H., Elliott J. A., Cochrane N. A., 1989, "Observing groups of solitary internal waves and turbulence with BATFISH and echo-sounder." *Journal of Physical Oceanography* 19,987-997.

Sherwin T. J., 1988, "Analysis of an internal tide observed on the Malin shelf, north of Ireland." *Journal of Physical Oceanography* 18,1035.

Simons J. T., 1980, "Circulation models of lakes and inland seas." *Canadian Bulletin of Fisheries and Aquatic Science* 203,pp146.

Stacey M. W., 1984, "The interaction of tides with the sill of a tidally energetic inlet." *Journal of Physical Oceanography* 14,1105.

Stacey M. W., 1985, "Some aspects of the internal tide in Knight Inlet, British Columbia." *Journal of Physical Oceanography* 15,1652-1661.

Stigebrandt A., 1976, "Vertical diffusion driven by internal waves in a sill fjord." *Journal of Physical Oceanography* 6,486-495.

Stigebrandt A., Aure J., 1989, "Vertical mixing in basin waters of fjords." *Journal of Physical Oceanography* 19,917-926.

Sturley D. R., Dyer K. R., 1990, "The Estuarine Thermistor Spar: an instrument for making thermal profiles in shallow water." *The Hydrographic Journal* 55,Jan 90,13-21.

Thompson R. O. R. Y., 1980, "Efficiency of conversion of kinetic energy to potential energy by a breaking internal wave." *Journal of Geophysical Research* 85,6631-6635.

Thorpe S. A., 1973, "Turbulence in stably stratified fluids: A review of laboratory experiments." *Boundary Layer Meteorology* 5,95-119.

Thorpe S. A., 1975, "The excitation, dissipation and interaction of internal waves in the deep ocean." *Journal of Geophysical Research* 80,328-338.

Thorpe S. A., 1987a, "Transitional phenomena and the development of turbulence in stratified fluids: a review." *Journal of Geophysical Research* 92,C5,5231-5248.

Thorpe S. A., 1987b, "On the reflection of a train of finite amplitude internal waves from a uniform slope." *Journal of Fluid Mechanics* 178,279-302.

Thorpe S. A., Hall A. J., 1977, "Mixing in upper layer of a lake during heating cycle." *Nature* 265,719-722.

Thorpe S. A., Hall A. J., Taylor C., Allen J., 1977, "Billows in Loch Ness." *Deep Sea Research* 24,371-379.

Uncles R. J., Elliott R. C. A., Weston S. A., 1985, "Observed fluxes of water, salt and suspended sediment in a partly mixed estuary." *Estuarine, Coastal and Shelf Science* 20,147-167.

van de Kreeke J., 1986, "Physics of Shallow Estuaries and Bays." *Lecture Notes on Coastal and Estuarine Studies*: 16. Springer-Verlag (Berlin), pp280.

Whitham G. B., 1974, "Linear and Nonlinear Waves." *Pure and Applied Mathematics series* - Wiley Interscience. J. Wiley & Sons Ltd. (New York), pp636.

Wilmott A. J., Edwards P. D., 1987, "A numerical model for the generation of tidally forced nonlinear internal waves over topography." *Continental*

Shelf Research 7,457-484.

Wolfe D. A. (ed.), 1986, "Estuarine Variability." Proceedings of the Eighth Biennial International Estuarine Research Conference, University of New Hampshire, Durham, July 28 - August 2, 1985. pp509.

Woods J. D., 1968, "Wave induced shear instability in the summer thermocline." Journal of Fluid Mechanics 32,4,791-800.

Ziegenbein J., 1969, "Short internal waves in the Strait of Gibraltar." Deep Sea Research 16,479-487.

Appendix I

The following is a copy from a reprint of Sturley & Dyer (1990), referred to in the text, and included in the reference list.

A Paper Reprinted from

**THE
HYDROGRAPHIC
JOURNAL**

No. 55

JANUARY 1990

The Hydrographic Society

**POLYTECHNIC OF EAST LONDON · LONGBRIDGE ROAD · DAGENHAM
ESSEX RM8 2AS · ENGLAND · TELEPHONE: 01-597 1946 · TELEX: 665080**

The Estuarine Thermistor Spar: an instrument for making thermal profiles in shallow water

D. R. Sturley, BSc, MSc.* K. R. Dyer, MSc, PhD*

Abstract

The Estuarine Thermistor Spar arose out of a need to make temperature (and indirectly salinity) measurements in the Tamar Estuary. It consists of a 6m alloy tube to which are attached 16 temperature sensors, at 0.25m intervals. The structure is pushed ahead of a launch to obtain vertical temperature profiles of the thermocline. The instrument is sampled at 10Hz by a computer which stores the data for later analysis. The temperature sensors are thermistors embedded in resin and attached to water tight steel connectors. The thermistor and sensor properties, the circuitry and noise levels have been examined and analysed in order to determine the useful resolution of the instrument. In preliminary tests the resolution has proved to be near the least significant bit of the ADC, namely 0.005°C. The Estuarine Thermistor Spar has proved itself capable of showing rich and interesting structures in the top 4m of the Tamar Estuary.

1. Introduction

Estuaries are often stratified vertically (or horizontally) in terms of salinity, and temperature. On any one occasion it is usual to find a strong correlation between salinity (measured as conductivity) and temperature. If the relationship is known, or can be simply determined, then salinity can be calculated from the measured temperature. The choice of measuring temperature rather than salinity directly was made on the basis of practicality, economy and versatility. It is also hoped that this instrument can be used in other environments, where temperature signals are much more dominant.

In order to measure adequately the temperature structure of estuarine stratification it is necessary to resolve small temperature changes. Typically the temperature may vary from the surface to 4m below by 1°C. A typical vertical temperature gradient might be

$$\frac{\partial T}{\partial Z} = 0.2^\circ \text{C m}^{-1}$$

It is also useful to be able to measure rapid changes in temperature and to measure these changes with small vertical resolution. For example, between two points spaced 0.25m apart there may be a temperature difference of 0.05°C. An instrument must be capable of a resolution much better than this. In the Tamar Estuary internal waves have heights that are typically 1 to 4 metres. To resolve these features well the vertical spacing of measurements must be less than 0.5m. Turbulence events occur on many time scales, and a temporal resolution of one second or less is required to witness some of the smaller events. The simultaneity of these measurements is vital for an understanding of processes involving the breaking of internal waves, and the turbulence and mixing that is produced.

An instrument which fitted these criteria partially was the IOS Towed Thermistor Spar^{1,2}. It was a spar mounted on a

catamaran towed from a moving ship. The spar was fitted with thermistors at approximately 1m intervals, a forward looking sonar and a pressure sensor. The spar was 10m long and was held vertical by a weight at its lower end. This spar provided valuable data on bubble clouds and thermal structure in Loch Ness and in the open ocean, but its suitability for work in shallow water was doubtful, as it was too long and bulky.

The basic design and performance of the IOS spar was sound, however, and in November 1987 it was decided to build a lighter, smaller, more manoeuvrable version for use in estuaries, incorporating innovations appropriate to that environment. The Estuarine Thermistor Spar is only 6m long and has 16 thermistors mounted at 25cm intervals. It can be pushed along in the water attached either at the front or to the side of a medium sized launch, out of the vessels wake.

The design specification for the spar arose out of a set of complementary but sometimes conflicting criteria. The length of the spar was chosen to be 6m as this was felt to be long enough to catch most of the interesting activity in the thermocline, but was not too long to make it unmanoeuvrable in the water when deployed. A sensor spacing of 0.25m is small enough to allow resolution of features like waves, and turbulence arising from them, but not so close as to make the instrument cost prohibitive. Other design specifications also arose out of similar needs for complement and compromise (see later).

2. Physical specification

2.1 Spar and cradle

The spar consists of a 6m length of alloy scaffold tube, of diameter 5cm, with sensor mountings pop rivetted onto one edge such that all sensors point in the same direction. When deployed 2m of the tube are out of the water. The sensors are bolted onto the mountings and the cables which connect to the sensor circuitry and ADC device run along the inside of the spar passing in through small holes in its leading edge and out through the top of the tube. A short length of tube is connected to the spar by a swivel coupler near the bottom to form a crucifix for attachment to the cradle and launch, see Figure 1. The cradle is a continually evolving structure made mostly from alloy scaffold tubes, fittings and nylon ropes, which performs the function of keeping the spar rigidly upright in the water ahead of the wake from the launch, see Figure 2. When the spar is deployed the sensors are protected by means of long sections of plastic pipe which allow water to flow past the sensors freely but protect them from drifting debris and collision damage.

2.2 Connectors

The sensors have stainless steel connectors which house gold plated two pin plugs. The water tight seal is effected by compressible bungs which are expanded in the steel housings

*Institute of Marine Studies, Polytechnic South West, Plymouth, UK.



Fig. 1: The whole spar out of the water showing all 16 sensors



Fig. 2: The spar and cradle on RV Catfish



Fig. 3: The connectors which make a watertight housing for the two pin gold-plated plugs

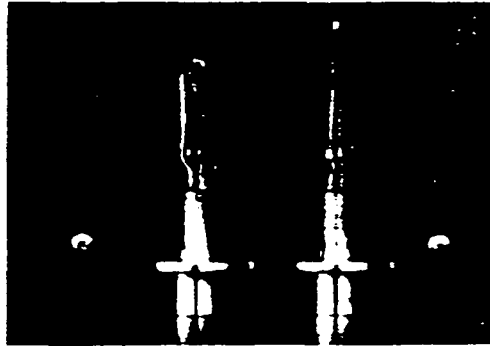


Fig. 4: The thermistors embedded in Epikote resin

when the electrical connection has been made (see Figure 3).

2.3 Sensor construction

The thermistors are embedded in a body of Epikote resin such that their connecting leads are soldered to the male two pin plugs, and their bodies are exposed to the environment. In turn the two pin plugs and the resin mouldings are attached to the stainless steel housings. In this configuration the sensors have an insulation resistance, in sea water, of $10^9 \Omega$ or higher (see Figure 4).

3. Circuitry and components

The variation of resistance with temperature of the chosen thermistors is monitored by conditioning circuits as an

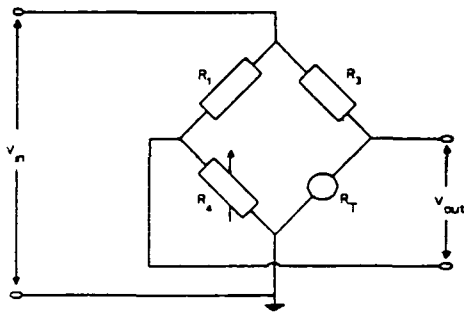


Fig. 5: The Wheatstone bridge which provides a linear relationship between resistance and temperature from the thermistor.

intermediate step to analogue to digital conversion by a microcomputer. The Fenwal Oceanographic sub-mini probe thermistors are each arranged in a Wheatstone bridge, with the other bridge resistances chosen such that the bridge is balanced at 10°C and has a linear relationship between output voltage and temperature (see Figure 5). This relationship was determined by fitting a curve of the form

$$R_T = A e^{(B/T)}$$

to the manufacturers supplied R_T vs T data, see Figure 6. This is the expected relationship between R_T and T for this type of thermistor. The curve fitted exactly at $T = 5.15^\circ\text{C}$, and the fit was to within 0.1% of the quoted R_T values elsewhere in the range $0 - 20^\circ\text{C}$. A, B were determined by simple arithmetic. Having derived the constants A, B the bridge equation

$$\frac{R_T}{R_T + R_1} - \frac{R_4}{R_4 + R_1} = \text{output}$$

was solved assuming that $R_1 = R_2$ and that $R_4 = R_{T-10^\circ\text{C}} = 27642 \Omega$. The bridge equation was solved for a range of values of R_1, R_2 until the best linear relationship of $R_1, R_2 = 15\text{k}\Omega$ was found. In this way the signal from the sensor was made to be essentially linear with temperature, facilitating easy calibration and with little loss in bridge sensitivity, as R_1, R_2 are fairly close to R_T, R_4 in value.

The bridge output has to be amplified before analogue to digital conversion and arranged such that the final conditioned signal ranges from $0 - 1\text{V}$ for the chosen full temperature range $0 - 20^\circ\text{C}$. The complete circuit diagram is

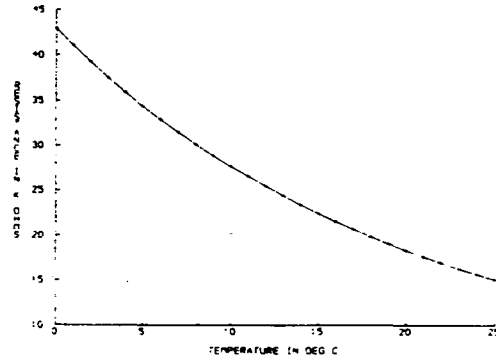


Fig. 6: The manufacturers quoted behaviour of resistance R_T with temperature T

shown in Figure 7. The bridge voltage supply was chosen to be about 0.2V at a low current to minimise noise, (see later). The last stage of the circuit for each thermistor is an active alternate Butterworth filter which passes low frequency signals, but which filters out high frequencies². The cut off frequency is determined using the formula

$$f_c = (2\pi R \sqrt{C_1 C_2})^{-1}$$

Figure 8 shows the filter circuit. The values currently in use are $R = 220\text{k}\Omega$, $C_1 = 0.1\mu\text{f}$, $C_2 = 0.22\mu\text{f}$ giving a cut off



Fig. 7: The conditioning circuit

frequency (-3db frequency) of $f_c = 4.88\text{ Hz}$. The roll off of the filter is -12db per decade, which is adequately sharp, assuming there are few fluctuations due to noise around f_c . The choice of f_c was not arbitrary, but is complementary to the sampling rate of the ADC and prevents aliasing errors.

3.1 Thermistors

The thermistor probes themselves are pairs of glass encapsulated thermistors of high stability (0.05°C change per year maximum). The probes are interchangeable as their R_T vs T curves are supposed to be identical. In practice, however, the whole device will need re-intercalibration after such a change.

The response time of the thermistors (the time taken to respond by $1 - e^{-1}$ of the temperature change applied) and the dissipation constant (the power required to raise the thermistor temperature by 1°C in a specified environment) given by the manufacturers are shown in Table 1. The dissipation constant has a bearing on the noise level of the probes and hence their resolution, as discussed later. The time constant must be taken into consideration when choosing a sampling rate for analogue to digital conversion, and is also linked to f_c .

Preliminary tests have shown the time constant to differ from

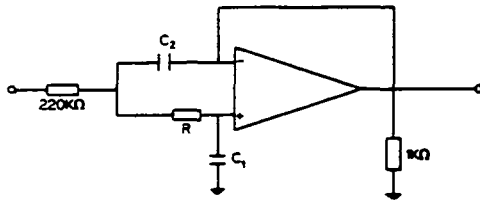


Fig. 8: The anti-aliasing filter stage of the circuit

Environment	Diss. const.	Nominal time const.
Still air	0.6m W°C ⁻¹	2.6s
Moving air	1.6m W°C ⁻¹	1.1s
Still water	6.0m W°C ⁻¹	70ms
Moving water	10.0m W°C ⁻¹	25ms

Table 1: The nominal thermistor properties - supplied by the manufacturer

the manufacturers quoted values. By suddenly immersing the thermistors in cold water from room temperature and sampling their signal at very high frequencies (eg. 1000Hz) it is simple to calculate the $1 - e^{-1}$ time constant. The thermistors tested so far have time constants of 84 - 117ms, before filtering. After the signal passed through the anti-aliasing filter this time constant was increased by between 14% and 58%. This degradation was possibly brought about by the thermistors being partially coated in Epikote resin, but it must also be borne in mind that the quoted values were determined rather crudely, and are thus nominal. Even so this development does not have too serious an effect on the quality of the instruments performance, although the design criteria assumed a time constant lower than that achieved in practise.

The circuits are mounted on etched printed circuit boards and are housed in a 19 inch racked instrumentation case. The cable used to connect the probes to this case is sub-mini co-axial cable of low conductance and high insulation resistance. Extensive decoupling of the circuits has been performed to prevent noise contamination. This decoupling has been mostly performed by connecting a variety of capacitors between the operational amplifiers and the power rails. These capacitors filter out high frequency oscillations selectively (see Figure 9).

4. Digitisation

The sensors and their circuits are attached to an OPUS microcomputer via a MICROLINK 12 bit analogue to digital converter. The 16 sensors are sampled sequentially (but extremely quickly, such that it is effectively simultaneous) and then a time interval elapses before the next sample. This elapsed time can be varied, but the spar and circuitry have been designed on the basis that it should be fixed at 0.1 seconds. The sampling frequency is then 10Hz which implies a Nyquist frequency (-3db cut off frequency) of 5Hz or less to prevent aliasing of high frequency variations into the digitised data³.

One approach in choosing the sampling and Nyquist frequencies is to determine the smallest eddy or turbulence scales that the instrument is likely to detect. If this is equivalent to the thermistor spacing L and the flow past the spar is U then the corresponding eddy time scale is L/U . Currently the assumption is that $L = 0.25m$ and that $U = 0.5 -$

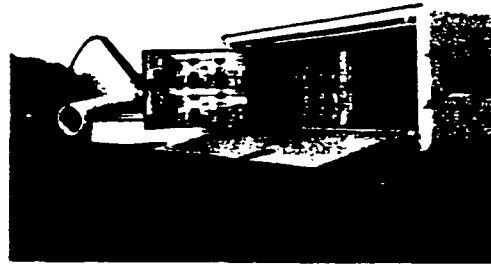


Fig. 9: The complete circuits mounted in a racked case

1.5ms⁻¹ giving motions with effective frequencies in the range 2 - 6Hz. The spar then can be assumed to only need to resolve frequencies of around 6Hz or less, and so a Nyquist frequency of 5Hz is not unreasonable. One other approach is to examine the time constants of the thermistors. These are quoted as being between 70ms and 25ms depending on the speed of the spar through the water. Assuming the slowest time constant (70ms) it takes 280ms (four time constants) for the thermistors to respond to 98% of the temperature change applied. At the fastest time constant (25ms) it takes 100ms to do the same. Thus a Nyquist frequency between 3.6Hz and 10Hz is indicated, with the lower value being the more conservative. Again 5Hz is in agreement with this analysis.

At present the digitisation is restricted to 12 bits, with the maximum number of samples allowed per sensor virtually unrestricted. This means that a voltage in the range of 0 - 1.024V is recorded as an integer number in the range 0 - 4096. For each sensor this is equivalent to a temperature reading which can only be resolved to plus or minus 0.005°C. Digitisation to a 16 bit number (0 - 65536) would greatly improve this accuracy, as would a reduction of the dynamic temperature range, and these might be future objectives, in line with other improvements in noise levels.

The data is stored on the microcomputer for analysis at a later date, but with provision for a cursory inspection immediately.

5. Noise levels and sensor resolution

The resolution of the instrument is a measure of the smallest change in temperature that it can detect. This is intrinsic to the instrument and is a function of the aggregate noise level of the various components of which it is composed and any externally generated noise to which it might be exposed. For most purposes it is safe to assume that the resolution is at the total noise level, as most real signals from the environment will swamp this noise. Noise in the instrument comes from many sources. These sources were carefully considered at the design stage, and are discussed in the following sections.

5.1 Noise and resolution determined by digitisation

The resolution as determined by the least significant bit of the analogue to digital converter is 5m°C. This will prove to be the most restricting limitation on the resolution of the instrument.

5.2 Quantization noise spectrum

There are at least two theories worth considering here. Some authors³ propose that the quantization noise is given by

$$\Phi_q = \frac{\Delta t 2^{-2N} C^2}{6}$$

Δt is the sampling interval, the reciprocal of the sampling frequency, of the ADC, N is the number of bits involved in the conversion and C is the dynamic range of the conversion i.e. the maximum-minimum value of the converted quantity. This quantization noise calculation is another way of treating the 5m°C resolution. So for $C = 1V$, $\Delta t = 0.1s$, and $N = 12$ bits, $\Phi_q = 10^{-9} V^2 Hz^{-1}$. Assuming that Φ_q is flat in the frequency domain and that this domain is 5Hz wide then this is equivalent to a noise level of $7.1 \times 10^{-5} V$ at all frequencies. In temperature signal terms this is 1.42m°C.

This analysis is confirmed by a simpler approach¹ where the RMS value of the quantization error (noise) is given as 0.29 ΔV . In this case ΔV is the value of the converted quantity corresponding to the least significant bit of the digitisation. This is equivalent to a noise level of $7 \times 10^{-5} V$ at all frequencies or 1.4m°C.

5.3 Johnson noise

Johnson noise (thermal noise) has a flat frequency spectrum and is calculated from²:

$$\Phi_j = 4kTR,$$

k is the Boltzmann constant $1.38 \times 10^{-23} J^\circ K^{-1}$, T is the temperature in degrees Kelvin, and R , is some dissipating resistance. It is noise generated in a resistance by electron vibration and energy dissipation as heat. For a 100k Ω resistance at 10°C this noise level is $\Phi_j = 1.6 \times 10^{-15} V^2 Hz^{-1}$. Across a bandwidth of 5Hz this is equivalent to a noise level of 0.09 μV in the circuitry, which in turn is equivalent to a noise level of 1.8 $\mu^\circ C$. The 100k Ω was chosen as it is the largest resistance represented in the conditioning circuitry and so forms an upper limit for noise generated in this way, in the post-amplification stage. In the pre-amplification stage a resistance of the same size will superimpose the same noise level on the smaller bridge signal and will be amplified by a factor of about 15. Thus the effective noise level will then be 30 $\mu^\circ C$. All the resistances in the circuitry will contribute similar, smaller, quantities to the noise level.

The amplifiers and other components will also introduce noise but their effect is felt to be similarly negligible, especially compared to the interference that is often introduced from external sources

5.4 Excess and ventilation noise

Excess noise is noise generated in resistors, thermistors and IC amplifiers in excess of the Johnson noise. There is no fully satisfactory treatment of this noise and its spectrum. The excess noise is poorly quantified but appears to play a large role at low frequencies³.

$$\Phi_e = ki^n f^{-1}$$

i is the dc current through the device, k a constant, n is in the range 1 - 1.5. The same authors have shown that excess noise from an operational amplifier can become comparable to Johnson noise at frequencies lower than 1Hz, and at 10^{-2} Hz can demonstrate a power level 10^2 times higher than the Johnson noise, i.e. the effective noise level at this frequency will be ten times higher than the Johnson noise level. The RMS value of Φ_e is thought to be negligible, due to its f^{-1} behaviour.

Ventilation noise is the change in temperature of the thermistor due to variable cooling by velocity fluctuations in the surrounding fluid. It is possible to examine the temperature change in the thermistor in the worst possible case of energy being dissipated, but not being conducted away from the device. The change in temperature is

$$\Delta T = \frac{P}{c}$$

P is the dissipation power ($\frac{V^2}{R}$), V -voltage across R , R -the thermistor resistance and c is the dissipation constant. For $V = 0.2$ volts, $R = 27k\Omega(10^\circ C)$, and $c = 6mW^\circ C^{-1}$ (see Table 1) we find that $\Delta T = 0.25m^\circ C$. So in this worst possible case the noise is limited to an acceptably low level, and the choice of $V = 0.2$ volts as a bridge voltage was made in line with this theory.

5.5 Noise in practise

The overall noise level and hence the resolution limit of the instrument is formed from some kind of aggregate of the contributions from all the components, and from external sources. The theory presented above, which is really an expression of worst fears at the design stage, predicts that the noisiest "component" will be the digitisation process. In practise noise can emanate from many sources. One source is from the break down of the insulation resistance of the thermistor assemblies leading to electrical leakages. Early results have shown that the spar is slightly noisier in the estuary (sea water is a good conductor) than out of it. Another source of noise is contamination by electrical equipment surrounding the instrument. The navigation system on RV Catfish has proved this well by introducing spurious signals into the data of 8mV magnitude (0.16°C)! By keeping such noise to a minimum it is possible to achieve confidence in the data to within 5m°C, or to the level of the least significant bit.

Estimating the level of the overall noise in the instrument is a subtle task. The most expedient way thought of so far, is to replace one or more of the thermistor assemblies with an identical one which houses a high stability resistor. In this way one receives a constant signal from those sensors (i.e. a constant temperature signal) with fluctuations superimposed which correspond to noise from the various parts of the system. This method has worked well so far, and has allowed noise sources, which would otherwise have gone undetected, to be identified and isolated.

6. Calibration

Calibration has always been and possibly will continue to be a major source of problems when developing instruments of this kind. Because of the need for consistency between sensors the calibration methods have been chosen so that although the sensors may not be accurate in determining absolute temperature, their accuracy relative to each other will be optimised. Their fine resolution plays an important role in this relative accuracy. The calibration is performed in stages.

6.1 Calibration of the conditioning circuitry

The circuits are given as input a fixed resistance corresponding to the thermistor manufacturers quoted value for 0°C. The output is arranged to be $0 \pm 0.0005V$, by balancing the Wheatstone bridge. This fine tuning is achieved by using an accurate digital voltmeter capable of four significant figures, or three decimal places in this context. This "dummy sensor" resistance is then set to the quoted value for 20°C and the amplifier gain is set such that the circuit output is $1 \pm 0.0005V$. In this way the desired linear

temperature and circuit output is achieved with $1^{\circ}\text{C} \cong 0.05\text{V}$. It is believed that the worst error incurred in using this method is about 0.1% in any reading, assuming high accuracy in the volt-meter.

This makes errors in temperature readings due to circuit calibration systematic, and hence more acceptable. Alone this would require the thermistors to behave identically, according to the manufacturers quoted standards. In reality they do not, so a further calibration is required.

6.2 Intercalibration of the sensors

If one makes the assumption that all the thermistors behave with the same shaped R_T vs. T curve, supplied by the manufacturers, but may differ from the ideal by some offset temperature, one can bring all the signals into line by an intercalibration, at a single temperature. By immersing the instrument in an isothermal fluid one can detect differences in the signals and hence allow for them, numerically, when analysing subsequent data. Finding a stable isothermal fluid large enough to accommodate a 6m spar can be an enormous problem. Alan Hall of IOS used the surface waters of Loch Ness and the open sea (personal communication). Some success has been found using this method for the spar in the Tamar, but better results have been achieved using the model ship manoeuvring tank at the Institute of Marine Studies at Polytechnic South West.

It may be desirable to decide which of the sensors is giving the best absolute measure of the temperature of the isothermal fluid, so that the others can be calibrated against it, and so that a correlation can be made with salinity measurements. This involves deciding what the temperature is by other means.

It may never be possible to get the spar to measure temperature with an accuracy better than 0.1°C , but every sensor will tell the same story and with fine resolution, so that thermal structures and subtle changes will be represented well.

7. Preliminary data from field trials

The spar was given its first full trials on the Tamar Estuary on 22nd February 1989. The vessel used for pushing the instrument through the water was RV Catfish of Polytechnic South West's Institute of Marine Studies. Axial surveys were repeated for sections of the estuary where it was felt a significant vertical temperature gradient might exist. The area examined was near the Tamar suspension bridge at Saltash, this being the furthest point up the estuary, near to the suspected position of the salt intrusion, that it was considered safe to go with an experimental spar. After several problems with noise contamination had been solved the data from the spar looked promising. On this occasion two constant resistance, or "dummy", sensors were employed as a check on system noise. These were both showing variations about a constant signal of only $5 - 10\text{m}^{\circ}\text{C}$, when the noise contamination had been removed. As an exercise, to test the reliability of the instrument during motion through the water, the spar was pushed all the way from the Tamar bridge to Mayflower Marina, recording temperature data continuously.

Figure 10 indicates the area of the exercise and the course taken. The data was collected from all 16 sensors at 10Hz in ten minute bursts. There were mostly 15 - 20 second gaps between bursts and on one occasion, near the end of the exercise, a three minute gap. This data then represents a nearly continuous record of the estuary temperature structure for the lower reaches. There are nine such ten

minute samples.

Two typical ten minute records are presented here in the form of raw data plotted as time series for each operational sensor (there were two dummies, and two sensors that failed on that day) in Figure 11 and Figure 12. The data consists of the first two ten minute samples collected near the Tamar suspension bridge at Saltash. This then is twenty minutes (equivalent to 1800m over ground) of continuous data. Also presented are four graphs depicting processed data. Figures 13, 14, 15 and 16 are plots of isotherms contoured around the raw data.

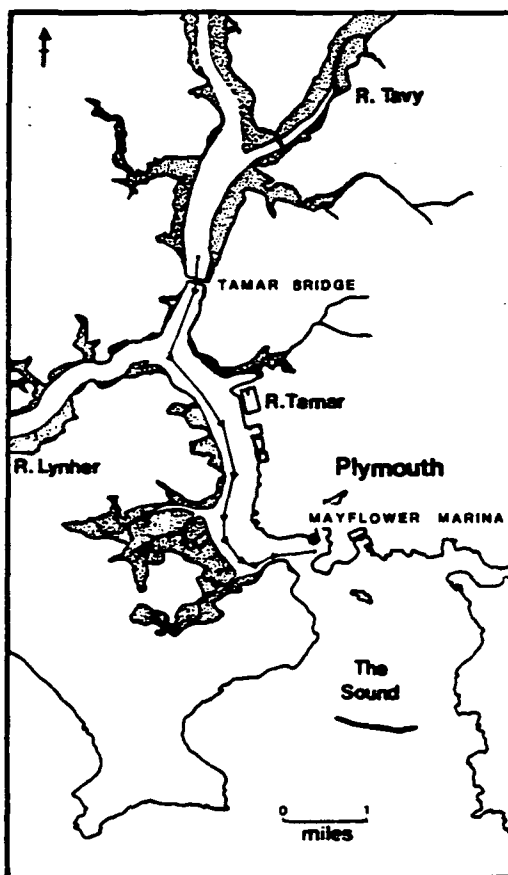


Fig. 10: A map showing the area in the Tamar Estuary where the exercise was conducted. The course steered by RV Catfish is indicated.

Figure 11 and Figure 12 have time series plotted from the bottom, shown in the same order as the sensors occur on the spar. Thus the bottom time series is for the sensor at 3.75m depth and the top series is for that at 0.25m depth. The series are offset by a constant amount (0.25°C) and the scale of the graph is indicated on the vertical axis ($0 - 4^{\circ}\text{C}$). The bottom

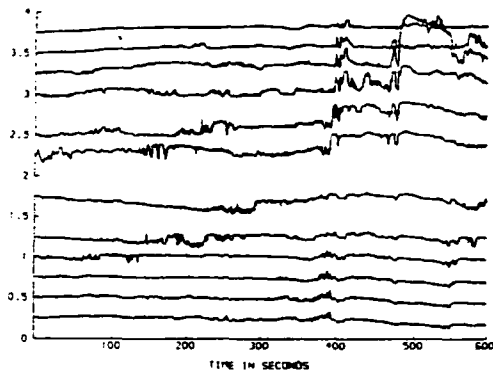


Fig. 11: The temperature time series for each operational sensor, starting at 14:24 hours. The vertical axis is scaled in degrees celsius, and the graph shows relative rather than absolute variations in temperature.

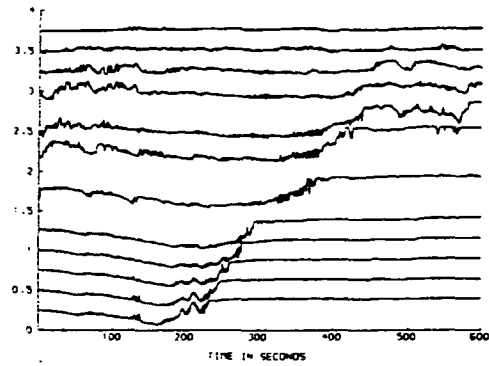


Fig. 12: The temperature time series for each operational sensor, starting at 14:34 hours. The vertical axis is scaled in degrees celsius, and the graph shows relative rather than absolute variations in temperature.



Fig. 13: Isotherm contours for the first 300 seconds of data collected in the ten minute burst starting at 14:24 hours, on 22nd February 1989.

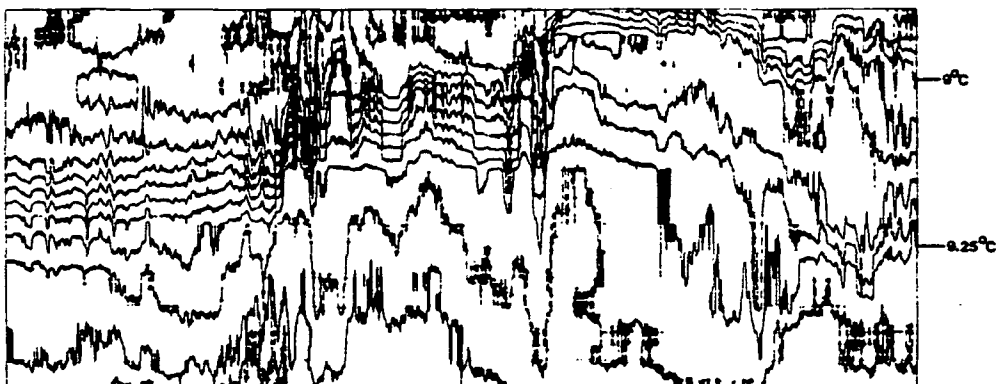


Fig. 14: Isotherm contours for the last 300 seconds of data collected in the ten minute burst starting at 14:24 hours, on 22nd February 1989.

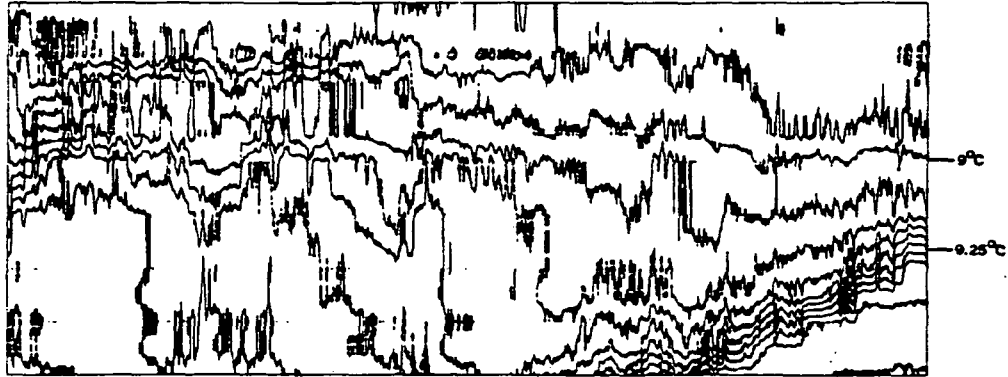


Fig. 15: Isotherm contours for the first 300 seconds of data collected in the ten minute burst starting at 14:34 hours, on 22nd February 1989.

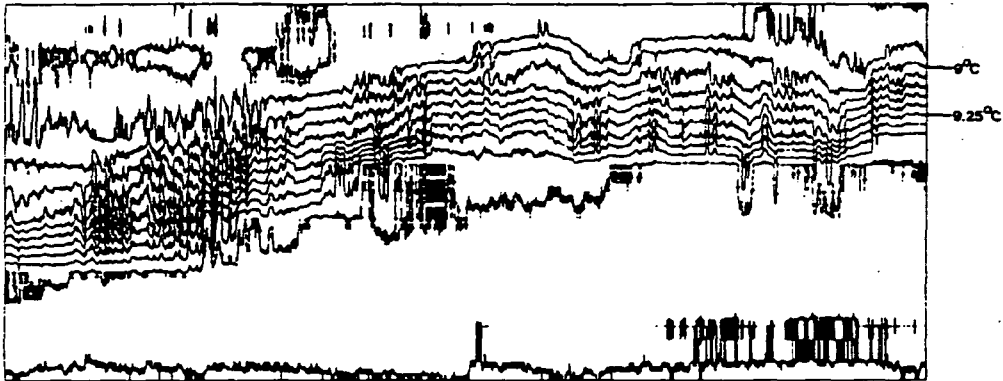


Fig. 16: Isotherm contours for the last 300 seconds of data collected in the ten minute burst starting at 14:34 hours, on 22nd February 1989.

axis indicates time elapsed, in seconds, during that sample period. Note the missing series corresponding to "dummy" or non-operational sensors. The series show relative, rather than absolute, variations in temperature.

The isotherm contour maps are split into two parts for each ten minute burst of data to try to establish a more natural scaling. Figures 13 to 16 represent sections of the water column 3.75m deep by 300 seconds long. Using the average speed of the boat through the water this can be converted to distance. Then each figure is a thermal map representing a vertical section of the estuary of dimensions 3.75m by approximately 450m. The contours are spaced 0.05°C apart, and the values of two of the contours are indicated. It is interesting to note how temperature variations in the time series translate to vertical variations in the isotherms (i.e. from Figure 11 to Figs. 13 and 14 and from Figure 12 to Figs. 15 and 16), depending on the size of the vertical temperature gradient in which the variations occur.

In all of the isotherm contour maps there is a strong vertical temperature gradient present at depths ranging from 0.25m to 3.75m which is undoubtedly the thermocline signature of the salt intrusion. The picture presented by the complete data

set (not depicted here) is of a strong salt intrusion with a thermocline which rises in the seaward direction (always on the right in the figures enclosed). The thermocline is not always shallowly sloping and horizontal, and disappears eventually near Plymouth Sound, but is omnipresent.

The overall impression gained from the data is that there are rich and subtle structures present which may be impossible to detect using any other kind of instrument. This seems especially true for wave-like oscillations found on the isotherms which form the thermocline. Future work with the spar will examine these features in detail.

Acknowledgements

We would like to thank Alan Hall of the Institute of Oceanographic Sciences Deacon Laboratory for advice with the design, and help with potting the thermistors.

References

1. Bendat J.S., Piersol A.G. 1986. *Random data analysis and measurement procedures* J. Wiley and sons.
2. Carr J.J., 1983. *Linear IC-OP AMP handbook - 2nd edition* TAB books Inc.

3. Gregg M. et al. 1978. *Low noise temperature microstructure measurements with thermistors* Deep Sea Research 25.843-856.
4. Hall A.J., Packwood A.R. 1987. *The towed thermistor spar* Fifth international conference on electronics for Ocean technology, Edinburgh, March 1987. London IERE (p. 13-19).
5. Soulsby R.L., 1980. *Selecting record length and digitisation rate for near bed turbulence measurements* Journal of Physical Oceanography 10.208-219.
6. Thorpe S.A., Hall A.J., 1987. *Bubble clouds and temperature anomalies in the upper ocean* Nature 328(6125), 48-51.

The Hydrographic Journal No. 55 January 1990

© 1990 — The Hydrographic Society